CIVIL ENGINEERING JOURNAL

číslo 3/2022

Obsah:

29	**SEISMIC VULNERABILITY ANALYSIS OF CABLE-STAYED BRIDGE DURING ROTATION CONSTRUCTION** *Wang Sukang, Sun Quansheng,Yu Haitao and Wang Hongyang*
30	**EXPERIMENTAL RESEARCH ON THE VIBRATION CHARACTERISTICS OF BRIDGE'S HORIZONTAL ROTATION SYSTEM** *Jiawei Wang, Bing Cao, Bo Huang and Yihan Du*
31	**THE COMPARATIVE STUDY OF THE PERFORMANCE OF CONCRETE MADE FROM RECYCLED SAND** *Chiraz Kechkar, Leila kherraf, Assia Abdelouahid and Houria Hebhoub*
32	**THE MULTI-FACTOR CONTROL AND EVALUATION OF HIGHWAY SOFT SOIL SUBGRADE STABILITY** *Ming Zhang, Nan-nan Li and Min Yang*
33	**TRATA SUBSIDENCE CHARACTERISTICS OF SHIELD TUNNELING IN COASTAL SOFT SOIL AREA** *Qingming Xiang , Youqian Gao, Jiaxuan Su, Xiaoshuang Li and Xuansheng Cheng*
34	**ANALYSIS OF CONTACT FRICTION BEHAVIOR IN THE BENDING PROCESS OF SEMI-PARALLEL STEEL WIRE CABLE** *Jianxi Yang, Hongyu Fei ,Quansheng Sun and Xiang Wei Hao*
35	**RESEARCH ON THE APPLICATION OF PILE-BUCKET COMPOSITE STRUCTURE IN THE SILT COAST** *Yao Liu, Jintian Chen and Wu Li*
36	**BEARING CAPACITY OF T BEAM UNDER DIFFERENT PRESTRESS LEVELS: FULL-SCALE EXPERIMENT AND FEM ANALYSIS** *Long Liu and Jinyan Ma*
37	**STUDY ON TIME-DEPENDENT OF BEARING CAPACITY OF OFFSHORE LARGE-DIAMETER MONOPILES** *Suchun Yang, Qiang Chen, Shean Bie and Fubo He*
38	**MECHANICAL CHARACTERISTICS AND DEFORMATION LAW OF TUNNEL IN DIATOMITE CONSIDERING VARIOUS SOFTENING CONDITIONS** *Wei Fang, Huijian Zhang, Shufeng Gao, Yuchao Zheng, Gongning Liu*

CIVIL ENGINEERING JOURNAL

Article no. 29

THE CIVIL ENGINEERING JOURNAL 3-2022

SEISMIC VULNERABILITY ANALYSIS OF CABLE-STAYED BRIDGE DURING ROTATION CONSTRUCTION

Wang Sukang, Sun Quansheng,Yu Haitao and Wang Hongyang

Department of Civil Engineering, Northeast Forestry University, Harbin， 150040, China; wangsukang2021@126.com

ABSTRACT

Due to the swivel construction, the structural redundancy of cable-stayed bridge is reduced, and its seismic vulnerability is significantly higher than that of non-swirling construction structure and its own state of formation. Therefore, it is particularly important to study the damage changes of each component and stage system during the swivel construction of cable-stayed bridge under different horizontal earthquakes. Based on the construction of Rotary Cable-stayed Bridge in Haxi Street, the calculation formula of damage exceeding probability is established based on reliability theory, and the damage calibration of cable-stayed bridge components is carried out, and the finite element model of cable-stayed bridge rotating structure is established. The vulnerable parts of the main tower and the stay cable components of the cable-stayed bridge are identified and the incremental dynamic analysis is carried out. Finally, the seismic vulnerability curves of the main tower section, the stay cable and the rotating system are established. The results of the study show that the vulnerable areas of the H-shaped bridge towers are the abrupt changes in the main tower section near the upper and lower beams, and the vulnerable diagonal cables are the long cables anchored to the beam ends and the short cables near the main tower. At the same seismic level, the damage exceedance probability of main tower vulnerable section of cable-stayed bridge under transverse earthquake is greater than that under longitudinal earthquake, the damage exceedance probability of vulnerable stay cables under transverse seismic action is less than that under longitudinal seismic action. On the premise of the same damage probability, the required ground motion intensity of the system can be reduced by 0.35g at most compared with the component. Under the same seismic intensity, the system damage probability is 6.60 % higher than the component damage probability at most. The research results have reference significance for the construction of rotating cable-stayed bridges in areas lacking seismic records.

KEYWORDS

Bridge engineering, Rotational cable-stayed bridge, Earthquake, Vulnerability analysis, System damage

INTRODUCTION

Earthquakes are accidental loads and may occur at all stages of bridge construction. The unfinished Mingshi Strait Bridge in Japan in 1995 was struck by an earthquake of magnitude 7.2, which resulted in displacement of the main tower foundation and the anchor ingot of the main cable, and the mid-span elevation of the stiffening girder by 1.27 meters [1]. In 1999, a strong earthquake with magnitude 7.3 occurred in Jixian County, Taiwan, which resulted in the main tower damage, cable damage and shear failure of the anti-seismic pin and tie of the Jilu Bridge under construction near the epicentre [2]. In the 2008 Wenchuan earthquake, the main girder of the Miaoziping Minjiang Bridge under construction was dropped [3]. The possibility of seismic damage in bridge construction. For the rotating cable-stayed bridge, in the construction process, it not only shows the characteristics

DOI 10.14311/CEJ.2022.03.0029

of its flexible bridge, but also has the characteristics of architecture, when the earthquake comes, the redundancy is extremely low and the vulnerability is strong. Through seismic vulnerability analysis of swivel cable-stayed bridge during construction, corresponding theoretical support is provided for design and construction in order to effectively reduce or avoid structural damage caused by earthquake during bridge construction.

Seismic vulnerability analysis of cable-stayed bridge is based on continuous beam and rigid frame bridge. With the continuous construction of long-span cable-stayed bridge, near-field seismic cable-stayed bridge and fault zone cable-stayed bridge in China, the seismic damage of cable-stayed bridge in operation stage reminds us to pay attention to the seismic analysis of cable-stayed bridge, for cable-stayed bridges in potential seismic areas without relevant seismic records, the theoretical analysis method of vulnerability becomes particularly important.

According to the statistics of 30 highway bridges damaged by earthquake by Japanese scholar Kubo [4], the seismic performance of bridges is analyzed by numerical evaluation method. The influence factors such as foundation type, pier height, main beam form and anti-falling beam structure are considered respectively, the vulnerability degree of bridges is judged by designing damage index. Shinozuka [5] obtained a simplified formula by counting the vulnerability of several typical reinforced concrete bridges. Using this formula, the vulnerability curve of similar bridges can be obtained without pushover analysis and dynamic time history analysis. Jong-Su [6] and other scholars used the idea of parameter analysis in the study of seismic vulnerability analysis of urban curved box girder viaducts, and obtained that piers and bearings were vulnerable components, and the damage probability of bearings was higher than that of piers. Karthik et al. [7] considered the influence of the change of seismic design concept on the seismic performance of bridges, and discussed the change of vulnerability curve of the same bridge in the three seismic concepts. Do-Eun [8] analyzes the seismic vulnerability of piers under the premise of corrosion of steel bars in piers. It is concluded that the corrosion of steel bars affects the constitutive relationship of steel bars and core confined concrete in piers, affects the probabilistic demand model, and then affects the change of vulnerability curve. Wu Shaofeng and Shang Guanping [9] studied the vulnerability of longitudinal and transverse ground motions of some single-pylon cable-stayed bridges. The finite element model was established by MIDAS software, and plastic hinge was set up at the weak position of each member. The vulnerability curves of the members and the whole bridge are obtained. Feng Qinghai [10] takes an extra-large cable-stayed bridge as the research object, only the geometric nonlinear factors of the structure are considered, the vulnerable section of the main tower is the bottom section of the main tower and the cross-section of the main tower above and below the cross-beam. GuYin [11] and other scholars studied the seismic vulnerability of low-pylon cable-stayed bridge based on performance. Aiming at the vertical and horizontal seismic input and considering the vertical seismic, incremental dynamic analysis was carried out on the finite element model of cable-stayed bridge, and the vulnerability curve was drawn by calculating the damage probability, the IDA method is feasible and the analysis idea is clear. Shen Guoyu [12] used the “Artificial neural network-orthogonal design method” to calculate the structural capacity, which not only improves the analysis efficiency, but also simplifies the calculation method. Huang Shengnan [13] adjusted the amplitude of the ground motion records and did a nonlinear dynamic analysis of the structure, with the gradual increase of the seismic intensity, the seismic response of the key components is obtained, the IDA curve is drawn, and the vulnerability curve is further obtained. Wang Chongchong [14] did not consider the vulnerability of the main girder and stay cable in the vulnerability analysis of long-span cable-stayed bridge for highway and railway as Ji Zhengdi did. After the time history analysis along the tower height and pier height under the action of multiple seismic waves, the weak section can be clearly located and IDA analysis can be carried out in a directional manner, which reduces the workload of finite element calculation. In the seismic vulnerability analysis of offshore cable-stayed bridge, Gu Qiong [15] considered the influence of chloride ions on the time-varying deterioration of materials. After determining the constitutive relationship of deteriorated materials, the finite element model was established for theoretical analysis, which was consistent with the analysis conclusions of Wu Shaofeng and other scholars, the damage probability of the system was greater than any single component. Thus, the seismic vulnerability analysis of cable-stayed bridge system is necessary. Fabio et al. [16] considered the structural uncertainties by defining a random variable, and used the time-history analysis method to analyze the seismic vulnerability of cable-stayed bridges. Chao [17] and other scholars put forward the vulnerability of offshore cable-stayed bridge under the combined action of marine environment and earthquake, and put forward the change of the overall vulnerability of cable-stayed bridge when considering the pile-soil interaction, the propagation of ground motion in different sand, the erosion of seawater on pile foundation and the change of pile depth. In order to obtain the most suitable ground motion evaluation parameters, Jun [18] and other scholars established a calculation model based on general linear regression. The analysis showed that the prediction ability of peak ground motion velocity on transverse seismic response was poor, and the analysis method was suitable for cable-stayed bridges and continuous girder bridges.

At present, bridge seismic vulnerability analysis has become an important part of bridge seismic theory research. From a large number of research results of the above scholars, most scholars study the vulnerability of cable-stayed bridge from the operation stage, mainly for the vulnerability analysis of key components, the acquisition of seismic parameters, the improvement of mathematical calculation model, the definition of time-varying damage state, and how to improve the calculation efficiency. However, few scholars have carried out research on the seismic vulnerability of cable-stayed bridges during the construction phase. Inspired by the research methods and ideas of the above scholars, this paper will take the large tonnage rotating cable-stayed bridge in northeast China as an example to analyze the seismic vulnerability of the cable-stayed bridge during the rotation process. The number of swivel cable-stayed bridge in our country is more and more, the span is more and more big, and the construction technology is more and more complex. Therefore, the safety performance of swivel cable-stayed bridge under seismic load including construction stage should be fully considered. By analyzing the seismic vulnerability of the rotating cable-stayed bridge in the construction stage, the exceeding probability of the earthquake to the various components of the bridge and the overall damage of the bridge in the construction process of the rotating cable-stayed bridge can be judged, which can play a guiding role in the design, prevention and maintenance of the cable-stayed bridge before construction.

RESEARCH OVERVIEW AND METHODS

Overview of bridges

The span of Haxi cable-stayed bridge is 118m+198m+118m, the span arrangement diagram of cable-stayed bridge is shown in Figure 1. The main beam adopts prestressed concrete π type main beam, concrete C60, according to A type prestressed system design. The stay cables are fan-shaped with double cable planes, and there are 112 stay cables in the whole bridge. The stay cable is anchored on the outer side of the π type rib plate of the main beam through the anchor block, and the longitudinal standard cable distance is 7 m. The standard strength of stay cable with steel strand is 1860 MPa.

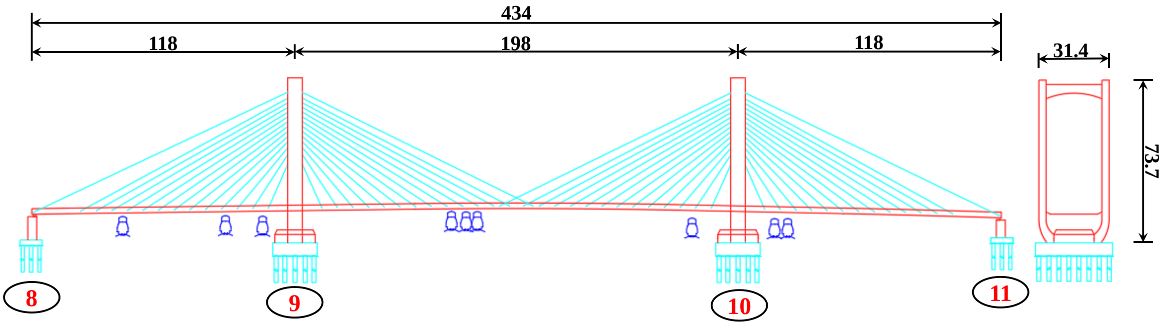

Fig. 1 – Layout diagram of span of cable-stayed bridge with rotation（m）

Cable-stayed bridge main tower height 73.7 m, H-shaped, C50 reinforced concrete structure. The main tower is set with one upper beam and one lower wall. The upper column is box section, the section size is 320cm (transverse)×650cm (longitudinal). The lower tower column is solid wall structure, the cross-sectional dimension is 2400cm~3140cm, the longitudinal dimension is 650cm, the main tower structure diagram is shown in Figure 2.

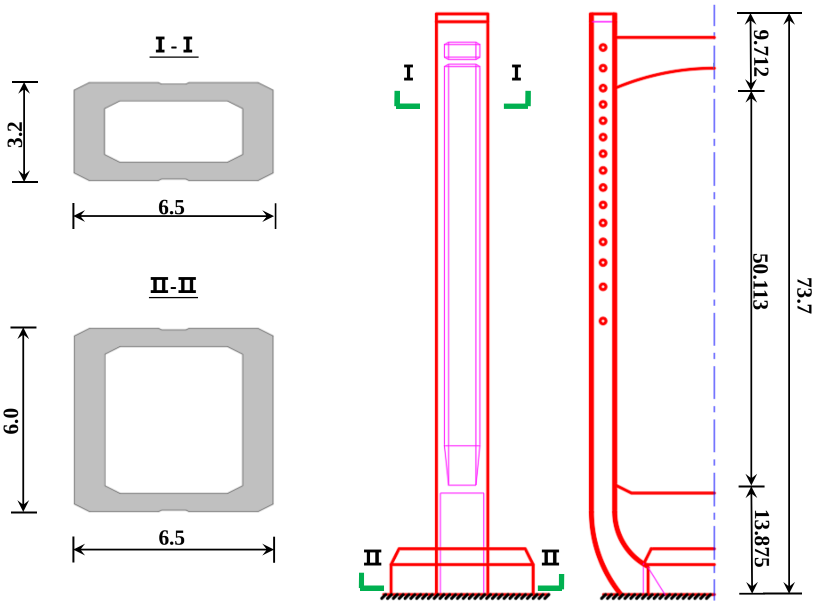

Fig. 2 – Structure diagram of main tower of rotary cable-stayed bridge（m）

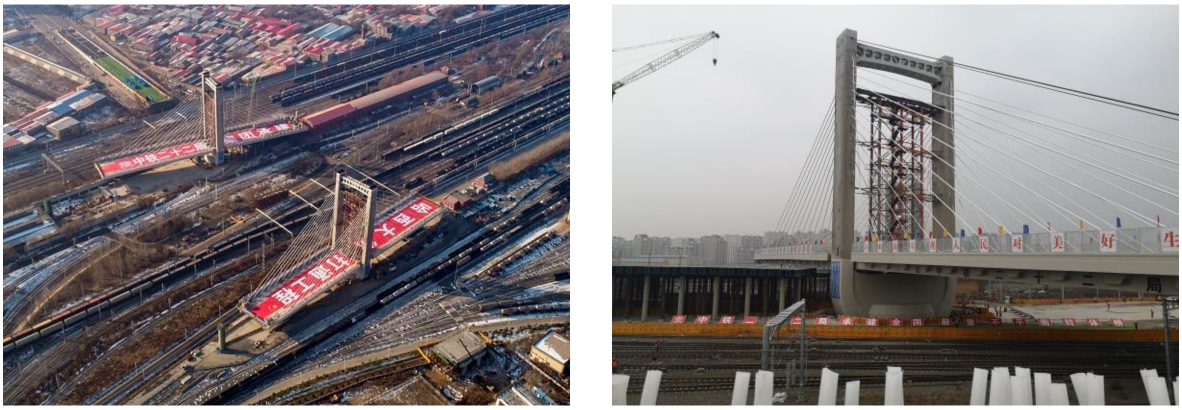

Fig. 3 – Structure diagram of main tower of rotary cable-stayed bridge（m）

Research method of seismic vulnerability of rotary cable-stayed bridge during construction

In the seismic vulnerability analysis, based on the incremental dynamic analysis method, Hwang [19] and Wang Xuewei [20] gave the calculation cases of seismic vulnerability of reinforced concrete girder bridges and long-span cable-stayed bridges in the area lacking ground motion records, and proposed the related research steps of vulnerability analysis. It is summarized into three main parts, namely, the establishment of finite element model, the input of ground motion, the calibration of structural damage index under seismic action, the calculation of structural seismic response and the drawing of vulnerability curve. In this paper, the vulnerability curve is established based on the incremental dynamic analysis method to analyze the seismic vulnerability of the cable-stayed bridge during the rotation construction stage.

Division of Construction Phases of Swivel Cable Stayed Bridge

The construction process of the rotating cable-stayed bridge can be divided into the foundation construction stage, the main pier cap construction stage, the support stage, the maximum cantilever stage, the rotating unsealed hinge stage, and the closing stage. However, due to the great influence of seismic action on the high-rise structure, the construction of the first two stages is below the ground. The embedded effect of structure and soil makes the seismic response of the structure relatively small. In the closure stage, the structure is mainly close to the bridge completion stage. Compared with the support and cantilever stage, the structural redundancy in the rotation stage is the lowest and the mobility is the highest. So, this paper mainly analyzes the seismic vulnerability of the cable-stayed bridge in the rotation stage.

The main components of the cable-stayed bridge in the rotation stage are the main tower, main beam and stay cable. Professor Ye Aijun draws a guiding conclusion in his research results. Under the action of seismic force, the material performance of the main beam is always maintained in the elastic stage and is not easy to damage [21,22]. Therefore, in the seismic vulnerability analysis of rotating cable-stayed bridge in this paper, the target component is the main tower and stay cable.

Seismic vulnerability analysis method of rotating cable-stayed bridge based on incremental dynamic analysis

The incremental dynamic analysis process is: (1) Establish a finite element model of the target structure; (2) Select the appropriate ground motion and amplitude modulation input; (3) Definition of damage indicators; (4) Time history analysis of the structure under various levels of earthquakes.

In this paper, the direct regression method is used to establish the vulnerability curve. Firstly, it is assumed that the logarithm of the seismic capacity of the structure and the logarithm of the seismic demand obey the normal distribution [23]. The probability density function see Equation (1).

$$f(x) = \frac{1}{\sqrt{2\pi}\,\sigma_{\ln x}} e^{\frac{(x-\mu_{\ln x})^2}{2\sigma_{\ln x}^2}} \tag{1}$$

See equation (2) for probability distribution function.

$$F(x) = \int_0^x \frac{1}{\sqrt{2\pi}\,\sigma_{\ln x} x} e^{\frac{(x-\mu_{\ln x})^2}{2\sigma_{\ln x}^2}} dx = \Phi\left(\frac{\ln x - \mu_{\ln x}}{\sigma_{\ln x}}\right) \tag{2}$$

Among them: *x* is the damage variable; $\mu_{\ln x}$ is the logarithmic mean of the random variable *x*; $\sigma_{\ln x}$ is the logarithmic standard deviation of random variable *x*; Φ is the standard form of normal distribution function.

The calculation result of seismic vulnerability is the probability that the structural response exceeds the damage degree at all levels under different seismic intensities. Here, *R* is used to represent the resistance of structural components, and *S* is used to represent the seismic demand. Then, the functional function of components based on the reliability theory is shown in Equation (3).

$$Z = R - S \tag{3}$$

The failure probability (exceedance probability) of structural components is shown in Equation (4).

$$P_f = P(Z < 0) = P\text{（}R - S\text{）} \tag{4}$$

Since the logarithm of *R* and *S* obeys the overall distribution, we can get:

$$\begin{gathered}\ln R \sim N\left(\overline{\ln R}, \sigma_{\ln R}^2\right) \\ \ln S \sim N\left(\overline{\ln S}, \sigma_{\ln S}^2\right)\end{gathered} \tag{5}$$

According to the statistical theory, $\ln R - \ln S$ also obeys the normal distribution, and we can get :

$$(\ln R - \ln S) \sim N\left(\overline{\ln R} - \overline{\ln S}, \sigma_{\ln R}^2 + \sigma_{\ln S}^2\right) \tag{6}$$

Then the failure probability is shown in Equation (7) and Equation (8).

$$P[(\ln R - \ln S) < 0] = P\left[\frac{(\ln R - \ln S) - \left(\overline{\ln R} - \overline{\ln S}\right)}{\sqrt{\sigma_{\ln R}^2 + \sigma_{\ln S}^2}} < \frac{0 - \left(\overline{\ln R} - \overline{\ln S}\right)}{\sqrt{\sigma_{\ln R}^2 + \sigma_{\ln S}^2}}\right] \tag{7}$$

$$P[(\ln R - \ln S) < 0] = \Phi\left(\frac{\overline{\ln S} - \overline{\ln R}}{\sqrt{\sigma_{\ln R}^2 + \sigma_{\ln S}^2}}\right) \tag{8}$$

Among them: $\overline{\ln R}$ is the logarithmic mean of the structural capacity value; $\overline{\ln S}$ is the logarithmic mean of the seismic demand value; $\sigma_{\ln R}$ is the logarithmic standard deviation of the structural capacity; $\sigma_{\ln S}$ is the logarithmic standard deviation of the seismic demand.

When the maximum value $P_{\max}$ under the short-term combination of accidental loads acts on the section when calculating the bending moment-curvature curve, the mean value of the logarithm lnR of the structural capacity value is itself after conservatively considering the randomness of the structure. We only need to consider the randomness of the earthquake, namely:

$$\begin{gathered}\overline{\ln R} = \ln R \\ \sigma_{\ln R} = 0\end{gathered} \tag{9}$$

In this way, the calculation formula for the probability of failure (exceeding probability) is:

$$\begin{aligned}P[(\ln R - \ln S) < 0] &= P\left[\frac{(\ln R - \ln S) - \left(\overline{\ln R} - \overline{\ln S}\right)}{\sigma_{\ln S}} < \frac{0 - \left(\overline{\ln R} - \overline{\ln S}\right)}{\sigma_{\ln S}}\right] \\ &= \Phi\left(\frac{\overline{\ln S} - \ln R}{\sigma_{\ln S}}\right)\end{aligned} \tag{10}$$

The first-order boundary method [24] is used to study the system vulnerability of cable-stayed bridge in swivel stage. Regarding the shape of the cable-stayed bridge at each stage as a series system, according to the reliability theory and ignoring the correlation of various components, the upper and lower bounds of the damage probability of the system at all levels are calculated by Equation (11).

$$\max_{i=1}^{m} [P_{fi}] \leqslant P \leqslant 1 - \prod_{i=1}^{m} [1 - P_{fi}] \tag{11}$$

Among them, P represents the system damage probability; P_{fi} represents the component damage probability, which is the maximum value of the damage exceeding probability of each damage unit (cross section, stay cable) under the same earthquake level.

Damage calibration

The research on damage degree of bridge structural members is one of the main contents of performance-based seismic research. At present, in order to evaluate the damage state of the structure, the damage of concrete members is usually divided into four grades: slight, medium, serious and complete damage.

At present, most scholars use the sectional curvature corresponding to the change of material strain as the damage index of bridge tower structure in the seismic vulnerability analysis of cable-stayed bridges. Various damage situations and corresponding sectional curvature levels are shown in Table 1 [25].

Tab. 1: Curvature damage index

Damage status	Damage feature	Corresponding parameters of curvature level
Slight damage	The first yielding of longitudinal steel bars	$\varepsilon_y < \varepsilon_s \leqslant \varepsilon_{sh}, \varepsilon_c \leqslant 2\varepsilon_{cd}$
Moderate damage	Non-linear deformation appears	$\varepsilon_{sh} < \varepsilon_s \leqslant 0.55\varepsilon_{su}, \quad 2\varepsilon_{co} < \varepsilon_c \leqslant 0.75\varepsilon_{ccu}$
Severe damage	The protective layer concrete is peeling off	$0.55\varepsilon_{su} < \varepsilon_s \leqslant \varepsilon_{su}, \quad 0.75\varepsilon_{ccu} < \varepsilon_c \leqslant \varepsilon_{ccu}$
Eventual failure	Confined concrete core is crushed	$\varepsilon_s > \varepsilon_{su}, \quad \varepsilon_{ccu} \leqslant \varepsilon_c$

Note: ε_s is the tensile strain of longitudinal reinforcement outside the section, ε_c is compressive strain of concrete with outer protective layer, ε_y is tensile yield strain of longitudinal reinforcement, ε_{cd} is the outermost compressive strain of cross-section core concrete, ε_{co} is the ultimate compressive strain of concrete cover with a value of 0.002, ε_{sh} is the initial hardening tensile strain of longitudinal reinforcement, taking 0.015, ε_{su} is the fracture strain of longitudinal reinforcement, and the value is 0.09. ε_{ccu} is the ultimate compressive strain at the outermost edge of the core concrete of the section, which depends on the stirrup structure.

The cable stayed in the cantilevered state in the rotating phase is more likely to have stress exceeding the limit under the action of strong earthquakes. In this paper, the damage calibration method based on the strength and deformation criterion of Wu Shaofeng[9] is adopted, and the stress ratio Equation (12).

$$\alpha_c = \frac{f_{y1}}{R_y^b} \tag{12}$$

Among them, f_{y1} and R_y^b are the cable stress and the ultimate tensile strength of the stay cable under the earthquake. And using the classification method of Professor Wang Jingquan[26] to calibrate the damage index : α_c=0.45 for mild damage, α_c=0.60 for moderate damage, α_c=0.75 for severe damage, α_c=0.90 for complete damage.

Establishment of finite element model

In References [21,22], the seismic plasticity analysis of the main girder of cable-stayed bridge structure is not carried out. At the same time, according to the principle of capacity protection, it is generally expected that the pier, main tower and other components will first enter the plastic stage in bridge design to ensure the safety of the main girder. Therefore, the plastic stage of the main girder is not considered in the seismic response analysis in this paper, the π-type main girder is simulated by elastic beam element. The stay cable component is simulated by nonlinear truss element, and the elastic modulus is corrected by Ernst formula.

In this stage, the main beam and the main tower are temporarily anchoraged by vertical prestress, and the connection between the main beam and the main tower is simulated by rigid connection; The beam end anchorage of stay cable is simulated by rigid master-slave connection, and the main node is the midline node of single beam. The tower end anchorage of stay cable is connected by common nodes; The inertia moment of the modified section of the tower root section is consistent with that of the upper cap; The connection between the upper and lower caps (rotating system) uses the relevant data of the weighing test to convert the rotational stiffness simulation of the elastic connection; There is a 5cm gap between the supporting foot and the slideway in the rotating system, Midas is used to simulate the general connection. The specific operation is as follows: select the spring element in the general connection characteristic value dialog box, define the inelastic characteristic value (clearance element), select the general link, the hysteresis model is "slip double polyline/compression only", and define the yield strength (The yield strength of the support foot is selected here), and the initial gap is 5cm, which simulates the mechanical characteristics of the gap between the support foot and the slide; at the same time, the pile-soil interaction is considered.

RESEARCH RESULTS AND ANALYSIS

Identification of vulnerable parts of rotary cable-stayed bridge

In this paper, the swivel structure of No.9 tower of swivel cable-stayed bridge is selected for vulnerability analysis. Due to the uncertainty of the vulnerable section, the vulnerable section is first identified, which can not only reduce the complexity of the analysis process, but also accurately locate the vulnerable section. At this stage, the main tower and stay cable are selected for vulnerability analysis. According to the site characteristics of the target cable-stayed bridge, 10 seismic waves are selected in the Pacific seismic center, as shown in Table 2, and the finite element model is input in longitudinal and transverse directions.

Tab. 2: Seismic wave name

Earthquake number	Earthquake name	Time	PGA（g）
1# seismic wave	Cape Mendocino	1992	0.1191
2# seismic wave	Chi-Chi Taiwan	1999	0.1777
3# seismic wave	Chuetsu-Koi	2007	0.1920
4# seismic wave	Imperial Valley-06	1979	0.1717
5# seismic wave	Irpinia Italy-01	1980	0.1097
6# seismic wave	Iwate	2008	0.3613
7# seismic wave	Landers	1992	0.2792
8# seismic wave	Loma Prieta	1989	0.1513
9# seismic wave	San Simeon Ca	2003	0.0906
10# seismic wave	Taft Lincoln School	1952	0.1048

When identifying the vulnerable section of the main tower, it mainly analyzes the changes in the section curvature of the main tower components along the height of the main tower under different earthquakes, and the analysis shows that the section with the largest curvature under the earthquake action is the earthquake vulnerable part of the main tower; The stress ratio is selected as the quantitative index for the vulnerability identification of stay cables, that is, the ratio of the stress of stay cables to the ultimate strength of stay cables under ground motion. The analysis shows that the stay cables with the largest stress ratio under seismic action are regarded as vulnerable stay cables.

The amplitude of the ground motion is modulated to 1.0g, under the action of the longitudinal and transverse bridge directions, the curvature envelope diagram of the main tower section of the cable-stayed bridge at the turning stage is shown in Figure 4~5; The stress ratio envelope diagrams of stay cables are shown in Figure 6~7.

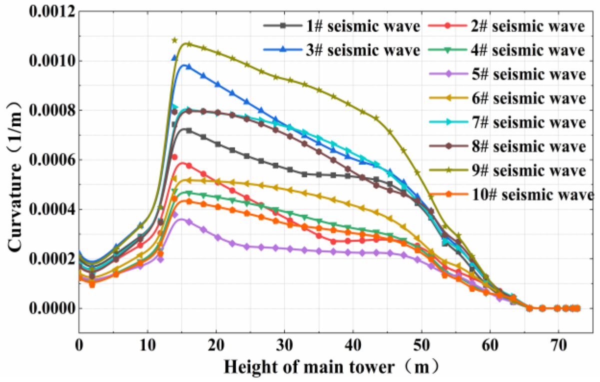

Fig. 4 – Curvature envelope diagram of longitudinal seismic main tower

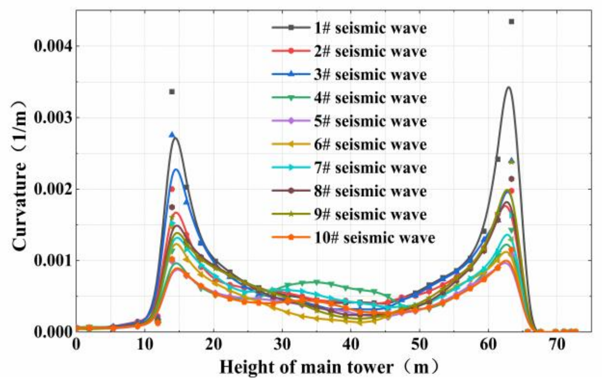

Fig. 5 – Curvature envelope diagram of transverse seismic main tower

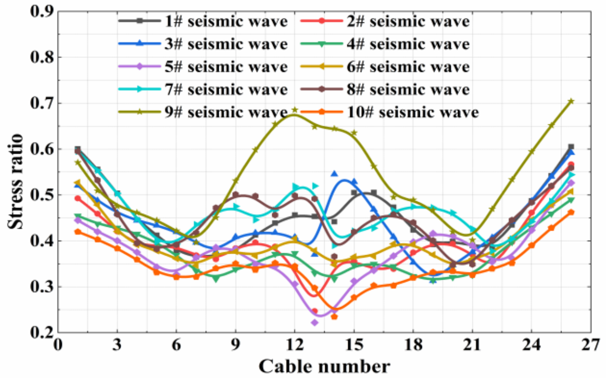

Fig. 6 – Envelope diagram of longitudinal seismic cable stress ratio

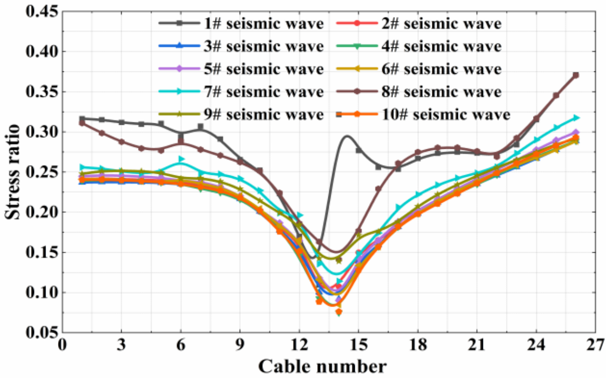

Fig. 7 – Envelope diagram of transverse seismic cable stress ratio

Under the action of 10 longitudinal bridge-directed ground motions with an intensity of 1.0g, the curvature of the main tower changes as follows: The section curvature of the pier from the tower root to the lower beam section decreases first and then increases gradually, and the peak section curvature of the lower column is obtained near the lower beam section; From the lower beam section to the upper beam section, the curvature of the tower column section decreases slowly from the maximum value and then drops sharply to 0. Select the lower tower column curvature peak section, the upper tower column curvature peak section, and the upper tower column curvature reduction rate change section as the longitudinal bridge seismic vulnerability analysis section. The change trend of the cable stress ratio is: At first, the cable stayed at the beam ends on both sides is the peak of the stress ratio, and then the stress ratio gradually decreases from the beam ends to the main tower and then gradually increases to the maximum. The third peak value of stress ratio was obtained in 12# cable. The 1#, 12#, 26# stay cables are selected as the longitudinal bridge seismic vulnerability analysis cables.

Under the action of 10 cross-bridge ground motions with intensity of 1.0 g, the variation trend of the main tower curvature is: The lower tower column gradually increases from the tower root to the lower beam, the section curvature appears two peak positions, namely the section near the lower beam and the section near the upper beam. The two peak curvature sections are set to the cross bridge seismic vulnerability analysis section; The change trend of the cable stress ratio is: From the beam end to the main tower direction, the peak stress ratio of stay cables is obtained at the beam end. The peak stress ratio of 14# cable is obtained under the action of 1# seismic wave. The 1#, 2#, 14#, 25# and 26# stay cables are selected as the horizontal bridge seismic vulnerability analysis stay cables.

In summary, the specific vulnerable stay cables and the vulnerable main tower section are shown in Figure 8~Figure 9. Analysis object : L1 cable, L2 cable, L14 cable, L25 cable and L26 cable on the left cable plane in the forward direction of the bridge are selected for the transverse seismic vulnerability cable, and R1 cable, R12 cable and R26 cable on the right cable plane are selected for the longitudinal seismic vulnerability cable; The cross section of the seismic vulnerable main tower is α section and β section, and the cross section of the seismic vulnerable main tower is γ section, δ section and η section.

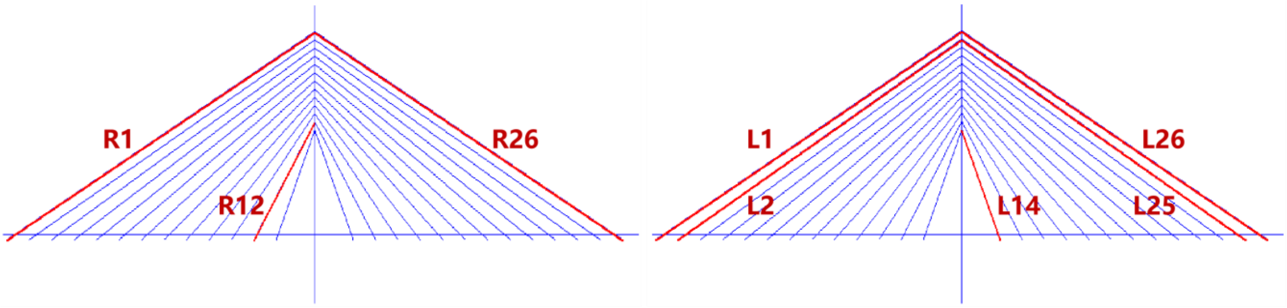

Vulnerable cable in longitudinal earthquake *Vulnerable cable in transverse earthquake*

Fig. 8 – Summary map of vulnerable stay cables

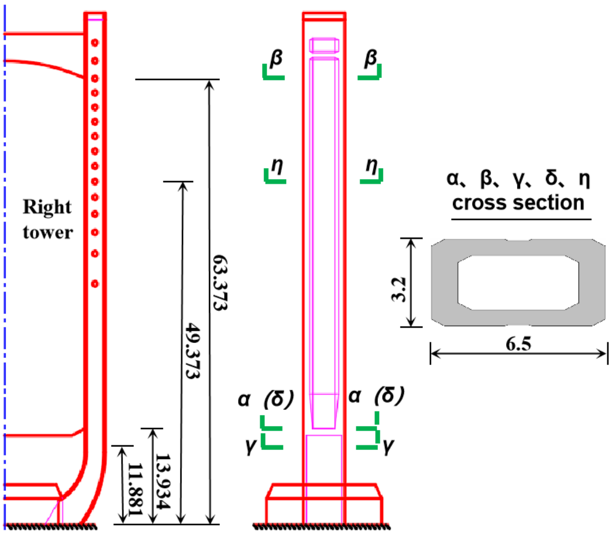

Fig. 9 – Summary of vulnerable section of main tower（m）

Vulnerability analysis of rotation

Vulnerability analysis of the main tower

The calculation of bending moment-curvature curve is to obtain the curvature of compression-bending members under different loads, and then establish the corresponding relationship between the curvature change and the ultimate strain of non-confined concrete, confined concrete and longitudinal reinforcement. Combined with the above damage calibration, the sectional curvature corresponding to each damage level can be calculated to classify the damage level. The section curvature of the main tower section is shown in Table 3 under the seismic action of the longitudinal bridge direction and the transverse bridge direction.

Tab. 3: Calibration table of damage limits of main tower section

Seismic direction	Vulnerable section	Damage grade (1/m)			
		Slight damage	Moderate damage	Severe damage	Complete damage
Transverse direction	α	9.912E-4	1.249E-3	6.943E-3	8.186E-3
	β	8.705E-4	1.169E-3	9.937E-3	12.000E-3
Longitudinal direction	γ	4.248E-4	5.380E-4	6.027E-3	11.21E-3
	δ	4.840E-4	5.936E-4	3.780E-3	4.094E-3
	η	4.554E-4	5.671E-4	4.397E-3	5.013E-3

Figure 10 shows the comparison of the fragility curves of the main tower section of the rotating cable-stayed bridge during the rotating phase.

（1） It can be seen from Figure 10 that under the same of the same seismic level, the damage exceeding probabilities at all levels of the vulnerable section of the cable-stayed bridge in the swivel stage under the action of earthquake are greater than those under the action of the longitudinal earthquake; It can also be found that the damage probabilities of β section at all levels are greater than those of α section under cross-bridge seismic action, within the range of PGA less than 2.5 g, both of them can certainly exceed slight damage, and the possibility of exceeding moderate damage is great, both of them have a small possibility of exceeding severe and complete damage states; It can also be found that the analysis section is more likely to exceed slight damage and medium damage under longitudinal and bridge seismic action, but there is almost no possibility of exceeding serious and complete damage. The exceeding probability of damage at all levels of η section is greater than that of the other two sections during the continuous increase of seismic intensity, and only the probability of exceeding slight damage of PGA in the range of 2.0g~2.5g is slightly less than that of γ section.

（2） According to the slope of the curve in the graph, in the analysis of minor damage and moderate damage, the slope of δ section is small, which indicates that the probability of cross-section damage increases slowly. The slopes of the other four sections are basically the same, and the probability of cross-section damage increases faster; The probability growth rates of α-section and β-section are roughly the same and relatively slow when they exceed severe and complete damage; The η section is less likely to exceed serious damage. In the severe and complete damage analysis of the γ section and the δ section, the slope of the curve indicates that the probability growth rate is the slowest, and the ultimate probability of exceeding is very low, so the two sections almost do not suffer from serious and complete damage.

On the whole, the most vulnerable section of the main tower in the rotation stage is the β section under the cross-bridge seismic action.

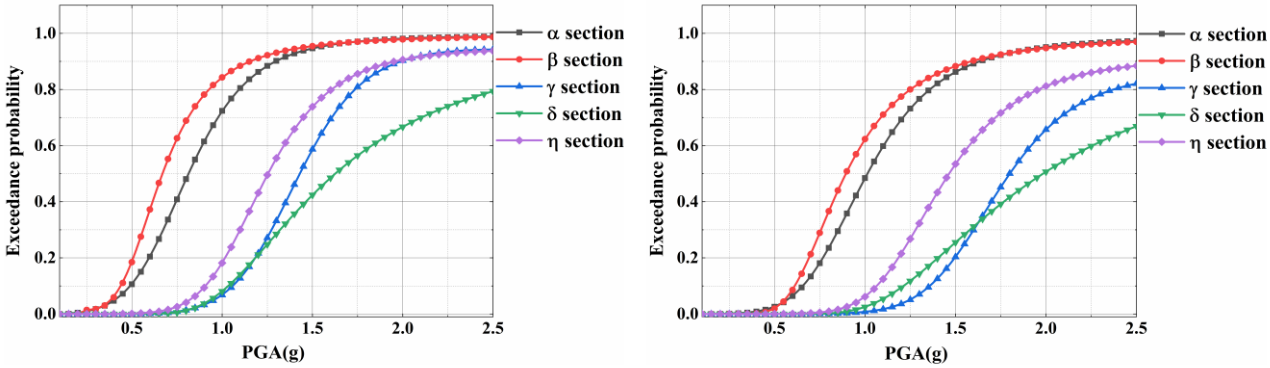

(a) Slight damage　　*(b) Moderate damage*

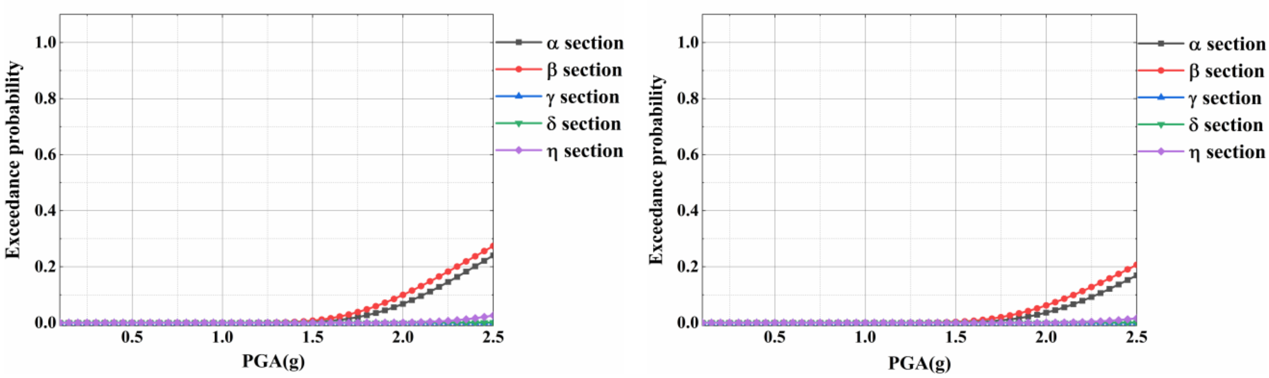

(c) Severe damage *(d) Complete damage*

Fig. 10 – Comparison of section vulnerability curves of main tower in rotation stage

Vulnerability analysis of stay cables

Vulnerability curves of stay cables in swivel stage of swivel cable-stayed bridge are shown in Figure 11.

（1） It can be seen from Figure 11 that the probability of the target stay cable exceeding the damage at all levels under the action of transverse bridge is smaller than that under the action of seismic longitudinal bridge. Under longitudinal bridge seismic action, except that the exceedance probability of R12 cable is slightly larger than that of R1 cable in complete damage analysis, the exceedance probability of other three-level damage is in the order of R26 cable > R1 cable > R12 cable, indicating that the damage probability of long cable at all levels under longitudinal bridge seismic action is large. Under the action of cross-bridge earthquake, the probability of each stay cable exceeding slight damage is large, followed by the probability of exceeding moderate damage, and the damage in turn to almost no exceeding complete damage.

（2） By analyzing the slope of cable vulnerability curve in longitudinal bridge direction, it can be seen that the slope of R26 cable is larger in all levels of damage. The slope of R1 cable and R12 cable vulnerability curve is slightly different in slight damage, and the slope of other levels of damage is roughly the same. It shows that the growth rate of exceedance probability of R26 cable at all levels of damage is the fastest, and the other two cables are followed. It can be seen that in the turning stage of the construction process of the rotating cable-stayed bridge, the stay cable also has the possibility to exceed the damage at all levels, which cannot be ignored.

（3） It can be seen from the analysis of the distribution of cable vulnerability curve in the cross-bridge direction in the figure that the probability of L14 cable exceeding slight damage is slightly smaller than that of L26 cable, and the probability of damage at all levels is the maximum at all levels of seismic level. The analysis shows that the short cable near the main tower in the rotation stage is most likely to be damaged under the cross-bridge seismic action.

Overall, the most vulnerable cable in the rotation stage is R26 cable under longitudinal earthquake.

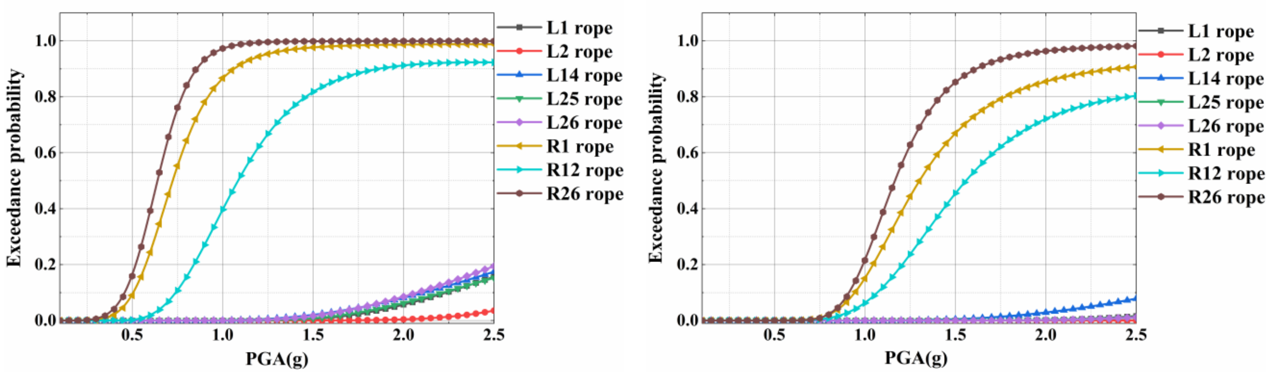

(a) Slight damage (b) Moderate damage

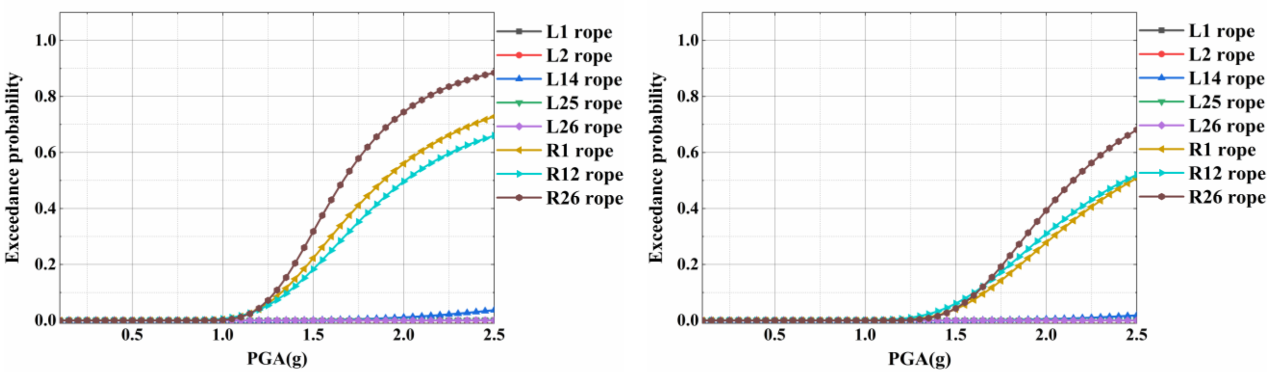

(c) Severe damage (d) Complete damage

Fig. 11 – Comparison of section vulnerability curves of main tower in rotation stage

System vulnerability analysis of rotary cable-stayed bridge

The seismic vulnerability analysis of swivel cable-stayed bridge includes two types of components: main tower and stay cable. The vulnerability curve of cable-stayed bridge system in rotation stage is calculated by Equation (11), as shown in Figures 12–15.

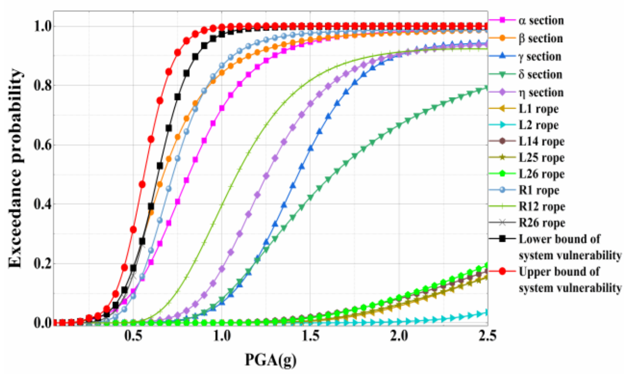

Fig. 12 – Limits of slight damage

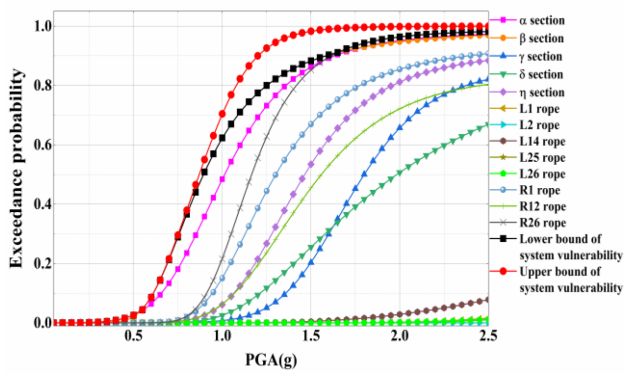

Fig. 13 – Limits of moderate damage

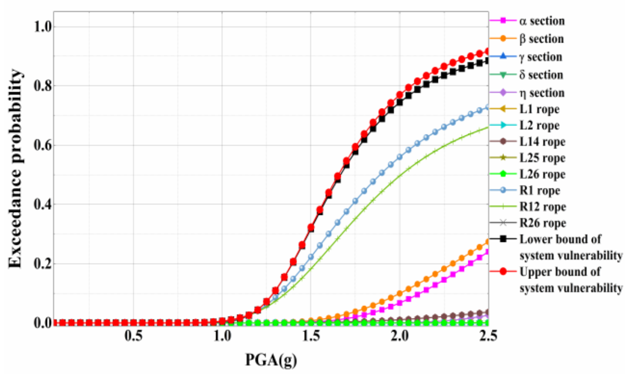

Fig. 14 – Limits of Severe damage

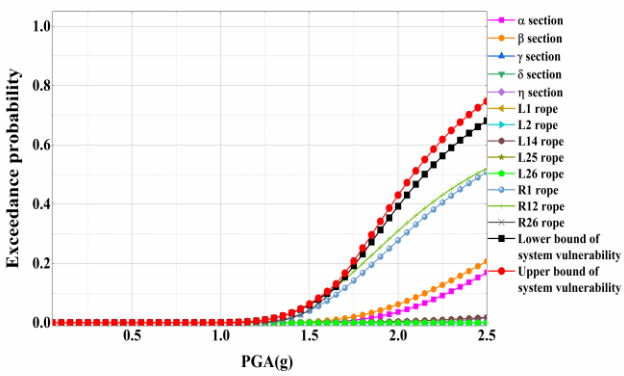

Fig. 15 – Limits of Complete damage

（1）It can be seen from Figs. 12–15 that the upper and lower bounds of the damage probability in the system vulnerability are greater than the damage exceeding probability at all levels of a single component. According to the slope of vulnerability curve, the upper bound probability growth rate of system damage at all levels is the largest.

（2）When the PGA reaches 0.95 g, the exceedance probability of the upper bound of the system slight damage reaches 99.22 %, and the lower bound reaches 99.19 % when the PGA reaches 1.15 g. It is considered that the slight damage must occur at this time. Compared with the vulnerability of the analysis unit in the system, the PGA required earthquake is reduced by at least 0.2 g. When PGA reaches 1.65 g, the upper bound exceeding probability of moderate damage in the system reaches 99.21 %, and the lower bound reaches 97.21 % when PGA reaches 2.15 g. The increase of the lower bound exceeding probability is very low. It is considered that moderate damage must occur at this time. Compared with the vulnerability of the analysis unit in the system, the PGA required for the earthquake is at least 0.35 g. When the PGA reaches 2.5 g, the upper bound exceeding probability of the system serious damage reaches 91.64 %, and the lower bound exceeding probability reaches 88.48 %. It is considered that the possibility of serious damage in the system is very large, and the exceeding probability is increased by 3.16 % compared with the maximum probability of the analysis unit in the system. When PGA reaches 2.5 g, the exceedance probability of the upper bound of the complete damage of the system reaches 74.71 %, and the exceedance probability of the lower bound reaches 68.11 %. It is considered that the possibility of the complete damage of the system is large at this time. Compared with the maximum probability of the analysis unit in the system, the exceedance probability increases by 6.60 % at most.

CONCLUSION

（1）In the rotation stage of cable-stayed bridge, under the action of earthquake, the vulnerable part of the main tower is the section mutation of the main tower near the upper and lower beams, and the vulnerable cable is the long cable at the end of the beam and the short cable near the main tower.

（2）Based on the incremental dynamic analysis method, the seismic fragility curve of vulnerable main tower section is established. When the vulnerable section of the cable-stayed bridge at the turning stage is under the same seismic level, the probability of damage at all levels when the transverse bridge is applied to the earthquake is greater than that of the longitudinal vulnerable section; When PGA does not change within 2.5 g, under the action of cross-bridge earthquake, the probability level of the vulnerable section of the main tower exceeding slight and medium damage is large, and there is little possibility of serious and complete damage; Under the action of the longitudinal bridge earthquake, the vulnerable section of the main tower has a greater probability of exceeding minor and moderate damage, but severe and complete damage will hardly occur; The most vulnerable section of the main tower in the rotation stage is the section near the cross beam of the main tower under the transverse earthquake.

（3）Based on the incremental dynamic analysis method, the seismic vulnerability curve of vulnerable cable is established. The probability that the vulnerable stay cables exceed the damage at all levels in the transverse direction of earthquake is smaller than that in the longitudinal direction of earthquake. The damage probability of cables at all levels under longitudinal bridge earthquake is large. Under the action of cross-bridge earthquake, the probability of each stay cable exceeding slight damage and medium damage is large, and the probability of serious and complete damage is very low, and the possibility of short cable damage near the main tower in the rotation stage is the largest. Therefore, the cable has a high possibility of damage in the construction process, which cannot be ignored. The most vulnerable cable stayed in the rotation phase is the R26 cable under the action of the longitudinal bridge earthquake.

（4）According to the vulnerability curve of the cable-stayed bridge system in the rotation stage, the upper and lower bounds of the damage probability are greater than the damage exceeding probability at all levels of a single component unit, and the growth rate of the upper bound probability of the damage at all levels of the system is the fastest. Under the same damage probability, the required ground motion intensity of the system can be reduced by up to 0.35 g compared with the component. Under the same seismic intensity, the system damage probability is 6.60 % higher than the component damage probability at most. When the PGA does not change within 2.5 g, slight and moderate damage of the system must occur, and the possibility of serious damage and complete damage is large.

To sum up, the seismic vulnerability of the cable-stayed bridge in the rotation stage should not be underestimated. This article has reference significance for the construction of the rotation cable-stayed bridge in areas lacking ground motion records.

ACKNOWLEDGEMENTS

The research in this paper was supported by the Science and Technology Project of the Department of Transportation of Heilongjiang Province (2020HLJ018) and the project of Jilin Province transportation innovation and development support (Science and Technology) (2020-1-9).

REFERENCES

[1] Hu Zhaotong, Liu Jianxin, 1997. Construction characteristics of Mingshi Strait Bridge. Journal of Foreign highway, vol. 1997(06):20-23. doi: 10.14048/j.issn.1671-2579.1997.06.006.

[2] Wang Shengbin, 2003. Earthquake response analysis of a cable-stayed bridge. Papers of the 12th National Conference on Structural Engineering, Addendum of Engineering Mechanics, vol. 2003:112-118.

[3] Zhang Yun, Zhou Xiaorong, Huang Jiadong, 2020. The theory and practice of seismic vulnerability analysis of bridge structures, section 1.4 (Science Press) 10 pp.

[4] Keizaburo Kubo,1984. Earthquake damage prediction of bridges. World Earthquake Engineering, vol. 1984, 4(5):8-11.

[5] Shinozuka Masanobu, 2000. Nonlinear static procedure for fragility curve development. Journal of Engineering Mechanics, voi. 2000,126(12):1287-1295. doi: 10.1061/(ASCE)0733-9399(2000)126:12(1287).

[6] Jong-Su Jeon, Reginald DesRoches, Taesik Kim, et al, 2016. Geometric parameters affecting seismic fragilities of curved multi-frame concrete box-girder bridges with integral abutments. Engineering Structures, vol. 2016,122:121-143. doi: 10.1016/j.engstruct.2016.04.037.

[7] Karthik Ramanathan, Jamie E Padgett, Reginald DesRoches, 2015. Temporal evolution of seismic fragility curves for concrete box-girder bridges in California. Engineering Structures, vol. 2015,97:29-46. doi: 10.1016/j.engstruct.2015.03.069.

[8] Do-Eun Choe, Paolo Gardoni, et al, 2008. Seismic fragility estimates for reinforced concrete bridges subject to corrosion. Structural Safety, vol. 2009,31(4):275-283. doi: 10.1016/j.strusafe.2008.10.001.

[9] Wu Shaofeng, Shangguan Ping, 2010. Seismic fragility analysis of partially cable-stayed bridge with single tower under cross-bridge ground motion. Earthquake Engineering and Engineering Dynamics, vol. 2010,30(02):142-149. doi: 10.13197/j.eeev.2010.02.009.

[10] Feng Qinghai, 2011. Preliminary seismic vulnerability distribution trend of extra-long span cable-stayed bridge. Highway, vol. 2011 (03):46-49.

[11] Gu Yin, Zhong Hua, Zhuo Weidong, 2012. Lower-tower cable-stayed bridge seismic vulnerability analysis. China Civil Engineering Journal, vol. 2012,45(S1):218-222. doi:10.15951/j.tmgcxb.2012.s1.012.

[12] Shen Guoyu, Yuan Wancheng, Pang Yutao, 2013. Cable-stayed bridge seismic fragility analysis. Journal of Tongji University (Natural Science), vol. 2013,41(07):970-976. doi:10.3969/j.issn.0253-374x.2013.07.002.

[13] Huang Shengnan, Yang Desheng, Song Bo, et al, 2014. Seismic vulnerability analysis for long-span cable-stayed bridge. Engineering Mechanics, vol. 2014,31(S1):86-90+98. doi:10.6052/j.issn.1000-4750.2013.04.S026.

[14] Wang Chongchong, 2017. Seismic fragility and risk analysis of long-span road-rail cable-stayed bridge, section 2.3 (Master's thesis, Southwest Jiaotong University) 18 pp. From: https://kns-cnki-net-443.webvpn.nefu.edu.cn/KCMS/detail/detail.aspx?dbname=CMFD201702&filename=1017129658.nh.

[15] Gu Qiong, 2019. Study on probabilistic seismic damage characteristics of offshore cable-stayed bridge under environmental corrosion. Beijing Jiaotong University. doi:10.26944/d.cnki.gbfju.2019.000733.

[16] Fabio Casciati, Gian Paolo Cimellaro, Marco Domaneschi, 2008. Seismic reliability of a cable-stayed bridge retrofitted with hysteretic devices. Computers & Structures, vol. 86(17-18):1769-1781. doi:10.1016/j.compstruc.2008.01.012.

[17] Chao Li, Hong-Nan Li, Hong Hao, et al, 2018. Seismic fragility analyses of sea-crossing cable-stayed bridges subjected to multi-support ground motions on offshore sites. Engineering Structures, vol. 2018,165(15):441-456. doi:10.1016/j.engstruct.2018.03.066.

[18] Junjun Guo, Shahria Alam, Jingquan Wang, et al, 2020. Optimal intensity measures for probabilistic seismic demand models of a cable-stayed bridge based on generalized linear regression models. Soil Dynamics and Earthquake Engineering, vol. 2020,131:106024. doi:10.1016/j.soildyn.2019.106024.

[19] H.Hwang, Liu Jingbo, 2004. Seismic fragility analysis of reinforced concrete bridges. China Civil Engineering Journal, vol. 2004,(06):47-51. doi:10.15951/j.tmgcxb.2004.06.009.

[20] Wang Xuewei, 2017. Failure mode, seismic fragility and risk assessment of rail-cum-road cable-stayed bridge under earthquake excitation (Master's thesis, Southwest Jiaotong University). From: https://kns-cnki-net-443.webvpn.nefu.edu.cn/KCMS/detail/detail.aspx?dbname=CDFDLAST2018&filename=1018824949.nh.

[21] Pang Yutao, Wang Jianguo, et al, 2018. Seismic fragility analysis of continuous rigid frame bridge made from steel fiber reinforced concrete. Journal of Harbin Engineering University, vol. 2018,39(04):687-694. doi:10.11990/jheu.201701020.

[22] Xiao Keli, 2019. Seismic vulnerability analysis and structure optimization of cable-stayed bridges. Southwest Jiaotong University. doi: 10.27414/d.cnki.gxnju.2019.000192.

[23] Huang Zhitang, 2015. Probabilistic seismic fragility and risk analysis of long span continuous rigid frame bridge with high steel tube-reinforced concrete column, section 5.2 (Doctoral dissertation, Southwest Jiaotong University) 98 pp. From: https://kns-cnki-net-443.webvpn.nefu.edu.cn/KCMS/detail/detail.aspx?dbname=CDFDLAST2015&filename=1015348501.nh.

[24] Wu Wenpeng, Li Lifeng, 2018. System seismic fragility analysis methods for bridge structures. Journal of Vibration and Shock, vol. 2018,37(21):273-280. doi: 10.13465/j.cnki.jvs.2018.21.039.

[25] Chen Yue, Zhao Bao, et al, 2018. Impact of parameter variation on seismic vulnerability of cable-stayed bridge. Highway, vol. 2018,63(02),63-67.

[26] Wang Jingquan, Li Shuai, Zhang Fan, 2017. Seismic fragility analysis of long-span cable-stayed bridge lsolated by SMA wire-based smart rubber bearing in near-fault regions. China Journal of Highway and Transport, vol. 2017,30(12):30-39. doi:10.19721/j.cnki.1001-7372.2017.12.004.

Article no. 30

THE CIVIL ENGINEERING JOURNAL 3-2022

EXPERIMENTAL RESEARCH ON THE VIBRATION CHARACTERISTICS OF BRIDGE'S HORIZONTAL ROTATION SYSTEM

Jiawei Wang, Bing Cao, Bo Huang and Yihan Du

Anhui Polytechnic University, School of Architecture and Civil Engineering,
Department of Civil Engineering, Wuhu City, Beijing Middle Road, China;
wjw526@126.com; caobing.0427@163.com.

ABSTRACT

As a new construction method, the bridge horizontal rotation construction method can reduce the impact of traffic under the bridge. During the horizontal rotation of the bridge, the overall structure will inevitably lead to a vibration response due to the construction error of the contact surface of the spherical hinge. Due to the large weight of the structure and the longer cantilever of the superstructure, the vibration at the spherical hinge will be amplified at the girder end, which will adversely affect the stability of the structure. Taking a 10,000-ton rotating bridge as a reference, a scaled model was made to test the vibration of the girder during the rotating process of the horizontal rotating system. And by analyzing the frequency domain curve of girder vibration and the results of simulation calculation, it is found that the vertical vibration displacement response is related to the first three modes of longitudinal bending of the girder structure, but has nothing to do with the higher modes or other modes. Applying the harmonic response analysis module in ANSYS software method, it is proposed that the structural vibration effect will reach the smallest by controlling the rotating speed in order to control the excitation frequency within the first-order mode frequency of girder.

KEYWORDS

Bridge rotation, Horizontal rotation system, Structural vibration test, Finite element simulation, Vibration control

INTRODUCTION

The rotating construction method of the bridge is an important construction method. The bridge is constructed along the parallel direction of the highway and the railway without affecting the traffic. After the bridge is completed, it is rotated 60°-120°along the central axis of rotation under the action of horizontal traction, and finally consolidated the middle and side piers. This is mainly used for the traffic node that crosses some busy roads and railways. The stability of the bridge's horizontal rotation system during the rotation process is the most important factor that will affect construction safety; indeed, the instability of the structure will cause serious accidents.

Presently, the research on structural stability mainly includes static factors and dynamic factors. In terms of static load: Wang Lifeng, Yuan Chongwei and others analyzed the sensitivity of design parameters in the monitoring of rotating construction. In their research, self-weight and concrete elastic modulus are selected. Also, they conduct a force analysis of the rotating structure on static load conditions such as cable tension, concrete shrinkage and creep, and temperature gradient. The results of the study show that the weight, tension and creep of the cable have a greater impact on the stability of the rotation process [1]. In the study of the control and stability of the rotating construction of a large-tonnage continuous rigid frame bridge, Lu Jinhua used the rate of change of deflection θ and the rate of stress change ω as the judgment index of the bridge stability [2]. Based on the analysis of concrete bulk density, the construction process, elastic modulus, overweight on

DOI 10.14311/CEJ.2022.03.0030

one side of the girder, the concrete shrinkage as well as the creep on the rotating bridge and the static wind load on the stability of the transverse bridge, they conclude that concrete bulk density, the change of tension control stress exerts a significant impact on the construction accuracy. Also, it is concluded that the influence of parameters such as the extension of the closing time on the bridge is within a controllable range. In the sensitivity analysis of the construction parameters of the large-span turning. When the static wind load acts alone, the center of rotation (the position of the spherical hinge) will not overturn [3-4]. Ma Shufen proposed that pre-stress effect and bulk density are the sensitive factors among the material factors, and the modulus of elasticity is the secondary factor. The temperature effect is the main sensitive factor, while the shrinkage and creep of concrete is the secondary sensitive factor [5].

In terms of dynamic factors, Xu Chao, Wang Changfeng and others used theoretical mechanics and material mechanics to derive and analyze the torque during the acceleration of the bridge rotation during the start-up phase of the construction of the bridge, and simplified the torque to the shear stress of the temporary support. In their research, they analyzed the influence of the bearing capacity of the temporary support with and without the stirrups, which provides a reference for the check calculation of the temporary support during the construction process [6]. Huang Weiwen used ANSYS software to establish a finite element model [7], and applied it to comparing and analyzing the dynamic characteristics of the rotating bridge so as to study the impact of wind loads on the main girder structure. The results show that the natural frequency of the maximum cantilever state is much lower than that of the bridge state and that the stability during rotation is poor because of its lower stiffness; the static wind response calculated according to the specification is the most unfavorable working condition. Gao Ri et al. studied the influence of train-induced vibration on the stability of rotating construction by using acceleration sensors to test the vibration of the bridge foundation when different trains passed. The results uncover that the train-induced vibration exerts little effect on the stability of the structure, and the vibration displacement and acceleration of the girder are less than the seismic fortification intensity value of the region [8]. Wang Changjie and He Wei analyzed the seismic response of a T-shaped rigid frame rotating bridge in the completed state, and calculated the bending moment envelope diagram of the main girder and piers of the superstructure under earthquake action by the response spectrum method. It is also found in the study that the structure is always in a state of elastic stress, and that the load-bearing capacity of the structure meets the design requirements [9].

During the production process of concrete and steel structure spherical hinges, certain flatness errors will inevitably occur. The bridge will cause self-excited vibration during the rotation process. When the frequency of the vibration reaches or approaches the natural frequency of the structure, it will cause violent vibration. Hence, research on the aforementioned factors should be paid enough attention.

MODEL TEST OF BRIDGE HORIZONTAL ROTATION SYSTEM

Model design

The bridge horizontal rotation system is generally composed of five parts: the superstructure, the pier, the cap and the hinge structure. The upper structure of a continuous rigid frame bridge is generally about 100m, and the length of a single cantilever is 50m. The scale of the model is 1/50: the girder adopts two 2-meter-long HW150x150 steel, the bridge pier adopting a reinforced concrete structure with a length, width and height of 400,200,500 mm separately, and 12 vertical compression steel bars of 14 mm, 6 of 8 mm stirrups respectively. The length, width, and height of the platform are 400, 400, and 150 mm respectively. The concrete spherical hinge structure between the caps, the diameter of the spherical hinge is 10 cm, the thickness is 5 cm, and the radius of the convex and concave surfaces of the spherical hinge is 0.225 m. In order to test the compressive stress distribution during the horizontal rotation of the spherical hinge, 17 stress measuring holes are uniformly arranged along the radial direction in the steel structure spherical hinge, located at 1/4R, 1/2R, 3/4R, and R respectively. The rotating model is shown in Figure 2-1. The vibration of the structure is collected by the 941-B vibration pickup, as shown in Figure 2-2.

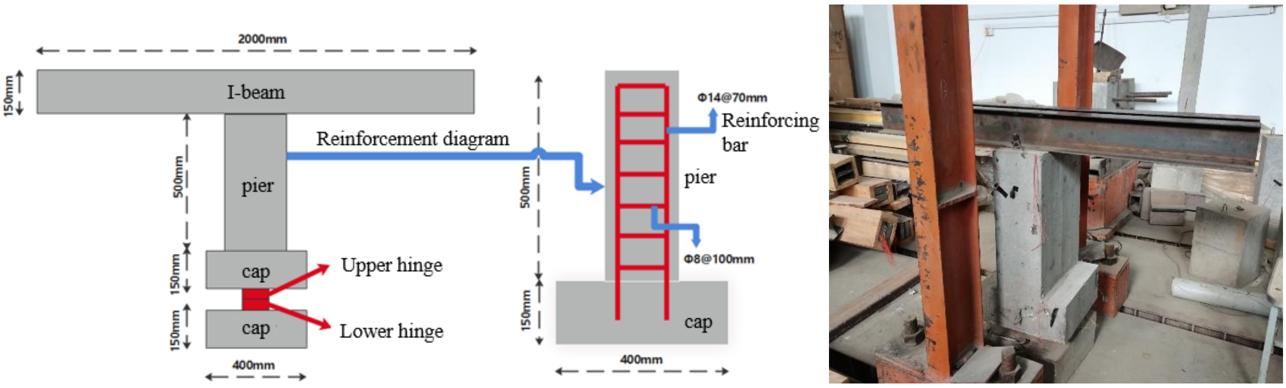

(a) *Model design* (b) *Model production*

Fig.2-1 Swivel model

(a) *Sensors at the girder end* (b)*Sensor debugging*

Fig. 2-2 Vibration test of girder

Vibration test during horizontal rotation

In the research, the continuous rigid frame bridge swivel model is placed on the rotating table, and two 941-B seismic vibration pick-up on both sides of the girder end are used to test the vertical vibration of the girder during the rotation, as shown in Figure 2-3.

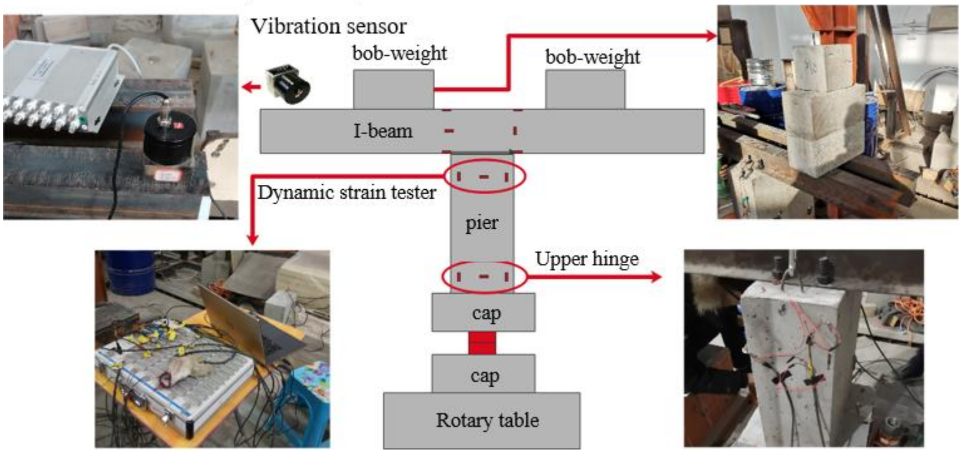

Fig.2-3 Rotation test and vibration test

Model making

The swivel model is poured into the girder field, and the piers and caps are made according to the design dimensions, and the cement, coarse aggregate, fine aggregate and other materials required for the C30 concrete are prepared. Based on the design, the steel frame in the cap and the pier body are tied up; then install the measuring point stress sensor on the stirrups and main bars in the measuring point. Then the concrete is poured; the standard maintenance lasts for 28 days. After the pier body is formed, bolts are implanted on the top of the pier, and two I-girders are installed on the top. Finally, the girder and pier strain gauge are pasted. The prefabrication process of the swivel model is shown in Figure 2-4. Before pasting the strain gauges, it is necessary to polish the steel bars, I-girder and concrete surfaces to remove the rusty parts and floating soil on the surface to ensure accurate stress testing. After pasting, the strain gauge should be insulated to prevent short-circuit and failure. Finally, waterproof the strain gauge at the measuring point, and lead the wire out of the model. After the test pier is prefabricated in the girder field, it is necessary to check the structure size, the position of the steel bar and the strength of the pier body. The maximum error between the actual size and design of the swivel model obtained by measurement is 3%; the position and quantity of the steel bars are checked by the steel bar locator, and the deviation range of the steel bars is around 3% to 5%; The concrete was tested, and the measured strengths were 37.1MPa and 38.2MPa respectively. The size and strength of the rotating model meets the design requirements. The supporting radius R_1 of the spherical hinge is 5 cm, the thickness 5 cm, and the radius R of the spherical hinge 22.5 cm. The structure of the spherical hinge is shown in Figure 2-4e. The supporting radius R_1 of the spherical hinge is 5 cm, the thickness 5 cm, and the radius R of the spherical hinge is 22.5 cm. The structure of the spherical hinge is shown in Figure 2-4e.

(a) *Pier body reinforcement skeleton* (b) *Rebar grinding*

(b) *Paste the strain gauge sensor and insulate it* (d) *Consolidation of girder and pier*

Fig.2-4 Prefabrication process of test model

（e）*spherical hinge*

Fig.2-4 Prefabrication process of test model

In order to test the radial compressive stress, sensors are installed at the rotation center and also at the positions of 1/4R, 1/2R, 3/4R, and R. The concrete spherical hinge is poured through a steel formwork, and positioning steel bars are set inside the spherical hinge, and strain gauges are embedded inside, as shown in Figure 2-5.

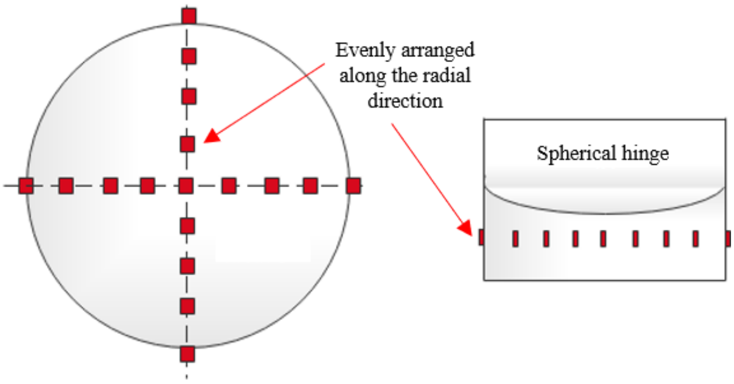

Fig.2-5 Sensor layout

ESTABLISHMENT OF SIMULATION MODEL OF BRIDGE HORIZONTAL ROTATION SYSTEM

Unit selection

This study applies ANSYS software to establish the solid element model of the swivel pier. The girder188 unit is used to establish the girder element model when the flatness error of the concrete spherical hinge was studied on the structural vibration response, and the solid65 element is used to establish the solid element model when the mechanical behavior of the spherical hinge was studied. The force of the spherical hinge during the rotation is actually a contact problem. The analysis of the contact problem is an important issue in elastic mechanics. In order to accurately simulate the relative sliding between the upper and lower spherical hinges, this research uses Contact170 and Contact174. Establish the spherical hinge contact unit [10].

Solid65 is a type of unit commonly used to simulate concrete materials. The characteristic of the unit is that the compressive strength is much greater than the tensile strength (usually about 10 times). It adds concrete strength parameter indexes on the basis of Solid45 unit, which can be used to simulate the state of cracking and crushing of concrete. The Solid65 unit diagram is shown in Figure 3-1. The Solid65 element has eight nodes and is a spatial hexahedron. When the four nodes of K, P, O, and L overlap, the unit turns a spatial tetrahedron. These parameters can be set when the unit is divided into nodes. When the unit is simulating cracking and crushing, attention should be paid to the loading rate. If the speed is too high, the fracture surface will be inaccurate. The spherical hinge model and unit division are shown in Figure 3-2a and b. Girder188 is a spatial three-dimensional finite strain element with 2 nodes [10]. Each node owning 6 degrees of freedom (3 degrees of freedom in translation and 3 degrees of freedom in rotation). The connection line between the two nodes of the girder unit is the X axis of the local coordinate system, and the unit possesses the ability to withstand various deformations; thus, this unit is often used in the girder of the bridge superstructure and can handle linear and nonlinear problems. The model and element division are shown in Figure 3-2c.

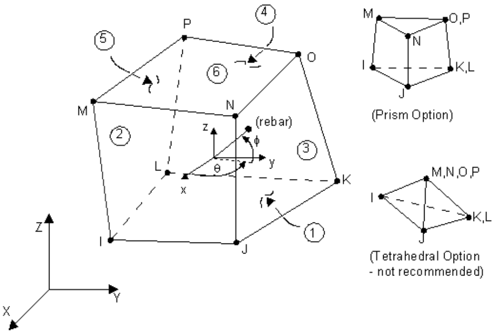

Fig.3-1 Solid 65 unit

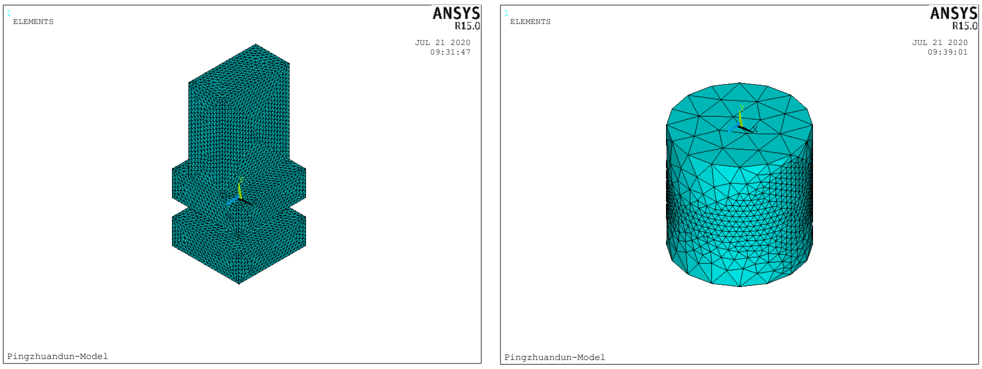

(a) *Solid65 Entity model* (b)*Spherical hinge meshing*

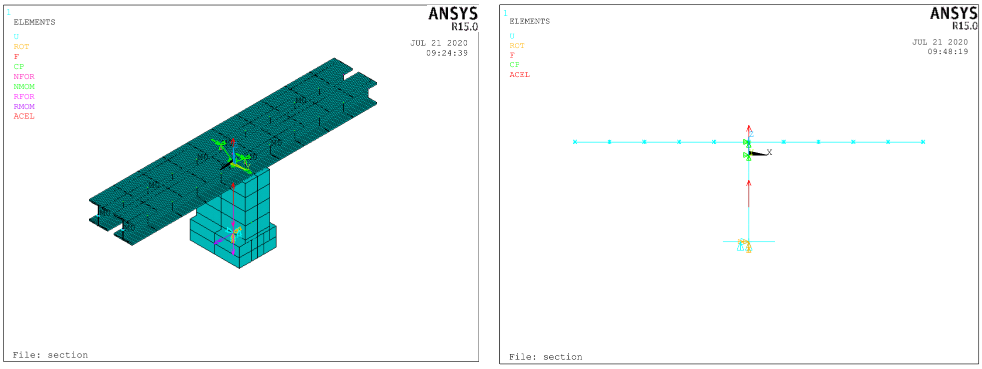

(c) *Girder unit model* (d) *mass21Relationship between unit and the girder*

Fig.3-2 Discrete diagram of ANSYS model element

In order to ensure the accuracy of the calculation of the compressive stress of the spherical hinge, the mesh simulation of the upper and lower spherical hinge contact surface area is encrypted, as shown in Figure 3-2b. And to simulate the counterweight of the upper structure of the main girder, mass21 mass units are set on the girder nodes. The mass unit has a total of six parameters, respectively, the mass *Mx*, *My*, and *Mz* and the moments of inertia *Ixx, Iyy*, and *Izz* in the three directions. The connecting position of the pier and the girder uses the cp command to transfer the bending moment and sheer force of the girder to the pier, as shown in Figure 3-2c. In order to accurately simulate the constraints of the turntable, horizontally, the girder unit model constrains the translational displacements *Ux, Uy* and *Uz* of the nodes at the pier bottom position; vertically, it constraints the rotation *Rotx* and *Rotz*, but relaxes the longitudinal rotation constraint *Roty*. The vertical translational displacement *Uz* of the node is constrained at a position that is 5cm from the center of rotation (the boundary position of the spherical hinge), as shown in Figure 3-2d.

Simulation of Boundary Conditions of Spherical Hinge

The connection between spherical hinges is a contact problem: contact analysis is generally divided into the contact between a rigid body and a flexible body and the contact between a flexible body and a flexible body. In the former study, it is assumed that one or more contact surfaces are rigid bodies, which have greater structural rigidity than flexible bodies. Generally, this method is used to analyze the contact between a soft material and a hard material, mainly used for analysis between steel structure and concrete structure, or concrete and soil structure, etc. The contact analysis between rigid bodies mainly involves their similar or equal structural rigidity. The structure would turn deformed during the whole process of contact. Based on this, this research adopts the flexible body-flexible body contact analysis. The contact methods are divided into three types, point-to-point contact, point-to-surface contact and face-to-face contact, each contact method corresponding to its own set of contact units. Among them, the point-to-point contact situation is like the boundary condition of a simply supported structure. This type of contact requires accurate positioning of the contact point. There could be a small sliding situation between the contact surfaces. At this time, the Contact178, Contact12 and Contact52 units in ANSYS will be used. The point-to-surface contact situation is used for the anchor bolt or orange connection of the steel structure under which condition it is not necessary to accurately locate the specific position of the point and the surface. When larger sliding and deformation are generated between them, the three units of Contact48, Contact49 and Contac26 in ANSYS will be applied. The surface-to-surface direct contact unit is suitable for the face-to-face contact unit of rigid body-flexible body and also flexible body-flexible body. The rigid surface is set as the target unit surface, the flexible surface as the contact unit surface. The target surface uses Targe169 and Targe170 to simulate 2D and 3D surfaces, and the contact surface uses Contact171, Contact172 and Contact173 to simulate 2D and 3D contact surfaces. In this research, the analysis methods of Contact170 and Contact174 elements are used in the finite element contact analysis.

When analyzing the force between spherical hinges, both the compressive stress on the contact surface and the relative sliding friction stress should be taken into consideration. They would act together on the contact surface, which conforms to the relevant theories on the Coulomb friction model. In other words, the cross section remains stationary when the upper and lower surfaces of the spherical hinge are in contact. When a rotational force is generated, the static friction of the cross section prevents this rotational force, and the structure remains stationary. The friction at this time is called the bonding state. When the rotation force reaches a certain limit, the structure begins to have a relative sliding tendency. At this time, the rotation force is greater than the frictional resistance. This state is called the sliding state. In the study, this limit was achieved by defining the coefficient of friction. ANSYS proposes a maximum equivalent shear stress value, which has nothing to do with contact pressure, but is manually specified. When the rotational force is greater than the equivalent shear force, the structure will slide. The TAUMAX value in ANSYS is then set to determine the shear stress value, which is used to solve the problem that the friction calculated in the Coulomb model is greater than the material limit [11-12]. The friction model is shown in Figure 3-3.

RESULTS AND DISCUSSION

Results of structural modal

This research uses ANSYS to calculate the first 6-order mode of the rotating model; the results are shown in Table 4-1 and Figure 4-1.

Tab. 4-1: Six modes in front of swivel pier

Mode Number	Frequency Hz	Vibration form
1	14.213	the girder and the bridge pier bent longitudinally, the 1st mode
2	16.465	The girder twisted transversely, the 1st mode
3	22.168	The girder bent transversely, the 1st mode
4	22.744	the girder transversely, the 2nd mode
5	35.448	the girder bent longitudinally, the 2nd mode
6	49.925	the girder bent longitudinally, the 3rd mode

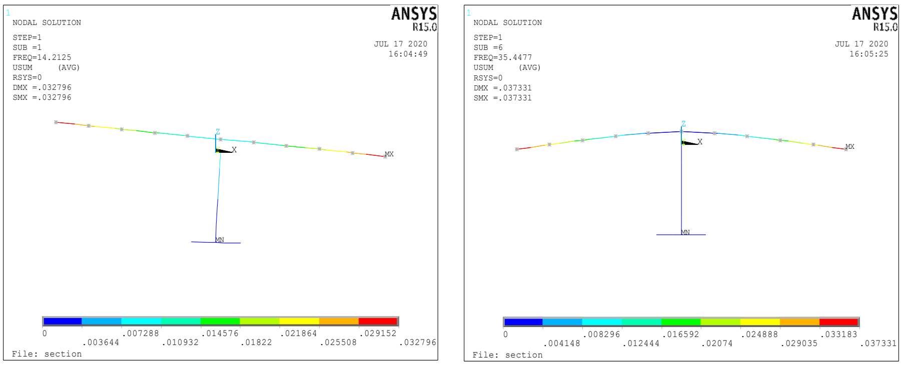

(a) *the girder bent longitudinally, the 1st mode* (b) *the girder bent longitudinally, the 2nd mode*

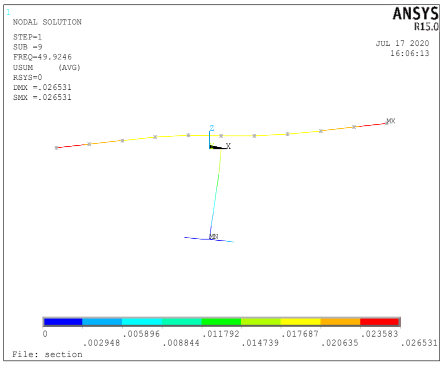

(c) *the girder bent longitudinally, the 3rd mode*

Fig.4-1 - Three modes before longitudinal bending of girder

Vibration test results of girder during horizontal rotation

The girder vibration form is forced vibration, which has nothing to do with the external load during construction. Therefore, the structure itself needs optimizing. The influence of such vibration can be effectively reduced by controlling the rotation speed and changing the boundary conditions of the spherical hinge. In the experiment, the concrete spherical hinge had certain unevenness during the prefabrication process. A displacement vibration picker was installed at the cantilever end of the girder to test the vertical displacement response of the girder during the horizontal rotation. A total of 42.5s was collected during the rotation, and the sampling frequency was 200 Hz. The measured displacement time history curves are shown in Figures 4-2a, 4-3a, and 4-3c, which are converted in the frequency domain, as shown in Figures 4-2b, 4- 3b, 4-3d.

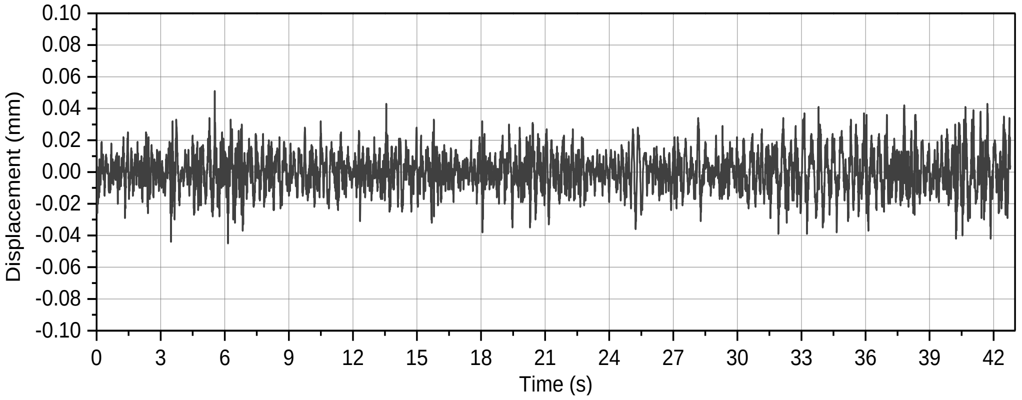

(a) *Displacement time history curve of girder end*

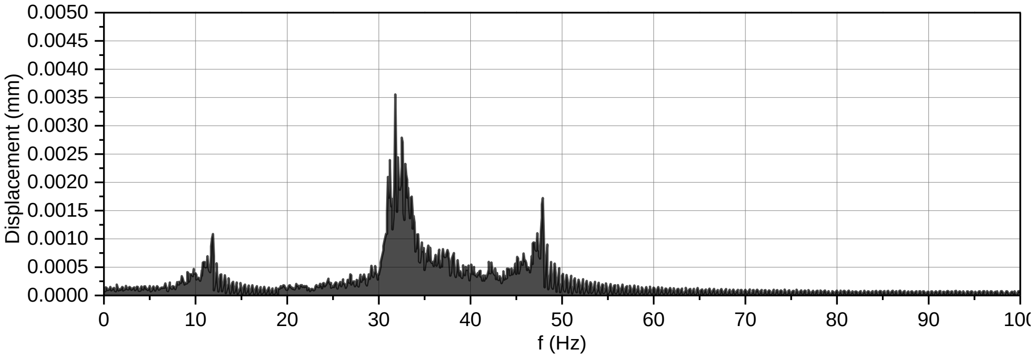

(b) *Frequency domain distribution curve*

Fig.4-2 Displacement time history and frequency domain distribution of girder

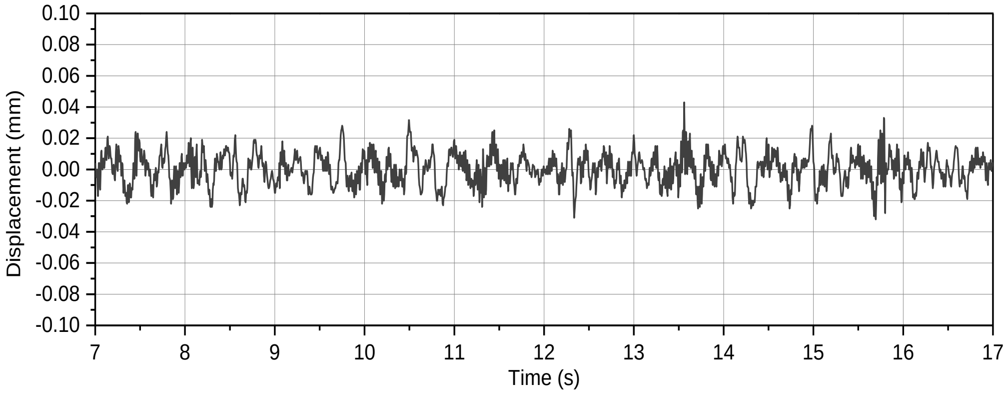

(a) *7-17s Displacement time history curve of girder end*

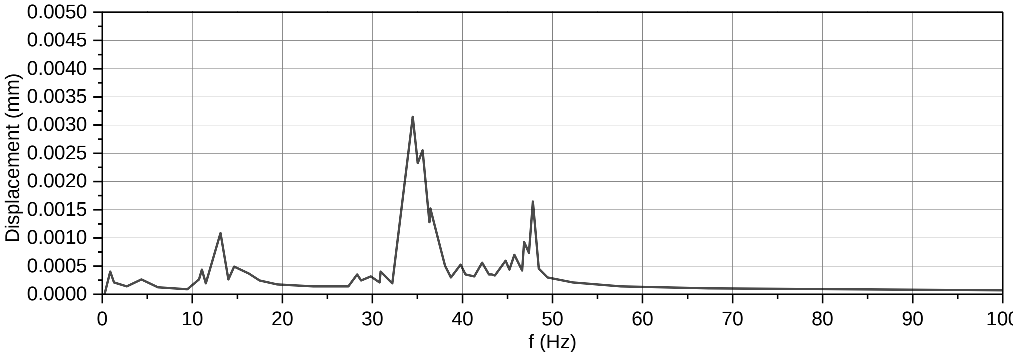

(b) *7-17s Frequency domain distribution curve*

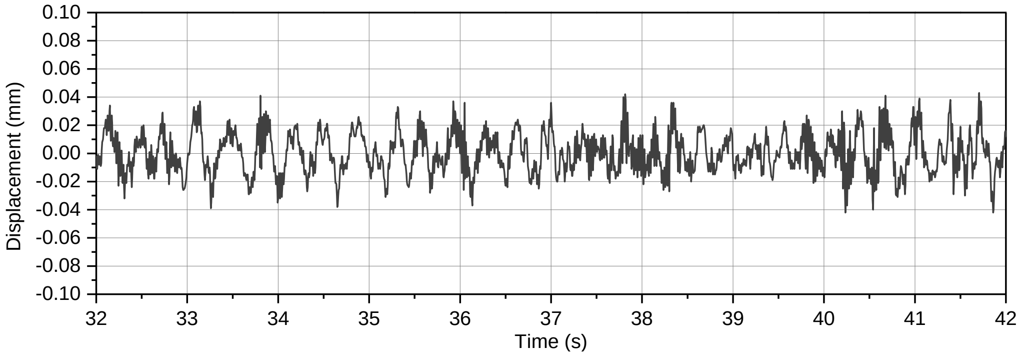

(c) *32-42 s Displacement time history curve of girder end*

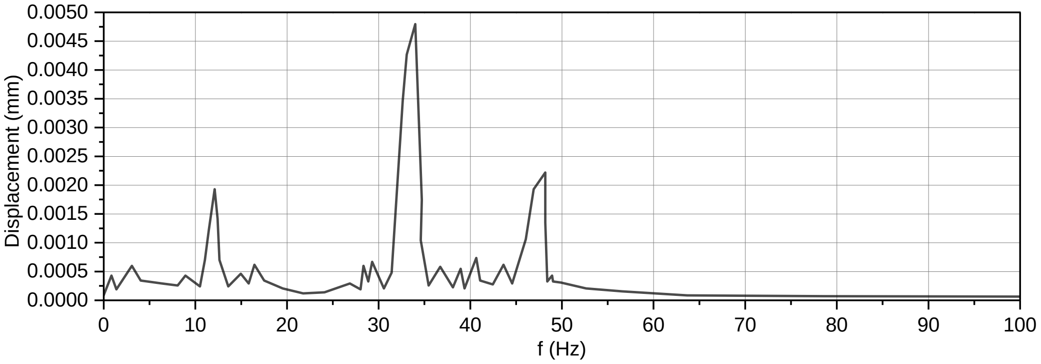

(d) *32-42 s Frequency domain distribution curve*

Fig.4-3 - Time history and frequency domain distribution of displacement in intercepted time interval

Figure 4-2a shows that the maximum vertical displacement value of the cantilever girder end during rotation is only 1/20000 of the span of the cantilever girder. According to the frequency distribution curve, there appear three peak displacements when the frequency reaches 13.1 Hz, 32 Hz, and 48 Hz. In order to obtain the vibration conditions in different periods, the displacement time history curves of the 7-17 s vibration displacement amplitude period are small and the 32-42s vibration displacement amplitude period are larger, as shown in Figure 4-3a and 4-3c. The frequency curve is obtained via Fourier transform. Based on Figure 4-3b and 4-3d, it can be seen that the vertical vibration at the end of the cantilever in the frequency domain space still produces three peak displacements when the frequency reaches13.1 Hz, 32 Hz, and 48 Hz. The three frequency is then tested and turns out to be irrelevant to the time period.

Simulation analysis results

The results of experiments and modal analysis show that during the horizontal rotation of the rotating model, the vibration response of the vertical displacement of the girder end is relatively large when the external excitation frequency reaches the second-order mode frequency of the longitudinal bending of the girder; when it reaches the first and third-order mode frequencies, the pier produces longitudinal unbalanced moments. In order to study the influence of the flatness of the concrete spherical hinge on the vibration of the girder, the flatness of the contact surface was simulated by changing the frequency and position of the dynamic load.

The vibration response of the load of different frequencies to the girder can be analyzed by the harmonic response in ANSYS [10]. In order to simulate the vibration response of the spherical hinge unevenness to the structure, a vertical excitation load is set at the edge of the spherical hinge, the magnitude of which is equal to the supporting reaction force, and the results of the Uz displacement response of the girder end under 0~100 Hz are analyzed, shown in Figure 4-4.

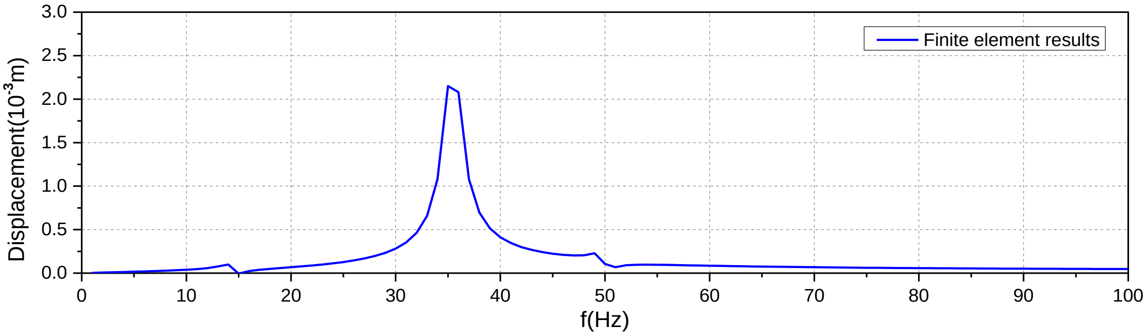

Fig.4-4 - Comparison of displacement response at 0 ~ 100 Hz

The calculation results of finite element and the test results uncover that the vertical displacement of the girder ends all produce peaks at the first three modes of longitudinal bending of the girder, which has nothing to do with the magnitude of the excitation but the frequency of the excitation. Due to the boundary conditions and the accuracy of the structural stiffness simulation, the natural frequency of the girder calculated by the finite element method is slightly larger compared with the simulation analysis results. The displacement response of the girder at the first and third frequencies is relatively small, the displacement response at the second frequency is relatively large, but the displacement-frequency curve is consistent with the experimental curve. The bending moment-frequency curve shown in Figure 4-5 is based on the change of the size and position of the excitation, and the analysis of the bending moment at the bottom of the pier and the bending moment at the root of the girder cantilever.

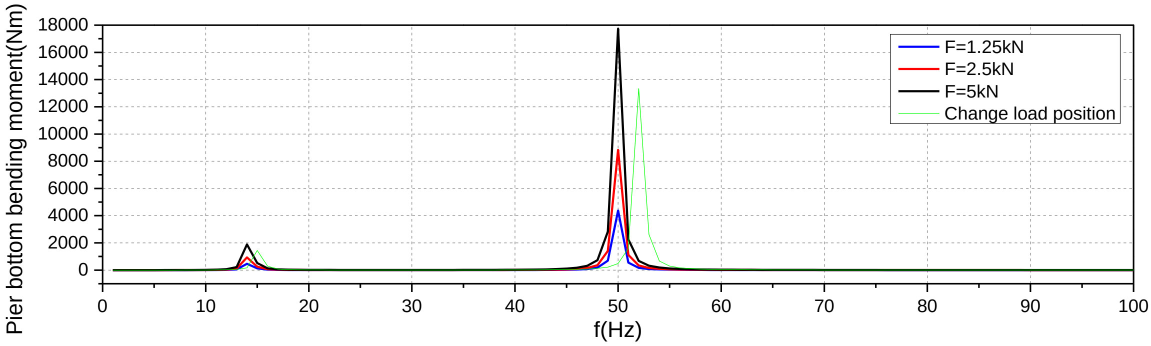

(a) *Pier bottom bending moment-frequency curve*

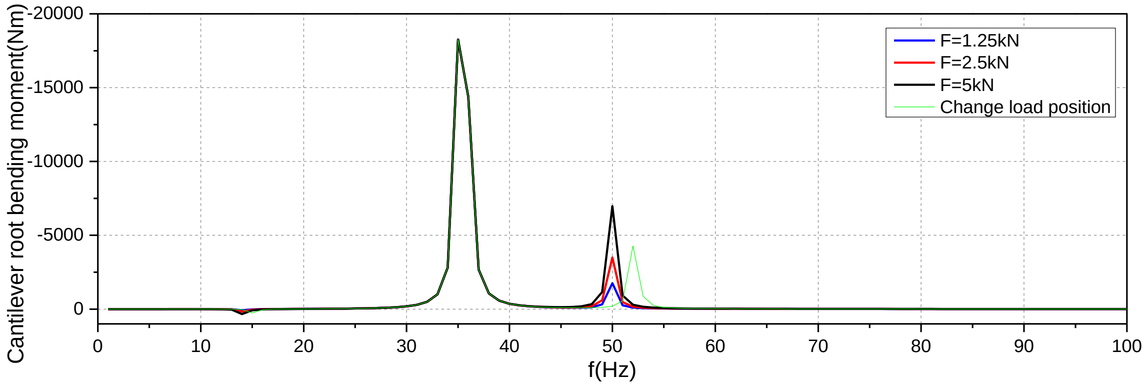

(b) *Bending moment-frequency curve at the root of the girder cantilever*

Fig.4-5 Time history curve of Bending moment-frequency curve

DOI 10.14311/CEJ.2022.03.0030

In the figure, F=2.5 kN means the spherical hinge reaction force, and the excitation load is 0.5, 1, 2 times the support reaction force for analysis. From Figure 4-5a, it can be seen that the pier bottom will have a larger bending moment under the first-order and third-order anti-symmetric modes, and the pier bottom bending moment is 0 under the second-order mode. The bending moment of the pier bottom changes linearly with the magnitude of the excitation. The bending moment values generated under the first and third mode frequencies are 464~1882 Nm and 4375~17735 Nm; the bending moments of the third mode frequency is ten times that of the first order. However, the third-order frequency value is relatively large, and it is difficult to induce the third-order mode of the girder during the rotation process, which is generally controlled by the first-order mode frequency. According to the test results of the anti-overturning moment of the spherical joint, the friction moment of the concrete spherical joint is 328.5 Nm, which is smaller than the bending moment caused by structural vibration, and the structure will lose stability along the longitudinal direction. The position of the maximum bending moment at the bottom of the pier is related to the frequency and position of the excitation. The curve in green below is gained is based on the increase of the diameter of the concrete spherical hinge. This kind of increase changes the position and constraint conditions of the excitation, and further changes the natural frequency of the structure, which cause the bending moment-frequency curve of the bottom of the pier to move backward.

Based on Figure 4-5b, it can be seen that the second-order mode frequency is the controlling factor of the girder amplitude, and its bending moment value has nothing to do with the magnitude of the excitation load and the location of the excitation load. It is also detected that the influence of the third-order mode on the bending moment of the girder is less than that of the second-order mode, and the first-order mode has basically no influence on the bending moment. Besides, the changing of the excitation position will change the frequency of the peak bending moment at the cantilever root of the girder. Therefore, in order to reduce the influence of the flatness error of the spherical hinge contact surface on the vibration of the girder structure, the excitation frequency should be controlled below one by reducing the excitation frequency to a value that is within the range of the first-order natural frequency. At this time, the vibration response of the girder during rotation is relatively small, and it will not cause dynamic instability.

When the spherical hinge rotates on a fixed axis of a rigid body around the center of rotation, the structure will be displaced along the vertical direction as the two areas on the contact surface are in contact with each other. At this time, the corresponding position of the lower spherical hinge will produce a vertical reaction force. According to the Load code for the design of building structures, the structural dynamic coefficient is generally taken as 1.1~1.3. When doing time history analysis, the magnitude of the excitation is 1.2 times the value of the vertical reaction force of the spherical hinge. The position where the excitation produces the greatest effect is at the R position of the outermost edge of the spherical hinge. At this time, the frequency of the excitation load is $\omega/2\pi$. When there are a total of n uneven areas on the contact surface, the excitation frequency is increased to $n\omega/2\pi$. Under normal circumstances, there are certain requirements for the flatness of the cross-section during the manufacture of the spherical hinge. Assuming that the maximum number of uneven areas of the spherical hinge is 10, the frequency range of the external excitation is $\omega/2\pi$~$5\omega/\pi$ at this time. The study of the relationship between the rotation angular velocity and the axial tensile stress of the girder proposes the calculation method of the limit rotation angular velocity. It is gained that the maximum rotation angular velocity of the rotating model is 3.77 rad/s, and the excitation frequency range is from 0.6 to 6 Hz. The vibration response is not significant when the excitation frequency is less than the first-order natural frequency. When ω reaches 8.9 rad/s, the excitation frequency is from 1.4 to 14.2 Hz, and the structure reaches the first-order natural frequency; when the ω reaches 22.3 rad/s, the excitation frequency is around 3.6~35.5Hz, and the structure reaches the second-order natural frequency; when ω reaches 31.4 rad/s, the excitation frequency is 5 to 50 Hz, and the structure reaches the third-order natural frequency. Therefore, the angular velocity of rotation should be less than 8.9 rad/s, and the limitation of angular velocity of rotation finally reaches 3.77 rad/s.

As the weight of the rotating model is relatively small and the natural frequency of the structure is relatively high, the calculated rotational angular velocity limit is then relatively high. Based on the literature, the first-order frequency of the girder of the 10,000-ton continuous rigid frame swivel bridge is generally between 0.4 and 1.5Hz [13], so the angular velocity of rotation should be controlled within 0.25 rad/s so as to avoid structural vibration caused by the unevenness of the spherical hinge [15]. Presently, the rotation angular velocity used in the actual domestic rotating engineering is generally between 0.01 and 0.02 rad/min, and the rotation time is between 90 and 120 min. The research results of this research then conclude that the rotational angular velocity can be increased to more than 0.05 rad/min, and the turning time will be shortened to 20-60 min, greatly improving the construction efficiency and reducing the impact of the construction on the railway traffic.

Theoretical derivation of girder end vertical vibration velocity and acceleration

In order to monitor the stability of the bridge horizontal rotation system in the process of turning in real time, the relationship between the vertical speed and acceleration of the girder end and the corresponding first three-order natural frequency should be established, and the stability of the structure should be judged by monitoring the speed and acceleration indicators.

In order to obtain the relationship between the frequency of the first three modes of the girder longitudinal bending and the vertical velocity Vz and acceleration az of the girder end, the vertical velocity and acceleration values of the cantilever girder end are monitored to determine the state of the structure during the turning process, and the girder is derived an expression between Vz, az and ω [14]. The expression of the vertical displacement y on the axis x of the girder is as follows:

$$y = Y(x)\sin(\theta + \omega t) \tag{4-1}$$

In the above formula, $Y(x)$ is the mode shape displacement function, θ the phase angle and ω is the mode shape frequency. Suppose $\lambda^4 = \omega^2 m/EI$, the expression of Y(x) solution can be:

$$Y(x) = C_1\cosh\lambda x + C_2\sinh\lambda x + C_3\cos\lambda x + C_4\sin\lambda x \tag{4-2}$$

For a bar with one end constrained and one end free, the node numbers on both sides are i and j respectively, and the translational displacement of constrained i is yi. At this time, the relationship between force and displacement is as follows:

$$\begin{bmatrix} M_i \\ F_j \\ M_j \end{bmatrix} = \begin{bmatrix} \frac{4EI}{L} & -\frac{6EI}{L^2} & \frac{2EI}{L} \\ -\frac{6EI}{L^2} & \frac{12EI}{L^3} & -\frac{6EI}{L^2} \\ \frac{2EI}{L} & -\frac{6EI}{L^2} & \frac{4EI}{L} \end{bmatrix} \begin{bmatrix} \theta_i \\ y_j \\ \theta_j \end{bmatrix} \tag{4-3}$$

The vibration at any point of the girder can be expressed by three parameters: vertical displacement y1, longitudinal displacement x1 and pier bottom rotation angle θ_{2i}, the vertical vibration displacement expression can be derived as follows:

$$\begin{aligned} y_1 &= Y_1(x_1) \times \sin(\theta + \omega t) \\ &= (C_5\cosh\lambda x_1 + C_6\sinh\lambda x_1 + C_7\cos\lambda x_1 + C_8\sin\lambda x_1) \times \sin(\theta + \omega t) \end{aligned} \tag{4-4}$$

$$X_1 = C_9\sin(\theta + \omega t) \tag{4-5}$$

$$\theta_{2i} = C_{10}\sin(\theta + \omega t) \tag{4-6}$$

In order to determine the coefficients $C_5 \sim C_{10}$, six equations need to be solved. On the other hand, six balance equations can be established according to cantilever girder boundary conditions and internal force balance conditions,

（1）When the bending moment at the end of the cantilever is 0, the formula can be like this:

$$C_5\cosh\lambda L_1 + C_6\sinh\lambda L_1 - C_7\cos\lambda L_1 - C_8\sin\lambda L_1 = 0 \tag{4-7}$$

In the above formula, L_1 represents the span of the cantilever girder.

（2）When the shear force at the end of the cantilever reaches 0, the formula is as follows:

$$C_5\sinh\lambda L_1 + C_6\cosh\lambda L_1 + C_7\sin\lambda L_1 - C_8\cos\lambda L_1 = 0 \tag{4-8}$$

（3）When the displacement of the cantilever root of the girder is 0, the formula can be derived like this:

$$C_5 + C_7 = 0 \tag{4-9}$$

（4）If taking the pier shear balance condition into consideration, the formula can be like this:

$$F_{2j}=\frac{12E_2I_2}{{L_2}^3}\times y_{2j}-\frac{6E_2I_2}{{L_2}^2}\times\theta_{2j}-\frac{6E_2I_2}{{L_2}^2}\times\theta_{2i} \qquad (4\text{-}10)$$

In the above formula, *E₂* and *I₂* represent the elastic modulus of the pier and the bending moment of inertia. The formulas of the pier angle and displacement are as follows:

$$\theta_{2j}=(C_6+C_8)\lambda\times\sin(\theta+\omega t) \qquad (4\text{-}11)$$

$$y_{2j}=C_9\sin(\theta+\omega t)-(C_6+C_8)h_k\times\lambda\times\sin(\theta+\omega t) \qquad (4\text{-}12)$$

Based on Newton's second law, the following formula is derived：$F=ma$=F_{2j}，

$$m=\frac{1}{2}m_1L_1+2m_2L_2 \qquad (4\text{-}13)$$

$$a=\frac{d^2x_1}{dt^2}=-\omega^2\times C_9\,sin(\theta+\omega t) \qquad (4\text{-}14)$$

In the formula, m_1 and L_1 are the quality and span of the main girder; m_2 and L_2 are the quality and height of the pier. Based on the equations from (4-10) to (4-14), a simplified equation can be obtained as follows:

$$\begin{aligned}6E_2I_2\times(L_2+2h_k)\lambda C_6+6E_2I_2\times(L_2+2h_k)\lambda C_8+6E_2I_2L_2C_{10}\\+\left(\frac{1}{2}m_2L_2^4 4\omega^2+2m_1L_2^3L_1\omega^2-12E_2I_2\right)C_9=0\end{aligned} \qquad (4\text{-}15)$$

（5）Similarly, according to the balance conditions of the bending moments of the top and bottom sections of the pier, the following formula is derived:

$$\begin{aligned}2E_1I_1\lambda^2L_2^2C_5-E_2I_2\times(4L_2+6h_k)\lambda C_6-2E_1I_1\lambda^2L_2^2C_7-E_2I_2\times(4L_2+6h_k)\lambda C_8\\-2E_2I_2L_2C_{10}+\left(\frac{1}{2}m_2L_2^3h_k\omega^2+2m_1L_1L_2^2h_k\omega_{+}^{2}+6E_2I_2\right)C_9=0\end{aligned} \qquad (4\text{-}16)$$

$$\begin{aligned}2E_2I_2\times(L_2+3h_k)\lambda C_6+2E_2I_2\times(L_2+3h_k)\lambda C_8-6E_2I_2C_9+(4E_2I_2L_2+kL_2^2)C_{10}\\=0\end{aligned} \qquad (4\text{-}17)$$

Combine the equations from (4-7) to (4-9), and (4-15) to (4-17), with the frequency ω and $C_5\sim C_{10}$ as unknowns. Since $C_5\sim C_{10}$ is not all zeros, while the result is zero, the determinant of the coefficient matrix composed of frequencies then should be zero. Therefore, the different frequencies and modes of the cantilever girder structure can be obtained, which can be used to obtain the coefficients.

During the rotation of the continuous rigid frame bridge, it is difficult to measure the speed and acceleration of the spherical hinge in order to test whether the cantilever girder structure reaches the first three-order natural frequency. However, it is relatively easy to test the vertical velocity and acceleration value of the end of the cantilever during rotating construction. Therefore, based on the formula (4-4), the vertical velocity *Vz* at the end of the cantilever girder, and the expression of acceleration a_z the following equation can be derived.

$$Vz=C_5\omega\cosh\lambda L_1+C_6\omega\sinh\lambda L_1+C_7\omega\cos\lambda L_1+C_8\omega\sin\lambda L_1 \qquad (4\text{-}18)$$

$$a_z=C_5\omega^2\cosh\lambda L_1+C_6\omega^2\sinh\lambda L_1+C_7\omega^2\cos\lambda L_1+C_8\omega^2\sin\lambda L_1 \qquad (4\text{-}19)$$

Substitute the natural frequency of the first three modes of the girder to obtain the coefficient value, and finally obtain the maximum vertical vibration speed limit *Vz* and acceleration value a_z at the end of the cantilever from equations (4-18) and (4-19). The speed and acceleration of the girder end are monitored to determine the stability of the structure during horizontal rotation. The measured vertical velocity and acceleration of the girder end should be smaller than *Vz* and a_z gained at the first three-order mode frequency of the girder; otherwise, only when the cause is found should the rotating construction be continued.

CONCLUSIONS

To conclude, this research starts with the model test, and draws the following conclusions after the test and simulation analysis.

(1) First, concrete spherical hinges will inevitably produce certain flatness errors during the manufacturing process, which will cause vibrations during rotation. Through the test of the vibration displacement of the girder, it is found that the vertical vibration displacement is related to the

frequency of the first three modes of the girder longitudinal bending, and has nothing to do with the higher modes of the girder longitudinal bending and other modes.

(2) Second, this research establishes finite element simulation models of the rotating structure and uses the harmonic response analysis method to simulate the influence of the flatness error of the spherical hinge contact surface on the structural vibration. It is then proposed that the control of the rotating speed and the excitation frequency within the first-order mode frequency range of the girder can make the structural vibration response at a minimal scale.

(3) Third, this research provides the expression of the relationship between the vertical vibration velocity and acceleration of the girder end and the vibration frequency of the main girder during the rotation of the bridge horizontal rotation system. It is finally proposed that the structure stability can be predicted by monitoring the vertical velocity and acceleration of the cantilever girder end during the horizontal rotation.

AFFILIATION

Supported by three projects:

(1) Research on the influence of ultra-high-performance concrete strengthened RC beams based on oriented fiber arrangement on shear performance, Natural science research project of universities in Anhui Province, and the project number is KJ2021A0504.

(2) Study on mechanical characteristics and design method of ultra-high performance concrete spherical hinge translational system under multi factor coupling, The Initial Scientific Research Funds of Anhui polytechnic University”, and the project number is 2021YQQ021.

(3) Study on mechanical properties of bolted fabricated circular concrete filled steel tubular columns, Natural science research project of universities in Anhui Province, and the project number is KJ2020A0366.

REFERENCES

[1] Wang Lifeng, Yuan Chongwei, Sun Yongcun. Parameter sensitivity analysis in construction control of swivel cable-stayed bridge[J]. Journal of Northeast Forestry University, 2007(06):42-43+62.

[2] Lu Jinhua. Study on Swivel Construction Control and stability of large tonnage continuous rigid frame bridge[D]. Lanzhou Jiaotong University, 2016.

[3] Davenport A G.Buffeting of a suspension bridge by storm winds[J].Journal of Structural Division,ASCE.1962,88(ST3):233-268.

[4] Scanlan R H, Tomoko J J. Airfoil and bridge deck flutter derivatives[J]. ASCE, Journal of Engineering Mechanics Division, ASCE, 1971,97(6):1717-1737.

[5] Xu Chao, Wang Changfeng, Dou Guokun, Li Ying. Design and anti overturning stability analysis of temporary support for bridge Swivel Construction[J]. Railway Engineering, 2018,58(11):50-52+62.

[6] Ma Sufen. Parameter sensitivity analysis of long-span T-frame bridge constructed by swivel[D]. Wuhan University of Technology,2014.

[7] Huang Weiwen. Study on wind resistance of T-shaped rigid frame bridge constructed by rotation[D]. Wuhan University of Technology, 2014.

[8] Gao Ri, Hu Zhibo, Gao Tao, Meng Xi. Analysis on the influence of train induced vibration on the stability of Swivel Construction Bridge[J]. Railway Engineering, 2014(05):16-18.

[9] Wang Changjie. Integral stress analysis and pier optimization design of T-shaped rigid frame bridge in Swivel Construction[D]. Southwest Jiaotong University, 2017.

[10] Wang Xinmin. Numerical analysis of engineering structure with ANSYS[M]. Bei Jing: People's Communications Press, 2007, 440-450.

[11] Wang Qiang. Research on some technologies of large tonnage Precast Pier Column component transportation[D]. Guangxi University of science and technology, 2013.

[12] Zhao Xia. Finite element analysis of contact problems and its engineering application[D]. Liaoning University of engineering and technology, 2007.

[13] Jiawei Wang, Quansheng Sun, Dynamic analysis of swivel construction method under multi-variable coupling effects. International Journal of Structural Integrity[J], 2019, Vol.10, No.4, pp:580-598.

[14] Ma Weilei, Xu Zhaodong. structural dynamics[M]. Beijing: Science Press,2007.

Article no. 31

THE CIVIL ENGINEERING JOURNAL 3-2022

THE COMPARATIVE STUDY OF THE PERFORMANCE OF CONCRETE MADE FROM RECYCLED SAND

Chiraz Kechkar[1], Leila kherraf[2], Assia Abdelouahid[2] and Houria Hebhoub[2]

1. *University of 8 May 1945, Faculty of science and technology, laboratory of civil and hydraulic engineering, P.B N°401, Guelma, Algeria; chiraz_kechkar@yahoo.fr (corresponding author)*
2. *University of 20 August 1955, LMGHU Laboratory, B.P.26 El-Hadaiek road, Skikda, Algeria; l kherrafleila@yahoo.com ; assiaabdelouahed@yahoo.fr ; hebhoubhouria@yahoo.fr*

ABSTRACT

The main objective of this study of research is to initiate and develop a comparative study of fresh and hardened properties of concretes made from recycled sand from three types of waste: marble waste, tiling waste and cinder block waste. And this, in the intention of contributing to the world effort relating to the preserve of natural aggregate resources and limit landfill to the ultimate waste thresholds.

To do this, in the composition of a current concrete with a water / cement ratio equal to 0.55, an equivalent volume of sand from the three wastes respectively replaced a volume of 15% of the ordinary sand. The properties in the fresh state: workability, air content and density and in the hardened state: compressive strength, flexural tensile strength, compressive strength determined with non-destructive tests, water absorption by immersion, absorption by capillarity and chloride penetration of the various concretes produced are analyzed, and compared to those of the ordinary concrete.

The results obtained show that the concretes containing the waste sands have acceptable characteristics. However, tiling waste sand performs better than the other two recycled sands.

KEYWORDS

Sand, Marble, Tiling, Cinder block, Waste, Performance, Concrete

INTRODUCTION

The building materials industry is always a source of waste which is most often throw out in landfills or in the nature, which has negative effects on the environment. For this purpose, in Western countries, this type of rejection is strictly prohibited and the management of solid waste, whether by valorization or recycling, remains a major concern [1]. The objectives are reducing the volume of waste and preserving natural resources [2].

The domain of civil engineering, like other domains, are increasingly interested in the recovery of this type of waste, given the obligation to take charge of waste by the regulations in force, and the economic, environmental and technical importance that some waste can bring to the construction sector. Moreover, it is clear that current research carried out in the field focuses on the development of new composites and building materials incorporating additions and aggregates from waste, with the aim of improving the mechanical, physical and the durability of the materials produced [3].

It should be noted that in Algeria, 12 million tons of industrial waste are produced each year. However, the recycled quantity does not exceed in the best case 10%. Among this waste, we

DOI 10.14311/CEJ.2022.03.0031

have the waste from the factories of tiles, marble and cinder blocks, which generate significant quantities of waste.

This study of research falls within this context and is concerned with the recovery of sands from this waste (marble waste, tiling waste and cinder block waste) in the manufacture of hydraulic concrete.

Several previous studies have been carried out on the recovery of marble waste as a substitute for fine aggregates in concrete, they have observed an improvement in mechanical characteristics [4], [5] and [6]; thus, improved properties when fresh [4]. Sudarshan and Vyas, 2015 [7] studied the behavior of concrete by substituting coarse aggregate with marble waste aggregate, they also observed that this waste improves the workability of concrete, their compressive strength and their resistance to attack of sulfuric acid. Chaid and al, 2011 [8] substituted a part of cement with marble powder; they observed an improvement in the physico-chemical properties of concrete. Djebien and al, 2015 [9], in the formulation of a self-compacting concrete, substituted the sand of dune by a sand of marble waste with variable percentages of 25%, 50%, 75% and 100% respectively and found that recycled sand reduces density, air content, flow in a confined environment as well as mechanical resistance. Benhalilou and al, 2020 [10] in their studies on sand concrete, substituted 5%, 10%, 15% and 20% of the volume of dune sand by a marble waste sand, they found acceptable results from the point of view of workability, mechanical strengths and durability. In a research on mortars established by Hebhoub and al, 2020 [11], in which they substituted 5%, 10%, 15% and 20% of the volume of natural sand by a marble waste sand, the results show that the introduction of Recycled sand in mortars gives good results and can be used as aggregate.

Concerning the tiling waste, there are very few studies on its effects on the properties of cement materials. Tennich and al, 2013 [12] studied the effect of adding tiling waste powder on the in the fresh state and in the hardened state properties of self-compacting concrete and showed that the addition of this waste gave satisfactory mechanical strengths and characteristics in the fresh state.

However, we note the absence of studies on the behavior of materials incorporating cinder block waste.

The research presented in this work consists of a comparative study between three types of concrete containing 15% of recycled sand (marble waste, tiling waste and cinder block waste) partially substituting in volume an ordinary sand in the composition of a hydraulic concrete of water/cement ratio equals 0.55. The experimental approach consists in observing the modifications induced by the recycled sands on the characteristics of the concretes studied in the fresh state, in the hardened state and on some aspects of durability, and to compare them with those of the ordinary concrete containing ordinary sand.

MATERIALS AND EXPERIMENTAL PROCEDURES

Materials

For our work, we used a CPJ-CEM II 42.5 (S-L) cement from the cement factory of Hdjar Soud- Skikda (East of Algeria). Two crushed gravel of class 3/8 and 8/15, and 04 types of sand:

- Ordinary sand (OS) of class 0/2,
- Marble waste sand (MWS) of class 0/2 of crushed nature, comes from quarry: derivatives of marble of Fil-fila (Skikda-East of Algeria);
- tiling waste sand (TWS) of class 0/2 obtained by crashing and sieving on a sieve of size 2 mm the falls of tiling;
- Cinder block waste sand (CWS) of class 0/2 obtained by crashing and sieving on a sieve of size 2mm the falls of cinder block.

Their particle size analyzes of sands used are presented in Figure 2, and their physical characteristics are given in Table 1.


(a) (b) (c)

Fig. 1 – Waste of marble (a), waste of tiling (b) and waste of cinder block (c).

Tab. 1: Physical characteristics of the 04 sands used.

	Sand (OS)	Sand (MWS)	Sand (TWS)	Sand (CWS)
Apparent density (g/cm^3)	1,510	1,660	1,590	1,520
Absolute density (g/cm^3)	2,590	2,750	2,620	2,610
Value of blue methylene (%)	1,10	0,50	0,50	1,00
Sand equivalent (%)	84	67	61	78
Water absorption (%)	1,12	2,37	3,50	3,33
Fineness modulus	1,88	1,87	2,36	2,64
Fines content (%)	1	12	8	6

From these results, we can say that:

- Marble waste sand (MWS) is the densest in comparison with tiling waste sand (TWS), cinder block waste sand (CWS) and ordinary sand (OS) respectively.
- Ordinary sand (OS) is cleaner than other sands.
- Tiling waste sand (TWS) and cinder block waste sand (CWS) have the highest absorption coefficients.
- The cinder block waste sand (CWS) gives the highest fineness modulus, which indicates that concrete made with this type of sand gives good resistance to the detriment of workability.

DOI 10.14311/CEJ.2022.03.0031

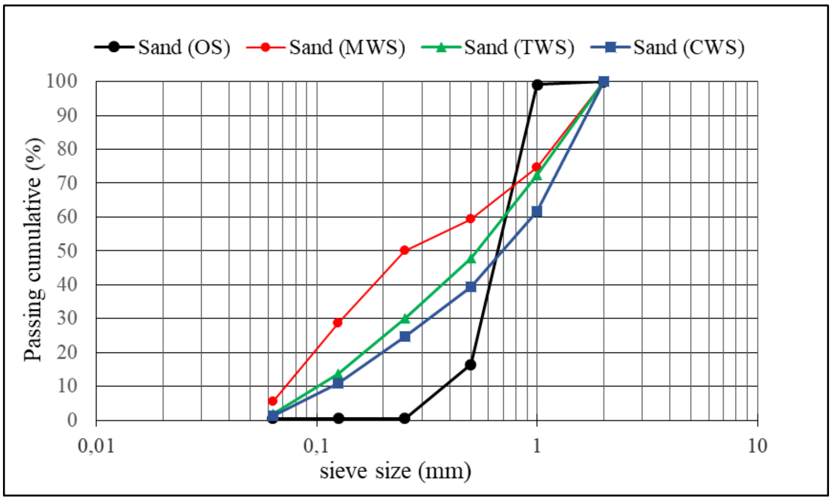

Fig. 2 – Sieve analysis for the 04 sands used.

According to the results of the particle size analyzes carried out on the study sands, it can be seen that:

- The three types of sands have a continuous granulometry and fall within the granular spindle.
- (MWS) sand is a finer compared to other sands used. While the (OS) and is very poor in fines elements.

The chemical characteristics of the different sands are given in Table 2.

Tab. 2: Chemical characteristics of the 04 sands used.

	Sand (OS)	Sand (MWS)	Sand (TWS)	Sand (CWS)
$CaCO_3$	--	98.67	--	--
CaO	0.80	55.29	53.53	47.49
Al_2O_3	2.36	0.14	1.47	1.28
FeO_3	1.5	0.09	0.63	0.72
SiO_2	94.09	0.53	4.00	2.20
MgO	0.14	0.2	1.58	1.83
Na_2O	0.20	0.00	--	--
K_2O	0.58	0.01	--	--
Cl^-	0.00	0.025	--	--
SO_3	0.01	0.04	--	--
PF	--	43.40	41.70	43.60
R. Insoluble	--	0.035	--	--

Referring on chemical analyzes, it can be seen that the recycled sands: MWS, TWS and CWS are calcareous in nature. In contrast, ordinary sand (OS) is siliceous in nature.

Experimental program

Mix design

In this experimental investigation, a volume of ordinary sand equal to 15% was substituted in the composition of a control ordinary concrete (OC) formulated using the Dreux Gorisse method and whose Water / cement ratio was set at 0.55, by three recycled sands: marble waste sand, tiling waste sand and cinder block waste sand.

Therefore, the other three formulations obtained are: concrete (MWC) based on marble waste sand, concrete (TWC) based on tiling waste sand and concrete (CWC) based on cinder block waste sand.

The different compositions of the concrete are grouped together in Table 3.

Tab. 3: Concrete mix constituents.

	OC (0%)	MWC 15%)	TWC 15%)	CWC (15%)
Cement (Kg)	350.00	350.00	350.00	350.00
Water (L)	192.50	192.50	192.50	192.50
OS (Kg)	711.75	605.00	605.00	605.00
MWS (Kg)	--	113.00	--	--
TWS (Kg)	--	--	108.00	--
CWS (Kg)	--	--	--	107.5
G 3/8 (Kg)	511.75	511.75	511.75	511.75
G 8/15 (Kg)	587.00	587.00	587.00	587.00

Testing methods

The tests carried out on the different formulations are:

- Characterization tests in the fresh state: slump test, density and air content were carried out according to the standards: Standard NA 431, Standard NA 436 and Standard NA 434 successively.
- Destructive tests: compressive strength on specimens of size (150x150x150) mm3 in accordance with standard NA 427 and flexural tensile strength on specimens of size (7x7x28) mm3 according to standard NA 428. These tests were studied at age 7, 28 and 90 days.
- Non-destructive tests: ultrasound test and sclerometer test were carried out on specimens of dimension (200x200x200) mm^3 according to standards NA 5027 and NF EN 12504-2 respectively.
- Capillary water absorption test and water absorption test by total immersion were carried out on prismatic specimens of (70x70x280) mm3 in accordance with standard NA 255, and on cubic specimens of (150x150x150) mm^3 in accordance with the standard NBN B 15-215 respectively.
- chloride Penetration, the test was carried out on specimens of dimension (70x70x280) mm^3 according to UNI 7928 and JIS A 1171 standards.

RESULTS AND DISCUSSIONS

Workability (slump)

According to the results shown in Figure 3, the workability of the concretes studied varies between 5 and 9 cm. Therefore, the range of concretes thus produced is plastic.

In addition, the substitution of ordinary sand by recycled sands (marble waste, tiling waste and cinder block waste) respectively decreased the subsidence by 22%, 33% and 44%.

This result is expected from the fact that:

- Recycled sands have higher absorption coefficients than ordinary sand,
- Their fines content is greater than that of ordinary sand,
- The fineness and the angular shape of the grains of recycled sands inducing a relatively high friction between the constituents of the cement matrix [13].

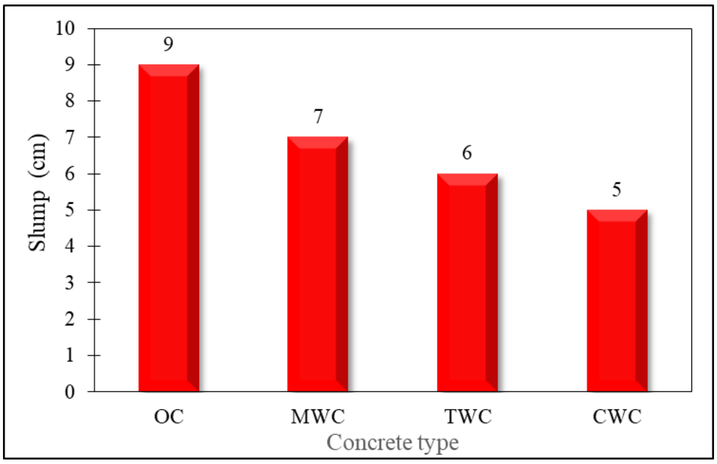

Fig. 3 – Variation of slump as a function as type of waste sand.

Density in the fresh state

It is clear from Figure 4 that the density in the fresh state of ordinary concrete is lower than that of concrete with recycled sands. This is logically explained by the fact that the substitute products (marble waste, tiling and cinder blocks waste) have a greater density than that of ordinary sand.

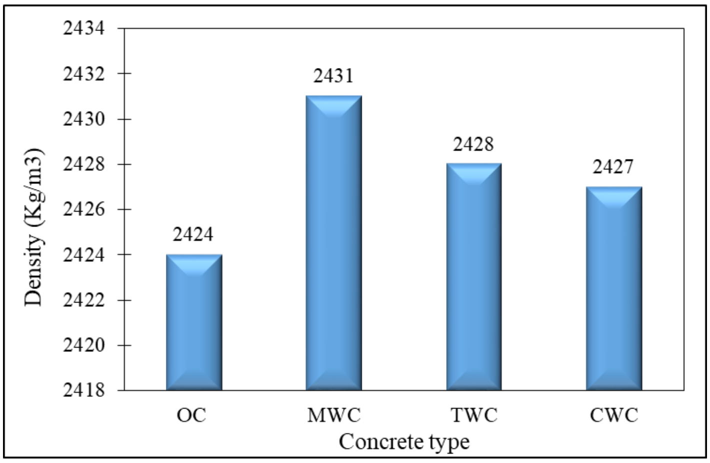

Fig. 4 – Density variation depending on the type of waste sand.

Air content

From Figure 5, it can be seen that the air content of the four formulations studied varies between 4 and 9%.

Substitution of ordinary sand by 15% marble and tiling waste sand reduced the entrained air content of the concrete by 9% and 5% respectively. This reduction is due to the high fines content of this waste compared to ordinary sand, which leads to good compactness. This result agrees with what was found by Hebhoub et al. 2011 [14]. On the other hand, the waste sand from cinder blocks increased the air content by 4% compared to ordinary concrete. This can be attributed to a poor spatial arrangement of the grains of sand of irregular angular shape resulting from the presence of an old mortar matrix attached to the grain of sand.

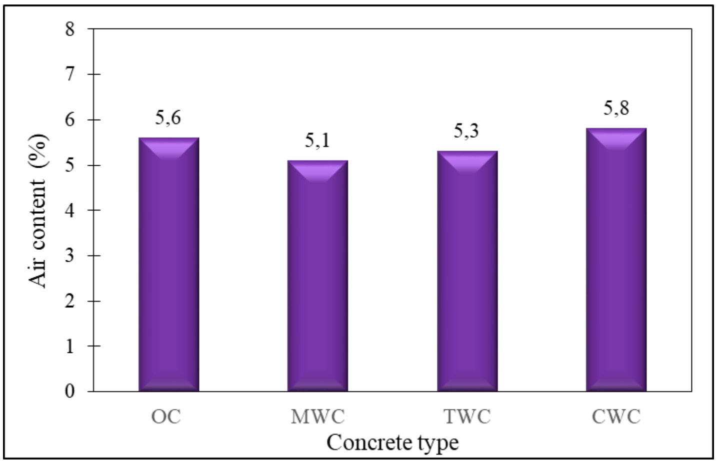

Fig. 5 – Variation of air content as a function as type of waste sand.

Compressive strength

The results, shown in Figure 6, indicate that the compressive strength increases as time passes regardless of the type of concrete tested. This can be explained by the development of the cement hydration phenomenon as a function of time in the presence of sufficient humidity.

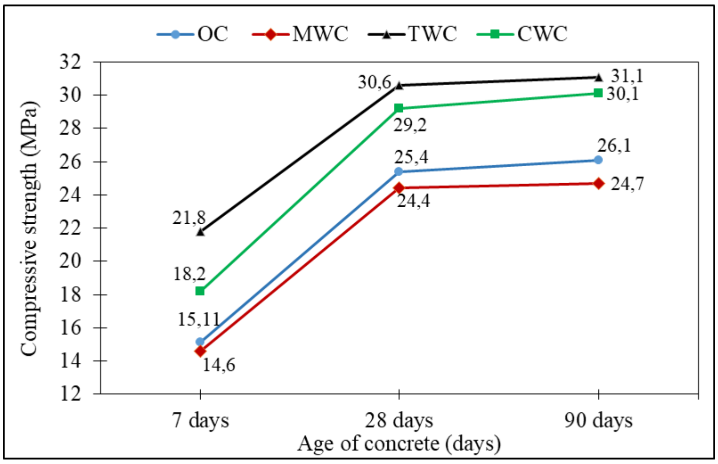

Fig. 6 – Evolution of compressive strength as a function of age and type of waste sand.

At all deadlines, concrete based on Waste Tile Sand (TWC) and concrete based on cinder block waste sand (CWC) exhibit higher strengths than ordinary concrete. After 90 days of storage, the strengths recorded exceed 30MPa and differ from that of the control concrete by 19% and 15% respectively. This can be attributed to the water absorption capacity of the tiling, cinder block waste which reduces the water / cement ratio [15], and to the role of the fines, which fill the granular interstices and make the mixture more compact.

The lowest compressive strength values are recorded by the concrete (MWC) with a decrease of around 5.6% compared to that of the control concrete. This reduction can be justified by a separation effect of the aggregates exerted by the cement paste incorporating the marble fines [16]. These results remain acceptable for ordinary concrete.

Flexural tensile strength

In Figure 7, we note that the introduction of recycled sands in the formulation of ordinary concrete leads to an improvement in Flexural tensile strength at all times.

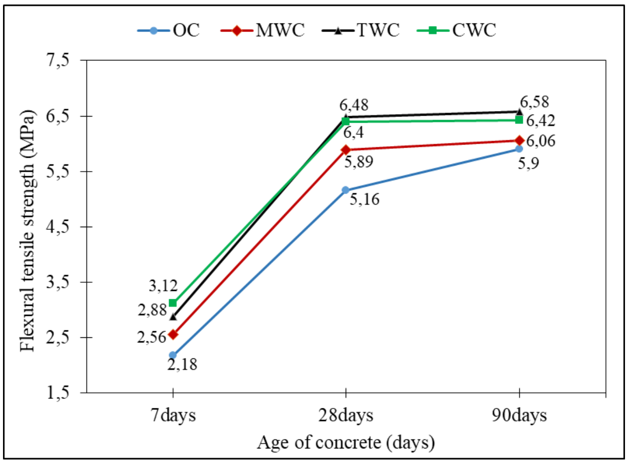

Fig. 7 – Evolution of flexural tensile strength as a function of age and type of waste sand.

At 7 days of age, the concrete made from cinder block waste sand (CWC) gave the best resistance, showing a value that exceeded that of the ordinary concrete by 21%. At 28 day, the resistance shown by the concrete with the waste tiling sand (TWC) deviates from that of the ordinary concrete (OC) by 25.5%.

At 90 days, the best resistance is obtained by (TWC) by exceeding the value of the ordinary concrete by 11%.

In the case of both tiling and cinder block waste sands, the growth of strengths is likely the result of the bond that developed as time elapsed between the hydrated cement paste and the grains of crushed sand having a rough and porous surface.

The increase in the tensile strength of the concrete containing the marble waste sand is justified by the plasticizing capacity of the marble.

Non-destructive testing

The results of non-destructive tests: the sclerometer test and ultrasound test for the four concretes studied at 28 days are shown in Figure 8.

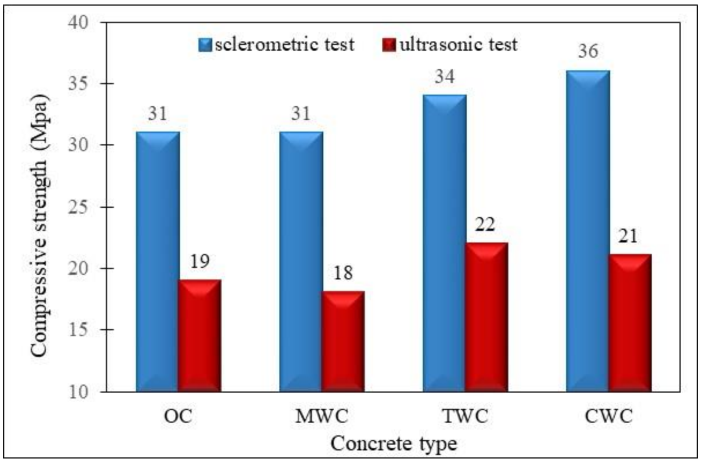

Fig. 8 – Evolution of compressive strength by non-destructive testing of the 04 concretes studied.

In general, there is an improvement in resistance for concrete based on recycled sands compared to ordinary concrete.

For the sclerometer test, it is noted that concrete with cinder block waste sand (CWC) gave the highest resistance compared to study concretes. This is due to the morphology of the cinder block waste aggregates, which offers better adhesion to the cement paste than ordinary aggregates due to the presence of an old cement matrix attached to the grain of sand.

On the other hand, for the ultrasound test, it was the concrete with tiling waste, which gave the best resistance. This means that the introduction of sand from waste tiling improves the homogeneity of the concrete.

Concrete with marble waste gave the lowest strengths compared to study concretes. This leads us to say that the rate of 15% of marble sand gives the lower adhesion to the paste than the other two mixtures.

Immersion absorption.

We can notice (Figure 9) that the water absorption by total immersion of ordinary concrete is greater than that of concrete based on recycled sand, and concrete (MWC) has the lowest water absorption by compared to other concretes.

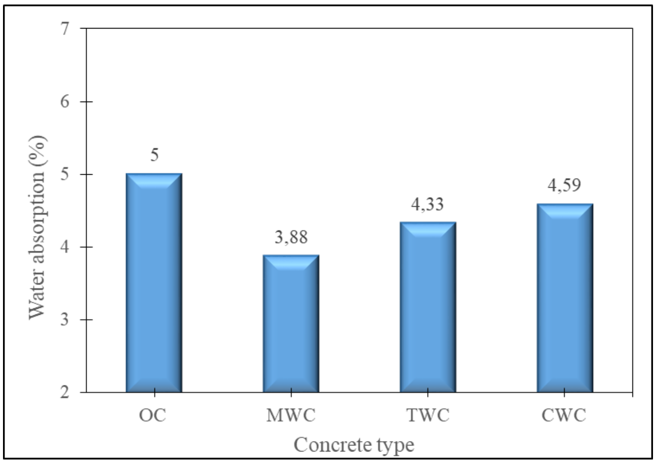

Fig. 9 – Evolution of water absorption of the 04 concretes studied.

DOI 10.14311/CEJ.2022.03.0031

Compared to ordinary concrete (OC), there is a decrease in water absorption of 8.2%, 13.4% and 22.4% for concretes (CWC), (TWC) (MWC) respectively. This result can be linked to the presence of the amounts of fine in the recycled sands, which are relatively high compared to ordinary sand, which leads to the decrease in porosity and to have concretes of good compactness.

Absorption by capillarity

Capillary porosity is a micro-structural characteristic that influences transfer properties [17]. The values of the capillary water absorption test for the different compositions are shown in Figure 10.

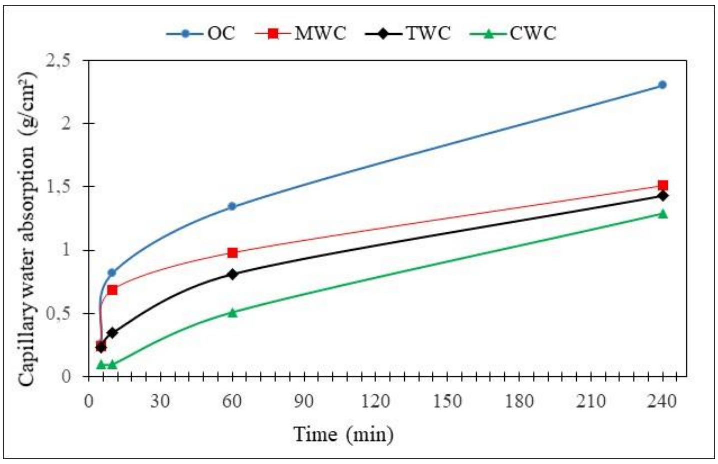

Fig. 10 – Evolution of capillary water absorption of the 04 concretes studied.

It can be seen that, compared to ordinary concrete (OC), the use of waste has reduced the amount of water absorbed. Concrete with cinder blocks waste gave the lowest values of capillary absorption.

After 24 minutes, the amount of water absorbed by the concretes (MWC), (TWC), and (CWC) decreased by 34.4%; 37.8% and 43.9% respectively compared to that of the ordinary concrete (OC). The incorporation of 15% of these wastes in the concrete tends to limit the water absorption of the composite.

These results can be justified by the plasticizing capacity of the marble waste sand, which closes the capillary pores. And the heterogeneity of the tiling and cinder block waste sand used given the presence of a residual mortar surrounding the particle of the waste sand, which reduces the interconnection of the pores of the capillary network.

Chloride penetration

We note that among the four concretes studied (Figure 11); concrete with marble waste (MWC) gave the greatest penetration depth (20.8 mm), with an increase of 7.2% compared to ordinary concrete.

For the other two concretes (TWC) and (CWC), the chloride penetration depth is lower than that of ordinary concrete. It goes from 19.3 mm for ordinary concrete to 17.2 mm; 16.2 mm for concrete TWC) and (CWC), therefore a decrease of 11.3% and 16.5% respectively. These results lead us to say that the chloride penetration rate depends on the porosity of the concretes and the size of the pores as well as the mobility of the chlorides inside the pores following their distribution in the cement matrix.

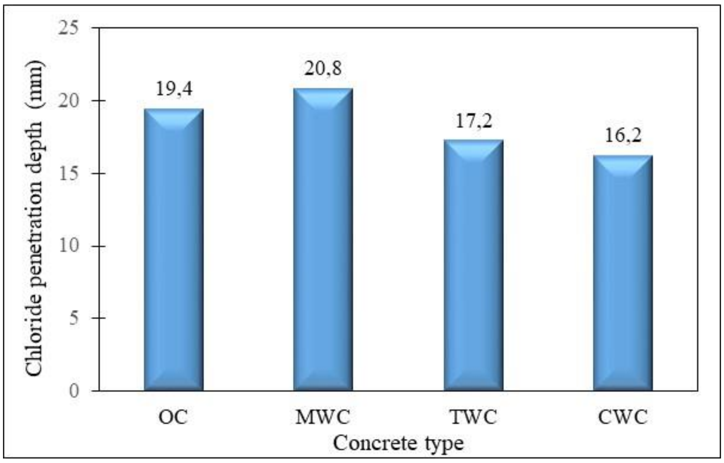

Fig. 11 – Chloride penetration depth of the 04 concretes studied.

CONCLUSION

This work presents an experimental study carried out with the aim of evaluating and comparing the performance of concrete made from recycled aggregates. The concretes studied are obtained by substituting a volume of 15% of ordinary sand by three different waste sands: marble waste, tiling waste and cinder block waste.

From the results obtained, the following main conclusions can be drawn:

- The substitution of ordinary sand by recycled sands increases the density and decreases the workability of the concrete.
- The substitution of ordinary sand by recycled sands decreases the entrained air content of the concrete except for concrete made from cinder block waste sand
- The volume substitution of 15% of ordinary sand by an equivalent volume of recycled sand improves mechanical properties. Concrete incorporating tiling waste sand gave the best mechanical resistance compared to other concretes.
- Recycled sands reduce the quantity of water absorbed by total immersion of concrete made from recycled sands. Concrete made from marble waste sand gave the lowest absorption.
- The introduction of recycled sands decreases the amount of water absorbed by capillary action of concrete made from recycled sands compared to ordinary concrete. The lowest capillary absorption value is recorded for concrete with cinder block waste sand.
- The use of recycled sands in concrete decreases the chloride penetration depth compared to ordinary concrete. Concrete with cinder block waste gave the lowest penetration depth.

The results obtained show a favorable effect of all the substituents both on the mechanical properties and on the durability of the concretes. However, the best results of the tests on the concretes are with cinder block waste sand and tiling waste sand.

Finally, the use of a percentage of 15% of cinder block and tiling waste sands in the manufacture of concrete seems a promising way to valorize these two types of waste.

REFERENCES

[1] Nadjoua B., 2017. Granulats recycles de substitution pour bétons hydrauliques : béton de démolition - déchets de briques - déchets de verre (Substitute recycled aggregates for hydraulic concrete: demolition concrete - waste bricks - waste glass). PhD Thesis, University of Constantine, Algeria.

[2] Lilia B., Dyhia B., 2017. Recyclage des déchets inertes de marbre et de granite de la marbrerie YAHIAOUI-DBK dans la fabrication des dallages de sol (Recycling of inert waste of marble and of granite from the YAHIAOUI-DBK marble factory in the manufacture of floor tiles). Master Thesis, University of Mouloud Mammeri Tizi-Ouzou, Algeria.

[3] Hamza C., Zahir T., 2017. Amélioration des propriétés mécaniques du plâtre de construction avec des déchets plastiques et verre," (Improvement of the mechanical properties of building plaster with plastic and glass waste). Master Thesis, University Akli Mohand Oulhadj, Bouira, Algeria.

[4] Hebhoub H., Belachia M., 2011. Introduction de sable de déchet de marbre dans le béton hydraulique (Introduction of marble waste sand into hydraulic concrete). Nature et Technologie, p. 6,

[5] Tugrul Tunc E., 2019. Recycling of marble waste: A review based on strength of concrete containing marble waste," Journal of Environmental Management, vol. 231, pp. 86-97. https://doi.org/10.1016/j.jenvman.2018.10.034

[6] Omar O. M., Abd Elhameed G. D., Sherif M. A., Mohamadien H. A., 2012. Influence of limestone waste as partial replacement material for sand and marble powder in concrete properties. Housing and Building National Research Center Journal, vol. 8, pp. 193-203. http://dx.doi.org/10.1016/j.hbrcj.2012.10.005

[7] Kore S., Vyas A., 2015. Behavior of Concrete Using Marble Waste as Coarse Aggregate. UKIERI Concrete Congress –Concrete Research Driving Profit And Sustainability. India.

[8] Chaid R., Jauberthie R., Abadlia M. T., Talah A., 2011. Effet des déchets de marbre sur la durabilité des bétons en milieu marin (Effect of marble waste on the durability of concrete in the marine environment). The XXIXe Rencontres Universitaires de Génie Civil. Tlemcen, Algeria.

[9] Djebien R., Hebhoub H., Belachia M., Berdoudi S., Kherraf L., 2018. Incorporation of marble waste as sand in formulation of self-compacting concrete. Structural engineering and mechanics: An international journal, vol. 67, pp. 87-91. DOI: https://doi.org/10.12989/sem.2018.67.1.087

[10] Benhalilou M. I., Belachia M., Houari H., Abdelouahed A., 2020. The Study of the Characteristics of Sand Concrete Based on Marble Waste Sand. Civil And Environmental Engineering Reports, vol. 30, No.1, pp 130-144. DOI: 10.2478/ceer-2020-0010.

[11] Hebhoub H., Kherraf L., Abdelouahed A., Belachia M., 2020. Introduction of Marble Waste Sand in the Composition of Mortar. In book: Use of Sandy Materials in Civil Engineering, Publisher: Intechopen. DOI: 10.5772/intechopen.91254

[12] Tennich M., Ben Ouezdou M., Kallel A., 2013. Béton autoplaçant à base de déchets de marbres et de carrelage (Self-compacting concrete made from waste of marble and of tiles). Journées nationales de béton : JNB'13. Tunisia.

[13] Djebien R., Belachia M., Hebhoub H., 2015. Effect of marble waste fines on rheological and hardened properties of sand concrete. Structural Engineering and Mechanics, vol. 53, pp. 1241-1251. DOI: 10.12989/sem.2015.53.6.1241.

[14] Hebhoub H., Aoun H., Belachia M., Houari H., Ghorbel E., 2011. Use of waste marble aggregates in concrete. Construction and Building Materials, vol. 25, pp. 1167-1171. https://doi.org/10.1016/j.conbuildmat.2010.09.037.

[15] Sancheti G., Bhargava S., Jain K., 2020. Mechanical and Durability Performance of Concrete Made with Waste Marble and Fly Ash. Jordan Journal of Civil Engineering, vol. 14, pp. 305-318.

[16] De Larrard F., Tondat P., 1993. Sur la contribution de la topologie du squelette granulaire à la résistance en compression du béton (On the contribution of the topology of the granular skeleton to the compressive strength of concrete). Materials and Structures, vol. 26, pp. 505-516.

[17] Belkadi A. A., 2018. Contribution à l'étude de la durabilité et les performances des bétons autoplaçants (fibres végétales, milieu agressif, formulation, modélisation) (Contribution to the study of the durability and performance of self-compacting concretes (vegetable fibers, aggressive environment, formulation, modelization)). PHD thesis, Mohamed Khider university – Biskra- Algeria.

Article no. 32

THE CIVIL ENGINEERING JOURNAL 3-2022

THE MULTI-FACTOR CONTROL AND EVALUATION OF HIGHWAY SOFT SOIL SUBGRADE STABILITY

Ming Zhang, Nan-nan Li and Min Yang

Henan University of Engineering, Institute of Civil Engineering, 1 Xianghe Road in Longhu, Xinzheng, Zhengzhou, China; mzhang@haue.edu.cn, 1511928525@qq.com, 2623169487@qq.com

ABSTRACT

When the surcharge preloading method is used in the treatment of soft soil subgrade, it is necessary to squeeze for more preloading drainage consolidation time under the premise of controlling the subgrade stability during the filling period. Considering the mutation of each monitoring indices and their interrelation when instability occurs in the fill subgrade, the inflection point analysis method through monitoring indices to control the subgrade stability comprehensively was proposed in this paper. The thin-layer rotary adding method was used to determine the ultimate filling depth and the loading plan for the highway soft soil subgrade during the filling period, with the inflection point analysis method in analyzing and evaluating the subgrade stability. The results showed that: (1) The ultimate fill height of the subgrade sections was obtained from the stability analysis results on the basis of the three indices of pore water pressure increment, settlement and lateral displacement, which was close to the prediction results of the thin-layer rotary adding method. (2) The stability control standard of the subgrade construction in the filling method was that the single-stage pore pressure coefficient should be within 1.2. (3) The subgrade stability control standard contained the maximum settlement rate of 20mm/d and the maximum lateral displacement rate of 3mm/d. (4) The geotextile setting in the highway subgrade effectively improved the ultimate bearing capacity of the subgrade, reduced the lateral displacement, improved the anti-slip stability, and increased the ultimate filling height and filling rate.

KEYWORDS

Soft soil subgrade, Stability, Ultimate filling height, Inflection point analysis, Thin-layer rotary adding method, Geotextile

INTRODUCTION

Deformation and stability control are the two major technical problems in the construction of high embankment highway [1], where the stability is the primary concern during the construction and filling period. Especially when constructing the highways in soft soil areas, due to the excessive fill speed and overfilling, and improper construction methods, once the foundation stability cannot be strictly controlled during the construction and filling period, the subgrade instability will occur. When constructing the high-grade highway on soft foundation such as silt, the surcharge preloading method is considered as a more economical and reasonable foundation treatment method. How to gain more time for the preloading drainage consolidation under the premise of controlling the subgrade stability during the construction and filling period, is a subject with great engineering and economic value.

The stability control methods for soft soil subgrade include both theoretical method and monitoring-based stability control. The theoretical method requires the accurate soil parameters, additionally, the application is limited by conditions. Rao Bo [2] considered the strength improvement of the soft soil with the growth of degree of consolidation, the effective consolidation

DOI 10.14311/CEJ.2022.03.0032

stress method was adopted in subgrade stability analysis, and according to the measured settlement, programmed to calculate the allowable filling height at any moment, which ensured the stability of the soft soil subgrade during filling construction period.

The stability control method based on monitoring usually used one or several observed empirical values as the control index of the subgrade stability, which is more intuitive and convenient. However, due to the different properties of the subgrade soil, loading method, loading rate and foundation treatment method, there are great differences between the quantitative control indexes of stability, leading to the obstacles in the stability control of soft soil subgrade construction. At present, the main monitoring items are the vertical settlement, lateral displacement and pore water pressure [3]. Many control methods for judging the stability of soft soil subgrade are put forward at home and abroad by the collation and analysis of these monitoring data. Tavenas et al. [4] defined the lateral deformation coefficient as the ratio of the filling rate Δq to the maximum lateral displacement rate ΔD_m at the toe of the embankment, and judged the stability of the embankment by establishing a relationship curve between $\Delta q/\Delta D_m$ and the embankment filling load q. Which verified this method is only effective for deep soft soil subgrade, but conservative. Brand and Brenner concluded that the stability discrimination method based on the pore water pressure increment $\sum\Delta U$ and cumulative filling load $\sum\Delta p$ ($\sum\Delta U$~$\sum\Delta p$) was more reasonable by studying on indoor and outdoor tests of soft clay [5]. However, when using this method, it is necessary to capture the peak value of excess pore water pressure in time and accurately, which is difficult for linear engineering such as highways. Ladd proposed the stability discrimination method on the basis of the lateral displacement and surface settlement [6]. Since the settlement caused by lateral displacement was a component of the surface settlement, consequently, when the lateral displacement changed abruptly, the surface settlement would also change, resulting in the hinder during the adoption of the method for stability discrimination. Because the lateral displacement test method cannot overcome the problems of inconsistent stiffness and deformation between soft soil and lateral displacement pipe, the accuracy of the test results remains to be further studied [7-10]. Huang Teng et al [11] proposed the stability discrimination method on the basis of measured settlement by combining the deformation and failure characteristics of soft clay, it could not only use the surface settlement information for stability discrimination, but also use the stratified settlement for stability discrimination of the weakest layer of the foundation. Wang Yanling [12] summarized three kinds stability control methods of high filled subgrades in soft soil areas, including the displacement rate method, the method of the ratio of maximum horizontal displacement and the settlement of the center of the subgrade, and the regression formula used in Japan. By analyzing an example, it is concluded that the ratio method was worthy of recommending method for the soft soil subgrade stability.

Wang Yanhui [13] used the settlement on daily filling to replace the undrained settlement, and proposed the grey system theory to generate cumulative treatment of the instantaneous settlement caused by each level of loading (AGO stability judgment method [14]) to estimate the stability of soft soil subgrade in mountainous areas. Although the method was simple and consistent with engineering practice, it was conservative.

Most scholars often took one field monitoring value as the control standard of soft soil subgrade stability, which was not comprehensive enough for the consideration of the monitoring and control standard of the stability, and the stability judgment was conservative in most cases. Before the instability failure of soft soil subgrade filling, the horizontal displacement and displacement rate of the subgrade slope foot, surface settlement at the subgrade center, stratified settlement, deep horizontal displacement, and excess pore water pressure would radically change. Therefore, when the above monitoring indexes were used as the stability control criteria for soft soil subgrades, the internal connection between them should be considered, and the comprehensive and multi-factor control method with multiple indexes simultaneously was adopted to evaluate the stability of soft soil subgrade.

In this paper, the thin-layer rotary adding method for the stability control and the loading plan determination for the soft soil subgrade during the filling period. Combined with the surcharge preloading method project in highway soft soil subgrade, using the thin-layer rotary adding method to calculate the ultimate filling height and the loading plan, and applying the inflection point analysis method (often used for monitoring indexes to control the stability of subgrades in a comprehensive way) on the stability analysis and evaluation of soft soil subgrade during the filling period, providing a feasible method with both theory and practice for the stability control and evaluation of highway soft soil subgrade.

THEORETICAL CALCULATION METHOD FOR STABILITY OF SOFT SOIL SUBGRADE

Ultimate filling height

The limit filling height was the maximum filling height of the natural foundation under sliding failure by using the limit equilibrium theory, which was generally calculated by the circular sliding method. To determine the location and radius of the center of the most dangerous sliding surface in the circular sliding method was quite tedious in the stability analysis of soft soil subgrade, which usually required a computer to do multiple calculations. To facilitate the application, the ultimate filling height was calculated using the following Fellenius formula [15]:

$$H_f = \frac{C_u N_c}{k\gamma} \tag{1}$$

Where C_u was the vane shear strength, k was the safety factor, γ was the bulk density of subgrade filling, and N_c was the bearing capacity factor, generally taken as 5.52.

Determination of loading plan by thin-layer rotary adding method

Drainage consolidation method was an economical and reasonable method of foundation treatment for soft soil subgrades, and the reinforcement effect would be better if sufficient drainage consolidation time was given to soft soil subgrade under surcharge loads. After many years of practical engineering experience and testing results, an effective and practical method of load stopping-the thin-layer rotary adding method was proposed. This method required that the strength growth of the foundation soil after one paving and compaction could just reach the capacity of filling next layer. Taking advantage of the strength growth of the foundation soil to achieve the purpose of rapid filling the embankment [16]. The detailed steps were as follows:

(1) Calculate the strength increase ΔC_{ui} in foundation soil required for the filling thickness Δh_i at level i. From Equation (1), we got:

$$\Delta C_{ui} = \frac{\gamma \cdot \Delta h_i \cdot k}{N_c} \tag{2}$$

(2) Calculate the loading time t_n for any filling load at n level

Let t_1, t_2, …, t_n be the time applying the 1, 2 and n level filling loads respectively (starting from zero, and t0=0 at the beginning of loading), t_i' was the loading duration time at the i level load, and t_0' was the loading duration time at the initial filling load. Δσ was the accumulated additional vertical stress when applying the n level of filling load, φ_{cu} was the consolidated fast shear internal friction angle of the foundation soil, and the weighted average value of each layer soil in the compression layer or the weakest layer of the foundation soil was selected as the control index. Δh_i and ΔP_i were the i level filling height and the corresponding load increment respectively, and Δh_0 and ΔP_0 were the ultimate filling height and the corresponding load increment respectively. U_t was the average degree of consolidation of foundation at instantaneous loading t, and U'_t was the average consolidation degree of foundation under the n-level constant speed loading at t time, calculated according to Equation (3).

$$U_t' = \sum_{i=1}^{n} \left(U_{t-\frac{t_i + t_{i-1}}{2}} \cdot \frac{\Delta P_i}{\sum \Delta P} \right) \tag{3}$$

Where t_{i-1} and t_i were the starting and ending times of the i-level load respectively. During each loading process, let ti=t. And $\sum \Delta P$ was the summation of n levels load. According to the strength growth formula, $\Delta C_u = U_t \cdot \Delta\sigma \cdot \mathrm{tg}\varphi_{cu}$. Considering the shear creep and the strength attenuation effect under shear stress and other factors, the reduction factor η should be multiplied (According to the measured results, η was taken from 0.8 to 0.85; If the foundation soil had no strength attenuation, η=1), we have:

$$\begin{aligned}
\sum_{i=1}^{n}\Delta C_{ui} &= \eta\cdot U_t'\cdot\Delta\sigma\cdot tg\varphi_{cu}\\
&=\eta\cdot tg\varphi_{cu}\cdot\left(U_{t_n-t_0'/2}\cdot\Delta P_0+U_{t_n-t_1-t_1'/2}\cdot\Delta P_1+\cdots+U_{t_n-t_{n-1}-t_{n-1}'/2}\cdot\Delta P_{n-1}\right)\\
&=\eta\cdot tg\varphi_{cu}\cdot\sum_{i=1}^{n}\left(U_{t_n-t_{i-1}-t_{i-1}'/2}\cdot\Delta P_{i-1}\right)=\eta\cdot tg\varphi_{cu}\cdot\sum_{i=1}^{n}\left\{\Delta P_{i-1}\cdot\left[1-\alpha e^{-\beta(t_n-t_{i-1}-t_{i-1}'/2)}\right]\right\}\\
&=\eta\cdot tg\varphi_{cu}\cdot\left\{\sum_{i=1}^{n}\Delta P_{i-1}-\alpha\sum_{i=1}^{n}\left[\Delta P_{i-1}\cdot e^{-\beta t_n+\beta(t_{i-1}+t_{i-1}'/2)}\right]\right\}\\
&=\eta\cdot tg\varphi_{cu}\cdot\left\{\sum_{i=1}^{n}\Delta P_{i-1}-\alpha\cdot e^{-\beta t_n}\cdot\sum_{i=1}^{n}\left[\Delta P_{i-1}\cdot e^{\beta(t_{i-1}+t_{i-1}'/2)}\right]\right\}
\end{aligned}\tag{4}$$

After sorting, we can get:

$$e^{-\beta t_n}=\frac{\eta\cdot tg\varphi_{cu}\cdot\sum_{i=1}^{n}\Delta P_{i-1}-\sum_{i=1}^{n}\Delta C_{ui}}{\eta\cdot tg\varphi_{cu}\cdot\alpha\cdot\sum_{i=1}^{n}\left[\Delta P_{i-1}\cdot e^{\beta(t_{i-1}+t_{i-1}'/2)}\right]}\tag{5}$$

After solving, we obtained:

$$t_n=-\frac{1}{\beta}\cdot\ln\left\{\frac{\eta\cdot tg\varphi_{cu}\cdot\sum_{i=1}^{n}\Delta P_{i-1}-\sum_{i=1}^{n}\Delta C_{ui}}{\eta\cdot tg\varphi_{cu}\cdot\alpha\cdot\sum_{i=1}^{n}\left[\Delta P_{i-1}\cdot e^{\beta(t_{i-1}+t_{i-1}'/2)}\right]}\right\}\tag{6}$$

If all loading were completed instantaneously, i.e., $t'_0 = t'_1 = t'_2 = \cdots = t'_{n-1} = 0$, Eq (6) could be simplified as:

$$t_n=-\frac{1}{\beta}\cdot\ln\left[\frac{\eta\cdot tg\varphi_{cu}\cdot\sum_{i=1}^{n}\Delta P_{i-1}-\sum_{i=1}^{n}\Delta C_{ui}}{\eta\cdot tg\varphi_{cu}\cdot\alpha\cdot\sum_{i=1}^{n}(\Delta P_{i-1}\cdot e^{\beta t_{i-1}})}\right]\tag{7}$$

Substituting Eq (2) into Eq (6), we could get:

$$t_n=-\frac{1}{\beta}\cdot\ln\left\{\frac{N_c\cdot\eta\cdot tg\varphi_{cu}\cdot\sum_{i=1}^{n}\Delta h_{i-1}-k\cdot\sum_{i=1}^{n}\Delta h_i}{N_c\cdot\eta\cdot tg\varphi_{cu}\cdot\alpha\cdot\sum_{i=1}^{n}\left[\Delta h_{i-1}\cdot e^{\beta(t_{i-1}+t_{i-1}'/2)}\right]}\right\}\tag{8}$$

Where α, β were adopted according to the drainage and consolidation conditions of foundation soil in accordance with Table 5.2.7 of Technical Specification for Building Foundation Treatment JGJ 79-2012 [17].

THE CONTROL METHOD OF SUBGRADE STABILITY

Apparent characteristics of foundation instability

There were usually some premonitions before the instability failure occurred in the subgrade, which mainly as followed [18]: (1) some microcracks appeared on the top of loading, slope site and slope surface; (2) ground uplift near the loading slope site; (3) the surface settlement, deep horizontal displacement and pore water pressure in the loading area increased sharply; (4) continued development of longitudinal cracks with circular shape after stopping loading; (5) continued increase in ground uplift near the loading slope site after stopping loading;

(6) continued increase in various monitoring indexes or insignificant convergence after stopping loading.

Inflection point analysis method on the basis of monitoring

In actual construction, the appearance of apparent characteristics does not necessarily represent the instability of subgrade. When one of the settlement rate, lateral displacement rate and pore water pressure coefficient during loading exceeds the quantitative control index, the foundation is not destabilized, and it is necessary to evaluate the stability of soft soil subgrade through the comprehensive analysis with the above monitoring data. Staged filling of soft soil subgrade with the thin-layer intermittently adding method, the two-level filling interval is about seven days, and each level filling is completed within one day. The loading rate far exceeds the dissipation rate of pore water pressure in the soil, which formed the effect of undrained shear. And the response of pore water pressure of embankment soft soil unit under undrained condition is divided into following three stages (as shown in Figure 1).

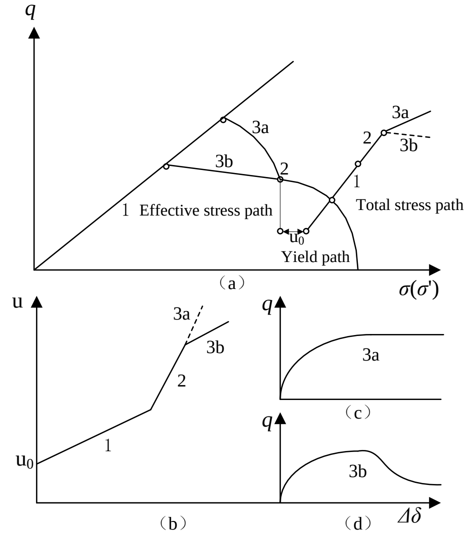

Fig. 1 – Stress path of the soft soil element of subgrade
(a) Stress path in the site; (b) The relationship between pore water pressure u and shear deformation $\Delta\delta$*;*
(c) Hardening phenomenon; (d) Softening phenomenon

(1) Elastic stage. At this stage, part of the additional stress is borne by the pore water due to the influence of soil structure, namely $\Delta u<\Delta\sigma_z$. The relationship between the pore water pressure increment and load increment at one subgrade soil point under large preloading load is given by $\Delta u=B\Delta p$, where B is the pore pressure coefficient and $B<1$, as shown in the stress path in curve 1 in Figure 1.

(2) Plastic stage. At this stage, as the external load increase, the shear stress in soil exceeds the shear strength between the soil particles, the bond between the soil particles breaks down, and the structure readjusts and begins to produce plastic deformation. Then the additional stress is basically borne by the pore water pressure, namely $\Delta u \approx \Delta\sigma_z$, and shear instability occurs locally in the subgrade, as shown in the stress path in curve 2 in Figure 1.

(3) Hardening or softening stage. At this stage, after the connection failure between the soil particles, the soil particles position moves, accompanied by the increase of plastic deformation. Due to the soil structural characteristics, the deformation of soil will be bifurcation. In one case, the arrangement between soil particles tends to a more stable state, with the so-called hardening phenomenon (Figure 1(c)) and the stress path shown in curve 3a in Figure 1; in the other case, the softening phenomenon (Figure 1(d)) occurs as the failure point of the soil increases, with the stress path shown in curve 3b in Figure 1.

From the above analysis, it could be shown that the key is the appearance of the plastic deformation stage, that is, the appearance of the first inflection point in $\Delta u \sim \Delta p$ curve, indicating that local shear failure has happened in the soil where the pore gauge is located. And if inflection points appeared in all the pore gauge at different depths, showing that the foundation is in a state of overall instability.

ENGINEERING EXAMPLE ANALYSIS

Test section overview

The first phase of Guangzhou-Zhuhai Expressway starts from Guangzhou in the north to Hainan Village in the south and ends at Bijiang, Beijiao Town, Shunde City, with a total length of 14.659km. The route is located in the alluvial plain of the Pearl River Delta, and the distribution of soft soils is extremely uneven, with a general thickness of 1 to 5m and local sections exceeding 10m. The main road section is the intersection of bridges and soft foundations, with thicker soft soil layers and higher embankment fill, problems of embankment stability and uneven settlement at the connection between bridge head and embankment are obvious. At the same time, the influence of lateral pressure generated by high fill on the embankment cannot be ignored, especially the abutment pile foundation of the that intersects the route diagonally, if not handled properly, the stability and safety of the embankment would be affected. Combined with local experience, proposing surcharge preloading method on soft foundation treatment, and a small amount of geotextile reinforcement is set in some soft soil and high fill sections to establish a soft soil foundation monitoring system, in accordance with the thin-layer rotary adding method for subgrade filling construction. The section from K11+021 to K11+220, where the thickness of silt layer is 13.5 m and the height of fill is large (maximum 7.2m, minimum 6m), was selected for soft foundation test. According to the geological conditions and design data of the test section, the test arrangement of geotextiles is shown in Table 1, the arrangement of monitoring and monitoring instruments is shown in Table 2, and the arrangement of the buried cross-sectional of monitoring and monitoring instruments is shown in Figure 2.

Tab. 1: Test Arrangement of Geotextiles

Pile no.	Original design scheme	Safety coefficient of subgrade stability	Test scheme	Remark
K11+021~K11+070	Three-layer geogrid	1.213	Two-layer geotextile	Equal load
K11+070~K11+166	Two-layer geogrid	1.259	One-layer geotextile	Surcharge
K11+166~K11+220			No geotextile	Surcharge

Tab. 2: Arrangement of Monitoring and Monitoring Instruments

Section	Inclinometer tube	Pore water pressure gauge	Earth pressure	Layered settlement hole	Surface settlement
K11+032	One hole (15m)	One hole (Three gauges)			
K11+045	One hole (15m)	One hole (Three gauges)	Three		Three
K11+116	One hole (15m)	One hole (Five gauges)	Three	One hole (15m)	Five
K11+166		One hole (Four gauges)			Three
K11+196	One hole (15m)	One hole (Five gauges)		One hole (15m)	Three

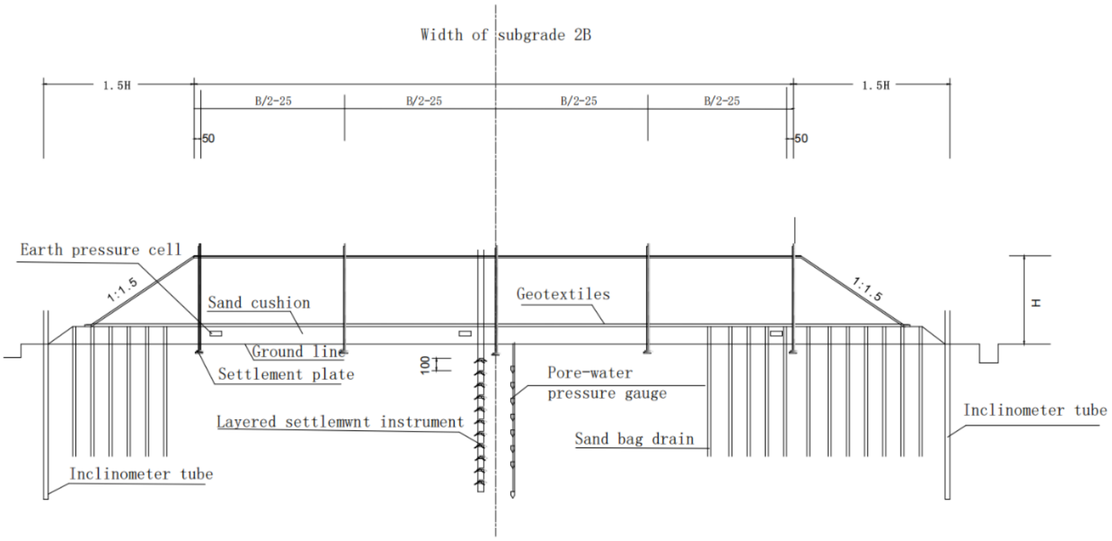

Fig. 2 – The cross-sectional schematic diagram of the buried monitoring instruments

Ultimate filling height

Due to the soil disturbance during the construction of bagged sand wells, reducing the soil strength. When the ultimate filling height was calculated with Eq. (1), the soil strength should be taken as the strength after construction disturbance. According to the test results of soft soil foundation of several highways in the region, the construction disturbance reduced the strength of surrounding soil by about 45%, and the ultimate filling height of each section of subgrade was calculated according to this strength loss, as shown in Table 3.

Tab. 3: Ultimate Filling Height of Each Subgrade Section

Section	γ /(kN/m^3)	Cu/kPa		k_{min}	H_f /m
		Initial value	Calculation value considering strength loss		
K11+045	19	13.34	7.34	1.0	2.0
K11+084	19	12.08	6.64	1.0	1.9
K11+116	19	12.71	6.99	1.0	1.9
K11+166	19	14.60	8.03	1.0	2.2
K11+196	19	16.80	9.24	1.0	2.6

Loading plan

According to the main calculation parameters of each section shown in Table 4, the loading plan of the corresponding section was obtained from Eq (8), as shown in Table 5. In Table 4, the sand drains were arranged in squares with spacing of 1.2m, and the treatment depth of K11+045 subgrade section was 13m and 12m for the other sections, with the height H from the bottom of soft soil layer to the ground.

Tab. 4: Main Calculation Parameters of Each Subgrade Section

Section	φ_{cu}/ (°)	C_v/(10^{-3}cm^2/s)	C_r/(10^{-3}cm^2/s)	H/m	β_v/(10^{-7}s^{-1})	β_r/(10^{-7}s^{-1})
K11+045	12.8	8.5	1.25	12.5	0.134	2.930
K11+084	12.9		1.15	8.8		2.695
K11+116	11.7		1.33	10.2		3.117
K11+166	14.6	9.0	0.86	12.4	0.144	2.016
K11+196	11.3	8.5	1.035	9.7	0.229	2.426

Tab. 5: Loading Plan of Each Subgrade Section

Section	Ultimate filling soil		Planned filling height /m	Planned filling height per level /m	Average loading time per level /d		Duration time of loading to design load /d
	Height /m	Loading duration time /d			Loading duration time	Intermittent time	
K11+045	3.2	10	10.8	0.25	1	4	145
				0.45	2	7	157
				0.65	2	11	169
K11+084	2.2	10	8.1	0.25	1	7	190
				0.45	2	13	199
				0.65	2	21	216
K11+116	2.2	10	7.8	0.25	1	9	243
				0.45	2	20	293
				0.65	2	45	437
K11+166	2.5	10	8.1	0.25	1	5	148
				0.45	2	9	157
				0.65	2	15	164
K11+196	2.5	10	7.5	0.25	1	9	215
				0.45	2	18	233
				0.65	2	34	295

Subgrade stability analysis

In order to comparative analysis, the pore water pressure increment $\Delta u_{7.5}$, single-stage pore pressure coefficient B (taking the middle of the soft soil layer), cumulative settlement S and lateral displacement rate V_c for K11+045, K11+166 and K11+196 subgrade sections are summarized in supplementary Tables 1 to 3. The cumulative filling height in the tables ignored the settlement value, which was considered in the actual cumulative filling height. The data in the tables were the observation data before the filling soil of the next layer, and the last layer of filling data was the data of 7 days after filling. $\Delta u_{7.5}$ in the tables indicated the pore water pressure increment of the pore gauge at the burial depth of 7.5m, $\delta_{7.0}$ indicated the cumulative lateral displacement at the burial depth of 7.0m, and the rest was the same. The relationship between these monitoring data and load could be used to determine the subgrade stability and reasonable loading time.

Analysis on the increment of pore water pressure

The relationship curves between the cumulative pore water pressure increment $\sum\triangle u$ and cumulative load $\sum\triangle P$ were obtained with the data in supplementary Tables 1 to 3, as shown in Figure 3. It could be seen from Figure 3 that the curve of $\sum\triangle u$~$\sum\triangle P$ for each section was approximately linear at initial loading stage, and the tangent slope of the curves decreased at the later loading stage, indicating that the cumulative pore water pressure increment decreased at the later loading stage, the consolidation degree of foundation increased, the strength increased, and the deformation tended to be stable. Figure 3 depicted that the turning points emerged in the

∑△u~∑△P curves during the loading period throughout the filling period. In Figure 3, at the section K11+045, the first turning point occurred at the fourth level filling load (corresponding to the filling height of 3.286m), namely, the curve was basically linear at the filling height of 3.286m, and when the next level of filling load (corresponding to the filling height of 3.799m) was to be filled again, the curve bended upward and the slope increased. According to the elastic-plastic theory of soil, the soil entered the plastic deformation stage when the filling height increased from 3.286m to 3.799m. Therefore, the filling height corresponding to the transformation of the section soil from elastic to plastic stage could be taken as the average value of 3.543m, which was close to the ultimate filling height calculated theoretically. Similarly, the filling heights corresponding to the transformation of the section K11+166 and K11+196 soil from elastic to plastic stage were 2.854m and 2.61m respectively, which were also close to the ultimate filling heights calculated theoretically.

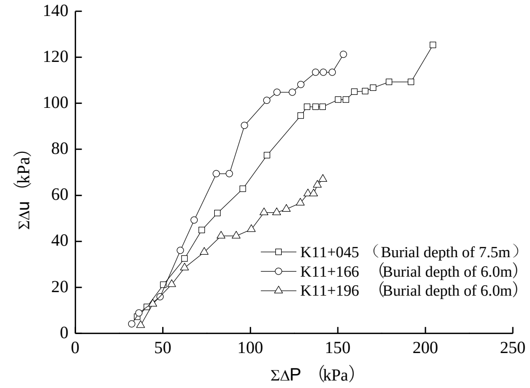

Fig. 3 – The relationship curve between ∑△u and ∑△P of each section

It could be seen from Figure 3 that when each section was loaded at the last two levels loading, the upward turning points emerged in the ∑△u~∑△P curves of each section, which was mainly because the loading rate is too fast, and the soil could not be consolidated by drainage, forming a fast-undrained shear state and making the soil instability. After taking the measures to stopping loading or unloading, the slope of the curve became smaller and the foundation tended to be stable.

The above analysis showed that within the ultimate filling height, ∑△u~∑△P curve was linear and the foundation soil was in elastic stage, at this time, the loading rate could be accelerated. After exceeding the ultimate filling height, an upward inflection point appeared in the ∑△u~∑△P curve, and the soil was in the plastic deformation stage. At this time, the loading speed should be slowed down, and the loading could continue until it reached the required consolidation degree. During the loading process, when the upward turning point emerged in the ∑△u~∑△P curve, indicating increasing the tangent slope of the curve, the foundation was unstable and should be stopped or unloaded immediately.

The relationship curves between the single-stage pore pressure coefficient B and cumulative load ∑△P were obtained with the data in supplementary Tables 1 to 3, as shown in Figure 4. Figure 4 and supplementary Tables 1 to 3 demonstrated that some of the single-stage pore pressure coefficients B exceeded the loading control standard of 1.0, but the subgrade soil was not instability. Which was mainly because the test section was constructed by the blowing filling method, and the sand contained a large amount of water, with the effect of power equipment, the ratio between the increment of excess pore water pressure and load increment was larger than the calculated value. And the single-stage pore pressure coefficient B exceeded 1.2 at the inflection point of the ∑△u~∑△P curve in all three sections. When adopting the blowing filling method, it is recommended that the single-stage pore pressure coefficient B control standard was smaller than 1.2.

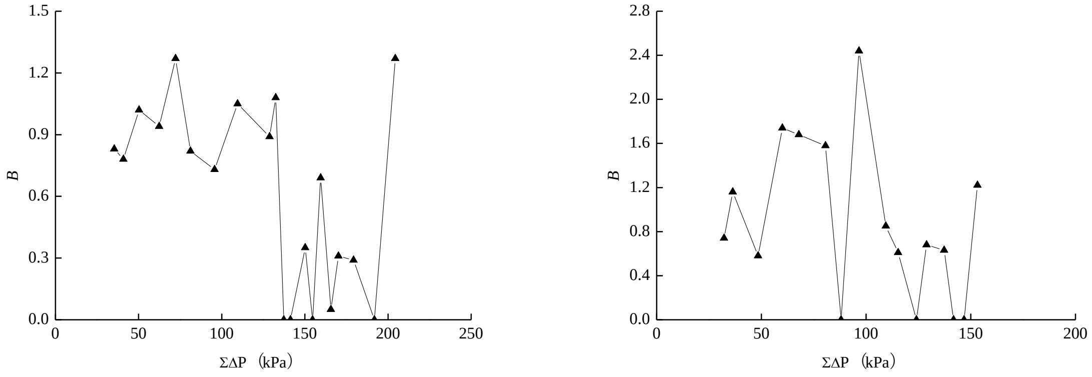

(a) Burial depth of 7.5m at the section K11+045 *(b) Burial depth of 6.0m at the section K11+166*

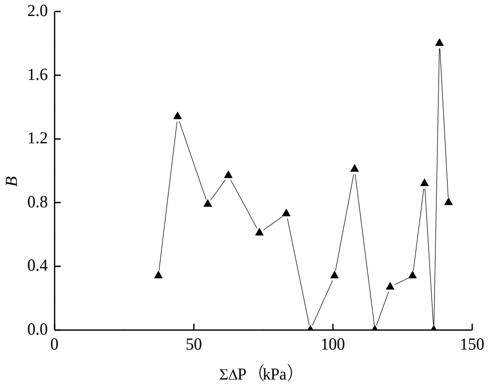

(c) Burial depth of 6.0m at the section K11+196

Fig. 4 – The relationship curve between B and ∑△P of each section

In Figure 3, taking the section K11+045 as the example to analyze the loading interval time. When the filling height increased from 0 to 3.286m (close to the ultimate filling height), it took 102 days, with an average of 32.2mm per day, including 40cm to 60cm of each loading height. When the filling height increased from 3.286m to 6.97m, it took 191 days, with an average of 19.3mm per day, including 50cm to 70cm of each loading. And when the filling height increased from 6.97m to 9.433m, it took 62 days, with an average of 39.7mm per day, which was close to the filling rate before the ultimate fill height. The average filling rate was 39.7mm per day for 62 days from 6.97m to 9.433m, which was close to the filling rate before the ultimate filling height, including 20cm to 30cm of each loading height. The above analysis showed that when proposing the thin-layer rotary adding method for loading, thinner the load of each layer would lead to the faster consolidation of the foundation, the faster the loading rate is, and the more stable foundation, which was consistent with the theoretical analysis results of the thin-layer rotary adding method using the foundation strength growth to guide the loading, indicating that adopting the thin-layer rotary adding method in guiding the filling construction was feasible both theoretically and practically.

Settlement analysis

The relationship curves between the cumulative settlement rate ∑V and cumulative filling height ∑Δh was obtained with the data in supplementary Tables 1 to 3, as shown in Figure 5. Figure 5 showed that the curve was a linear relationship in the steady state of the foundation. Excessive filling rate would lead to the larger soil shear deformation, significant increase of the settlement, and significant increase of the loading rate of the level. And an upward inflection point emerged in the curve, namely, the slope of the curve increased, indicating that the subgrade was at risk of instability. At this time, the observation of lateral displacement and pore water pressure should be strengthened, and measures such as stopping loading and unloading should be taken when necessary. which was consistent with the analysis results of the ∑△u~∑△P curve.

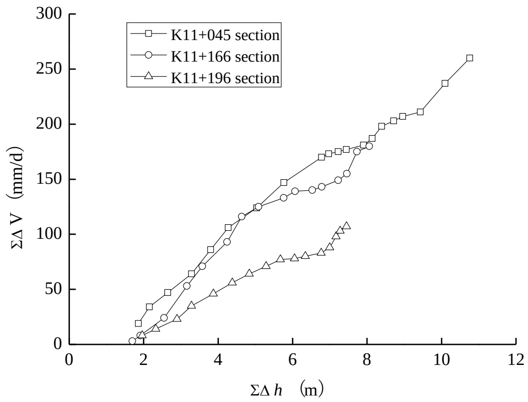

Fig. 5 – The relationship curve between ∑V and ∑△h of each section

From supplementary Tables 1 to 3, it can be seen that when the ∑△u~∑△P curve of K11+045 and K11+166 sections appeared the upward inflection point, the corresponding settlement rates exceeded 20mm/d (the maximum is 29mm/d). When the settlement rate was less than 20mm/d, no upward inflection point appeared. However, the settlement rate of K11+196 section during the whole loading process was small, which is less than 12mm/d. To make it clear, the fast settlement rate could not indicate the immediate instability of the foundation, but through observing the change of lateral displacement and judging whether the settlement was mainly caused by the undrained shear deformation under the current load. If the lateral displacement or lateral displacement rate increased too fast, it indicated that the foundation would be at risk of instability. Otherwise, the excessive settlement could only be explained by the consolidation settlement under the previous levels filling load or the insufficient foundation bearing capacity under the current level filling loading. The former would lead to the increase of foundation strength and the foundation tend to be stable, and the latter would lead to the soil to enter the plastic deformation stage from the elastic stage, prompting the consolidation of the foundation. Therefore, When the surface settlement rate was used as the standard to control the loading rate, the settlement rate should be greater than 20mm/d. However, the surface settlement rate was only regarded as a reference standard, and the horizontal lateral displacement was used as the main control standard.

Lateral displacement analysis

The relationship curve between the cumulative lateral displacement rate ∑Vc and cumulative filling height ∑Δh was obtained with the data in supplementary Tables 1 to 3, as shown in Figure 6. It could be seen from Figure 6 that the upward inflection point appeared in the curve of each section at the last two levels of filling. The slope of the curve increased and the growth of the lateral displacement rate accelerated. This is mainly due to the rapid filling, and the maximum lateral displacement rate reached 8.75mm/d. According to supplementary Tables 1 to 3, when the lateral displacement rate was close to 3mm/d, the upward inflection point in the curve showed up, consequently, the control standard of the lateral displacement rate was 3mm/d.

The relationship curve between the cumulative lateral extrusion V_h, the cumulative lateral displacement $\delta_{7.0}$ and cumulative filling height ∑Δh were obtained with the data in supplementary Tables 1 to 3, as shown in Figure 7 and Figure 8. It could be seen from Figure 7 and Figure 8 that if the filling rate was too fast, the shear deformation of the soil increased, the accumulated lateral extrusion V_h and the accumulated lateral displacement $\delta_{7.0}$ increased significantly, and the appearance of the upward inflection point in the curve, namely, increasing the slope of the curve, indicating that the subgrade would become instability, measures such as stopping load and unloading should be taken at this time, which was consistent with the analysis results of the previous ∑△u~∑△P curve.

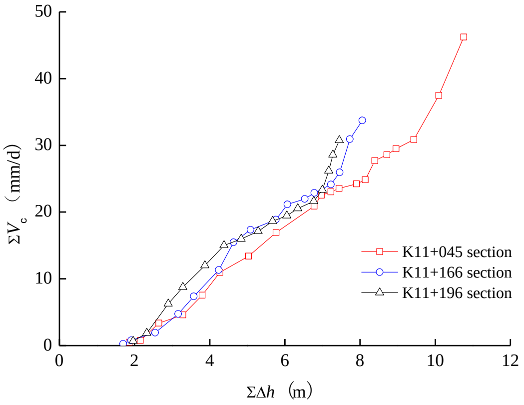

Fig. 6 – The relationship curve between $\sum V_c$ and $\sum \Delta h$ of each section

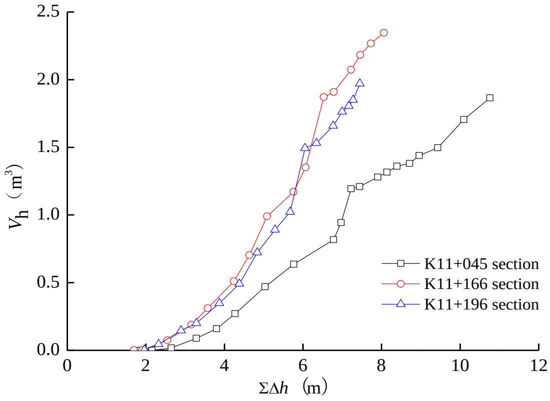

Fig. 7– The relationship curve between V_h and $\sum \Delta h$ of each section

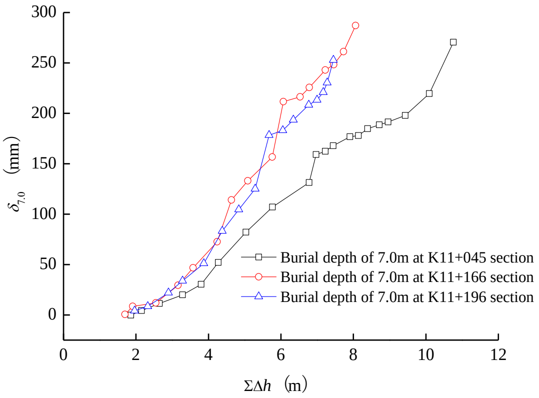

Fig. 8 – The relationship curve between $\delta_{7.0}$ and $\sum \Delta h$ of each section

Within the ultimate filling height, the soil was in the elastic deformation stage, the curve was straight. When the filling height exceeded the ultimate filling height, the soil would enter the plastic deformation stage from elasticity, the lateral displacement rate, lateral extrusion, lateral displacement would increase significantly, the slope of the curve increased, and then the first upward inflection point appeared. Consequently, the ultimate filling height could be approximately determined according to the first upward inflection point of the curve. As shown in Figures. 6-8, there was an upward inflection point of K11+045 section when the filling height reached 3.286m, namely, when the filling height increased from 3.286m to 3.799m, the soil properties changed from the elastic stage to the plastic deformation stage, and the ultimate filling height of K11+045 section could be approximately determined as 3.543m. Similarly, the ultimate filling heights of K11+166 and K11+196 sections could be determined as 2.854m and 2.61m respectively, which were consistent with the analysis results of the previous $\sum \triangle u \sim \sum \triangle P$ curves.

Reinforcing effect of geotextiles

The geotextile was often used to improve the anti-sliding stability of subgrade and increase the ultimate filling height. The comparisons of the theoretical ultimate fill height of each subgrade section and the results of analysis through monitoring data were shown in Table 6. The one layer geotextile and two layers geotextile increased the ultimate filling height by 0.65m and 1.55m respectively, accordingly, the geotextile had a greater effect on improving the anti-sliding stability of the foundation and speeding up the filling rate of the subgrade.

Tab. 6: Comparison between the Theoretical Calculation of Ultimate Filling Height and the Analysis Results of Monitoring Data

Section	Theoretical calculation of ultimate filling height A/m	Analysis results of ultimate filling height by the monitoring data C /m	C-A /m	Remarks
K11+045	2.0	3.543	1.543	Two layers geotextile
K11+166	2.2	2.854	0.654	One layer geotextile
K11+196	2.6	2.61	0.01	no geotextile

The comparison curves of $\sum V_c \sim \sum \Delta V$, $\delta_{7.0} \sim S$, $V_h \sim S$ and $\delta_{7.0}/S \sim S$ of each section were obtained with the data in supplementary Tables 1 to 3, as shown in Figure 9. It could be seen from Figure 9 that the curve of section K11+045 was at the bottom, the curve of section K11+196 was at the top, while the curves of section K11+166 was in the middle, indicating that the geotextile could effectively constrain the lateral displacement and lateral extrusion, reduce the final settlement of the foundation and increase the anti-sliding stability of the foundation.

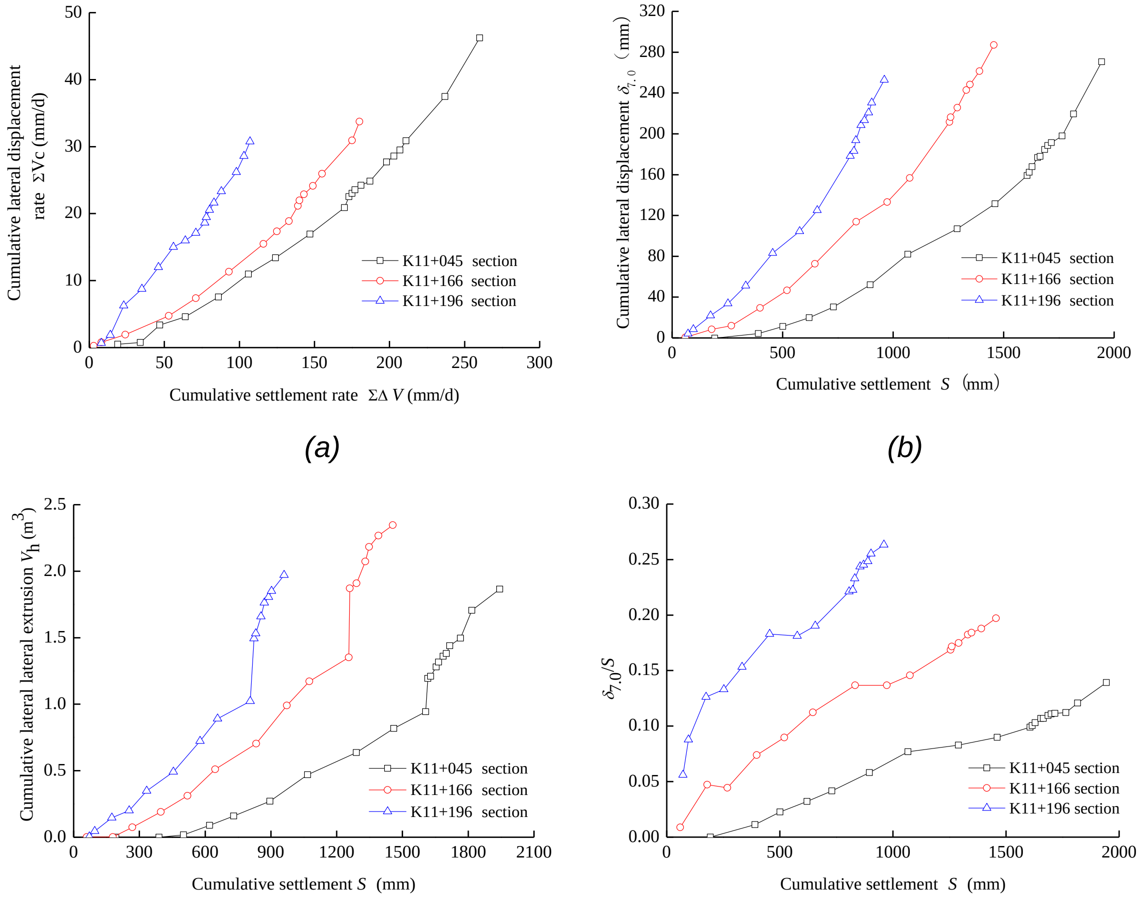

(a)

(b)

(c)

(d)

Fig. 9 – The comparison curves of $\sum V_c \sim \sum \Delta V$, $\delta_{7.0} \sim S$, $V_h \sim S$ and $\delta_{7.0}/S \sim S$ of each section

When the geotextile was set in the subgrade soil, due to the effect of friction between the geotextile and the subgrade soil, the tensile stress in the soil was transferred to the geotextile. Therefore, the geotextile was under tensile stress, and the subgrade soil was under compressive stress and shearing stress between geotextiles. The geotextile and subgrade soil could live up to their potential, so the cohesion effect and the built-in function between the geotextile reinforced body and the soil had generated, which could enhance the integrity and continuity of soil, limit the lateral displacement of soil and increase the stability of subgrade.

In addition, due to the stress diffusion effect of the geotextile, the additional stress of the subgrade soil under the geotextile decreased, so that the vertical compression deformation of soil decreased. Because the geotextile was subjected to tensile stress, the tensile stress was balanced by the interface shear stress. Under the action of the interface shear stress, the subgrade soil produced uplift deformation, which could offset the partial settlement of the subgrade, reduce the final settlement of the subgrade and increase the stability of the subgrade.

Comprehensive comparative analysis

Through the comprehensive comparative analysis of Figures 3 to 6, the internal relations between them was analyzed. In Figure 3 (section K11+045), the curve was basically straight during the first four levels load (corresponding to the filling height of 3.286 m), and then the slope of the curve increased slightly from the fifth level load (corresponding to the filling height of 3.799 m). The corresponding settlement rate of the section K11+045 in Fig 5 increased slightly and the lateral displacement rate of the section K11+045 In Figure 6 also increased obviously, with an upward inflection point, indicating that the local shear failure of the soil began to occur, and then the part of the soil continued to undergo shear failure, and began to harden, consolidation, and the slope of the curve gradually decreased. After maintaining a straight section, and the foundation strength gradually increased and the subgrade tended to stabilize. The same results could be obtained from the curve analysis of other sections, indicating that the $\sum\triangle u$ to $\sum\triangle P$ curve, $\sum\Delta V$ to $\sum\triangle h$ curve and $\sum V_c$ to $\sum\triangle h$ curves were consistent. At the same time, the lateral displacement rate was highly sensitive to the foundation state. Therefore, in the monitoring process of soft soil subgrade, the lateral displacement and displacement rate should be used as the main monitoring indexes, which were the important indicators to determine whether the foundation was stable.

When drawing the curves of $\sum\Delta V \sim \sum\triangle h$ and $\sum V_c \sim \sum\triangle h$, the attention should be paid to the treatment of load levels. Because the daily settlement or lateral displacement of the filling load at this level contained the daily consolidation deformation under the previous levels filling load and the undrained shear deformation produced by the filling load at this level. When the loads at all levels were similar and the loading interval time was similar, the curve could basically eliminate the influence of the daily consolidation deformation under the previous levels filling loads, and the slope of the curve could reflect the change direction of the undrained shear deformation produced by the filling load at the corresponding level. If a certain level load is very small, comparing the daily consolidation deformation under the previous levels filling loading and the undrained shear deformation produced by this level filling load, the increasing of the former proportion, would result in a larger slope of the curve. while the surface settlement and lateral displacement rate may not actually increase. Therefore, when the load was small, it could be combined with the previous levels load into the first level load, and the slope of the curve was comparable. Similarly, the unloaded load should be treated as the previous level load when unloading, otherwise the curve would be reversed.

CONCLUSION

(1) Drainage consolidation method was always used to treat soft soil subgrade, and the thin-layer rotary adding method was proposed to determine the loading plan and the ultimate filling height to control the graded surcharge thickness, which was a practical method to effectively control subgrade stability both in theory and practice.

(2) According to the soil failure theory and the pore water pressure response generated by the graded filling subgrade with the thin-layer rotary adding method, the deformation of soft soil subgrade was divided into the elastic stage, plastic stage, hardening or softening stage, and the inflection point analysis method based on monitoring was proposed to evaluate the stability state of soft soil subgrade.

(3) The proposed stability calculation theory and control method were applied on the comprehensive analysis of the monitoring data of the test section of soft soil subgrade in the

highway to evaluate the stability of soft soil subgrade. The results showed that: 1) When the inflection point appeared in the $\sum\triangle u$~$\sum\triangle P$ curve, that is, the slope increased, the soft soil subgrade was near to instability, and the subgrade monitoring should be strengthen. When the blow-filling method was used for the subgrade construction, the stability control standard was that the single-stage pore pressure coefficient B should be controlled within 1.2 during loading. 2) When no upward inflection point emerged in the $\sum\Delta V \sim \sum\triangle h$ and $\sum V_c \sim \sum\triangle h$ curves, the soft soil subgrade was stable. When an upward inflection point appeared in the curve, the soft soil subgrade was close to instability, so the monitoring of the change trend of the lateral displacement rate should be strengthened. If the lateral displacement rate continued to increase, and the subgrade was close to instability, measures such stopping load or unloading should be taken. 3) The control standard of soft soil subgrade stability was the maximum settlement rate was controlled within 20mm/d, and the maximum lateral displacement rate was controlled within 3mm/d.

(4) Theoretical calculations and monitoring results showed that the geotextiles was able to effectively improve the ultimate bearing capacity of the subgrade soil, reduce lateral displacement, improve the anti-sliding stability of the subgrade, and accelerate the filling rate.

Appendix

Tab. 1: Monitoring Data of K11+045 Section

Calculation value of cumulative filling height(m)	Actual cumulative filling height $\sum\triangle h$(m)	Actual cumulative load $\sum\triangle P$ (kPa)	Lateral displacement rate V_c (mm/d)	Cumulative lateral displacement rate $\sum V_c$ (mm/d)	Cumulative lateral extrusion V_h (m^3)	Maximum settlement rate V(mm/d)	Cumulative settlement rate $\sum V$ (mm/d)	Cumulative lateral displacement $\delta_{7.0}$ (mm)	Cumulative settlement S(mm)	B	$\triangle u_{7.5}$ (kPa)	$\sum\triangle u_{7.5}$ (kPa)
1.785	1.860	35.34	0.490	0.490	0	19	19	-0.22	193	0.83	7.2	7.2
1.959	2.152	40.89	0.260	0.750	0	15	34	4.35	390	0.78	4.3	11.5
2.255	2.645	50.26	2.610	3.360	0.0176	13	47	11.32	501	1.02	9.6	21.1
2.785	3.286	62.43	1.220	4.580	0.089	17	64	19.90	620	0.94	11.4	32.5
3.179	3.799	72.18	2.960	7.540	0.16	22	86	30.31	730	1.27	12.4	44.9
3.544	4.274	81.21	3.440	10.980	0.271	20	106	52.07	896	0.82	7.4	52.3
4.138	5.034	95.65	2.430	13.410	0.469	18	124	82.10	1067	0.73	10.5	62.8
4.699	5.766	109.55	3.540	16.950	0.636	23	147	106.92	1290	1.05	14.6	77.4
5.490	6.780	128.82	3.950	20.900	0.817	23	170	131.39	1461	0.89	17.2	94.6
5.509	6.970	132.43	1.620	22.520	0.943	3	173	159.08	1606	1.08	3.9	98.5
5.621	7.227	137.31	0.500	23.020	1.194	2	175	162.40	1616	0.00		98.5
5.825	7.441	141.38	0.530	23.550	1.21	2	177	167.79	1629	0.00		98.5
6.278	7.907	150.23	0.670	24.220	1.28	4	181	176.69	1654	0.35	3.1	101.6
6.482	8.136	154.58	0.610	24.830	1.317	6	187	177.90	1665	0.00		101.6
6.730	8.395	159.51	2.890	27.720	1.361	11	198	184.69	1686	0.69	3.4	105.0
7.031	8.717	165.62	0.860	28.580	1.381	5	203	188.64	1700	0.05	0.3	105.3
7.257	8.957	170.18	0.910	29.490	1.439	4	207	191.36	1716	0.31	1.4	106.7
7.717	9.433	179.23	1.370	30.860	1.497	4	211	197.95	1765	0.29	2.6	109.3
8.330	10.095	191.81	6.610	37.470	1.705	26	237	219.49	1817	0.00		109.3
8.941	10.758	204.40	8.750	46.220	1.865	23	260	270.55	1944	1.27	16.0	125.3

Tab. 2: Monitoring Data of K11+166 Section

Calculation value of cumulative filling height(m)	Actual cumulative filling height $\sum\triangle h$(m)	Actual cumulative load $\sum\triangle P$ (kPa)	Lateral displacement rate V_c (mm/d)	Cumulative lateral displacement rate $\sum Vc$ (mm/d)	Cumulative lateral extrusion V_h (m^3)	Maximum settlement rate V(mm/d)	Cumulative settlement rate $\sum V$ (mm/d)	Cumulative lateral displacement $\delta_{7.0}$ (mm)	Cumulative settlement S(mm)	B	$\triangle u_{7.5}$ (kPa)	$\sum\triangle u_{7.5}$ (kPa)
1.651	1.695	32.21	0.26	0.26	0.0015	3	3	0.53	60	0.74	4.09	4.09
1.850	1.910	36.29	0.52	0.78	0.002	5	8	8.45	179	1.16	4.72	8.81
2.370	2.549	48.43	1.14	1.92	0.074	16	24	11.90	268	0.58	7.06	15.87
2.891	3.159	60.02	2.82	4.74	0.1904	29	53	29.44	398	1.74	20.16	36.03
3.176	3.574	67.91	2.64	7.38	0.3109	18	71	46.60	520	1.68	13.22	49.25
3.722	4.242	80.60	3.94	11.32	0.51	22	93	72.61	646	1.58	20.10	69.35
3.988	4.634	88.05	4.16	15.48	0.704	23	116	113.93	833	0.00		69.35
4.254	5.087	96.65	1.87	17.35	0.9905	9	125	133.06	973	2.44	21.00	90.35
4.786	5.759	109.42	1.51	18.86	1.1714	8	133	156.66	1075	0.85	10.88	101.23
4.992	6.067	115.27	2.29	21.15	1.351	6	139	211.63	1255	0.61	3.56	104.79
5.272	6.527	124.01	0.82	21.97	1.8707	1	140	216.24	1260	0.00		104.79
5.526	6.786	128.93	0.92	22.89	1.9087	3	143	225.67	1291	0.68	3.36	108.15
5.935	7.226	137.29	1.26	24.15	2.0724	6	149	242.86	1331	0.63	5.29	113.44
6.130	7.461	141.76	1.81	25.96	2.183	6	155	248.30	1348	0.00		113.44
6.378	7.726	146.79	4.96	30.92	2.267	20	175	261.30	1391	0.00		113.44
6.671	8.062	153.18	2.80	33.72	2.346	5	180	287.04	1456	1.22	7.82	121.26

Tab. 3: Monitoring Data of K11+196 Section

Calculation value of cumulative filling	Actual cumulative filling height	Actual cumulative load $\sum\triangle P$ (kPa)	Lateral displacement rate V_c (mm/d)	Cumulative lateral displacement rate $\sum Vc$	Cumulative lateral extrusion V_h (m^3)	Maximum settlement rate V(mm/d)	Cumulative settlement rate $\sum V$	Cumulative lateral displacement $\delta_{7.0}$	Cumulative settlement S(mm)	B	$\triangle u_{7.5}$ (kPa)	$\sum\triangle u_{7.5}$ (kPa)
1.933	1.962	37.28	0.66	0.66	0.004	8	8	4.03	72	0.34	3.55	3.55
2.253	2.325	44.18	1.21	1.87	0.045	6	14	8.42	96	1.34	9.21	12.76
2.801	2.897	55.04	4.38	6.25	0.146	9	23	21.97	174	0.79	8.56	21.32
3.110	3.284	62.40	2.51	8.76	0.201	12	35	33.67	253	0.97	7.15	28.47
3.620	3.873	73.59	3.23	11.99	0.348	11	46	51.06	333	0.61	6.87	35.34
4.049	4.382	83.26	3.03	15.02	0.491	10	56	83.19	455	0.73	7.02	42.36
4.382	4.837	91.90	0.94	15.96	0.723	8	64	104.48	577	0.00		42.36
4.714	5.291	100.53	1.15	17.11	0.891	7	71	125.01	657	0.34	2.90	45.26
5.015	5.672	107.77	1.54	18.65	1.023	6	77	178.30	806	1.01	7.28	52.54
5.248	6.054	115.03	0.82	19.47	1.494	1	78	183.12	823	0.00		52.54
5.522	6.345	120.56	1.07	20.54	1.531	2	80	193.52	831	0.27	1.47	54.01
5.937	6.768	128.59	1.07	21.61	1.659	3	83	208.36	855	0.34	2.71	56.72
6.139	6.994	132.89	1.72	23.33	1.762	5	88	213.34	870	0.92	3.95	60.67
6.297	7.167	136.17	2.85	26.18	1.805	10	98	220.84	889	0.00		60.67
6.389	7.278	138.28	2.40	28.58	1.851	5	103	230.49	903	1.80	3.79	64.46

6.543	7.446	141.47	2.17	30.75	1.971	4	107	252.76	960	0.80	2.55	67.01

ACKNOWLEDGEMENTS

The research is mainly supported by Henan Science and Technology Project (182102310003) in China. The authors thank all anonymous reviewers for reviewing the manuscript.

CONFLICTS OF INTEREST

The authors declare that they have no conflicts of interest.

REFERENCES

[1] XU Renping, WANG Shuliang, YE Yong (2006) Monitoring of Highway Soft Soil Road Bed Stability. Technology of Highway and Transport (4): 9-13.

[2] RAO Bo, WEI Limin (2005) A Stability Control Method for Fill Embankment on Soft Ground. Journal of Highway and Transportation Research and Development 22(2):46-49.

[3] LI Yuanming (2004) Stability Evaluation during Staged Construction of Embankment. Nanjing: Southeast University.

[4] TAVENAS F, MIEUSSENS C, BOURGES F (1979) Lateral Displacement in Clay Foundation under Embankments. Canadian Geotechnical Journal (16): 532-550.

[5] BRAND Edward, BRENNER R.P (1981) Soft Clay Engineering. Elserier scientific publishing company, Amsterdam.

[6] LADD C.C (1991) Stability Evaluation during Staged Construction: 22nd Terzaghi Lecture. Journal of Geotechnical Engineer, ASCE 117(4): 537-615.

[7] TAVENAS F, et al (1978) The Stability of Stage-constructed Embankments on Soft Clays. Can. Geotech (15): 285-305.

[8] ZHOU Jing (1999) Settlement Analysis of Embankment on Soft Clay. China Railway Science 20(2): 17-29.

[9] LIU Zengxian, TANG Liansheng. (2003) Analysis on Lateral Squeeze Settlement of Soft Clay Foundation under Embankment. Geotechnical Investigation and Surveying (2): 1-4.

[10] LI Fei, CHENG Penghuan, SHAN Haiyin, et al (2004) Testing Study on Lateral Deformation of Soft Road Ground and its Control.Chinese Journal of Rock Mechanics and Engineering 23(12):2114-2117.

[11] HUANG Teng, TAN Xiangshao, WU Yugang (2007) A Practical Stability Analysis Method for the Soft Soil Foundation on Pearl River Delta. Chinese Journal of Geotechnical Engineering 29(3): 391-397.

[12] WANG Yanling, CHEN Jianfeng (2002) Monitoring Methods of High Filled Road Bed in Soft Soil Areas. Journal of Engineering Geology 10(S1): 668-671.

[13] WANG Yanhui (2016) Stability Judgment of Soft Soil Subgrade in Mountainous Area based on AGO Method. Highway Traffic Technology (Applied Technology Edition) (7):104-106.

[14] HUANG Teng, WU Yugang (2005) A Method for Stability Analysis of Soft Subgrade Based on Measured Settlement Data. The Proceeding of National Symposium on Expressway Foundation Treatment 49-56.

[15] Fellenius W (1927) Earth Stability Calculations Assuming Friction and Cohesion on Circular Slip Surfaces. Ernst, Berlin.

[16] WANG Yongping, ZHANG Gongxin, ZENG Qingjun, et al (2005) Determination of Loading Plan Using Thin-Layer Rotary Adding Method. Port & Waterway Engineering (9): 62-64,100.

[17] Ministry of Housing and Urban-Rural Development of the People’s Republic of China (2012) Technical Code for Ground Treatment of Buildings (JGJ 79-2012), Beijing: China Building Industry Press.

[18] XIE Chuang (2015) Stability Control Method of Highway Soft Soil Foundation Treatment Construction. Theoretical Research in Urban Construction 5(3): 489-490.

Article no. 33

THE CIVIL ENGINEERING JOURNAL 3-2022

STRATA SUBSIDENCE CHARACTERISTICS OF SHIELD TUNNELING IN COASTAL SOFT SOIL AREA

Qingming Xiang [1], *Youqian Gao*[1], *Jiaxuan Su*[2], *Xiaoshuang Li*[3] *and Xuansheng Cheng*[3]

1. *Wenzhou Traffic Engineering Management Center, No. 2, East Road, Nanbaixiang Street, Ouhai District, Wenzhou, China; e-mail: 347363807@qq.com, gaoyouqian@qq.com*
2. *Wenzhou Traffic Engineering Test and Inspection Limited Company, No. 110, Haitong Road, Wenzhou Economic and Technological Development Zone, Wenzhou, China; e-mail: 164528647@qq.com*
3. *School of Civil Engineering, Lanzhou University of Technology, No. 287, Langongping Road, Lanzhou, China; e-mail: 2857309418@qq.com, chengxuansheng@gmail.com*

ABSTRACT

In order to study the strata subsidence characteristics caused by large diameter shield tunneling in soft soil area, based on the project of North Oujiang shield tunnel, the displacement field, seepage field and stress field of surrounding rock soil considering fluid-solid coupling effect during shield tunneling were analyzed using finite difference method. The results show that when the shield passes through the monitoring section, the surrounding rock soil in a certain range above the tunnel will be uplifted. Shield tail grouting can effectively control the settlement of the strata, and the increasing range of the strata subsidence gradually decrease. With the advance of the shield the pore water pressure increases, and the pore water pressure in the soil will rise sharply due to the shield tail grouting. When the shield passes through the monitoring section of the tunnel, the strata stress above the tunnel increases due to uplift extrusion, and the strata stress below the tunnel decreases due to stress release. When the shield tail grouting is completed and the shield machine gradually moves away from the monitoring section, the stress release leads to the decrease of the soil stress around the tunnel, and the strata stress distribution is funnel-shaped.

KEYWORDS

Coastal soft soil area, Shield tunnel, Numerical simulation, Displacement, Pore water pressure, Stress

INTRODUCTION

With the continuous development of shield technology, slurry balance shield technology is widely used in the construction of the submarine tunnel in soft clay strata. During the process of shield tunneling, the disturbance to the surrounding rock soil will inevitably occur. If the disturbance is too large, it will pose a threat to the safety of the surrounding buildings or adjacent structures, and it is not conducive to the stability of the tunnel structure in the later period. Therefore, it is of great engineering significance to study the displacement field, seepage field and stress field in the surrounding rock soil during the shield tunneling.

Researchers have studied the ground settlement during tunnel construction using different methods. Based on the measured data of the project, Peck [1] induced and analyzed the surface settlement during tunnel construction, and obtained that the shape of settlement trough in non-cohesive soil and cohesive soil strata presented error function or normal distribution curve shape. Due to its clear concept and simple calculation, this formula has been widely applied in practical engineering and has been continuously improved by some scholars [2-8]. For example,

DOI 10.14311/CEJ.2022.03.0033

Zhu [9] considered the fill rate of grouting, shield eccentricity and support pressure ratio during shield tunneling, the modified Peck formula was established based on the modified gap parameters. Sagaseta [10] assumed that the soil was homogeneous, isotropic and linearly elastic incompressible material in a semi-infinite space. Combined with the Mindlin solution and the virtual mirroring technology, the analytical solution of formation displacement caused by formation loss was obtained. Based on Mindlin solution and Loganathan formula, Lu et al. [11] solved the additional load on the tunnel face, the friction force on the side wall and the loss of the soil at the tail of the shield by numerical integration, respectively, and obtained the elastic displacement field of the soil.Based on the Mindlin solution, Liang et al. [12] considered the influence of the support force on the shield tunnel face, the lateral friction between shield shell and soil, the shield tail grouting pressure and other factors on the ground settlement. The vertical and horizontal displacement prediction formulas of the ground during shield tunneling were obtained. Liu and Zhang [13] applied the stochastic medium theory to the prediction of ground subsidence caused by tunnel construction, and obtained two-dimensional and three-dimensional analytical formulations for settlement prediction. Later some researchers analyzed the ground settlement of shield tunnel under different soil layers and construction conditions, and further developed the theory [14-16]. Rowe and Kack [17] employed the finite element method to simulate the ground settlement during shield construction, and analyzed the influence of segment weight, soil parameters, formation loss, and shield tail grouting on the ground settlement. Jallow et al. [18] combined with the shield tunnel of Taipei MRT system, the influence of consolidation on long-term settlement was evaluated by using PLAXIS 3D software and small strain soft soil and hardened soil models. Taking the overlapping section of the left and right lines of the Ludao Lake-Liantang segment of Foshan Metro Line 2 as the main research object, Wu and Liu [19] effectively predict the ground settlement of the overlap section caused by construction using the numerical method and the field measured data, and the results showed that reasonable reinforcement measures could be taken to effectively control the ground settlement before the construction of the overlapping section. Jin et al. [20] analyzed the influence of new shield tunnel construction on the deformation characteristics of existing tunnel and ground through a large number of monitoring data of undercrossing construction examples in Shenzhen metro area. An empirical formula of the settlement of existing tunnels caused by new shield tunnel excavation was proposed. Combing with practical engineering, Chen et al. [21] used empirical formula (assuming that the settlement curve above the tunnel is a Gaussian distribution curve) and finite element analysis to conduct reverse analysis to the ground settlement of the tunnel. Based on the shield tunnel project of Guangzhou Metro Line 8, Lv et al. [22] investigated the settlement of shield construction in upper-soft and lower-hard strata by using the numerical simulation and the monitoring data of the project. They concluded that with the decrease of the height ratio of soft and hard rocks (soft rock height/hard rock height), the ground settlement decreased and the settlement trough became shallower. Groundwater seepage is also an important factor affecting ground settlement during shield construction. Zhang and Huang [23] summarized stratum response caused by excavation disturbance, synchronous grouting, seepage and creep behavior of soft soil during shield tunneling. Wei and Zhu [24] assumed that the groundwater inside and outside the tunnel was one-dimensional steady seepage, and the seepage drainage model was established. Combined with practical engineering, the influence of seepage on the effective stress of stratum around the tunnel was analyzed and the ground subsidence caused by seepage was calculated. For water-rich loess tunnel, Wei and Zhu [25] introduced the method of sealing groundwater seepage and controlling surrounding rock masses deformation by base grouting and curtain grouting technology. He and Wei [26] established a three-dimensional finite element model of reinforced soil during shield launching, and analyzed the influence of seepage on surface settlement during shield launching.

Scholars have made many rich achievements in the research on the strata subsidence characteristics during tunnel excavation. However, most studies do not consider the influence of the seepage effect of pore water on the strata subsidence, and there are few studies considering the fluid-solid coupling effect in surrounding rock soil on the strata settlement. In addition, for the crossing-river tunnels, it is necessary to systematically investigate the displacement field, seepage field and stress field in surrounding rock soil during shield tunneling. Therefore, based on the North Oujiang tunnel of S2 railway line in Wenzhou city, the displacement field, seepage field and stress field of surrounding rock soil considering the fluid-solid coupling effect during shield tunnel construction were analyzed by using finite difference method. This paper will provide theoretical guidance for the construction and design of similar underwater tunnel engineering.

NUMERICAL EXAMPLES

Numerical model and boundary conditions

The shield construction process at the typical section in the middle section of the river is simulated. The excavation diameter of shield machine is 14.9m, the outer diameter D of the tunnel is 14.5m, and the inner diameter d is 13.3m. The tunnel is buried 20m below the riverbed, and the water depth above the riverbed is 12m. A three-dimensional numerical model of tunnel construction is established by using the finite difference software FLAC3D. Due to the symmetry of the structure, half of the structure model is selected for calculation and analysis. In order to eliminate the influence of boundary effect, the distance between the left and right boundary, and the lower boundary of the model and the tunnel axis is 3~5 times tunnel diameter. Figure 1 shows the numerical model of shield construction and its dimensions.

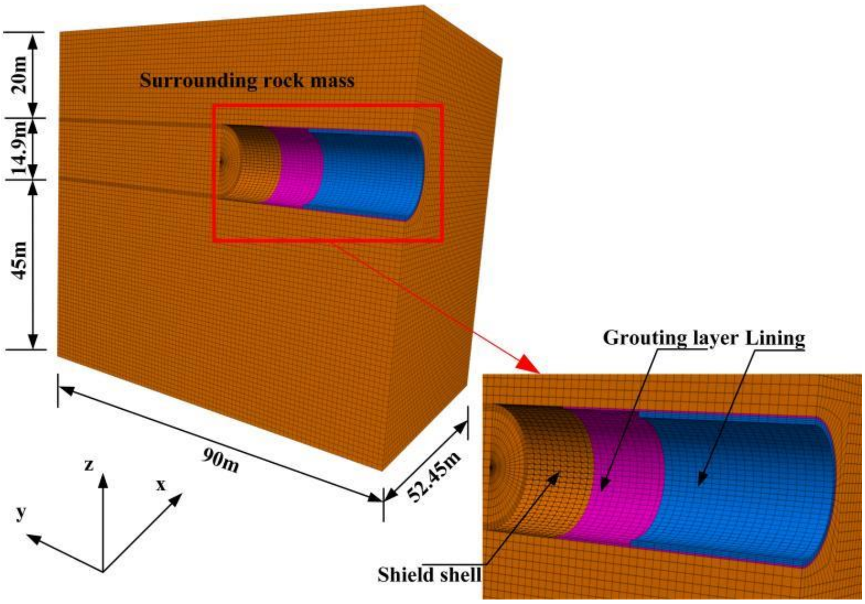

Fig. 1 – Numerical model of shield construction

The elastic constitutive models are used for the lining, grouting layer and shield of the tunnel, and the Mohr-Coulomb model is used for the surrounding rock soil. The 8-node solid element is used for the lining, grouting layer and surrounding rock soil, and shell element is used to simulate shield shell of the shield machine. Physical parameters of surrounding rock soil are shown in Table 1. The material parameters and elements of the shield shell, shield tail grouting body and lining are shown in Table 2. Considering the influence of staggered assembled segments and bolt connection on the stiffness of lining structure, the reduction coefficient of bending stiffness is selected as 0.8. The boundary conditions are that the top of the model is free, the horizontal displacement of the left and right sides and the two sides perpendicular to the axis of the tunnel are constrained, while the vertical displacement of the bottom is constrained. The sides and the bottom are set as impervious boundaries. Pore water pressure and vertical stress are applied on the upper surface of the model depending on the water level. The boundary condition diagram of the model is shown in Figure 2.

Tab. 1: Physical parameters of surrounding rock soil

Soil	Natural gravity γ/(kN/m^{3})	Thickness of soil /m	Internal friction angle φ/(°)	Cohesive force c /kPa	Poisson's ratio v	Modulus of elasticity E/MPa	Porosity n	Permeability coefficient k_s/(m/s)
②^{1}Mud	16.4	14	3	6	0.4	10	0.63	7×10^{-7}
②^{2}Mud	16.7	12	3	6	0.4	10	0.6	5×10^{-7}
③^1 Silt clay	17.2	12	4	8	0.35	15	0.58	1×10^{-7}
④^{2}Clay	18.2	7	7	12	0.3	20	0.5	6×10^{-8}
⑥^{3}Tuff	25	>50	-	-	0.25	1500	0.3	2×10^{-8}

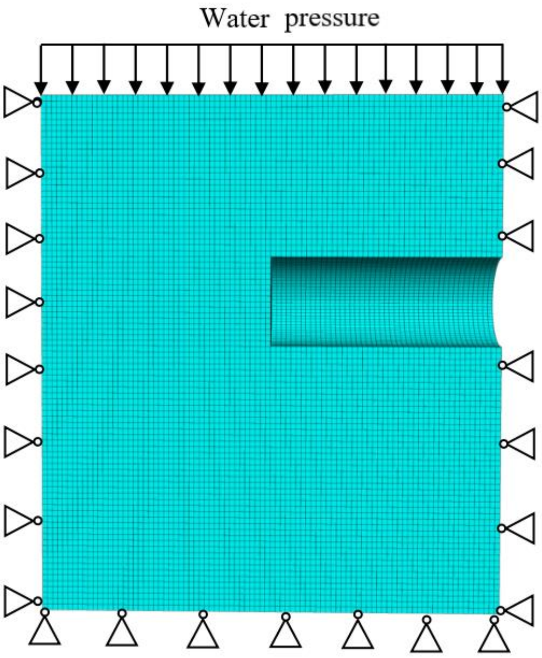

Fig. 2 – Boundary condition diagram of the model

Tab. 2: Material parameters

Material	Gravity γ/(kN/m^3)	Thickness /mm	Poisson's ratio v	Modulus of elasticity E/MPa	Unit
Lining（C50）	25	600	0.2	2.67×10^4	8-node element
Shield shell	78.5	60	0.3	2.1×10^5	Shell element
Grouting material (Beginning)	21	200	0.46	0.4	8-node element
Grouting material (Condensation)			0.2	4	

Shield construction load parameter and construction simulation

The calculation results show that the support pressure at the center of the excavation face is 545.456kPa, and the change gradient of the support pressure on the excavation face is 15.537kPa/m. The grouting pressure is taken 1.1 times the original lateral water and soil pressure, and the grouting pressure at the central axis of the tunnel is 532.434kPa, with a gradient of 16.998kPa/m. The slurry balance shield machine is selected, the total weight is 2126t. The weight of the whole shield machine is evenly distributed on the whole shield shell, and the uniform weight is 71.342kPa.

The 30 rings excavation process of shield tunnel is simulated, and the length of each ring is 2m. The coupling calculation between fluid and solid is adopted to carry out mechanical calculation and seepage calculation at the same time, and the actual shield construction process is simulated and analyzed. Firstly, the in-situ stress balance is carried out for the model without considering the seepage in the surrounding rock soil. After tunneling and excavating, seepage calculation and mechanical calculation are carried out simultaneously, and the fluid modulus is set as 2×10^6 kPa. The empty model is used to excavate each ring of the tunnel. The support pressure is applied on the tunnel face, and the shell element is used to generate shield shell on the excavation ring. The excavation is carried out step by step. When tunneling to the 6th ring, the shield shell element of the first ring is deleted to generate the lining and the grouting layer of the first ring. Grouting pressure is applied on the soil and lining of the first ring, respectively. In this way, the excavation is carried out step by step, the grouting pressure is set behind the ring for the fluid-soild coupling calculation until the excavation of the 30th ring is completed.

CALCULATION RESULTS AND ANALYSIS OF RESULTS

The construction process of underwater shield tunnel is numerically simulated. According to the five stages of shield tunnel construction, the displacement field, seepage field and stress field of the surrounding rock soil are analyzed. In order to eliminate the influence of the boundary on calculation results of the surrounding rock soil, the 15th ring (Y=30m plane) is taken as the monitoring section.

Displacement field

Taken the 15th ring (Y=30m plane) as the monitoring cross section, the stratum settlement of monitoring section are analyzed when the 14th ring (Shield is close to the monitoring section), the 16th ring (Shield passes through the monitoring section.), the 18th ring (Shield passes through the monitoring section.), the 21st ring (The stage of shield tail grouting.), the 23rd ring (Hardening stage 1.), the 30th ring (Hardening stage 2.) are excavated, respectively. The formation depths of Z=0m, 10m and 18m are selected to analyze the laws of strata subsidence during shield tunneling, and the calculation results are shown in Figure 3.

DOI 10.14311/CEJ.2022.03.0033

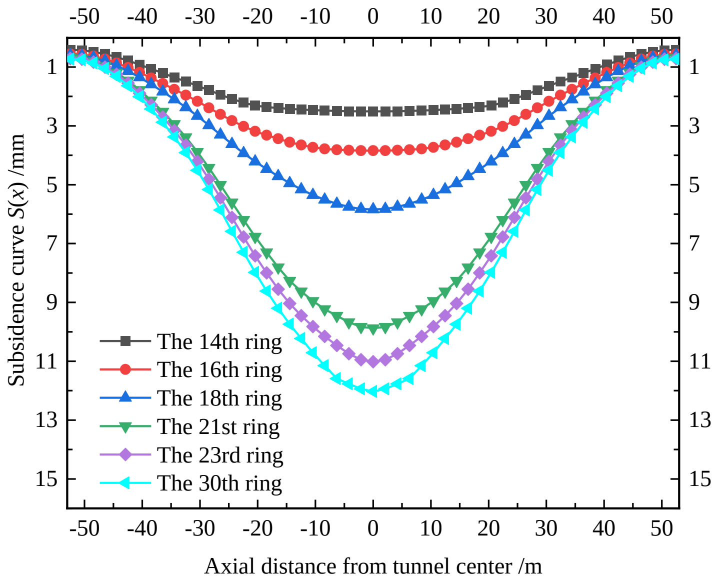

(a) Formation depth z=0m

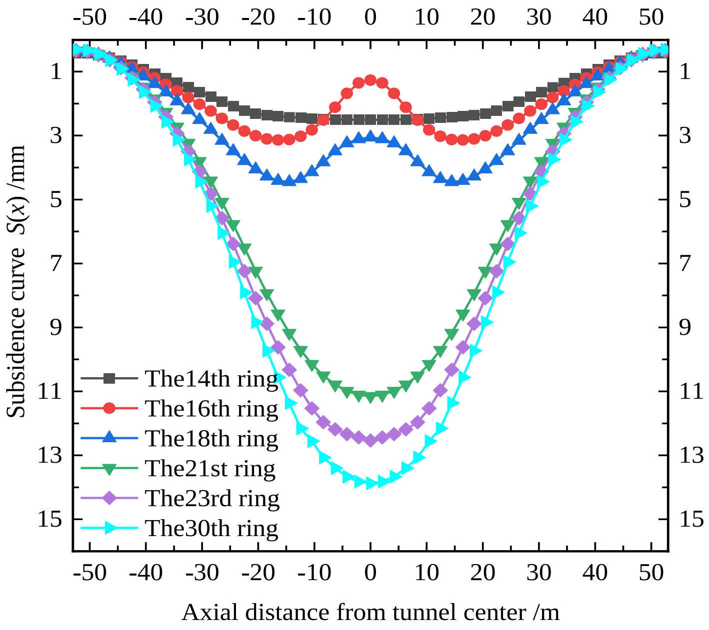

(b) Formation depth z=10m

Fig. 3 – Subsidence curve during excavation

DOI 10.14311/CEJ.2022.03.0033

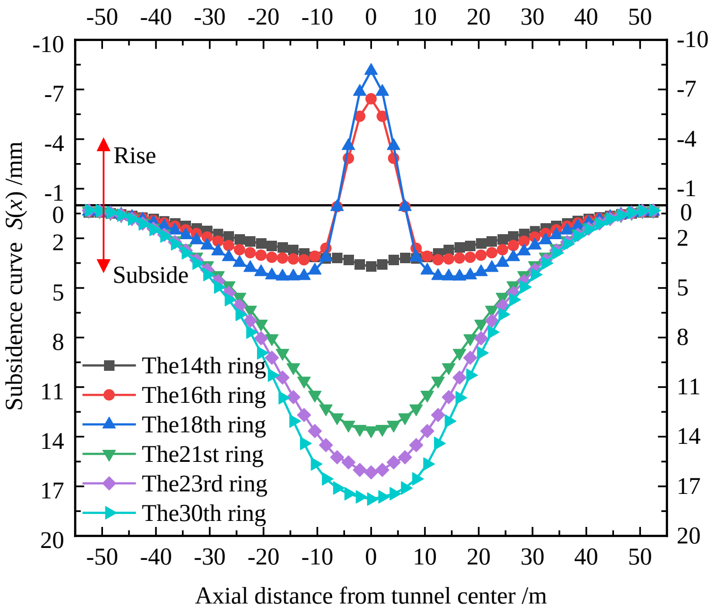

(c) Formation depth Z=18m

Fig. 3 – Subsidence curve during excavation

The Figure 3(a) shows that with shield advancing step by step, the stratum settlement (z=0 m plane) is slowly growing, the settlement curve is basically the same in each shield stage, which all fit to Gaussian normal distribution of Peck curve, and the largest settlement occurs in the center of the tunnel axis. And after the completion of the 14th ring, 16th ring, 18th ring, 21st ring, 23rd ring and 30th ring shield tunneling, the maximum settlements on the plane z=0m are 2.6 mm, 3.8 mm, 5.8 mm, 9.9 mm, 11.0 mm and 12.3 mm, respectively, which indicates that the settlement at the riverbed surface mainly occurs between 14th ring and 21st ring (the period of shield machine crossing and shield tail leaving the monitoring section) during shield construction, and the settlement at the riverbed surface is small during grouting completion and slurry consolidation, which shows the grouting pressure is appropriate, and strata subsidence can be controlled. Combined with Figure 3 (b) and (c), it can be seen that after the completion of the 16th and 18th rings of shield tunneling, the settlement curve in the ground does not conform to the Gaussian normal distribution, and the curve shows the shape of gradually decreasing around and bulging in the middle, which is related to the upward floating of the machinery caused by the stress redistribution in the construction process of the shield tunneling, so it is necessary to carry out counterweight on the shield machine in the process of shield construction to anti-floating. After the completion of shield tunneling in the 21st, 23rd and 30th rings, the settlement curve at any depth of the stratum still conforms to the Gaussian normal distribution because the formation stress has been released due to the existence of the grouting layer. The existence of buffer layer reduces the pressure difference between the top and bottom of the tunnel, so that the floating effect will no longer occur. As can be seen from the figure, in the whole process of shield construction, with the shield gradually approaching the monitoring section, the ground will be disturbed and vertical settlement will occur. With the shield tunneling passing through the tunnel section, A certain range of the surrounding rock soil above the tunnel will be uplifted, but the settlement of the riverbed will continue to increase. With the shield tail grouting gradually away from the tunnel section, the shield tail grouting can effectively control the subsidence of the ground. The subsidence of the ground is still gradually increasing, but after the condensation and hardening of the grouting layer, the subsidence of the ground will gradually tend to be stable.

Pore water pressure

The positions above the central axis of the tunnel, which are 2 m, 6 m, 10 m, 14 m, 16 m, 18 m and 20 m from the riverbed surface, are selected to study the change of pore water pressure in surrounding rock soil caused by the whole excavation process, as shown in Figure 4.

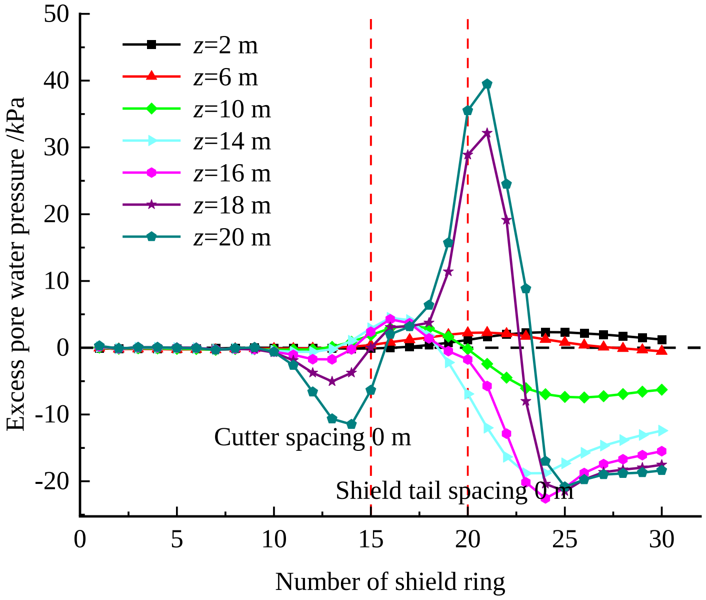

Fig. 4 – Change curve of pore water pressure during excavation

As can be seen from Figure 4, during the shield tunneling, as the cutter head gradually approaches the tunnel excavation face of the monitoring section, the pore water pressure in the formation will gradually decrease due to shield disturbance. When the shield passes through the tunnel face, the excess pore water pressure will be formed in the soil due to the disturbance, and the pore water pressure will increase with the shield advancing. When the grouting at the shield tail is completed, the pore water pressure in the soil within 4m of the upper strata above the tunnel will rise sharply, and the maximum excess pore water pressure is 39.5kPa. As the shield tail gradually moves away, the pore pressure in the upper strata above the tunnel gradually decreases, then increases and finally tends to be stable. The final pore water pressure is less than the original hydrostatic pressure. By contrast, the pore water pressure at the top of the tunnel eventually decreases by 18.4kPa. It can be seen from the figure that the influence range of pore water pressure is roughly within the range of 10m above.

Stress field

Distribution of transverse stress field

Figure 5 shows the vertical stress in the transverse direction at the position of the monitoring section (Y=30m plane) during shield construction

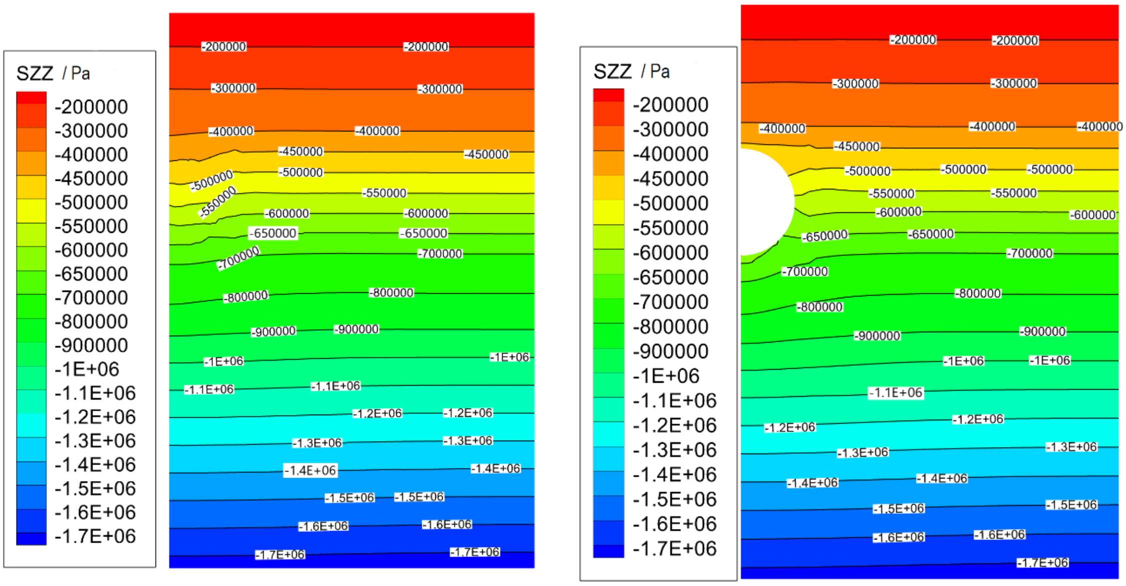

（a） The 14th ring *（b） The 18th ring*

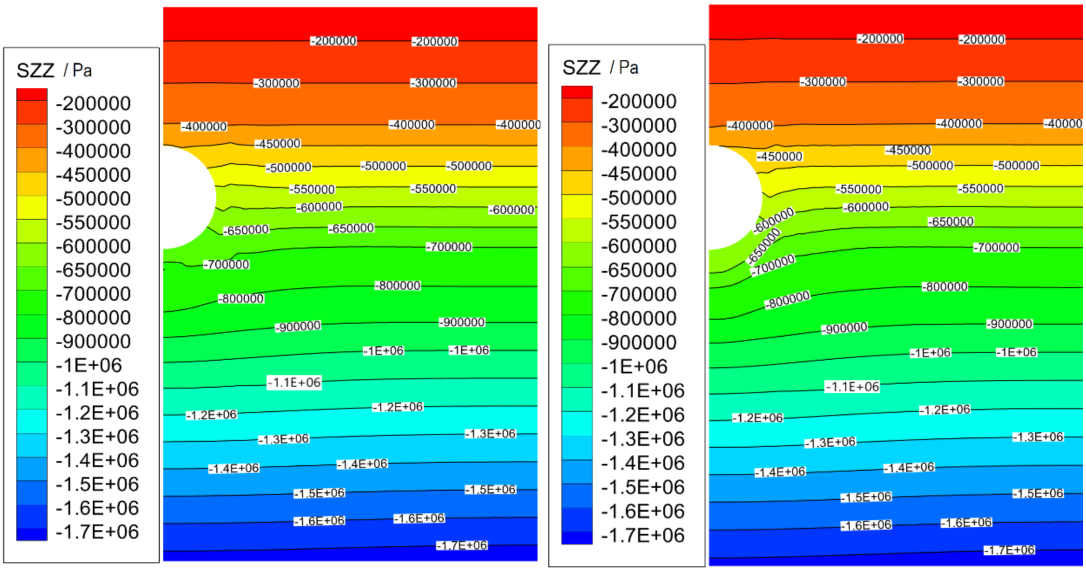

（c） The 21st ring *（d） The 30th ring*

Fig. 5 – Transverse stress distribution during shield construction

According to Figure 5 (a), when the shield approaches the tunnel face (the 14th ring), the vertical stress of the stratum decreases slightly compared with the initial stress, and the shield has begun to affect the soil stress in front of the tunnel face. As can be seen from Figure 5 (b), when the shield passes through the tunnel face, the vertical stress of the upper soil layer increases due to the extrusion of the floating effect and presents an upward protrusion, while the bottom decreases due to the release of the stress. It can be seen from Figure 5 (c),and Figure 5(d) that when the shield tail moves away, there is a stratum loss. The existence of the gap leads decreases of the stress due to the release of the strata stress around the tunnel, and the disturbance also gradually decreases from the tunnel position to both sides, and the surrounding vertical stress presents funnel shape. In addition, it is seen from Figure 5 (d) that after the grouting body solidifying and hardening, the vertical stress of the formation is basically the same and tends to be stable.

Distribution of axial stress field

Figure 6 shows the vertical stress on the longitudinal section where the tunnel axis is located during shield construction, and the vertical stress of the stratum in the shield construction process is analyzed.

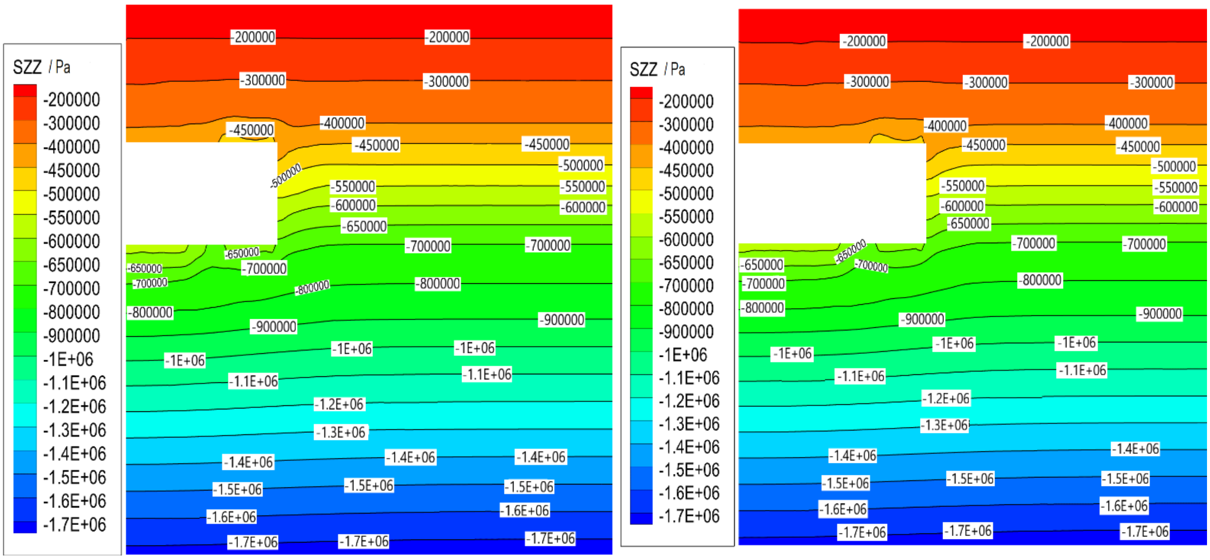

(a) The 14th ring *(b) The 18th ring*

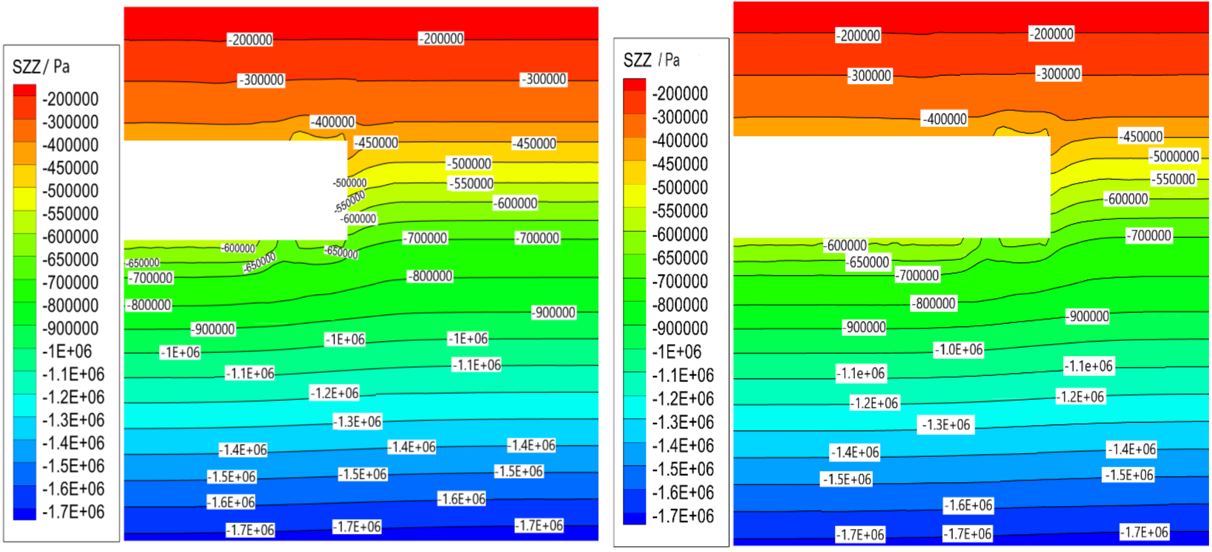

(d) The 21st ring *(d) The 30th ring*

Figure 6 – Axial stress distribution during shield construction

The Figure 6 (a) shows as the tunneling approaches the tunnel face, the degree of disturbance increases, and the stress release of the formation in front of the tunnel face increases, and the formation stress distribution presents a funnel shape. In Figure 6 (b), the stress in the range around 8m in front of the shield face decreases due to the stress release, and the undisturbed area is still in the initial stress state. The formation stress at the shield tail gradually tends to be stable with the gradual advancing of the shield. When the shield passes through the strata, the stress of the upper soil above the tunnel increases due to the floating effect, and the stress of the bottom soil under the tunnel decreases due to the stress release. The distribution of vertical stress in Figure 6 (d) is almost the same as that in Figure 6 (c), and the formation stress tends to be stable as the shield tail gradually moves away.

CONCLUSIONS

(1) During the shield tunneling, as the shield gradually approaching to the monitoring section, the strata will be disturbed and vertical subsidence will occur. When the shield tunneling passes through the monitoring section, the surrounding rock soil in a certain range above tunnel uplifts, but the settlement of the strata under the riverbed will continue to increase. Shield tail grouting can effectively control the subsidence of the strata, the increasing range of the strata subsidence gradually decreases, and the strata subsidence tends to a stable state with the consolidating and hardening of the grouting layer.

(2) As the shield approaching to the tunnel monitoring section, the pore water pressure of the formation decreases gradually due to the shield disturbance. When tunnel shield passes through the monitoring section, excess pore water pressure will be formed in the stratum. With the shield advancing, pore water pressure will increase. The pore water pressure of the soil will rise sharply when the shield tail grouting. With the shield moving away from the monitoring section, the pore pressure in the stratum above the tunnel gradually decreases, then increases and finally tends to be stable.

(3) With the shield advancing the monitoring section, the vertical stress of the stratum around the tunnel decreases due to disturbance. When the shield passes through the monitoring section, the stress in the strata above the tunnel increases due to uplift extrusion, and the soil stress under the tunnel arch bottom decreases due to stress releasing. When the shield is away from the monitoring section, the formation loss occurs around the tunnel, and the stress decreases in the surrounding stratum due to the stress release and shows a funnel-shaped distribution.

ACKNOWLEDGEMENTS

This paper is supported in part by the National Natural Science Foundation of China (Grant number: 51968045), and the Science and Technology Planning Project of Zhejiang Traffic Quality Supervision Industry (Grant number: ZJ201906).

REFERENCES

[1] Peck R. B., 1969. Deep excavations and tunneling in soft ground. In the 7th ICSMFE. Mexico, 311-375.

[2] Mair R. J., Taylor R. N., Bracegirdle A., 1993. Subsurface settlement profiles above tunnels in clays. Géotechnique , Vol. 43: 315-320. https://doi.org/10.1680/geot.1993.43.2.315

[3] Celestino T. B., Gomes R. A. M. P., Bortolucci A. A., 2000. Errors in ground distortions due to settlement trough adjustment. Tunnelling and Underground Space Technology, Vol. 15:97-100. https://doi.org/10.1016/S0886-7798(99)00054-1

[4] Jiang X. L., Zhao Z. M., Li Y., 2004. Analysis and calculation of surface and subsurface settlement trough profiles due to tunneling. Rock and soil mechanics, Vol. 5: 1542-1544. https://doi.org/10.1007/BF02911033

[5] Qu J. L., Ge X. R., 2005. Analysis of characteristics of settlement trough induced by shield construction in soft soil area. Industrial Construction, Vol. 35: 42-46.

[6] Shen Y. S., He Y. H., Zhao L., et al., 2017. Improvement of Peck formula of surface construction settlement of rectangular tunnel in soft soil area. Journal of Railway Science and Engineering, Vol. 14: 1270-1277.

[7] Cai Y., Zhang C. P., Min B., et al., 2019. Deformation characteristics of ground with voids induced by shallow metro tunnelling. Chinese Journal of Geotechnical Engineering, Vol. 41: 534-543.

[8] Lu D. C., Lin Q. T., Tian Y., et al., 2020. Formula for predicting ground settlement induced by tunnelling based on Gaussian function. Tunnelling and Underground Space Technology, Vol. 103: 1-22. https://doi.org/10.1016/j.tust.2020.103443

[9] Zhu C.H., 2017. Control of surface settlement by considering shield tunneling technology. KSCE Journal of Civil Engineering, Vol.21:2896-2907. https://doi.org/10.1007/s12205-017-0761-0

[10] Sagaseta C.,1987. Analysis of undrained soil deformation due to ground loss. Géotechnique, Vol. 37: 301-320. https://doi.org/10.1680/geot.1987.37.3.301

[11] Lu D.Y.,Wang S. M.,He C., et al., 2016. Research on effects of adjacent construction of new shield tunnel on longitudinal deformation of existent tunnel. Journal of the China Railway Society, Vol.38:108-116. https:// doi.org/10.3969/j.issn.1001-8360.2016.10.015

[12] Liang R. Z., Xia T. D., Lin C. G., et al., 2015. Analysis of ground surface displacement and horizontal movement of deep soils induced by shield advancing. Chinese Journal of Rock Mechanics and Engineering, Vol. 34: 583-593. https://doi.org/10.13722/j.cnki.jrme.2015.03.016

[13] Liu B. C., Zhang J. S., 1995. Random medium method for surface subsidence caused by near surface excavation. Chinese Journal of Rock Mechanics and Engineering, Vol. 14: 289-296.

[14] Zhu Z. L., Zhang Q. H., Yi C. H., 2001. Stochastic theory for predicting longitudinal settlement in soft-soil tunnel. Rock and soil mechanics, Vol. 22:56-59.

[15] Shi C. H., Peng L. M., 2004. Application of stochastic medium theory to predicting settlement in longitudinal surface due to tunnel construction by shield. Rock and soil mechanics, Vol. 25: 320-323. https://doi.org/10.1007/BF02911033

[16] Fang T., Xu X. C., 2015. Improved calculation of parallel twin tunnel settlement based on stochastic medium theory. Urban Mass Transit, Vol. 18:19-23.

[17] Rowe R. K., Kack G. J., 1983. Theoretical examination of the settlements induced by tunnelling: four case histories. Canadian Geotechnical Journal, Vol. 20: 299-314. https://doi.org/10.1016/0148-9062(83)90716-7

[18] Jallow A., Ou C. Y., Lim A., 2019. Three-dimensional numerical study of long-term settlement induced in shield tunneling. Tunnelling and Underground Space Technology, Vol.88:221-236. https://doi.org/10.1016/j.tust.2019.02.021

[19] Wu X. T., Liu Z. W., 2019. Numerical simulation of ground settlement caused by over-lapping tunnel shield construction and measures of stratum reinforcement. Journal of Physics: Conference Series, Vol.1176:1-8. https://doi.org/10.1088/1742-6596/1176/5/052070

[20] Jin D. L., Yuan D J., Li X. G., et al., 2018. Analysis of the settlement of an existing tunnel induced by shield tunneling underneath. Tunnelling and Underground Space Technology, Vol.81:209-220. https://doi.org/10.1016/j.tust.2018.06.035

[21] Chen S. L., Gui M. W., Yang M. C., 2012. Applicability of the principle of superposition in estimating ground surface settlement of twin- and quadruple-tube tunnels. Tunnelling and Underground Space Technology, Vol. 28:135-149. https://doi.org/10.1016/j.tust.2011.10.005

[22] Lv J. B., Li X. L., Fu H. L., et al., 2020. Influence of shield tunnel construction on ground surface settlement under the condition of upper-soft and lower-hard composite strata. Journal of Vibroengineering, Vol. 22: 1126-1144. https://doi.org/10.21595/jve.2020.20967

[23] Zhang D. M., Huang X.,2018. Proceedings of GeoShanghai 2018 International Conference: Tunnelling and Underground Construction. Springer Nature Singapore Pte Ltd, Singapore.

[24] Wei Z. D., Zhu Y. P., 2021. A theoretical calculation method of ground settlement based on a groundwater seepage and drainage model in tunnel engineering. Sustainability, Vol.2021:1-12. https:// doi.org/10.3390/su13052733

[25] Wei Z. D., Zhu Y. P., 2021. Seepage in water-rich loess tunnel excavating process and grouting control effect. Geofluids, Vol. 2021:1-13. https://doi.org/10.1155/2021/5597845

[26] He J. F.,Wei G., 2021. The influence of seepage during the shield launching process on ground settlement ahead of the shield face. Low Temperature Architecture Technology, Vol. 2021:125-129. https://doi.org/10.13905/j. cnki. dwjz. 2021.11.027

Article no. 34

THE CIVIL ENGINEERING JOURNAL 3-2022

ANALYSIS OF CONTACT FRICTION BEHAVIOR IN THE BENDING PROCESS OF SEMI-PARALLEL STEEL WIRE CABLE

Jianxi Yang, Hongyu Fei ,Quansheng Sun and Xiang Wei Hao

Northeast Forestry University, Department of Civil Engineering, Harbin, 150040, China;
hxw_75@126.com

ABSTRACT

In the bending process of semi-parallel steel wire cable, with the increase of the lateral displacement of the bending, the interaction between the steel wires in the cable is remarkable and the mechanical behavior is complicated. In order to study the mechanical behavior of the contact friction between the inner steel wires in the process of cable bending, this paper uses the 37-φ7 semi-parallel steel wire as the research object and uses the ANSYS to set up the finite element model of the cable bending, and verifies the correctness of the refined finite element model by bending test data. Based on the refined finite element model of the test data verification, the variation rule of the contact friction between the inner steel wires in the semi-parallel steel wire of different boundary conditions in the bending process is studied, and the axial sliding behavior of the steel wires in the cable bending process is analyzed. The results show that the bending and mechanical properties of the semi-parallel steel wire cable can be calculated more accurately by considering the refined finite element model of the contact friction, and the amount of deformation between the steel wires during the bending process of the semi-parallel steel wire cable can be calculated. The contact pressure and the contact friction stress are non-linear with the increase of the lateral displacement of the bending, and there is a maximum value for the contact friction stress for the pre-tension semi-parallel wire cable, and the maximum position of the axial accumulated slip amount between the steel wires is located at the bending cable section of the calculated span of 1/4 or 3/4 times.

KEYWORDS

Semi-parallel steel wire cable, Refined finite element analysis (RFEA) model, Extrusion deformation, Contact pressure, Contact friction stress, Axial cumulative slip

INTRODUCTION

During the operation of cable-supported bridges, different degrees of local bending problems can be found for the cables of cable-stayed bridges, arch bridges and the suspension cables of suspension bridges [1]. Semi-parallel steel wire cable, as a common cable structure for cable-supported bridges, is the key force-transmitting and force-bearing component of this type of bridge. When it is locally bent, the contact friction mechanical behaviour between internal steel wires is complex. Finite element numerical simulation is commonly used in research on the interaction between the inner wires of a cable. Jiang [2] established a refined three-dimensional solid model of a simple seven-wire steel strand under pure bending. For the overall mechanical behaviour of the strand, the moment–curvature curve is consistent with the theoretical model in literature. The finite element model can accurately predict the continuous nonlinear plastic behaviour of the strand. Zhang [3] established a solid finite element model with two boundary conditions to study the bending stiffness of steel strands by taking the internal friction between steel wires into consideration. The results showed that ignoring the contact between the wires will reduce the bending stiffness of the strand leads due to the rotation of the cross section of the wires; the bending stiffness increased with increasing tension and decreasing curvature. Wu [4] and Chen [5] conducted a static bending test

DOI 10.14311/CEJ.2022.03.0034

on semi-parallel steel wire cable under three boundary conditions. The unstressed cable was similar to an elastic-plastic steel beam. The load–displacement curve under bending was of elastic–plasticity. The welded end cable ensured the integrity of the cable, but the reinforcement effect was weak and limited. The pretension can improve the bending stiffness of the cable, which increased with increasing pretension level but decreased with increasing cable size. A simplified evaluation method for effective bending stiffness was proposed. Yu [6] simplified the extrusion and frictional slip between steel wires as spring action in three directions and established a semi-refined finite element model of beam–beam spring combination to evaluate the bending mechanical properties of wire cables. The model calculation was consistent with the bending test data but had huge errors. The semi-refined model was not accurate enough for the bending calculation and simulation of semi-parallel wire cables. Zeng [7] established a balanced equation and obtained variations in the wire slip with the section angle based on the layered slip model of cable strands and wires; the equation considered the influence of slip on the inertia moment of the section and used equal shear force between the wires and the ultimate friction force. However, the effect of friction between adjacent layers of steel wires on axial force was ignored in the theoretical model. Liang [8] established a simplified numerical model of the cable considering the friction between wires. Through the analytical solution of Costello theory and the verification of experimental data, scholars analysed the bending mechanical properties of the cable and determined the influence of broken wire on the dynamic response of the cable. The model can track the slip between the wires and be applied to dynamic analysis. Zhang [9-10] established a theoretical mechanical model for the bending of parallel steel wire cables considering the contact friction between layers through laminated beam theory and studied the change law of the bending stiffness of the steel wire cables. Data from the theoretical model were consistent with the experimental results obtained through experimental verification. Lalonde S [11] proposed a method for simulating multi-layer helical steel wire cables based on 3D finite element beam–beam contact model. In this model, a multi-level friction coefficient model that can better represent the bond and slip regions was proposed, and the concept of friction orthogonality was introduced. The axial direction was controlled by the inter-wire adhesion, while the orthogonal direction was related to the inter-wire adhesion and deformation contribution. The above research mainly focused on the bending mechanical properties and bending stiffness of the cable. The changing laws of extrusion deformation, contact pressure and contact friction stress between steel wires during the bending of semi-parallel steel wire cables remain unclear. In this paper, the changing law of extrusion deformation, contact pressure and contact friction stress between steel wires inside the cable structure during the bending of semi-parallel steel wire cables was studied under the action of vertical load at mid-span based on the refined finite element model of semi-parallel steel wire cable verified by experimental data. The axial slip behaviour between the wires during the bending process was also analysed.

REFINED FINITE ELEMENT ANALYSIS (RFEA)METHODS

Establishment and experimental verification of the finite element model of semi-parallel wire cable bending

Basic assumptions

Before establishing the refined finite element model of the semi-parallel wire cable, the following basic assumptions are made:

(1) The contact friction between the wrapping tape and the steel wire, the sheath and the wrapping tape is not taken into consideration; the gripping force of the sheath on the inner steel wire is simplified as a radially uniform load applied to the outermost steel wire of the wire cable.

(2) During the bending deformation process of the steel wire cable, each steel wire is allowed to be moved with each other; the contact part between the steel wires is simulated by the surface-to-surface contact element; the same friction coefficient is applied for all the steel wires of the same cable.

(3) The plastic development of the steel wire is not taken into consideration in the bending model; all the steel wires are assumed to be made of the same material, and the inner steel wire is always in the elastic stage during the bending process of the wire cable.

Establishment of refined finite element model

Based on the bending test of the semi-parallel steel wire cable in literature [4] (Figure 1), the three-dimensional finite element full contact model of the semi-parallel steel wire cable is established by finite element software ANSYS considering the three boundary conditions of the cable:①Free at both ends: The steel wire at both ends of the cable is allowed for sliding(Figure 1(a));②Weld at both ends: the cable end wire does not allow sliding and maintain a flat section(Figure 1(b));③Applying different pretensions at both ends(The pretension force was 50kN and 100kN):the cable is anchored at one end and prestressed after welding the articulated joints at the other end(Figure 1(c)).

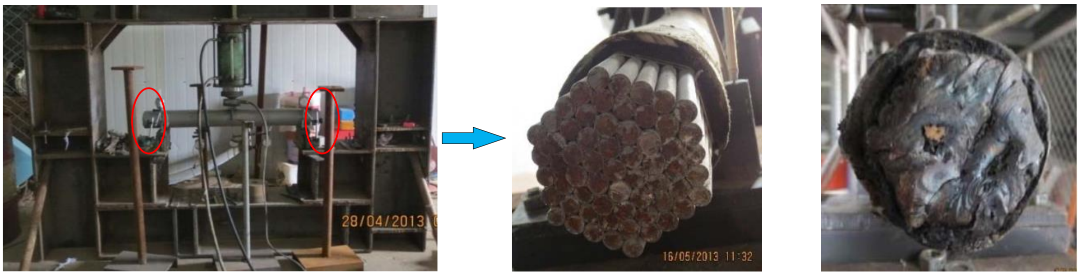

Cable bending test（Free end or weld end） *（a）Free end* *（b）weld end*

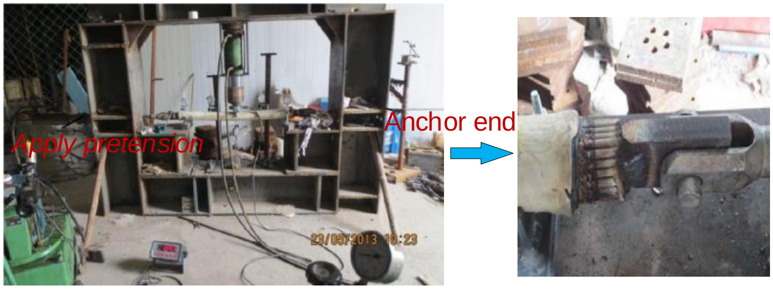

Cable bending test（Apply pretension） *（c）Pretension cable end*

Fig. 1 –Bending test of semi-parallel steel wire cable [4]

Semi-parallel wire cable is formed by parallel steel wire concentric same direction for left mild twist, twist angle between 2°to 4°, the cable section is positive hexagonal or missing hexagonal closely arranged, and then tied with fiber polyester wrap belt, and finally in the outer layer directly crowded wrapped single layer or double layer high density polyethylene sheath (HDPE Sheath) cover as a protective layer. According to the structural characteristics of the semi-parallel wire cable, twist angle is 3°, the order from bottom to top (generating points, lines, surfaces and bodies in turn) is adopted. The wire surface is divided into meshes, and the surface is rotated at a certain angle to stretch into a cube to establish a geometric model of the cable. The steel wire adopts the SOLID186 element. The target element of the contact surface between the steel wires adopts the TARGE170 element. The contact element adopts the CONTA174 element.

The physical parameters of the main components of the steel wire cable in the finite element model are as follows:

① HDPE Sheath: the elastic modulus of the material is 150 MPa, and the density is 0.942 kilograms per cubic meter. The gripping force q of the sheath to the steel wire is calculated according to the formula $q=2\pi E\beta\Delta th/m$ in literature [12], where E is the elastic modulus of the sheath, β is the thermal expansion coefficient of the sheath, generally 0.00012~0.00013/℃ [13], where 0.00012/℃is taken. In the sheath making process, the upper limit of the melt temperature of HDPE sheath extrusion is generally set at 230℃, and it is generally controlled at about 200℃. HDPE sheath needs to be cooled in cooling water with temperature below 20℃. Therefore, the temperature change Δt in the production process of the sleeve is about 180℃ [14-17], where h is the wall thickness of the sheath, and m is the number of wires in the outermost layer of the wire cable. For a 37φ7 semi-parallel steel wire cable, the sheath thickness h is 8 mm and the number m of the outermost steel wires of the steel wire cable is 18. Therefore, the grip force allocated to each steel wire is calculated as q=9.04 kN/m.

② High-strength galvanised steel wire: the elastic modulus of the material is 200000 MPa, the density is 7850 kilograms per cubic meter, and the Poisson's ratio v is 0.3.

③ The friction coefficient between steel wire μ is taken according to the boundary conditions at both ends of the cable. Through cross-over wire vibration and sliding experiments, the friction coefficient between cable wire is 0.3~0.4[18]. By studying the influence of the interface contact force of the transverse contact steel strand, Gnanavel obtains the dry friction without sliding action between steel wires, and the friction coefficient μ can be 0.5[19]. The μ of free and welded at both ends is taken as 0.3. The pre-tension force applied at both ends μ is taken as 0.5. The space finite element model of 37φ7 semi-parallel steel wire cable and the representative contact point number of the cross-section contact surface are shown in Figure 2.

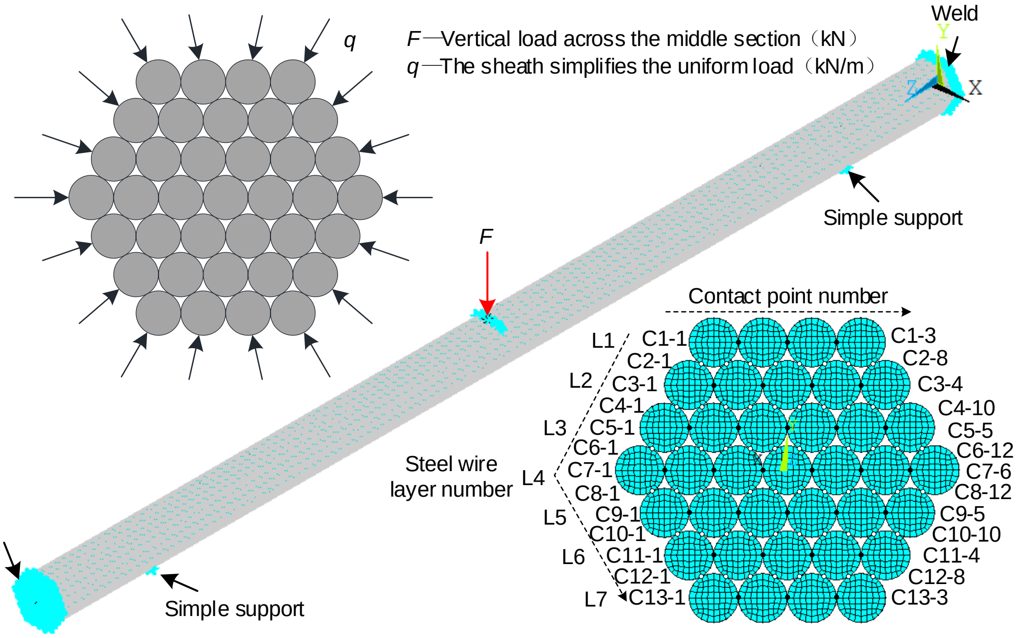

Fig. 2 – Finite element model and contact point number of 37φ7 semi-parallel steel wire cable（weld end）

Bending calculation and test verification of refined finite element model

A 37φ7 semi-parallel steel cable is taken as an example to verify the correctness of the refined finite element model. The correctness of the calculation of the bending refined finite element model is verified by comparison and analysis of the calculation results of the semi-refined finite element model in the bending test and literature [4] with the calculation results of the refined finite element model in this paper. The results of the lateral load–lateral displacement curve of the 37φ7 semi-parallel steel cable during mid-span bending under the boundary conditions of free ends, welded ends and different pretensions applied to both ends are shown in Figure 3.

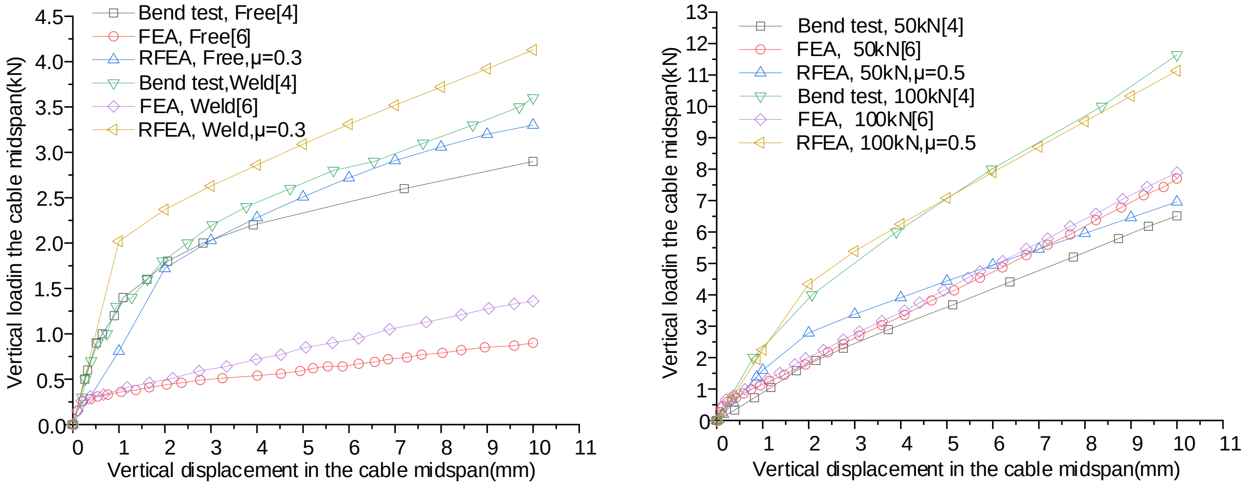

(a) Both ends of the cable are free and weld (b) Different pretensions are applied at both ends of the cable

Fig. 3- Comparison of lateral load-displacement curves in mid-span bending of 37φ7 semi-parallel steel wire cables

As shown in Figure 3, the lateral load–displacement curve in mid-span bending calculated by the refined finite element model is consistent with the change trend of the bending test data, indicating that the laws are basically the same. However, the semi-fine finite element calculation value of the beam-beam-spring combination used in literature [6] is small and has huge error and poor simulation accuracy. For the pre-tension cable, the lateral bearing capacity of the cable is not significantly increased with increasing pre-tension and mid-span lateral displacement, which is not consistent with the test results. Reference [6] believes that the reason for the large difference in the calculation results is due to the wrapping effect of the cable sheath on the wire bundle in addition to the measurement error, thereby increasing the inertia moment of the cable section. Part of the lateral force will be shared during the bending process. However, the simulation calculation results of the refined finite element model show that the contact friction between the wires poses a great influence on the lateral force during the bending of the semi-parallel wire cable. The calculation results of the refined finite element model are closer to the experimental data. For the pre-tensioned semi-parallel wire cable, the calculation results are basically consistent with the experimental data, which verifies the correctness of the refined finite element model.

Mechanical behaviour analysis of contact friction between steel wires during bending of semi-parallel steel wire cables

For the 37φ7 semi-parallel wire cable, the boundary conditions as of free ends, welded ends and initial tension of 50kN and 100kN at both ends are mainly considered. The lateral displacement of the cable under mid-span bending is 10 mm. The changing law of the extrusion deformation, contact pressure and contact friction stress of the contact points on the contact surface between the steel wire layers of the mid-span section during the bending of the cable is obtained through the calculation of the refined finite element model of the cable. The rules for the maximum extrusion deformation, contact pressure and contact friction stress of the contact point on the contact surface are analysed. Finally, the axial slip behaviour between the wires during the bending process is analysed.

Contact extrusion deformation between steel wires

For different boundary conditions of 37φ7 semi-parallel steel wire cables, the change in the contact extrusion deformation of the indirect contact in the same or adjacent steel wires in the mid-span section of the cable is different. When the lateral displacement applied in the midspan is 0–10 mm, the maximum extrusion deformation of the contact point in the adjacent steel wire layers in the midspan section of the cable is obtained by calculating the refined finite element cable model at contact Point C2-1 between steel wire layers L1 and L2. The maximum extrusion deformation of the contacts of the same steel wires in the same layer is located at the contact point C11-4 of the steel wire layer L11. Figure 3 shows the changes in the contact extrusion deformation at the contact points C2-1 and C11-4 under different boundary conditions during cable bending.

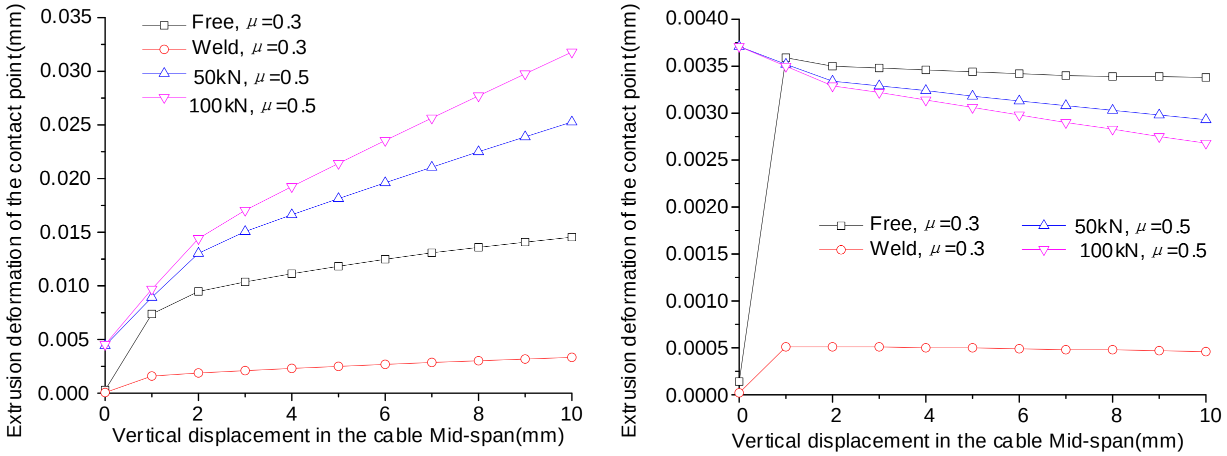

(*a*)contact Point C2-1 between steel wire layers L1 and L2

(*b*)contact Point C11-4 of steel wire layer L11

Fig. 4 –Extrusion deformation change of indirect contact of adjacent or the same steel wire layer

During the bending process of the 37φ7 semi-parallel steel wire cables, Figure 4(a) shows that for the extrusion deformation of the contact in adjacent steel wire layers, the maximum extrusion deformation of the contact point C2-1 in the mid-span section tends to nonlinearly increase with increasing lateral displacement. The extrusion deformation produced by the contact point of the pretension cable during the bending process is significantly higher than that of the free and welded boundary cables at both ends. For the extrusion deformation of the contacts in the same steel wire layers, Figure 4 (b) shows that for the free and welded cables at both ends, the extrusion deformation increases rapidly at the contact point C11-4 in the initial bending stage. When the lateral displacement is greater than 1 mm, the extrusion deformation at the contact point C11-4 slightly decreases with increasing lateral displacement and tends to be gentle; for the pre-tension cable, huge extrusion deformation can be found at the contact point C11-4 before it is bent due to the pre-applied tension. With increasing lateral displacement applied at the mid-span, the extrusion deformation at the contact point C11-4 decreases, and the greater initial pre-tension leads to the more extrusion deformation decrease of the contact point.

Contact extrusion stress between steel wires

For cables with different boundary conditions, the variations in the contact extrusion pressure of the indirect contact of the same and adjacent steel wires in the mid-span section of the semi-parallel steel wire cable are different. When the lateral displacement applied in the midspan is 0–10 mm, the maximum extrusion stress of the contact point of the adjacent steel wire layers in the midspan section of the cable is obtained through the calculation of the refined finite element cable model at contact point C2-1 between the steel wire layers L1 and L2. The maximum extrusion stress of the contacts in the same steel wires is located at the contact point C3-4 of the steel wire layer L3. Figure 5 shows the variations in the extrusion stress of indirect contacts in adjacent or the same steel wire layer under different boundary conditions during cable bending.

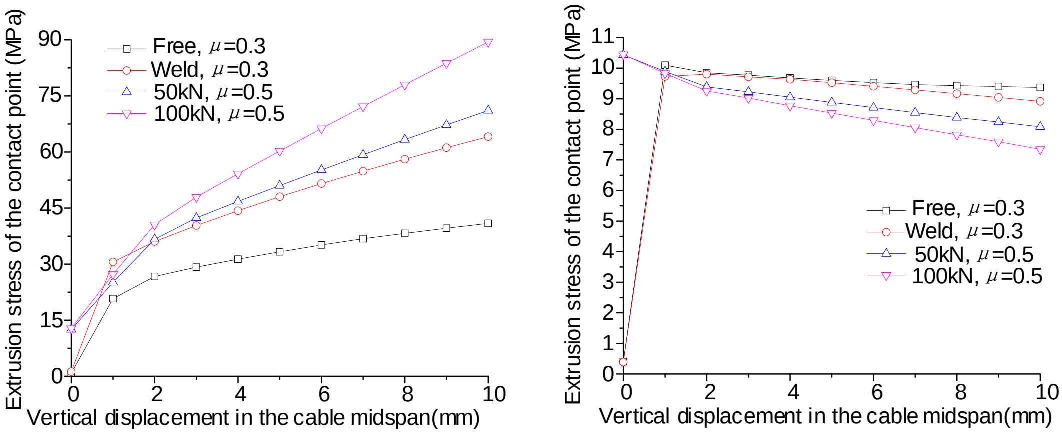

(*a*)contact Point C2-1 between steel wire layers L1 and L2 (*b*)contact Point C3-4 of steel wire layer L3

Fig. 5 -Variations in the extrusion stress of indirect contacts in adjacent or the same steel wire layer

During the bending process of the 37φ7 semi-parallel steel wire cables, Figure 5(a) shows that for the extrusion stress of the contact in adjacent steel wire layers, the maximum extrusion stress of the contact point C2-1 in the mid-span section tends to nonlinearly increase with increasing lateral displacement. The extrusion stress produced by the contact point in the pretension cable during bending is significantly higher than that in the free and welded boundary cables at both ends. For the extrusion stress of the contacts in the same steel wire layers, Figure 5 (b) shows that for the free and welded cables at both ends, the extrusion stress increases rapidly at the contact point C3-4 in the initial bending stage. When the lateral displacement is greater than 1 mm, the extrusion stress at the contact point C3-4 slightly decreases with increasing lateral displacement and tends to be gentle. For the pre-tension cable, a huge extrusion stress can be found at the contact point C11-4 before it is bent due to the pre-applied tension at both ends of the bending cables. With increasing lateral displacement applied at the mid-span, the extrusion stress at the contact point C3-4 is nonlinearly decreased, and the greater initial pre-tension leads to the more extrusion stress decrease of the contact point C3-4, similar to the variation law of contact deformation of contacts in adjacent steel wires.

Contact friction stress between steel wires

For cables under different boundary conditions, the change in the contact friction stress at the contact point in the adjacent or the same steel wires at the mid-span of the semi-parallel steel wire cable is different. When the lateral displacement applied in the midspan is 0–10 mm, the maximum extrusion deformation of the contact point of the adjacent steel wire layers in the midspan section of the cable is obtained through the calculation of the refined finite element cable model at contact point C2-1 between the steel wire layers L1 and L2. The maximum extrusion deformation of the contacts in the same steel wires is located at the contact point C3-4 of the steel wire layer L3. Figure 6 shows the contact friction stress of indirect contacts in adjacent or the same steel wire layer under different boundary conditions during cable bending.

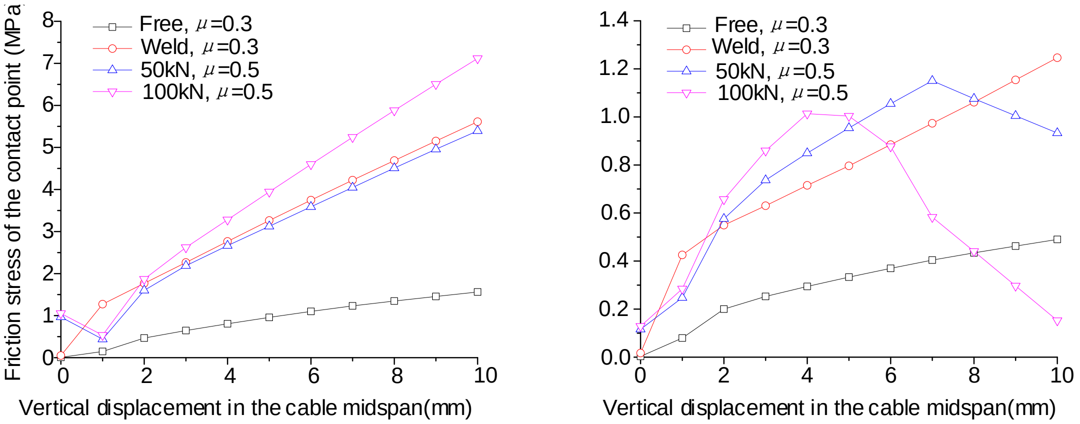

(*a*)contact Point C2-1 between steel wire layers L1 and L2 (*b*)contact Point C3-4 of steel wire layer L3

Fig. 6-Variations in the contact friction stress of indirect contacts in adjacent or the same steel wire layer

During the bending of the 37φ7 semi-parallel steel wire cables, Figure 6(a) shows that for the contact friction stress of the contact in adjacent steel wire layers, the maximum contact friction stress of the contact point C2-1 in the mid-span section tends to nonlinearly increase with increasing lateral displacement for cables with free ends and welded boundary conditions. The contact friction stress produced by the contact point in the cable with two ends welded during the bending process is significantly higher than that in the free cables at both ends. For the cable with the boundary condition of 50kN and 100kN pretension force, the maximum contact friction stress of the contact point C2-1 decreases firstly and then increases with increasing lateral displacement. When the lateral displacement is 1 mm, the maximum contact friction stress value of the contact point C2-1 is the smallest. The contact friction stress generated at the contact point during the bending of the cable with a pre-tension of 100kN is significantly higher than that of the free and welded boundary cables at both ends. For the contact friction stress of the contacts in the same steel wire layers, Figure 6 (b) shows that for the free and welded cables at both ends, the extrusion deformation increases rapidly at the contact point C3-4 in the initial bending stage. When the lateral displacement is greater than 2 mm, the contact friction stress at the contact point C3-4 nonlinearly increases with increasing lateral displacement. For the pre-tension cable, a huge contact friction stress can be found at the contact point C3-4 before it is bent due to the pre-applied tension at both ends of the cables. With increasing lateral displacement applied at the mid-span, the contact friction stress at the contact point C3-4 nonlinearly increases. The friction stress has a maximum value. For cables with a pretension of 50kN and 100kN, the mid-span lateral displacement values corresponding to the maximum frictional stress are 7 and 4 mm, respectively. During the bending of the cable, the larger initial pre-tension force applied leads to the smaller critical value of the mid-span lateral displacement corresponding to the decreasing trend of the contact friction stress at the contact point C3-4 of the mid-span section.

Analysis of axial slip behaviour between steel wires

According to the refined finite element model of the 37φ7 semi-parallel steel wire cable, the maximum cumulative amount of the indirect contact between the steel wires during the bending process is calculated, and the most unfavourable position of the cable is determined. The maximum lateral displacement applied at the mid-span of the semi-parallel steel cable is 10 mm, and the cross-sectional position of the maximum cumulative slip of the steel wire cable during the bending process of the 37φ7 semi-parallel steel cable is calculated (Figure 7).

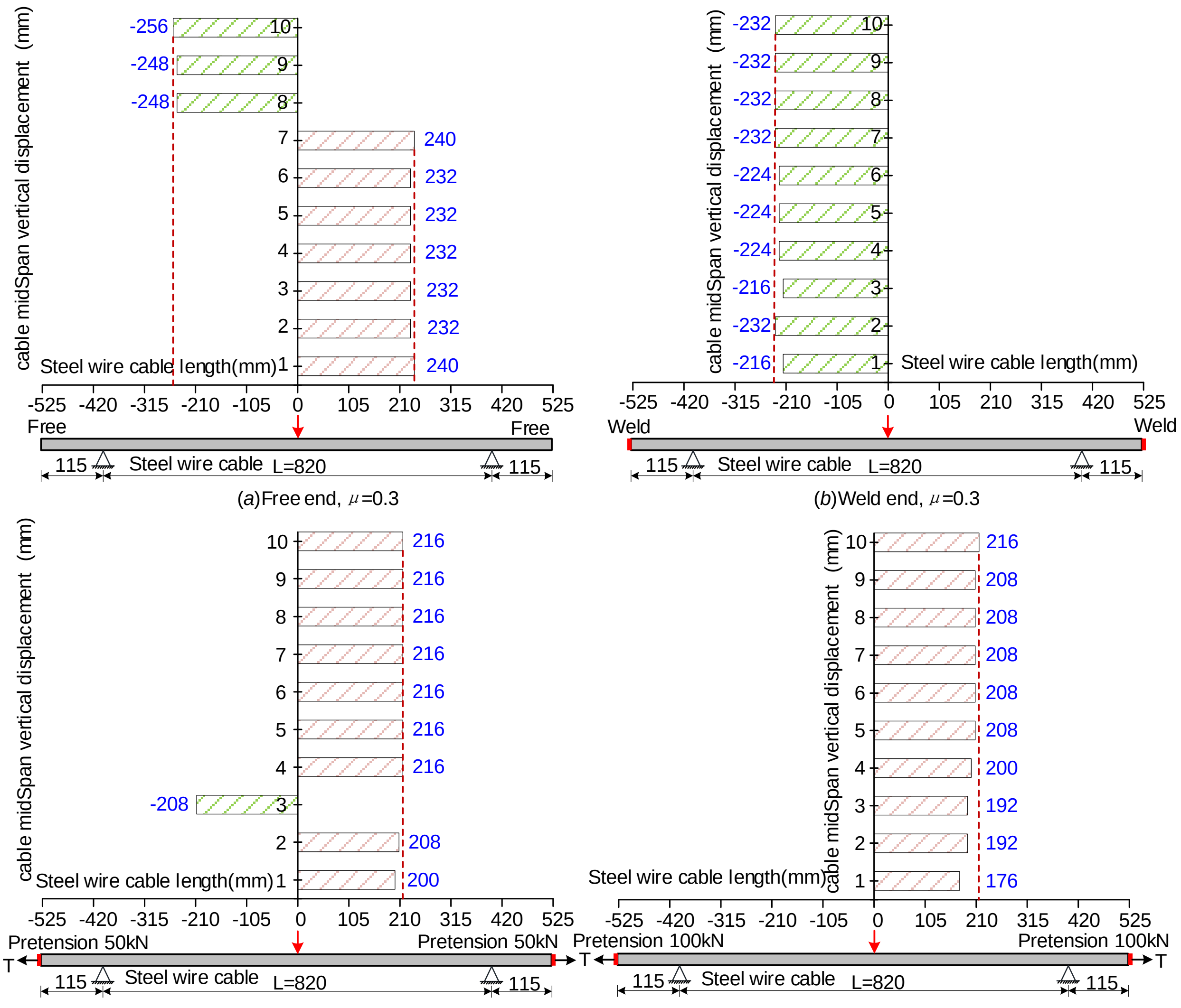

(a)Free end, μ=0.3

(b)Weld end, μ=0.3

(c) Pretension50kN, μ=0.5

(d) Pretension 100kN, μ=0.5

Fig.7-Section position of maximum cumulative slip of 37φ7 semi-parallel steel wire cable during bending

As shown in Figure 7, for 37φ7 semi-parallel steel wire cables with different boundary conditions, the position of the maximum cumulative slip between the steel wires varies with increasing mid-span bending degree of the cables. The maximum slip is mainly located in the bending cable segment near 1/4L or 3/4L (L is the calculated span of the cable).

CONCLUSION

(1) The refined solid finite element model of the semi-parallel steel wire cable taking the contact friction into consideration is more accurate for calculating the bending mechanical properties of the cable than the semi-refined finite element model in literature. For the pre-tension cable, the calculation results of the refined finite element model are basically close to the experimental data.

(2) With increasing mid-span lateral displacement of the cable, the contact deformation and contact extrusion stress of the indirect contact in the adjacent or the same steel wire cables under the three boundary conditions. The contact friction stress of the cables with free ends and welded boundary tends to nonlinearly increase, while the contact friction stress of the pretension cable tend to first decrease and then increase.

(3) Under the condition of cables with both free ends and welded boundary, the contact deformation and contact extrusion stress of the indirect contacts in the same steel wire layers are

first rapidly increased and then slightly increased; it then tends to be stable with increasing cable midspan lateral displacement. The frictional stress at the contact point is increased nonlinearly with increasing mid-span lateral displacement. Under different pretension boundary conditions, the contact deformation and contact extrusion stress of the contacts in the same steel wire layers tend to nonlinearly decrease with increasing mid-span lateral displacement. The frictional stress of the contact points is increased firstly and then decreased, and a maximum frictional stress can be found during bending.

(4) For 37φ7 semi-parallel steel wire cables with different boundary conditions, the position of the maximum cumulative slip between the steel wires is variable with increasing mid-span bending degree of the cables. The maximum cumulative slip between the wires is in the bending cable segment near 1/4L or 3/4L (L is the calculated span of the cable).

ACKNOWLEDGEMENTS

This paper is supported by the Fundamental Research Funds for the Central Universities (grant number: 2572020BJ02).

REFERENCES

[1] Gang Zheng. et al., 2015. Bridge cable structure, chapter 4 (China Communications Press Co., Ltd.) 187 pp.

[2] Jiang W. G.,2012. A concise finite element model for pure bending analysis of simple wire strand. International Journal of Mechanical Sciences, vol. 54(1), 69-73

[3] Zhang D., Ostoja-Starzewski M.,2016. Finite element solutions to the bending stiffness of a single-layered helically wound cable with internal friction. Journal of Applied Mechanics, vol. 83(3): 031003-1~8

[4] Xiaofeng WU., 2013. Research on Bending Performance of cable, (Tianjing University Master Dissertation)

[5] Zhihua Chen., Yujie Yu., Xiaodun Wang. et al., 2015.Experimental research on bending performance of structural cable. Construction & Building Materials, vol.96, 279-288

[6] Yujie Yu.,2015. Semi-refined Finite Element Model of Cable and its Application on Bending Behavior and Wire Break. (Tianjing University Ph.D. Dissertation)

[7] Faquan Zeng.,2017. Research on nonlinear bending characteristics of parallel wire cable strands. (Southwest Jiaotong University Master Dissertation)

[8] BingLiang., Zhongwei Zhao., Xiaofeng Wu., Haiqing Liu., 2017.The establishment of a numerical model for structural cables including friction. Journal of Constructional Steel Research, vol. 139 :424-436

[9] Yongping Zhang., Jinfeng Wang., Guiru Ye.,Rongqiao Xu.,2018.Bending Stiffness of Parallel Wire Cables Including Interfacial Slips among Wires. Journal of Structural Engineering, vol.144(10):04018164.1-04018164.9

[10] Yongping Zhang., Qian Feng., Guannan Wang., Rongqiao Xu.,2021. Analytical model for the bending of parallel wire cables considering interactions among wires.International Journal of Mechanical Sciences, vol.194(3):106192.

[11] Lalonde S., Guilbault R., Légeron F.,2017. Modeling multilayered wire strands, a strategy based on 3D finite element beam-to-beam contacts - Part I: Model formulation and validation. International Journal of Mechanical Sciences, vol.126:281-296

[12] Jianxi Yang.,2018. Study on bending effect of semi - parallel steel wire suspender of arch bridge. (Tongji University Ph.D. Dissertation)

[13] Shanhong Liu.,2013. Damage mechanism and prevention countermeasures of HDPE protective sheath for stayed cables. Journal of Chongqing Jiaotong University (Natural Science), vol.32 (Add 1): 888-893

[14] Shiwei Ning., 1985. Polyethylene hot-extruded sling-a new kind of cable protection structure. Gonglu, (3): 23-28

[15] Chengguang Huang., 1993.Brief introduction of cable-stayed bridge and protection technology of hot-extruded slings. Yunnan Highway Technology, (4): 41-45

[16] Shibin Li., 2001 Research on the key technology of secondary extrusion colored PE sheath for bridge cables. Nanjing: Southeast University, 2001

[17] Chongzhe Wang., Jianfei Pan., Gaoyou Feng., et al.,2012. Production technology of SHG Haval sheath for bridges. Theoretical Research in Urban Construction: Electronic Edition

[18] Judge R., Yang Z., Jones S W., et al.,2012. Full 3D finite element modelling of spiral strand cables. Construction and Building Materials, vol.35: 452-459

[19] Gnanavel B K., Parthasarathy N S., 2011.Effect of interfacial contact forces in lateral Contact Wire Strand. Archive of Applied Mechanics, vol.81: 303-317

Article no. 35

THE CIVIL ENGINEERING JOURNAL 3-2022

RESEARCH ON THE APPLICATION OF PILE-BUCKET COMPOSITE STRUCTURE IN THE SILT COAST

Yao Liu[1,2], Jintian Chen[3] and Wu Li[4]*

1. *College of Civil Engineering, Northeast Forestry University, Harbin 150040, China; dltmly@nefu.edu.cn*
2. *College of Engineering, Department of architectural Engineering, Kangwon National University, Chuncheon-si, 24341, Republic of Korea*
3. *College of Civil and Architectural Engineering, Heilongjiang Institute of Technology, Harbin 150050, China; cccjt2003@163.com*
4. *CCCC Third Harbor Consultants Co., Ltd, Shanghai 200023, China; liw@theidi.com*

ABSTRACT

With the over-exploitation of high-quality coastlines, the site selection and construction of new ports have to be expanded to silt coast, which will bring about quite many technical difficulties in the construction of wharves and revetments, and the cost of investment will also rise sharply. In this paper, a kind of combined design scheme of the high-pile wharf and the bucket structure is proposed to solve the problems mentioned above. The high-pile wharf structure is meant to adapt to the silt foundation, while the bucket can help to improve the ground bearing capacity. The stability and displacement of the bucket structure, and the influence of displacement on high-pile wharf during the service period are analyzed using a finite element model. Analysis results indicate that the horizontal and vertical displacements of the bucket structure in the service period are reduced to same extent compared with those in the construction period, and the maximum horizontal displacements of the lower barrel structure are 0.4cm more than those of the upper part. The difference between the vertical displacement on the seaside and the portside is 10.5cm, and a rotation of 0.2° occurred in the bucket. Besides, the working loads above the bucket have a significant influence on the horizontal displacement and sliding stability of the bucket in the service period. It can be known from the above conclusion that the composite structure is a kind of structure that can adapt to the conditions of soft soil underwater, and it has advantages of the construction period and cost when used in water depth and silt area, which provides useful experience for the silt coastal projects.

KEYWORDS

Pile-bucket combination, Silt coast, Stability, Displacement analysis

INTRODUCTION

In order to meet the demands of economy, society and environment, the scale of ports is constantly expanded, and large-scale, deep-water, specialized and multifunctional wharfs have become a trend of port development. However, many ports are faced with problems such as limited function and overloading operations, the conflict between the development of ports and cities, environmental issues, and unmatched modes of transport, which need to be further improved. To ease the tensions mentioned above, new ports have to be built in seas where the hydrogeological conditions are very complicated, thus greatly increases the technical difficulty of wharf, revetment and other projects. Silty coastal zones are widely distributed around the world, Holland in western Europe, Bohai Bay in China and the south-central coast of Jiangsu are the most famous silty coasts

DOI 10.14311/CEJ.2022.03.0035

in the world. 4000km of the 18000km continental coastlines are silty [1-3]. The critical technical difficulties in those areas are mainly concerned with the treatment of thick weak soil stratum and the improvement of its high sensitivity and poor mechanics properties. As shown in figure1-3, the traditional way of drainage consolidation, layered filling of sand, and mud replacement by blasting are defective in that the amount of engineering is tremendous, the duration of the project is long, the influence on the environment is great, and the process is easily interrupted by gales. In particular, mud replacement by blasting will make a severe impact on the marine environment, a large number of sea creatures will be killed during the construction [4,5].

Fig.1- A drainage plate

Fig.2 - Filling sand

Fig.3 - Blasting compaction

The development of main technologies of bucket foundation can be traced back to the 1960s. Since Statoil successfully applied bucket foundation platform at sea for the first time in 1994, the research and application of bucket foundation platform has been gradually popularized all over the world [6]. The use and research of bucket foundation started relatively late in China.Bucket foundation structure is a new type of structure suitable for offshore soft soil foundation. At present, scholars at home and abroad have carried out relevant research on bucket infrastructure [7,8]. Liu et al. studied the horizontal limit bearing capacity of bucket foundations and the distribution of the active and passive earth pressure by means of model tests and finite element method. The formula for evaluating the horizontal limit bearing capacity is suggested, and the horizontal bearing capacity of double buckets foundation is investigated and a means to estimate the bearing capacity of the double buckets foundations is given [9]. Cai et al. studied the numerical analysis of earth pressure, anti-overturning calculation, and numerical simulation during construction and operation period of bucket foundation structure, which provides a theoretical basis for the design and construction of large cylinder structure [10-12]. Cao et al. analyzed of the soil pressure and the barrel’s vertical and circular distributions are performed with different thickness of reclamation silt, which provides a reference for checking the stability of new bucket foundation revetment structure [13]. Byrne et al. based on the experimental results, an incisive understanding of the relationship between load and displacement is obtained, and a simple theoretical and numerical model is proposed [14]. Park et al. established the finite element model of bucket foundation on sandy soil foundation and layered foundation, and studied the characteristics of vertical bearing capacity. The results show that the shear strength of sand and clay will affect the shape of failure surface of bucket foundation [15,16].

The traditional gravity wharf has high requirements for foundation. In the deep-sea area with thick, soft soil layer, it needs a lot of foundation treatment. The project investment is large and the construction period is long. It is unreasonable from the economic and technical considerations. As one of the main structural types of port terminals, high pile wharf is widely used because of its light structure, adaptability to soft soil foundation and little impact on water flow. little influence on water flow [17]. It is widely used in China's coastal and inland rivers and other soft soil foundations, such as the Yangtze River Delta region, Pearl River Delta region, Lianyungang, Tianjin and other areas, where there is a deep silt layer, especially suitable for deep foundation structures such as high pile wharf. In order to adapt to the complex characteristics of various foundations, which has experienced different forms of development and derived many new structural types.

In this paper, a new type of structure pile-bucket wharf is proposed, shown in Figure 4. The configuration is of great practical use in that it helps to save much effort from the treatment of soft soil, which is substituted by the soil concealing by cover plate, wallboards, septums, and the hard soil below. The new structure has good performance in that it has low permeability, which means that the silt in the barrel is rigid without drainage passage and cannot be compressed. The loads from the cover plate can be transferred directly to the lower foundation, and because of the interaction between the soft soil and the structure, the structural bearing capacity can be greatly enhanced. The revetment that retains soil is connected to the high-pile wharf by simple spans in the front, which will serve as berths for ships and vessels [18,19]. As a new type of structure, bucket foundation structure has been successfully applied in breakwater engineering, but the mechanical stability and displacement of bucket foundation structure combined with high pile wharf are not clear. Therefore, it is necessary to analyze the impact of bucket foundation structure displacement on the wharf structure in front, so as to provide reference for the design and construction of similar projects in the future.

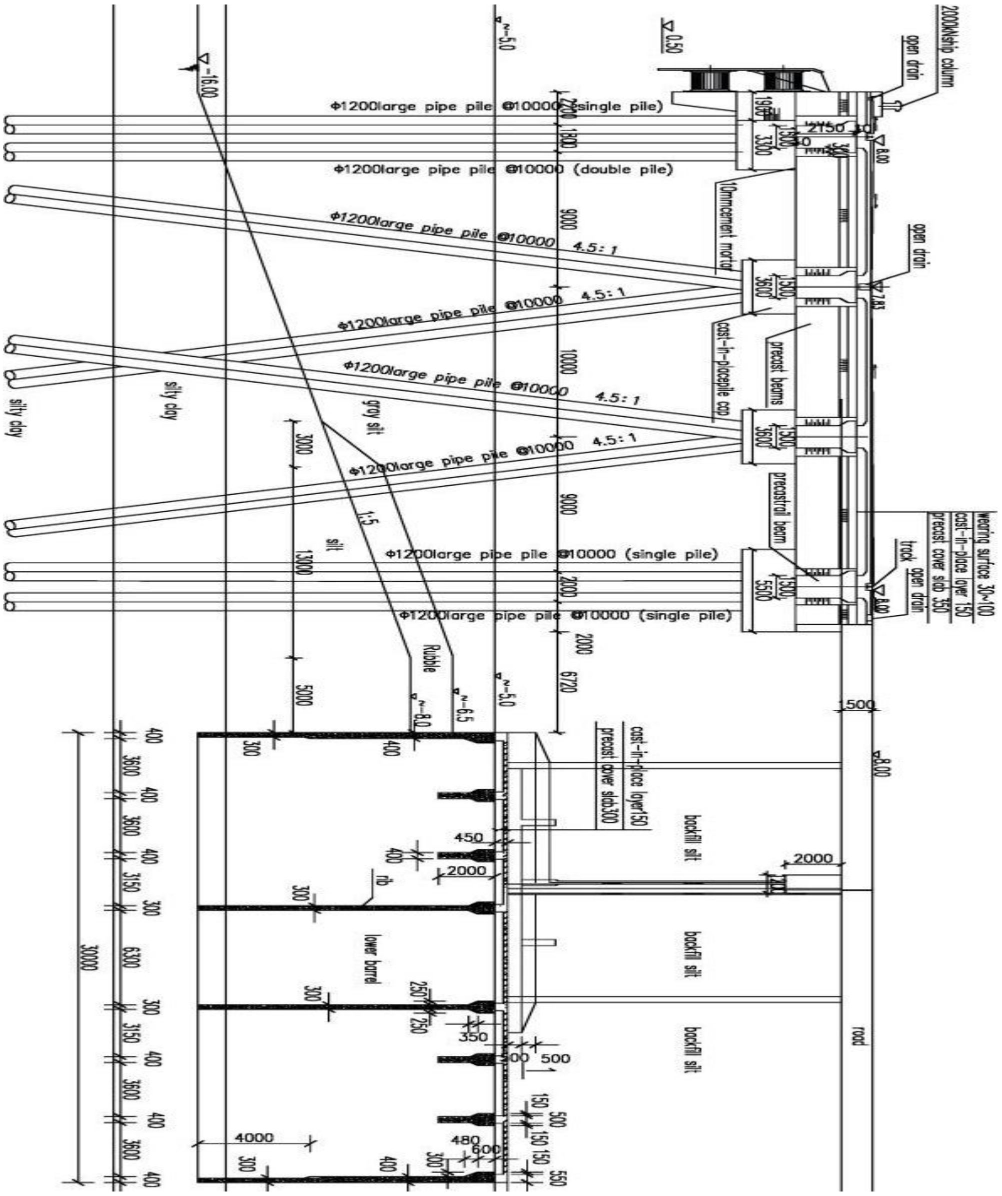

Fig.4 -Section configuration of a pile-bucket wharf

DESIGN BACKGROUND OF THE STRUCTURE

Lianyungang is located in the middle of China's coastline; the planned engineering area is a typical silt coast. The sea bottom of the port area is covered with deep silt clay, which has high porosity ratio, high water content, low strength and bad structure. It is necessary to explore a new type of hydraulic structure to adapt to the port construction under complex natural conditions. Aiming at the safety and stability of the breakwater during its construction and service period, the combined scheme of bucket structure and high-piled wharf structure is put forward. The bucket foundation structure is adopted in the vertical embankment structure of the revetment project. The section of the structure is composed of a cavity structure and block stone protecting the bottom. Each group is composed of a lower bucket structure and two upper cylinders, the bucket foundation is ellipse, with a long axis of 30m, a short axis of 20m and a height of 9m. The barrel is divided into nine compartments through septums; the two upper cylinders are located on the bottom plate of the bucket foundation and are connected by the ring beam on the bottom plate. The schematic diagram of bucket foundation is shown in Figure 5.

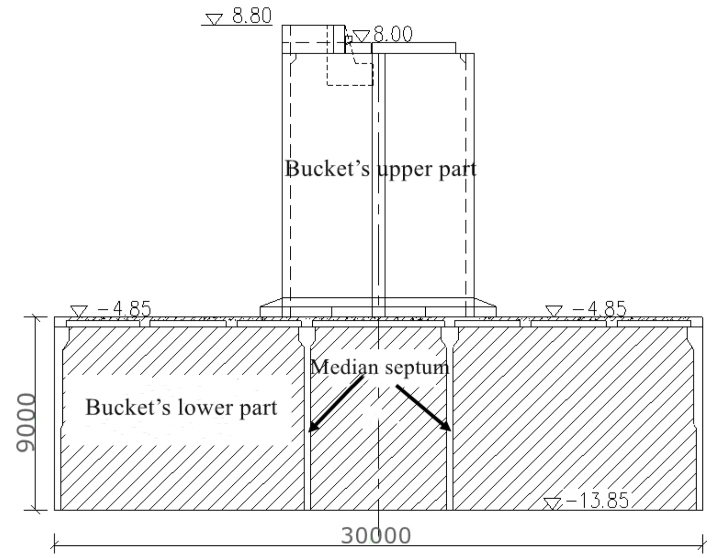

（a）*Side view of bucket structure*

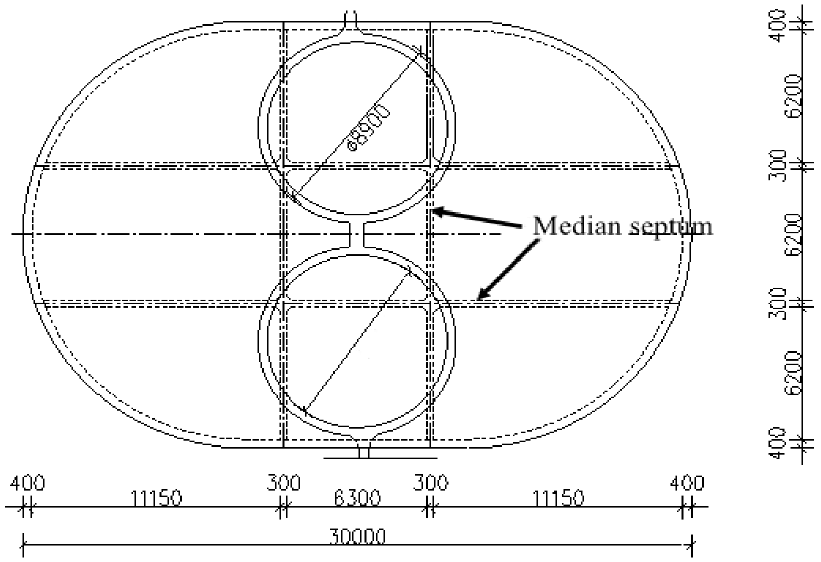

(b) Plan view of bucket structure

Fig.5 - Schematic diagram of bucket structure

COMPUTING MODEL AND PARAMETERS

Numerical model calculation assumptions

The numerical analysis software used is PLAXIS, and the 2D plane finite element method is used for the theoretical analysis. Bucket structure runs longer in vertical direction. According to the characteristics of the structure and deformation, such structure should have the properties of plane strain. To ensure the accurate reflection of its properties, the plane strain model is used in this paper to simulate the bucket structure, not only can reflect the essence of the problem, but also can save a lot of calculation time. The constitutive relationship of soil often plays a decisive role in the calculation results, so the Mohr-Coulomb Model is used for calculation [18]. According to the characteristics of the project and geological reports, several typical soils in different strata are selected as samples. In the period of construction and service, the fluid-solid interaction has been considered in the computing model. The dewatering boundary status is set as the left side, and the upside of the model is to drain, while the right side and the bottom are not to drain.

As shown in Figure 5, because of the medial septum, the structure has a strong metope connection that enhances the flexural rigidity, so it must be considered in computing. The upper wall, the lower wall, sidewall, and inner septum of the bucket are simulated in plate units. Considering the support served by the lower wall of the bucket in the longitude direction, it is simulated in the horizontal plate unit model, in which the longitudinal compressional stiffness of the coverage area is adopted as the rigidity. The status of material is supposed as elastic. The inner configuration is set as actual, and the fillings are taken as corresponding soil or rocks.

Numerical model meshing

In the simulating process, the properties of the soil, the composite soil for strengthening the sand piles, the backfill sand, the riprap, and the dredger soil are taken as the Mohr-Coulomb elastic-plastic model. The piles of the wharves are simulated in pile units. The caps, the roads, the surface layer of the yard, the upper bucket wall, the top cover, and the inner septum of the lower bucket are simulated in isotropic elastic plate units [20]. In order to simulate the interaction and how loads are transferred between the structure and the ground, the surface of the structure is simulated in interface units, whose parameters are set as those of the adjacent stratum. According to the basic requirements and structural characteristics of the numerical simulation, the range of the numerical simulation soil is5 times the horizontal dimension of the structure on each side in the horizontal direction, 2 times the depth of the structure in the depth direction, and the boundary of the soil is fixed.

Based on the characteristics of the project and previous experience, the calculating area is determined as: in the horizontal direction. The portside and seaside boundary are set as 65 meters and 55 meters separately away from the axle wire of the bucket's foundation; in the depth direction, the upside and bottom boundary are set as 50 meters and 8 meters separately away from the sea level [21]. The numerical calculation model is shown in Figure 6, and how the mesh is divided is illustrated in Figure 7.

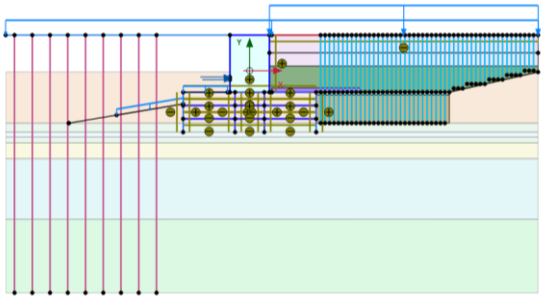
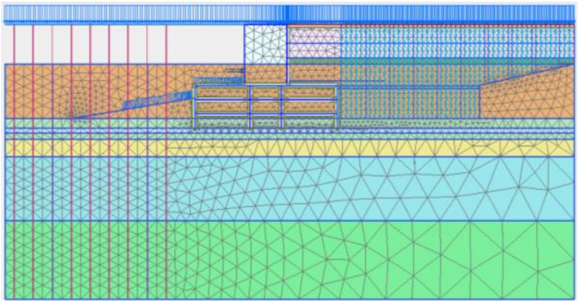

Fig.6 - Finite element analytical model *Fig.7 - Mesh model of bucket's foundation*

Parameter selection of soil and engineering structure related material

The parameters in the numerical model are mainly concerned with the physical and mechanical properties of the soil, the composite soil for strengthening the sand piles, the reclaimed silt, the sandbags, the riprap, the piles and caps of the wharf, the surface layer of the yard, the walls of the upper part of the bucket, the top cover of the lower part of the bucket, the inner septum and the inner walls of the lower part of the bucket [22].

Physical and mechanical parameters of soil

The calculation parameters are selected according to the report of engineering geological exploration, including: bulk density of soil, elastic modulus E, Poisson's ratio μ, cohesion c', internal friction angle φ', permeability coefficient k. According to the geological data, the detailed selection of the main physical and mechanical parameters of the soil on both sides of the structure is shown in Table 1. The values of c' and φ' are the rapid shear strength of consolidation. The drainage type used for silt and silty clay is no-drainage, and that of sandy silt and silty sand is drainage.

Tab.1: Physical and mechanics properties of the soil

Stratum name	Moisture content w (%)	Natural weight-specified density γ kN/m3)	Initial void ration e0	Poisson ration μ	Compression modulus Es (MPa)	Compression coefficient a (MPa-1)	Strength parameters	
							Cohesion c'(kPa)	Internal friction angle φ' (°)
Silt	69.7	15.8	1.963	0.42	1.4	2.17	8.5	8
Silty clay	28.4	19.7	0.807	0.42	5.8	0.31	35	15
Sandy silt	25.1	19.8	0.701	0.40	11.1	0.16	4.5	31.5
Silty sand	22.9	20.0	0.649	0.40	13.8	0.12	1.5	38

Physical and mechanical parameters of reclaimed silt

Layered backfilling is adopted for the backfilling behind the bucket. Considering that the compactness of the lower reclaimed silt increases under the action of the upper reclaimed silt, in order to more reasonably simulate the characteristics of the reclaimed silt, the reclaimed silt is divided into the upper layer (0-7m in depth) and the lower layer (7m in depth to the excavation face), and the corresponding calculation parameters are adopted. The drainage type adopted for reclaimed silt is no-drainage. The physical and mechanical parameters are shown in Table 2.

Tab 2: Physical and mechanics properties of the reclaimed silt

Stratum	Natural weight-specified density γ(kN/m3)	Initial void ration e0	Poisson ration μ	Compression modulus Es (MPa)	Strength parameters (service period)		Strength parameters (construction period)	
					c'(kPa)	φ'(°)	c'(kPa)	φ'(°)
Reclaimed silt (0-7m in depth)	14	1.4	0.42	2	15	0.6	5	0.6
Reclaimed silt (7m in depth to the excavation face)	14	1.4	0.42	2	15	0.6	9	0.6

Physical and mechanical parameters of soil reinforced by sand pile

The depth range of about 10m behind the bucket body is mainly silty soil. In order to ensure the stability of the reclaimed silt, sand piles are needed to reinforce the soil layer below. The vertical drainage lines are arranged at an interval of 1m within the area of sand pile reinforcement to simulate the vertical drainage effect of sand piles. At the same time, the sand cushion is above the sand pile reinforcement area. The sand pile reinforcement scheme for ramp wharf, the diameter of sand pile is 1m. In order to facilitate finite element analysis and calculation by conventional stability analysis program, the values of c and φ needs to be expressed by equivalent strength. That is, the Priebe method is used. The equivalent physical and mechanical parameters of composite foundation reinforced by sand pile are shown in Table 3.

Tab.3: Mechanics properties of the composite soil reinforced by sand piles

Stratum	Displacement ratio of sand piles	Natural weight-specified density γ (kN/m3)	Initial void ration e0	Poisson ration μ	Compression modulus Es (MPa)	Strength parameters	
						Cohesion csp (kPa)	Internal friction angle φsp (°)
Composite soil reinforced by sand piles	30%	16.6	0.5	0.40	3.12	12.69	15.44

Note：Es = compression modulus of sand pile composite foundation; csp = cohesion of composite foundation; φsp = internal friction Angle of composite foundation.

Physical and mechanical parameters of riprap bedding and backfill sand in upper bucket

The bottom protection at the seaside is filled with 200~400kg block stones with a thickness of about 2m, and the filling range is 25m outside the bucket; the bottom protection at the portside is filled with 200~400kg block stones with a thickness of about 1m, and the filling range is 20m outside the bucket. The riprap on the seaside can be simulated in the form of uniform load, and the solid element simulation is applied to the riprap on the portside because of the need of backfilling silt and the reinforcement of the foundation. The bucket foundation is a gravity structure and the gravity of the backfill sand in the upper bucket is the resistance to prevent the bucket structure from slipping or overturning. The physical and mechanical parameters of riprap bedding and backfill sand are shown in Table 4.

Tab.4: Mechanics properties of the riprap bedding and the backfill sand of the bucket's upper part

Stratum	Weight-specified density γ (kN/m3)	Poisson ration μ	Elasticity modulus E (MPa)	Cohesion c' (kPa)	Internal friction angle φ '(°)
Riprap bedding	10	0.3	20	0	45

Backfill sand	18	0.3	20	0	28

Mechanical parameters of bucket structure

Considering the structural form and stiffness characteristics of the barrel body, the compression and flexural stiffness of each part of the bucket body are converted respectively according to the principle of equivalent stiffness, and the unit weight of each part of the bucket structure is calculated according to the principle of equal weight. In the finite element model, the semi-circular parts at both ends of the lower bucket walls are simulated by the vertical plate elements, the vertical plate element is also used to simulate the vertical septum in the short axis direction inside the bucket. The outer bucket wall in the long axis direction of the foundation bucket and the internal vertical septum have the function of supporting the bucket in the horizontal direction, and are simulated by the horizontal plate element, its mechanical parameters are converted according to the equivalent flexural stiffness in the horizontal direction. The walls of the bucket's upper part are simulated by vertical plate element, the top cover of the bucket's lower part is simulated by horizontal plate element. The corresponding mechanical parameters of each part of the bucket structure are shown in Table 5.

Tab. 5: Mechanics properties of the bucket

Locations of structure	Compressive stiffness EA (kN/m)	Bending stiffness EI (kN·m)	Weight-specified density W (kN/m²)	Poisson ration μ
Walls of the bucket's upper part	1.72E7	4.00E5	12.72	0.2
Inner cross septum of the bucket's lower part	9.70E6	7.30E6	4.5	0.2
Inner vertical septum of the bucket's lower part	2.93E7	1.97E6	7.2	0.2
Walls of the bucket's lower part	1.95E7	5.84E5	14.40	0.2
Top cover of the bucket's lower part	1.30E7	1.73E5	9.60	0.2

Mechanical parameters of wharf high pile, wharf roof and wharf yard

Wharf high piles are precast concrete pipe piles, which are simulated by embedded pile element. Plate element is used to simulate wharf roof and yard. The corresponding mechanical parameters are shown in Table 6 and Table 7 respectively.

Tab.6: Properties of the wharf's high-piles

Type of piles	E (kN/m²)	γ (kN/m³)	D (m)	Thickness (m)	Distance between piles Lspacing (m)
Precast circular pipe pile	3.6E7	24.00	1.2	0.145	4

Tab.7: Properties of the wharf's roof and yard

Structural part	Compressive rigidity EA (kN/m)	Bending rigidity EI (kN·m)	Weight-specified density W (kN/m2)
Wharf roof	7.65E7	4.15E7	61.20
wharf yard	1.50E7	3.10E5	12.00

DOI 10.14311/CEJ.2022.03.0035

NUMERICAL SIMULATION ANALYSIS AND DISCUSSION

Considering the drainage consolidation effect of the soil during the service period, the consolidation time of the soil is taken as 5 years in order to achieve full drainage. For the sake of simplicity, the service life mentioned later, if not indicated, is calculated after 5 years.

Excess pore water pressure during the service period

In order to analyze the excess pore water pressure during the service period, four sample points are selected，namely A (30, 4), B (30, 1.749), C (30, -12.743), D (30, -25.795), based on which the curve of the excess pore pressure in the construction period and service period (5 years in total) is depicted，shown in Figure 8. The first and second points are selected from the reclaimed silt, the 3rd point is selected in the lower part of the silty clay, and the 4th point is selected from the stratum of silty sand. The construction period is terminated in the 20th month [18,22].

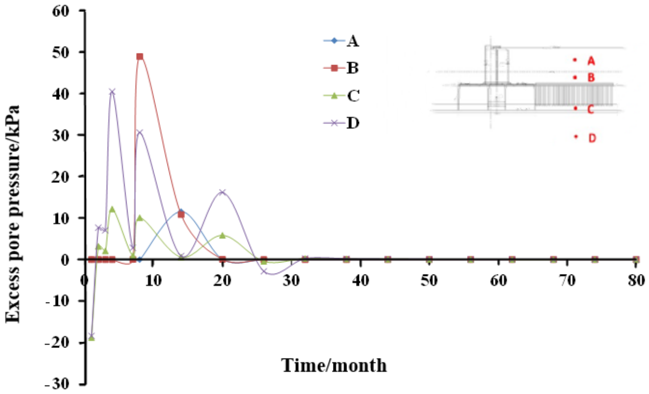

Fig.8 - Excess pore pressure curve of sample points in soil

It can be known from Figure 8 that in the construction period, the excess pore pressure firstly rises rapidly as a consequence of the preloading and the increased pressure caused by reclaimed silt, whereas it has shown a decline after the reclaimed silt is air-cured and the soil is drained and consolidated. In the service period, the excess pore pressure in reclaimed silt decreases with the removal of the preloading. In the next stage, it goes up with the imposing of loads in the service period. At last, the excess pore pressure dissipates. What's more, both curves almost overlap with each other, and the values are relatively close. By the end of the first year, the value of excess pore pressure is close to 0. The excess pore pressure in the lower part of the sand piles and the stratum of silty sand firstly goes down and then goes up in the first year. Afterward, it slowly decreases, and by the fifth year, the value is close to 0. With the installation of the drainage pipes, the shallower the stratum is, the more rapid the excess pore pressure dissipates. From the conclusions drawn above, we can see that it is reasonable to set the simulation duration as 5 years for the working condition in the service period, for by this time, the structure and the displacement of soil is relatively stable, and the results can be identified as the final values.

Horizontal displacement during the service period

At the condition of extremely low water level during the service period, after the sand piles and the foundation of reclaimed silt are reinforced, there is a working load of 3t to 5t distributed on the structure. In the calculating, a uniform load of 50kPa is used. The extremely low water rests at -0.68m, whose recurrence interval is 50 years [18,23-25]. The nephogram of the horizontal displacement during the service period is demonstrated in Figure 9.

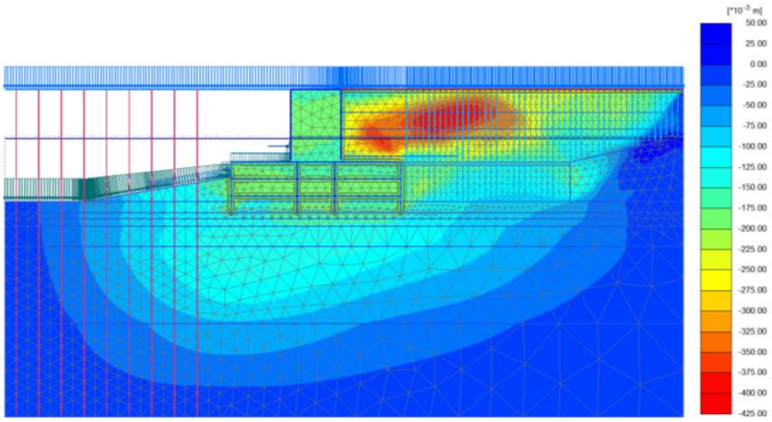

Fig.9 - Horizontal displacement nephogram in-service period

The horizontal displacement distribution along the direction of depth of the upper part of the bucket is illustrated in Figure 10, and how the maximum horizontal displacement of the upper part of the bucket changes over time during the construction and service period is shown in Figure 11. The figures show that the maximum horizontal displacement of the upper part of the bucket roughly follows the distribution of the parabola. At the beginning of the service period, with the withdraw of the preload (10t) and the exerting of comparatively small loads (5t), the horizontal displacement of the bucket decreases rapidly because of the unloading and resilience, whose reduction weights at 2cm. As time goes on, the horizontal displacement shows a minor decline and tends to be stable afterward. The total spring back in 5 years is about 0.4cm. After the fifth year, the maximum final horizontal displacement appears at the elevation of +2.11m, which is measured as 18.8cm. According to the numerical calculation results, the horizontal displacement of the barrel is 20cm in the silt foundation, which has little influence on the soil deformation beyond 200cm and can be neglected. In addition, the straight pile foundation has a certain ability to resist horizontal pressure, the strength index of the silt foundation is low, so the soil deformation can be dissipated around the pile foundation.

The region of the moving soil mass extends below the wharf structure, which affects the three rows of piles on the land side of the wharf, the bending moment on the pile shaft increases, but it is within the bearing range of the pile foundation. Therefore, it is suggested that the batter piles are arranged in the front of the wharf and stay away from the area of moving soil mass, so that the stresses caused by it can be decreased.

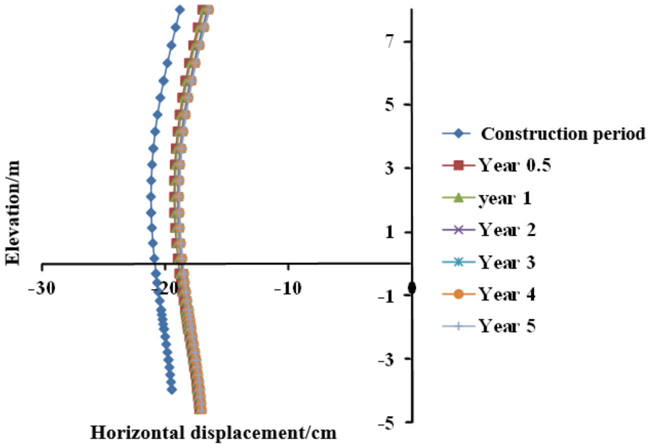

Fig.10-Distribution of horizontal displacement in the depth direction of upper part of the bucket

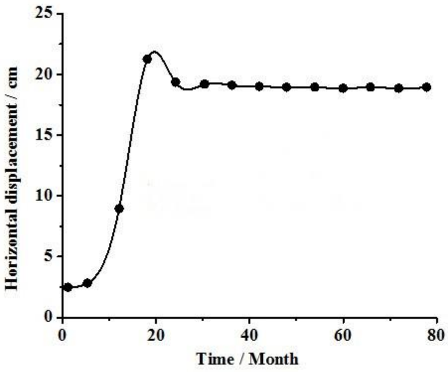

Fig.11-The maximum horizontal displacement of the upper part of the bucket

The horizontal displacement distribution along the direction of depth of the lower part of the bucket is illustrated in Figure 12, and how the maximum horizontal displacement of the lower part of the bucket changes over time during the construction and service period is shown in Figure 13. The figure shows that the horizontal displacement in the direction of depth in the service period roughly increases with depth, except for some abrupt breaks at the interfaces. At the beginning of the service period, with the withdraw of the preload (10t) and the exerting of comparatively small loads (5t), the horizontal displacement of the bucket decreases rapidly because of the unloading and resilience, whose reduction weights at 3cm. As time goes on, the variation trend of horizontal displacement over time is almost the same as that of the upper bucket. The total spring back in 5 ars is about 0.2cm. After the fifth year, the final maximum horizontal displacement happens at -13.85m, measured as 19.2cm [22,26].

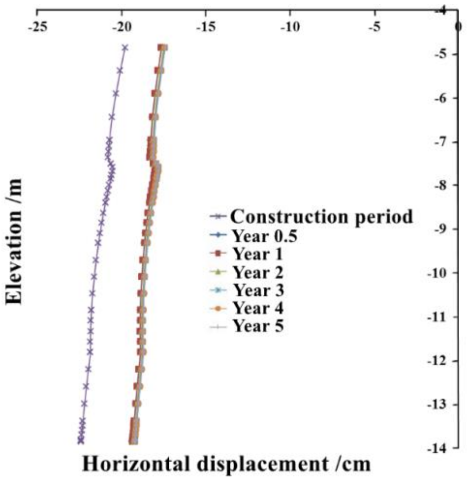

Fig.12-Distribution of horizontal displacement in the depth direction of lower part of the bucket

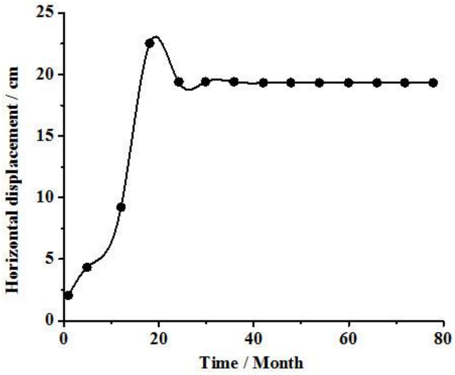

Fig.13-The maximum horizontal displacement of the lower part of the bucket

After the completion of the construction of bucket foundation structure and backfilling silt behind it, a 50kPa load is applied above the structure and backfilling silt to represent the vehicle load during the service life. Under the action of this service load, the instantaneous excess pore water pressure is generated in the silt and acts on the bucket wall on the portside. At this time, the effective stress of the soil has not yet played a role, the lateral pressure coefficient is close to the water pressure state of 1.0. Therefore, the bucket body will have a large horizontal displacement increment at the beginning of service period (the first year). With the development of time, the excess pore water pressure in soil dissipates continuously, the force acting on the barrel wall gradually transformed into the synergy of effective soil pressure and water pressure, the lateral pressure coefficient of soil is smaller than that of water, so the value of horizontal pressure in the later service period will be lower than that in the early service period. Hence, the bucket body has a certain rebound, the horizontal displacement decreases, but not much reduction in total.

Therefore, it is suggested that the ground treatment behind the bucket structure should be started as early as possible, making sure that the soil deformation is completed within the duration of foundation construction. Then proceeds with the front wharf construction, which can effectively reduce the soil deformation caused by the load during the service life.

Analysis of slippage of the structure in the service period

The vertical displacement of the top cover of the bucket's lower part along the long axis during the service period (5years) is shown in Figure 14, the maximum vertical displacement will reach 31.6cm, and the variation trend of slip angle of the bucket over time is shown in Figure 15. The figures show that the vertical displacement of the top cover of the lower part of the bucket keeps on increasing from the seaside to the portside in the service period. In the construction period and service period, the vertical displacement on the portside in both conditions is almost the same. However, the vertical displacement on the seaside in the service period shows an increase compared with that in the construction period, and the rotation angle decreases to a certain extent. The vertical displacement on the portside and seaside is 31.6cm and 21.1cm respectively, it can be seen that the differential settlement is quite large. Considering the length of bucket's lower part in axial direction (30m), a rotation of 0.2°occurred in the bucket. Therefore, it is possible to slip [27].

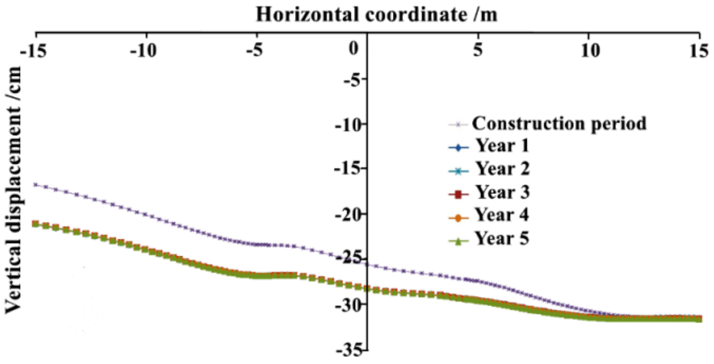

Fig.14-Distribution of vertical displacement along the horizontal direction of the top cover of bucket's lower part in-service period

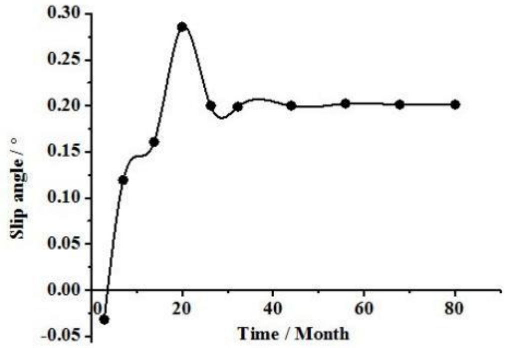

Fig.15-Changing curve of slip angle of the bucket

Stability analysis of the bucket under different working loads

The working load in the previous calculating is 50kPa, which is uniformly distributed over the structure and the backfilled silt. In this paper, the stability analysis is made under different working loads in service periods. In this paper, an exploratory analysis is made on the stability of the bucket under different working loads. It can be seen from Figure 16 to Figure 18 that the sliding angle of the bucket and the maximum displacement of both the upper part and the lower part of the bucket are concerned with working loads. The sliding angle of the bucket increases approximately linearly with working loads. The maximum horizontal displacement of the upper part and the lower part of the bucket grows with working loads, which shows a tendency to accelerate [28,29].

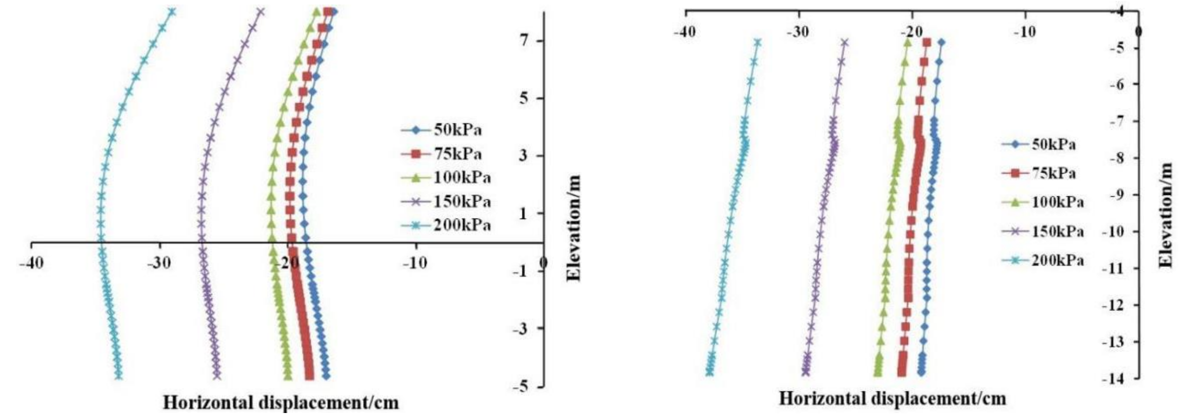

(a) Horizontal displacement of upper bucket (b) Horizontal displacement of lower bucket

Fig.16 - Horizontal displacement of the bucket under different working loads in service period

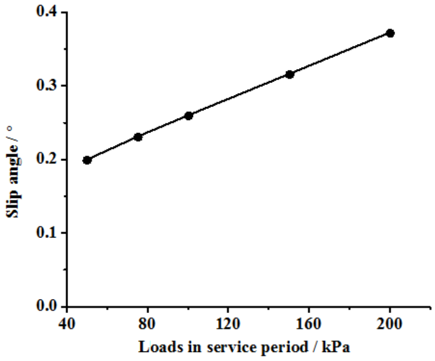

Fig.17 - Sliding angle of the bucket under different working loads in service period

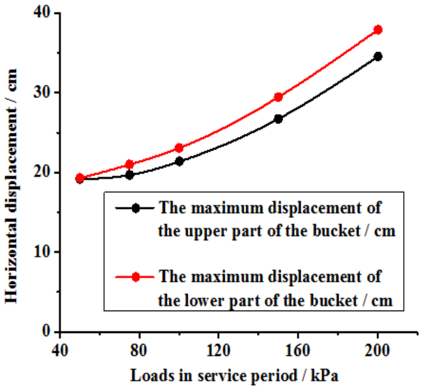

Fig.18 -The maximum horizontal displacement of the bucket under different working loads in service period

The working loads applied from above have an obvious influence on the horizontal displacement and the sliding stability of the bucket. The working loads in service period should be controlled properly according to the actual deflection indexes. In this way, the sliding of the structure caused by excess horizontal displacement and uniform settlement, which results from long-term overloading, can be avoided.

Distribution of plastic zones in soil mass during the service period

The distribution of soil plastic zone in the first and fifth years is shown in Figure 19. Figure 20 illustrates the distribution of shearing stress of the soil mass (1m below the end of the lower bucket) in service period. As can be seen from the figures below, the distribution of plastic zone in the soil during the service period does not expand significantly, it is mainly distributed in the soil below the bucket and the natural silt at the right side of the reinforced area by sand pile, without connecting with each other to form a sliding surface, and the shearing stress in the soil below the bucket is lower than the shearing strength [19, 30]. The average utilization rate of shearing strength is distributed between 0.4 and 0.9.

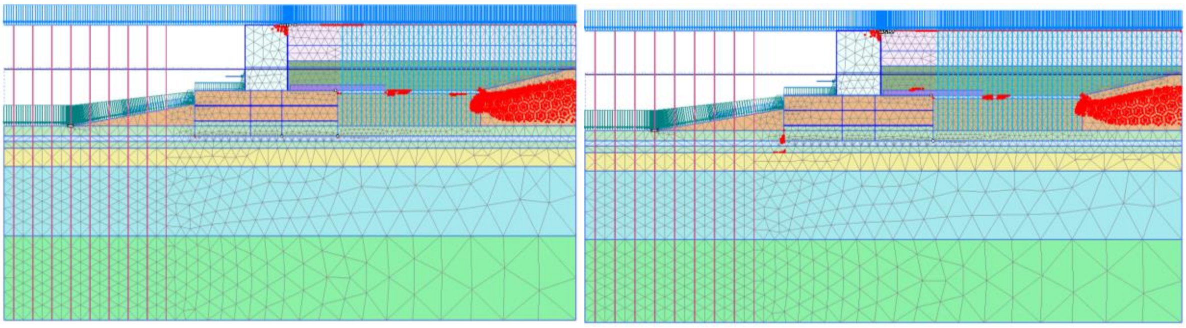

(a) The first year *(b) The fifth year*

Fig.19 - Distribution of plastic zones in soil mass in service period

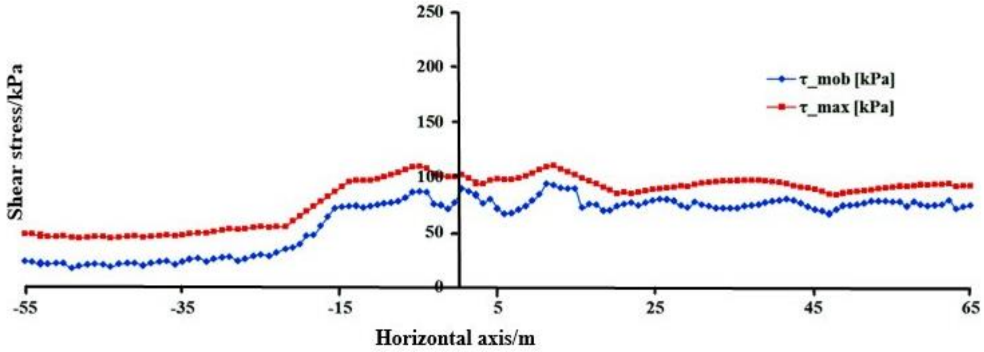

(a) Comparison of shearing stress τmob and shearing strength τmax of the soil mass

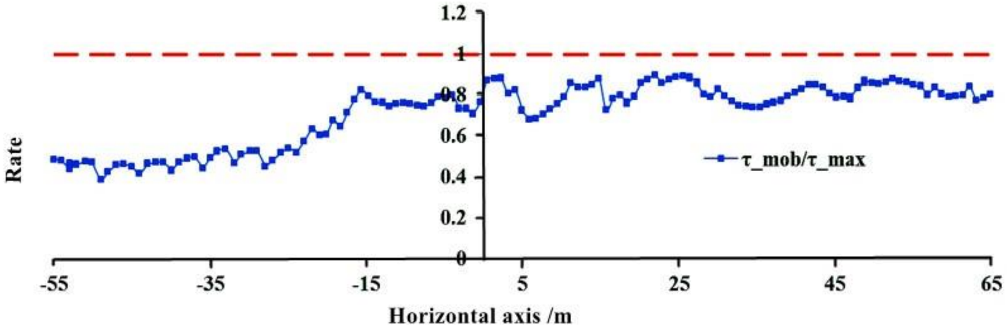

(b) Utilization rate of shearing strength of soil mass β=τmob/τmax

Fig.20 - Distribution of shearing stress of the soil mass below the bucket

CONCLUSION

The new bucket-based structure is proposed according to actual project in this study, the research results are mainly to solve application problems in engineering. Based on the numerical simulation and analysis of the interaction between bucket and soil during the service period, the conclusions can be drawn as below:

(1) During the service period, the horizontal displacement and vertical displacement of the bucket structure have a certain change comparing with the construction period, that is, various displacements decrease due to the rebound effect of the load reduction. However, the deformation tends to be stable due to the drainage consolidation effect of preloading, so the change is small. After 5 years of drainage consolidation, the maximum horizontal displacement of the upper bucket structure is 18.8cm and the horizontal displacement of the lower part reaches 19.2cm.

(2) The slippage degree of bucket structure is reduced compared with the construction period. The maximum vertical displacement of the bucket is 31.6cm in the service period, which occurs on the port side. The difference of the vertical displacement between the seaside and the portside of the bucket is 10.5cm, and the bucket rotates 0.2°, which is 0.08° less than that of the construction period.

(3) The working loads from above bucket have a significant influence on the horizontal displacement and sliding stability of the bucket in the service period. The slip Angle of the bucket increases with the increase of the working load linearly. The maximum horizontal displacement of the upper and lower bucket also increases and has a trend of accelerating increase. Therefore, it is suggested that the working loads in the service period should be controlled strictly according to the actual deformation control index of the bucket to avoid excessive horizontal displacement caused by long-term overload and structural sliding caused by uneven settlement.

(4) In the stable phase of the service period, the plastic zone of the soil in the lower part of the bucket does not form a through plastic shear zone, the shearing strength of the soil has not been fully utilized. The average utilization rate of the shear strength is distributed between 0.4-0.9, and the overall stability of the bucket foundation will not be damaged.

(5) It is recommended that the wharf's construction go after that of the bucket and the ground treatment behind the bucket, for it will help reduce the impact of the deflection of the soil caused by the bucket on the foundation of the wharf. Besides, it is best that the batter piles are furnished in the front of the wharf to stay away from the area of moving soil mass, for it helps to reduce the stresses caused by it.

(6) According to the actual monitoring data of the barrel structure, the displacement of the barrel is smaller than the result of the numerical calculation, the displacement trend is consistent, and the displacement is on the same order of magnitude. For the actual project, this error is within the allowable range of the project.

ACKNOWLEDGEMENTS

This research was funded by the Fundamental Research Funds of the Central Universities, grant number 2572018BJ15, and the Science and Technology Project of the Department of Transportation of Heilongjiang Province, grant number 2021HLJ01K42.

REFERENCES

[1] Wang, Y.Q. Some understandings in soft soil improvement in Tianjin Port. China Harbour Engineering 2006, 1, 6-19.

[2] Ding, J.H.; S.X.; G.Z. Theory and practice of deep waterway on silt coast in LianYungang (Preliminary basics). China Communications Press: Beijing, China, 2012.

[3] Wang, Y. Coastal and Marine sciences. Beijing: Science Press, 2016.

[4] Baerheim, M.; Hoberg, L.; Tjelta, T. I. Development and structural design of the bucket foundations for the Europipe jacket. Offshore Technology Conference, Houston, Texas, 1-4 May, 1995.

[5] Yu, Y.H.; T, S.L. Method of quick construction of wharf on weak soil. Journal of Ocean Technology 2006, 25, 122-126.

[6] Bye, A.; Erbrich,C.; Tjelta, T.I.Geotechnical design of bucket Foundations.TC7793,OTC'27,1995,869-883.

[7] Zhang, S.H.; Zheng, Q. A.; Liu, X. N. Finite element analysis of suction penetration seepage field of bucket foundation platform with application to offshore oil field development. Ocean Engineering 2004, 31(11): 1591-1599.

[8] WANG, Y. Z.; LU, X.; WANG, S. The response of bucket foundation under horizontal dynamic loading. Ocean Eng 2006, 33 (7), 964-973.

[9] Liu, Z.W.; Wang, J.H.; Qin, C.R. Research on the horizontal bearing capacity of bucket foundations. Chinese Journal of Geotechnical Engineering 2000,22(6),691-695.

[10] Cai, Z.Y.; Yang, L.G.; Guan Y.F.;Huang, Y.H. Numerical analysis of soil pressure on single bucket wall of new bucket foundation breakwater [J]. Hydro-Science and Engineering 2016, 16(5),39-46.

[11] Yang, H.D.; Yang, L.G. Computation method of anti-sliding stability of new bucket breakwater [J]. Port ＆Waterway Engineering. 2016, 26(4), 40-44.

[12] Ding, W.Q.; Z.hang, D.; Huang, H.W.; Li, W. Numerical study on the new bucket revetment foundation in the stages of construction and operation . Journal of Hydraulic Engineering 2015, 46 (S1), 343-348.

[13] Cao, Y.Z.; Yao, W.j.; Cheng, Z.K. Analysis of soil pressure and displacement on bucket-based structure under reclamation silt. Journal of Shanghai University (Natural Science Edition) 2019,25(2), 328-336.

[14] Byrne, B.W.; Houlsy, G.T. Experimental investigations of the cyclic response of suction caissons in sand. OTC12194, 2000: 787-795.

[15] Park, J. S.; Park, D.; Yoo, J. K. Vertical bearing capacity of bucket foundations in sand. Ocean Eng 2018, 121(1),453-456.

[16] Park, J. S.; Park, D. Vertical bearing capacity of bucket foundation in sand overlying clay. Ocean Eng 2017, 134(1),362-376.

[17] Wu, F.; Pang, D.G.; Zhang, Z. Fuzzy evaluation for durability of high-pile wharf in service. Port&Waterway Engineering 2013, (2),62-67.

[18] Li, W.; Cheng, Z.K. Design of bucket-based structure on silt coast. Port & Waterway Engineering 2015, 1, 42- 47.

[19] Liu, H.; Zhang, Q.; Ren, L. Mechanical Performance Monitoring for Prestressed Concrete Piles Used in a Newly-Built High-Piled Wharf in a Harbor with Fiber Bragg Grating Sensor Technology When Pile Driving. Appl. Sci 2017, 7 (5), 489.

[20] Wu,M.; Wang, L.; Xiang, X.H. Research and design of high-pile wharf on weak soil. Soil Engineering and Foundation 2009, 23,26-29.

[21] CCCC Third Harbor Consultants Co.,Ltd. Preliminary design of East Upright-breakwater in of Xuwei Port in Lian Yungang. Shanghai, 2012.

[22] Sun, D.P.; Yang, Z.L.; Zhu, Q.M. Experimental study on bearing capacity of bucket foundation model of intertidal platform. Petroleum Engineering Construction 1999, 2, 12-19.

[23] Liu, R.; Li B.R.; Ji, J.; Ding, H.Y. Bearing Characteristics of Pile-Bucket Composite Foundation for Offshore Wind Tubine. Journal of Tianjin University (Science and Technology) 2015, 48(5), 429-437.

[24] Wang, Y.; Lu, X.; Wang, S.; Shi, Z. The response of bucket foundation under horizontal dynamic loading. Ocean Eng 2006, 33, (7), 964-973.

[25] Zhang, X.; Gui, J. Study on stability of bucket foundation under backfill. 2018 International Conference on Civil and Hydraulic Engineering, Qingdao, China, 23–25 November, 2018, 2-6.

[26] Ding, H.; Zhao, X.; Le, C.; Zhang, P.; Min, Q. Towing Motion Characteristics of Composite Bucket Foundation for Offshore Wind Turbines. Energies 2019, 12 (19).

[27] Zhu, C.H. Computation of earth pressure on large diameter cylinder under service ultimate state. Chinese Journal of Geotechnical Engineering 2002,24(3) ,313-318.

[28] Chen, X.; Liu, T.; Jiang, Y.; Liu, H.; Kou, H.; Xu, J.; Liu, X.; Liu, J.; Ma, T.; Feng, T. J. M. G. Stability analysis of suction bucket foundations under wave cyclic loading and scouring. Mar. Georesour. Geotec 2018, 36(7),749-758.

[29] Liu, M.; Yang, M.; Wang, H. Bearing behavior of wide-shallow bucket foundation for offshore wind turbines in drained silty sand. Ocean Eng 2014, 82, 169-179.

[30] Feng, Y.R.; Wang, Y.B.; Gu, Y.J.; Zhang S.H.; Chu, X.J. Vertical Stability Simulation and Analysis for Single Bucket Foundation Platform. EJGE 2010, 36, 749-758.

Article no. 36

THE CIVIL ENGINEERING JOURNAL 3-2022

BEARING CAPACITY OF T BEAM UNDER DIFFERENT PRESTRESS LEVELS: FULL-SCALE EXPERIMENT AND FEM ANALYSIS

Long Liu and Jinyan Ma

Anyang Institute of Technology, the west end of Huanghe Avenue, Anyang 455000, China; email: 20160913@ayit.edu.cn

ABSTRACT

Insufficient prestress will cause cracks in the T beam, which will influence its stiffness and bearing capacity. This paper is devoted to studying the influence of prestress levels on the bearing capacity of the T beam and then judging its working state. A full-scale model experiment is carried out on the 13 meters prestressed concrete T beam. At the same time, a nonlinear finite element model is established and verified. The experimental results show the numerical simulation results are in good agreement with the experimental results. Finally, the finite element model is used to simulate the bearing capacity of T beams under different prestress levels. The mathematical relationship between prestress levels and bearing capacity is obtained based on the results of the finite element model. The relationships between the mid-span deflection and load of the experimental beam are the same under different prestress levels, including three stages: elastic stage, crack development stage, and failure stage. With the increase of the prestress levels, the stiffness of the experimental beam before cracking is improved significantly.

KEYWORDS

FEM, Prestressed concrete, T beams, Prestress levels, Full-scale experiment, Bearing capacity

INTRODUCTION

The prestressed concrete beam has the advantages of small structure height, convenient construction, reasonable force, good durability [1], and the micro-cracks generated after bearing load can be closed [2]. Therefore, it is a widely used structure type. However, a variety of reasons will cause the reduction of prestress, such as concrete shrinkage and creep, anchor end shrinkage, broken wire, etc. The removal of prestress will lead to the decrease of prestress level, which may have a harmful effect on its bearing capacity. Up to now, there has been no quantitative study on the relationship between the level of prestress and the bearing capacity of prestressed concrete beams.

Ardalan et al. [3] found that only when a certain prestress level is exerted on the beam can the micro-cracks be closed, thereby increasing its fatigue life. However, in practical engineering, due to insufficient tensioning of steel bars, delayed grouting, poor filling, and steel bar corrosion fatigue. There exists deviation between actual and designed prestress [4-5]. Liu et al. [6] found the actual prestress was only 40% to 50% of the theoretical design values in prestressed concrete bridges by detection, which had a significant impact on the compressive stress reserves of the lower edge concrete [7], such as the premature appearance of cracks [8]. On the one hand, the aesthetics of the bridge will be influenced because of the formation of cracks, on the other hand, it will cause a reduction of the cross-sectional stiffness of the bridge, and the typical feature is a more significant beam deflection [9-11]. At the same time, cracks caused by insufficient prestress have a significant impact on the working condition and bearing capacity of the bridge [12-13]. The

DOI 10.14311/CEJ.2022.03.0036

damage stiffness assessment method was established by Zhao et al. [14] based on the characteristics of flexural cracks. The results showed that after cracking of prestressed concrete, the section stiffness would have rapid attenuation, and the bearing capacity would be reduced obviously.

The prestress level has a significant impact on the bearing capacity of prestressed concrete beams, so it is necessary to study the prestress influence to judge the working state of the bridge accurately. Conducted static load tests were carried out by Jure et al. [15] on partially prestressed concrete beams and fully prestressed concrete beams under different prestress levels. It was found that by increasing the prestress level, the service state and bearing capacity of the beams could be improved. Through experimental comparison, Guo et al. [16] found the bearing capacity and section stiffness were greatly increased, and the crack width was significantly reduced after the prestressed reinforcement of reinforced concrete beams. In addition, the higher the prestress levels were, the better the reinforcement influences would be. An experimental research was carried out on the cracked unbonded prestressed concrete beams by Han et al. [17], the results showed that when prestress levels increased, the stress of the tensile reinforcement and the deflection of the control section reduced significantly, and the flexural rigidity of the cracked section increased obviously.

In recent years, various commercial finite element analysis software has provided better analytical methods for evaluating the bearing capacity of prestressed concrete complex structures [18]. The nonlinear finite element model was established by Hu et al. [19] using the finite element analysis software ABAQUS, the accuracy and reliability of the model were verified through the experimental results, and the model was also used to study the mechanical properties of prestressed concrete (PC) beams reinforced with CFRP. Simulation and analyses were made to the whole process of three externally prestressed supported beams from loading to failure by Qin et al. [20] with ABAQUS. The results showed the nonlinear finite element analysis software could simulate the beam better. Meng et al. [21] conducted experiments on the flexural performance of 14 prestressed steel-ultra-high-strength concrete composite beams, and made numerical simulation calculations with ANSYS software. The results showed the calculated values were in good agreement with the experimental values among the three elements of cracking load, yield load, and ultimate load of the experimental beams, which verified the correctness of the finite element model. Anil et al. [22] used ABAQUS to model the culvert with a three-dimensional shell element and solid element. They made a comparison between the load-deflection curve obtained by the finite element model and the experimental results. The two curves showed a high consistency, and the finite element model could predict the location of cracks accurately. Wu et al. [23] studied the impact of the prestress levels on the bearing capacity of bridges by using the theory of three-dimensional entity degradation virtual laminated unit. They found that different prestress levels had a significant impact on the bearing capacity of bridges. Mohammadali et al. [24] made a proposition of three-dimensional nonlinear finite element method by conducting four-point loading experiments on five beams with different prestress levels to make simulations of the nonlinear behaviors of the experimental beams, and the bearing capacity of the beams increased obviously with the increase of the prestress levels. Gao R. et al. [25] carried out loading experiments, and ANSYS software simulations on RC beams strengthened by external prestressing and concluded that the higher the prestress levels are, the greater the bearing capacity of the reinforced beams will be.

The relationship between the prestress levels, and the bearing capacity of T beams is seldom discussed in existing literature, and most of them are qualitative analyses; quantitative research is blank. Therefore, to study the relationship between different prestress levels and the bearing capacity of T beams, a full-scale T beam model with a length of 13 meters is made. At the same time, nonlinear finite element analysis software MIDAS/FEA [26] is used for numerical simulation. The accuracy of finite element analysis results is verified by comparing with experimental results. The load-deflection curve of T beams under different prestress levels is figured out by the finite element model. Then the mathematical expression of the relationship between prestress levels and bearing capacity is obtained by fitting.

Experiment description

Specimen Preparation

The experimental beam is a full-scale model of a prestressed concrete T-beam made under the guidance of China's "Code for Design of Highway Reinforced Concrete and Prestressed Concrete Bridges and Culverts" (JTG 3362-2018) [27]. The geometric dimensions and reinforcement layout of the experimental beam are shown in Figure 1, and the characteristics of steel bars and concrete materials used in the experimental beam are shown in Table 1 and 2.

The experimental beam is prestressed by the post-tensioning method, the design tensile stress is 500MPa, and the prestress level is [6].

The prestress level is defined as Equation (1).

$$\alpha = \frac{\sigma_1'}{\sigma_1} \times 100\% \tag{1}$$

In Equation (1), the theoretical tensile control stress (σ_1') is 1395MPa, and the actual tensile stress is 500MPa.

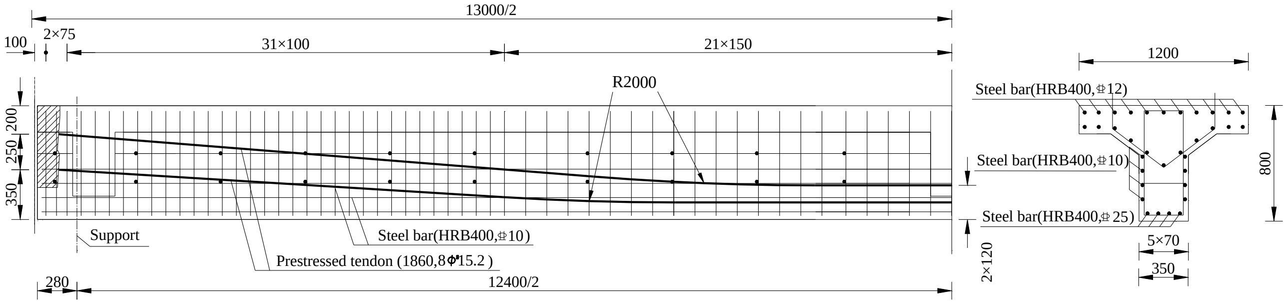

Fig. 1 - Geometric dimension and steel bar layout of the experimental beam (mm)

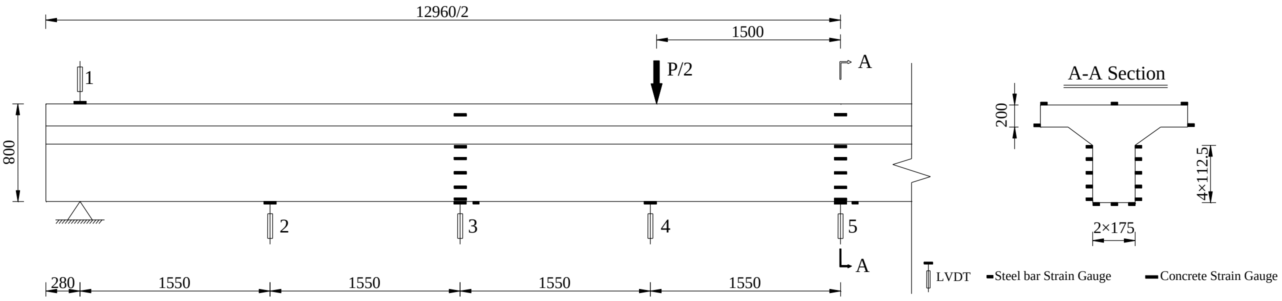

Fig. 2 - Layout of loading position and measuring point of the experimental beam (mm)

Tab. 1: Material Properties of Steel Bar

Type	Steel bar			Prestressed Tendon
	Ø10	Ø12	Ø25	$\emptyset^s$15.2
f_y(MPa)	403.5	412.4	422.1	-
f_u(MPa)	572.2	570.3	568.6	1879.4
E_s(MPa)	2.0×10^5	2.0×10^5	2.0×10^5	1.95×10^5

Tab. 2: Material Properties of Concrete

Item	f_{cu}(MPa)	f_t(MPa)	E_c(MPa)	v
Value	52.3	3.21	3.47×10^4	0.2

Experimental procedure and measuring points

Two loading points are arranged 1.5 meters away from the middle span of the experimental beam, and the load is exerted step by step through jacks. During the loading processes, the deflection and strain of the experimental beam are paid close attention. The loading position and measurement point layout are shown in Figure 2.

Nonlinear finite element analysis

MIDAS/FEA nonlinear finite element software is used to build the experimental beam, and the bearing capacity of the experimental beam under different prestress levels is studied. The model details are consistent with the experimental beam described in the following section. The concrete is simulated by adopting hexahedral units. Different prestress levels are simulated by modifying the tensile stress at both ends of the prestressed tendon.

Concrete constitutive model

In the numerical analysis of prestressed concrete structures, the constitutive model of concrete has an important impact on the calculation results [28]. The total strain crack model in MIDAS/FEA is adopted in this paper [29]: After the concrete cracks, cracks develop along the cracking direction and will not change with the main tensile strain direction. Figure 3(a) is the schematic diagram of the model. The constitutive relationship of concrete under compression and tension are shown in Figure 3(b) and (c). The shear stress of concrete is constant. That is, the shear stress and shear strain have a multiple linear relationship with the concrete stiffness. According to the research results of Zuo et al. [30] on shearing failure components, this paper selects =0.5, which is shown in Equation (2):

$$\tau = (\beta G)\cdot\gamma = (0.5G)\cdot\gamma \tag{2}$$

Steel bar constitutive model

The implantable rod units simulate steel bars and prestressed tendons [28]. The steel bars have no degree of freedom and are completely bonded to the concrete elements without relative slippage. After the definition of the steel bar information, the program automatically calculates the intersection point between the concrete units and the steel bars, thus adding the stiffness of the steel bars to the stiffness of the concrete units, and calculating the strain of the steel bars from the deflection of the concrete units. The Von Mises model [31] is adopted for the constitutive model of the steel bars, and the constitutive relation is shown in Figure 4.

Figure 5 shows the finite element model of the experimental beam.

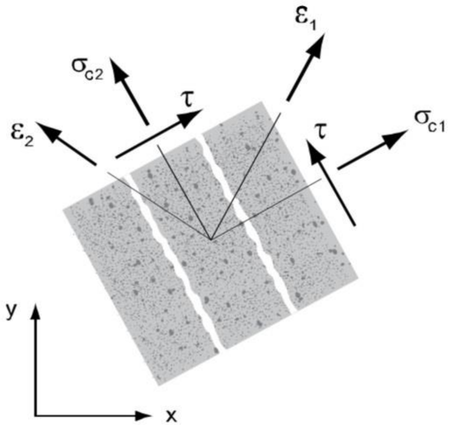

(a) Total Strain Crack Model

(b) Fig. 3 - Concrete constitutive model

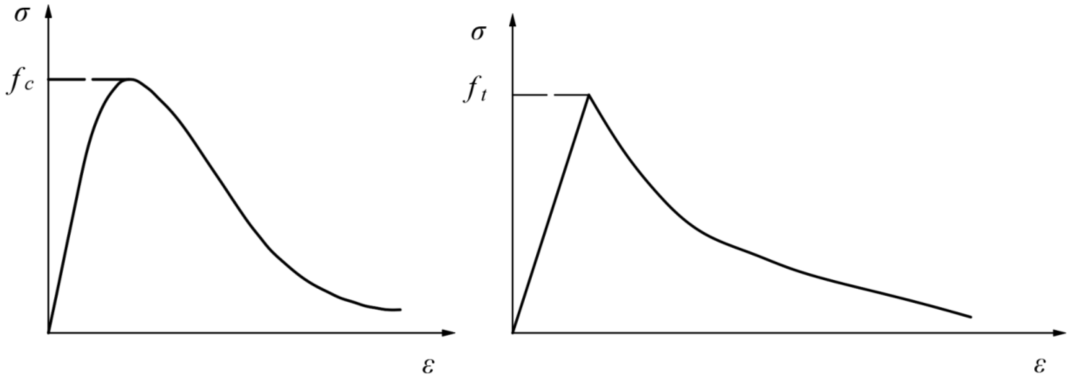

(b) Compressive stress vs. Inelastic strain *(c) Tensile stress vs. Cracking strain*

Fig. 3 - Concrete constitutive model

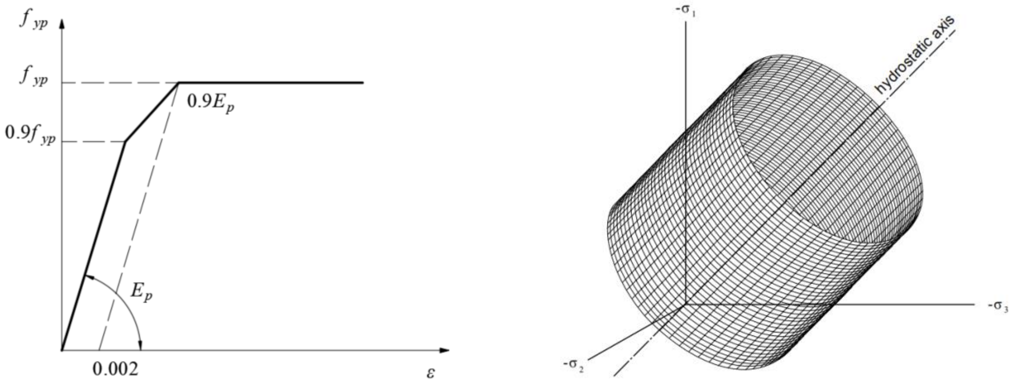

(a) Stress-strain curves for steel bars. *(b) Von Mises yield surface in principal stress space*

Fig. 4 - Steel bar constitutive model

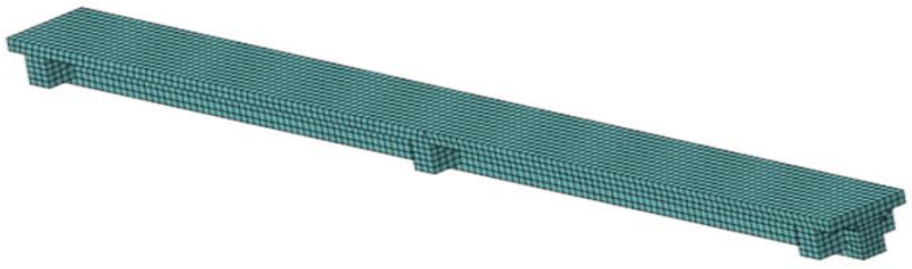

Fig. 5 - Nonlinear finite element model

Results and discussion

Model validation

During the experiment, data such as the deflection of the experimental beam, and the strain of concrete and steel bars are collected. The accuracy of the finite element model is verified by comparing the deflection and strain data of the experimental beam and the finite element model under the same loading conditions [32]. Figure 6 shows the comparison between the measured deflection and strain data with the finite element calculation results during the loading process. The measured strain data gradually become invalid due to exceeding the strain gauge range during the loading process.

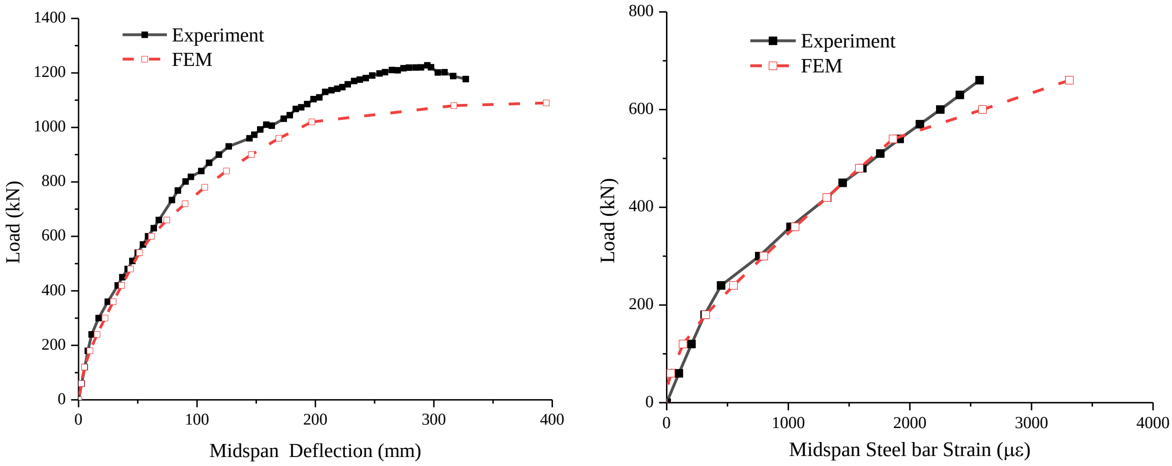

(a) Load-deflection curves *(b) Load-strain curves of lower edge*

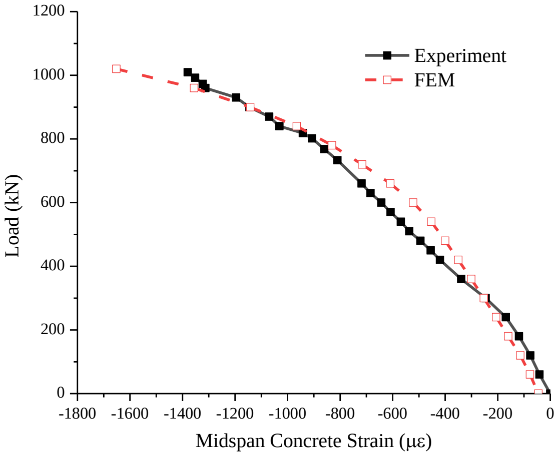

(c) Load-strain curves of concrete at the upper edge

Fig. 6 - Comparison of measured data and finite element results

It can be seen from Figure 6 the finite element calculation values of the deflection of the experimental beam, the tensile strain of the steel bar, and the compressive strain of the concrete at the upper edge are in good agreement with the experimental values. The measured ultimate loading of the experimental beam is 1227.8kN, and the ultimate loading is predicted to be 1088.8kN by the finite element model. The difference between the expected failure loading and the measured value is 11.32%. The error may be caused by simplifying the finite element model, the deviation between the actual deformation of concrete and steel bar materials, and the finite element constitutive model. Considering the unevenness of the concrete materials, the corresponding error is within the acceptable range. According to Li et al. [32], when the calculated finite element values are in good agreement with the measured values, the results of the finite element model can be extrapolated to make reasonable predictions.

Bearing capacity prediction

To study the relationship between the prestress levels and the bearing capacity of the experimental beam, the bearing capacity is calculated when the tensile stress of the prestressed tendon varies from 100 MPa to 1400 MPa. The corresponding prestresses levels changes from 7.2% to 100.4%. The details are shown in Table 3.

Tab. 3: Different prestress levels

Tensile stress(MPa)	100	200	300	400	500	600	700	800	900	1000	1100	1200	1300	1400
Prestress levels (%)	7.2	14.3	21.5	28.7	35.8	43.0	50.2	57.4	64.5	71.7	78.9	86.1	93.2	100.4

Load-deflection curves

The load-deflection curves of the experimental beam under various loadings can be obtained by solving the finite element model under different prestress levels, as shown in Figure 7.

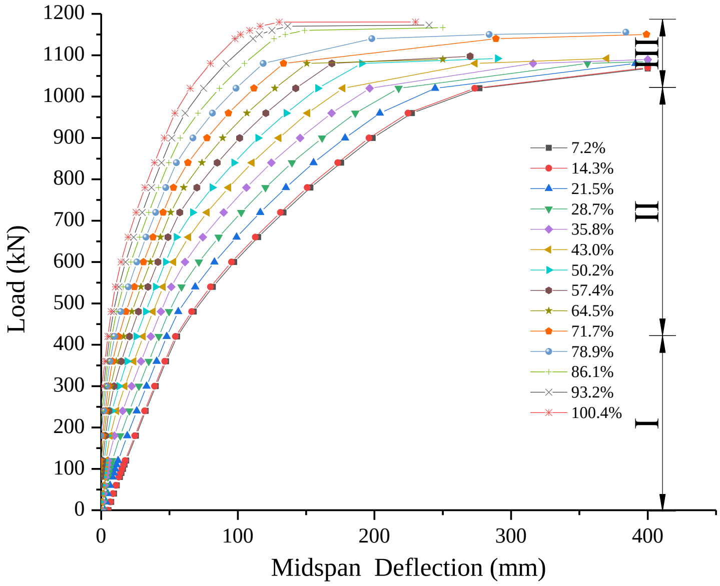

Fig. 7 - Load-deflection curves under different prestress levels

It can be seen from Figure 7 that the load-deflection curves change gently under different prestress levels. With the increase in loading, the deflection of the experimental beam can be divided into three distinct stages: Ⅰ is the elastic stage, in which the deflection of the experimental beam increases linearly with the increase of the loading, and the rigidity remains the same. With the increase of the prestress levels, the length of the elastic stage gradually increases; Ⅱ is the crack development stage, during which the deflection of the experimental beam increases nonlinearly with the loading increase. Since the concrete at the bottom of the experimental beam cannot continue to bear the tensile stress due to cracking, the slope of the curve gradually decreases at this time, which means, the stiffness of the experimental beam decays faster after cracking; Ⅲ is the destruction stage, in which the loading increases slowly, but the deflection increases rapidly. With the rise of prestress levels, the mid-span deflection of the beam decreases during the destruction.

The slope of the load-deflection curve represents the stiffness of the beam. Before the experimental beam cracks, the stiffness is linearly related to the prestress levels. After the appearance of the cracks, the curve slope changes at different prestress levels are the same. It can be seen the stiffness of the experimental beam before cracking is improved with the increase of prestress levels.

The relationship between prestress levels and bearing capacity

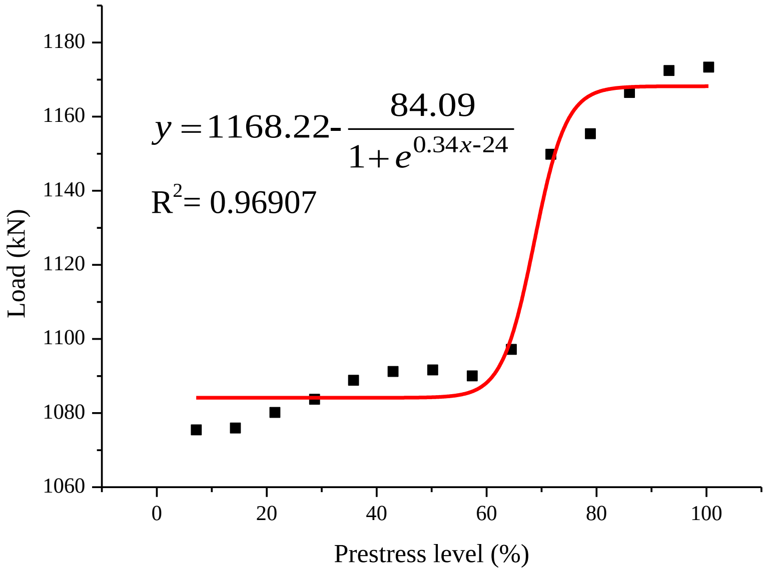

Fig. 8 - The curve of the relationship between prestress levels and bearing capacity

As seen in Figure 8, when the prestress level increases from 7.2% to 14.3%, the bearing capacity has barely increased. When the prestress level increases from 21.5% to 64.5%, the bearing capacity increases from 1069.4kN to 1097.18kN. When the prestress level increases to 71.7%, the bearing capacity increases to 1149.86kN significantly, with an 8% increase. After that, the bearing capacity increases linearly with the increase of prestress levels. This rule is consistent with the conclusion of Gao et al. [25], that is, when the prestress level is low, changing the tension control stress has little effect on the bearing capacity. Through data fitting, the mathematical relationship between prestress level and bearing capacity obtained is shown in Equation 3:

$$y=1168.22-\frac{84.09}{1+e^{0.34x-24}} \tag{3}$$

CONCLUSION

Based on the full-scale model experiment, the accuracy of the finite element model is verified, and the relationship between prestress levels and bearing capacity is discussed. The conclusions are as follows:

(1) The finite element model is in good agreement with the experimental beam. Based on the results of the finite element model, the mathematical relationship between prestress levels and bearing capacity is obtained.

(2) Under different prestress levels, the mid-span deflection curves of the experimental beams are alike, which can be divided into three stages: elastic stage, crack development stage, and destruction stage.

(3) With the increase of the prestress levels, the stiffness of the experimental beam before cracking is significantly improved. After the cracking, the trend of the slope of the curves under different prestress levels is the same.

ACKNOWLEDGEMENTS

This study is supported by two key funds: 1) Science and technology planning project of Anyang, Henan Province, China (2022C01GX038); 2) Science and technology planning project of Henan Province, China (222102320040).

REFERENCES

[1] Zhang, W., Liu, X. and Gu, X. (2016), “Fatigue behavior of corroded prestressed concrete beams”, Construction and Building Materials , Vol. 106, pp.198-208.

[2] Zhou, X. and Feng, X. (2011), “Experimental research on crack width of retard-bonded partially prestressed concrete T beam”, Highway Traffic Technology, Vol. 28 No. 1, pp. 56-61.

[3] Ardalan, H., Elyas, G., Masoud, M., Alain, N. and Zhao, X. (2017), “Mode I fatigue crack arrest in tensile steel members using prestressed CFRP plates”, Composite Structures, Vol. 178, pp. 119-134.

[4] Li, Y., Fu, D. and Deng, X. (2020), “Application of stress test technology under anchor in continuous rigid frame bridge construction”, Highway, Vol. 65 No. 2, pp. 120-124.

[5] Yan, L., Li, Y. and He S. (2017), “Statistical investigation of influenceive prestress in prestressed concrete bridges”, ASCE-ASME Journal of Risk and Uncertainty in Engineering Systems, Part A: Civil Engineering , Vol. 3 No. 4, pp. 1-8(06017001).

[6] Liu, F. and Zhang, Y. (2018), “Application of influenceive prestress detection in strengthening bridge structure”, Highway Traffic Technology (Applied Technology Edition), Vol. 14 No. 9, pp. 230-231+275.

[7] Zhou, J., Tan, S., Tan, H., Lv, Y., Teng, G. and Liu, B. (2018), “Experimental study on improved structure of prestressed concrete T-beam simply supported variable continuous negative moment section”, Foreign Highway, Vol. 38 No. 4, pp. 89-95.

[8] Jörg, F., Anne, T. and Guido, D. (2006), “System identification and damage detection of a prestressed concrete beam”, Journal of Structural Engineering, Vol. 132 No. 11, pp. 1691-1698.

[9] Lv, Z. and Pan, Z. (2010), “Several problems in the design of large span prestressed concrete box girder bridge”. China Civil Engineering Journal, Vol. 43 No. 1, pp. 70-76.

[10] Liu, C. and Xu, D. (2009), “Reasons for shear cracking and deflection of large span concrete box girder bridge”, Journal of Tongji University(Natural Science Edition), Vol. 37 No. 1, pp. 1-5.

[11] Deng, L., Ghosn M., Znidaric A., and Casas, J. (2001), “Nonlinear flexural behavior of prestressed concrete girder bridges”, Journal of Bridge Engineering, Vol. 6 No. 3, pp. 276-284.

[12] Peng, B. (2000), “Cause analysis and treatment countermeasures of cracks in highway prestressed concrete beam bridge”, Proceedings of the 2000 Annual Conference of China Association for Science and Technology, p. 840.

[13] Zhang, G., Li, D., Xie, J. and Pan B. (2017), “Cause analysis and treatment of vertical cracks in webs of prestressed concrete T-beam bridges”, Highway Traffic Technology (Applied Technology Edition), Vol. 13 No. 1, pp. 12-14.

[14] Zhao, Y., Zhou, B. and He, S. (2011), “Damage stiffness evaluation method of PC simply supported beam based on crack characteristics”, Journal of Chang'an University(Natural Science Edition), Vol. 31 No. 4, pp. 39-44.

[15] Jure, R., Radoslav, M., Dragan, Ć. and Nikola, G. (2016), “Experimental testing of concrete beams with different levels of prestressing”, Proceedings of the Institution of Mechanical Engineers, Part L: Journal of Materials: Design and Applications, Vol. 230 No. 3, pp. 760-779.

[16] Guo, J., Deng Z., Lin J. and Lu H. (2012), “Experimental research on strengthening of reinforced concrete slabs with stressed high strength steel stranded wire mesh”, China Civil Engineering Journal, Vol. 45 No. 5, pp. 84-92.

[17] Han, Z., Guo, W., Liu, Z., Zhang G. and Guo, X. (2016), “Experiment on the influence of prestress on the flexural rigidity of prestressed concrete beams”, Journal of China Highway, Vol. 29 No. 7, pp. 103-109.

[18] Meng, S, Wu, C., Xiong, J. and Zhou, Z. (2009), “Discussion on related issues of nonlinear finite element analysis of prestressed concrete complex structure”, Industrial Building, Vol. 39 No. 12, pp. 1-4.

[19] Hu, L., Ju, P. and Zhang J. (2019), “Numerical simulation of partially prestressed concrete beams strengthened with CFRP sheets based on ABAQUS”, Seismic Engineering and Reinforcement, Vol. 41 No. 2, pp. 67-72+79.

[20] Qin, H., Zhao, Y. and Jin, L. (2010), “ABAQUS nonlinear finite element analysis of externally prestressed concrete simply supported beams”, Foreign Highway, Vol. 30 No. 5, pp. 158-161.

[21] Meng, G., Jia, Q. and Zhu, W. (2014), “Experimental study on flexural performance of prestressed steel super high-strength concrete beams”, Engineering Mechanics, Vol. 31 No. 5, pp. 203-210+217.

[22] Anil, K., and Ali A. (2009), “Finite-element modeling and analysis of reinforced concrete box culverts”, Journal of Transportation Engineering, Vol. 135 No. 3, pp. 121-128.

[23] Wu, G., Lin, W., Wang, J., Jia Y. and Xiang Y. (2013), “Study on the influence of influenceive prestress on the ultimate bearing capacity of long-span p.c. bridges”, Journal of Computational Mechanics, Vol. 30 No. 3, pp. 362-369.

[24] Mohammadali, R., Inês, C., and Joaquim, B. (2014), “Influence of level of prestress on NSM CFRP laminates for the flexural strengthening of RC beams”, Composite Structures, Vol. 116 No. 9, pp. 489-500.

[25] Gao, R., Wu, G., Le, Y., Gao, Z. and Yang, J. (2017), “Test on the mechanical performance of RC beams strengthened by external prestress”, Journal of China Highway, Vol. 30 No. 10, pp. 69-80+136.
[26] Beijing Midas Technology Co., Ltd. (2005), Midas FEA analysis and calculation principle, Beijing Midas Technology Co., Ltd., Beijing.
[27] China Communications Highway Planning and Design Institute, (2018), Design code for highway reinforced concrete and prestressed concrete bridges and culverts, China Communications Press, Beijing.
[28] Zhang, H. (2013), “Analysis and research on bridge reinforcement influence using Midas FEA”, Master thesis of Changan University, Xi'an.
[29] Li, Q., Liu, H., Ling T., Gui, X. and Wang, Z. (2019), “Research on repair mechanism of box girder concrete glue injection based on total strain crack constitutive”, Journal of China Three Gorges University (Natural Science Edition), Vol. 41 No. 5, pp. 70-73.
[30] Zuo, X., Ye, X. and Yang, Q. (2009), “Shear force transfer coefficient and its numerical experiment in reinforced concrete nonlinear finite element”, Building Structure, Vol. 39 No. 3, pp. 14-16+33.
[31] Song, W. and Song, W. (2017), “Nonlinear analysis of external prestressed reinforcement of PC box girder”, Journal of Chongqing Jiaotong University (Natural Science Edition), Vol. 36 No. 6, pp. 1-10.
[32] Li, L., Zhang, Z. and Lv, Y. (2016), “Experimental study on flexural bearing capacity of prestressed concrete T-beams and Ansys numerical simulation”, Foreign Highway, Vol. 36 No. 3, pp. 183-188.

Article no. 37

THE CIVIL ENGINEERING JOURNAL 3-2022

STUDY ON TIME-DEPENDENT OF BEARING CAPACITY OF OFFSHORE LARGE-DIAMETER MONOPILES

Suchun Yang[1 2], Qiang Chen [2], Shean Bie [1] and Fubo He [2]

1. *Tianjin University, School of Civil Engineering, Tianjin; China; e-mail：18560609732@qq.com*
2. *Tianjin Port and Channel Engineering Co., Ltd., Tianjin, China*

ABSTRACT

To improve the accuracy of predicting the bearing capacity of offshore large-diameter monopiles, the initial high strain detection and repeated high strain detection with an interval of 10-84 days were carried out on 6 large-diameter monopiles with a diameter of 7.2m-7.4m in the offshore wind field dominated by clay soil layer. The results show that the time-dependent increment of tip resistance, side resistance and the total resistance of large-diameter monopiles in the same offshore wind farm has great discreteness, and the axial force increment of monopiles has a consistent change trend. This paper puts forward the prediction interval of 95% guarantee rate of bearing capacity increment of the offshore large-diameter monopiles based on depth, which provides a basis for the design of large-diameter monopiles.

KEYWORDS

Offshore, Large diameter, Monopiles, Side resistance, Time-dependent

INTRODUCTION

As the most common foundation type of offshore wind turbine [1], large-diameter monopiles are widely used in sea areas where the sea depth does not exceed 35m. Large-diameter monopiles can only be driven by a hammer with high strike energy. The process of driving monopiles by hammer with high strike energy will weaken the soil around the pile. The high strain detection after the monopiles reach the design elevation can only obtain a small bearing capacity, and there is often no effective bearing capacity near the pile head. Offshore strata often have thick weak layers, and offshore monopiles need to be embedded at great depth in the mud to meet the requirements of bearing capacity. They often cross several soil layers, and the calculation of bearing capacity is cumbersome. After the rest period, the high strain detection of monopiles requires the ship to be stationed again, which is difficult and costly. The mechanical properties of offshore monopiles from driving to using are different from those of onshore small-size piles, and their time effect also shows great differences [3]. Existing research results [4-8] are difficult to meet the needs of engineering practice. In particular, the design basis for monopile bearing capacity in API and DNV specifications[9, 10] are derived from the test data of small-diameter pile foundation [11, 12], and the size effect significantly affects the bearing capacity of pile foundation [13], which is not well applicable to large-diameter monopiles.

TEST OVERVIEW

The test site is the No. 4 offshore wind farm in the south of the Shandong Peninsula, located in the sea area in the south of Haiyang City, Shandong Province, with an offshore distance of about 30km. The seabed terrain changes gently with a water depth of 29-31m. The surface layer of foundation soil in the site area is mainly muddy silty clay, silty clay and silty soil. The survey conditions and static cone penetration parameters of the test pile base are shown in Table 1.

DOI 10.14311/CEJ.2022.03.0037

High strain detections were carried out immediately after 6 large-diameter monopiles were hammered and sunk, and high strain detections were carried out after a certain rest period, as shown in Figure 1. Among them, 4 large-diameter monopiles obtained a relatively complete pile shaft force distribution curve, and the pile shaft parameters are shown in Table 2.

Tab. 1: Geological parameters of the test site

Monopile 1			Monopile 2			Monopile 3			Monopile 4		
Soil layer	Bottom height/ m	Side friction /kPa	Soil layer	Bottom height/ m	Side friction /kPa	Soil layer	Bottom height/ m	Side friction /kPa	Soil layer	Bottom height/ m	Side friction /kPa
Mud top	-29		Mud top	-30		Mud top	-30		Mud top	-31	
Muddy silty clay	-32	9	Muddy silty clay	-35	9	Muddy silty clay	-37	9	Muddy silty clay	-40	9
Silty clay	-33	21	Silt	-38	50	Silty clay	-39	21	Silt with sand	-42	53
Silt with sand	-36	53	Silty clay	-48	21	Sand with silt	-40	93	Sand with silt	-47	93
Silty clay	-45	21	Sand with silt	-50	93	Silt with sand	-41	53	Silty clay	-51	21
Silt with sand	-46	53	Silt with sand	-55	53	Silty clay	-50	21	Silt with sand	-53	53
Silty clay	-46	37	Sand with silt	-57	171	Sand with silt	-51	93	Silty clay	-60	37
Sand with silt	-49	93	Silt with sand	-58	53	Silty clay	-52	37	Silt with sand	-65	124
Silty clay	-56	37	Sand with silt	-62	171	Medium sand	-57	201	Silty clay	-69	52
Sand with silt	-57	171	Silty clay	-63	52	Silt with sand	-58	124	Silt with sand	-75	124
Silty clay	-58	52	Silt with sand	-67	124	Silty fine sand	-61	222	Silty clay with silt	-80	50
Medium sand	-59	201	Silty fine sand	-71	222	Silt with sand	-62	124	Pile tip	3.08 MPa	
Silty clay	-61	52	Pile tip	20.89 MPa		Silty clay with silt	-66	50			
Silt with sand	-64	124				Silt with sand	-67	125			
Silty fine sand	-65	222				Silty clay with silt	-73	50			
Silty clay	-67	52				Silt with sand	-75	125			
Silty fine sand	-68	222				Silty fine sand	-78	446			

Silty clay with silt	-72	50			Pile tip	31.47MPa		
Pile tip	3 MPa							

Fig. 1 – High strain detection of large-diameter monopile

Tab. 2: Monopile parameters

Monopile No.	Length/m	Mud elevation/m	Pile tip elevation/m	Penetration depth/m	Pile diameter /m	Pile tip thickness /mm	Pile tip area / m^2
1	84	-28.65	-72	43.35	7.2	70	1.57
2	81	-29.8	-69	39.2	7.2	70	1.57
3	88	-30.5	-76	45.5	7.4	72	1.66
4	88	-30.8	-76	45.2	7.2	70	1.57
5	92	-29.9	-80	50.1	7.4	70	1.61
6	86.5	-30.5	-74.5	44	7.2	70	1.57

TEST RESULTS AND ANALYSIS

After the initial driving high strain detections of No. 1-6 piles were completed, the repeated driving high strain detections were carried out at an interval of 10d-84d. The change of monopiles bearing capacity is shown in Table 3. The results of the literature [14] show that most of the bearing capacity of offshore monopiles can be recovered within 24h. The bearing capacity data in Table 3 shows that when the rest period exceeds 10d, the increase of pile tip resistance, pile side resistance and total bearing capacity does not increase with time, which is consistent with the research results in the literature [14].

Tab. 3: Bearing capacity of monopiles

Pile No.	Stage	Pile side resistance /kN	Pile tip resistance /kN	Total resistance /kN	Side resistance increment /kN	Tip resistance increment /kN	Total resistance increment /kN	Side resistance growth rate /%	Tip resistance growth rate /%	Total resistance growth rate /%	Rest period /d
1	Initial	7685	10064	17749	22807	6006	28813	297	60	162	34
	Repeated	30492	16070	46562							
2	Initial	19514	10014	29528	12780	6351	19131	65	63	65	31
	Repeated	32294	16365	48659							
3	Initial	23047	7898	30945	17073	5406	22479	74	68	73	10
	Repeated	40120	13304	53424							
4	Initial	18171	3926	22097	25821	2040	27861	142	52	126	18
	Repeated	43992	5966	49958							
5	Initial	19060	6527	25587	38147	910	39057	200	14	153	54
	Repeated	57207	7437	64644							
6	Initial	22243	6328	28571	29182	923	30105	131	15	105	84
	Repeated	51425	7251	58676							

Time-dependent tip resistance

When the pile tip is in the silty fine sand layer, the growth rate of pile tip resistance is relatively consistent. Table 3 shows that the pile tip resistance increases by 63%-68% after the 10d-31d rest period.

Similarly, the growth rate of pile tip resistance also shows a similar law when the pile tip is in silty clay mixed with silty, and the pile tip resistance increases by 52%-60% after the 18-34 day rest period.

From the perspective of soil bearing capacity, silty clay, silty clay mixed with silt, and silty soil mixed with silt are enhanced in turn. The soil layer at the pile tip of the No. 6 pile is silty soil mixed with silt, but the pile tip resistance is only increased by 15% after the 84-day rest period, which is far lower than the 52% increase in the 18-day rest period of No. 4 pile. According to the bearing capacity of the soil, the restoring capacity of soil can not be well judged.

Time-dependent side resistance

It can be seen from Table 1 that more than 75% of the stratum where the test pile is located is the clay soil layer, the side resistance of the No. 3 pile increases by 74% in 10d, and the total friction of No. 1 pile increases by 297% in 34d. This difference in increase is not caused by time accumulation, but due to the weakening of soil around the pile caused by heavy blows, or even the occurrence of liquefaction. Whether the weakening range of soil around the pile is concentrated at the pile tip, there is no definite answer for large diameter monopiles. The recovery value of the pile side resistance can quantify the degree of weakening of the soil around the pile. The recovery value of the side resistance of each section is shown in Table 4.

Tab. 4: Recovery value of side resistance of each section of piles

Pile shaft section	No. 1 pile/kN	No. 2 pile/kN	No. 3 pile/kN	No. 4 pile/kN
1/4	7978	3005	3834	3653
2/4	7667	2135	2713	2363
3/4	4994	2819	4608	4612
4/4	2167	4820	5919	7550

It can be seen from Table 4 that the peak value of side resistance recovery is uncertain in a certain section, indicating that the impact energy during pile sinking can be dispersed in the soil around the whole pile.

Time-dependent total resistance

It can be seen from Table 3 that the increase of total resistance after 10d-84d rest period is 65%-162%, and the soil layer in the same wind farm is relatively uniform, but the increase of total resistance of large-diameter monopiles fluctuates greatly, which is due to the large difference in residual bearing capacity of each pile position after initial driving. The axial force of No. 1-4 piles during initial driving and repeated driving is shown in Figure 2. According to Table 3, the total resistance of No. 1 pile after initial driving is 17749kN, while the total resistance of No. 3 pile is 30945kN, with a large difference. The number of hammers and the hammering energy used in the process of pile sinking are mainly determined by factors such as the nature of the stratum, the self-weight of the pile body, hammering equipment, etc. even if the same wind farm and different pile positions will have the phenomenon of pile sliding and hammer refusal, which also makes it difficult to quantify the weakening of the soil around the pile.

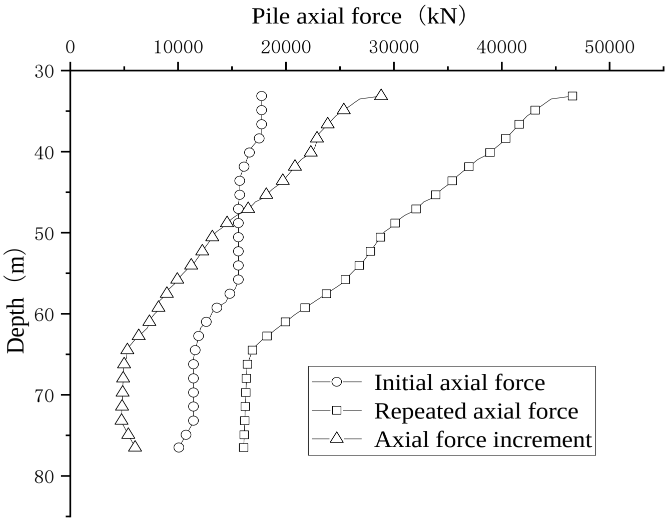

（1）No. 1 pile

Fig. 2 – Initial driving and repeated driving of axial force

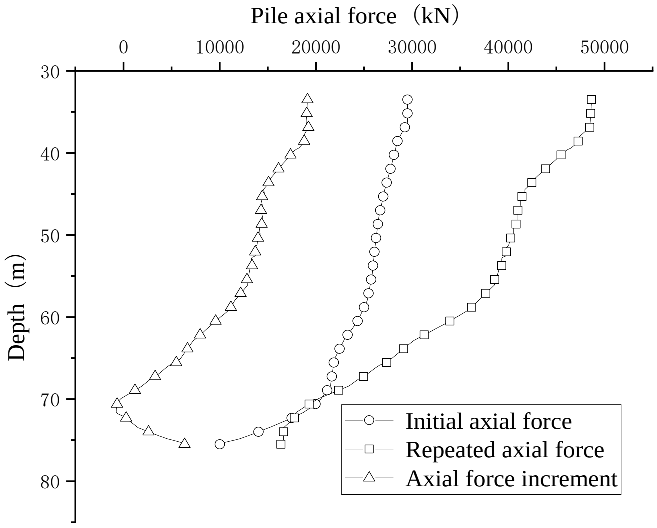

（2）No. 2 pile

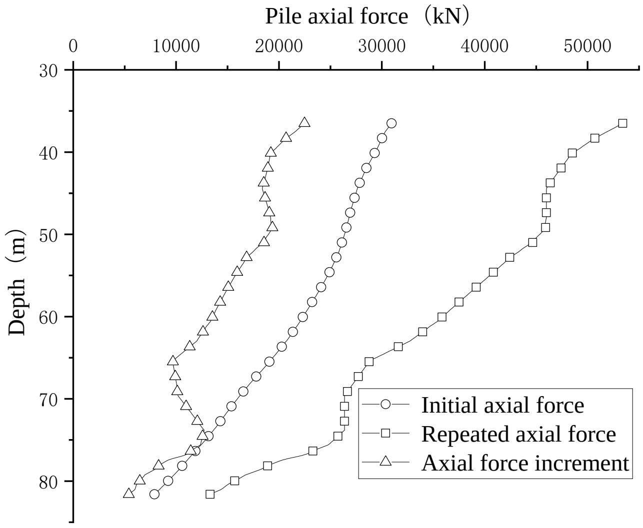

（3）No. 3 pile

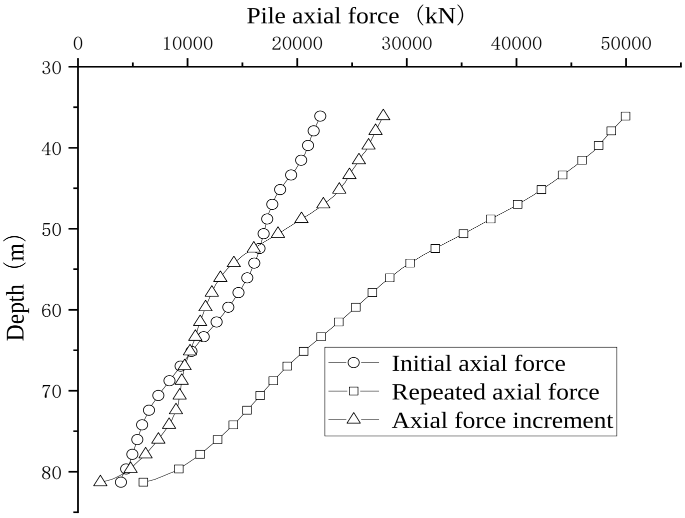

（4）No. 4 pile

Fig. 2 – Initial driving and repeated driving of axial force

Comparison of bearing capacity

The bearing capacity of large-diameter monopiles can be calculated by Equation (1) according to the side resistance per unit area and pile tip resistance per unit area in Table 1.

$$Q_u = Q_{su} + Q_{pu} = u_i \sum l_i q_{sui} + A_p q_{pu} \tag{1}$$

Where Q_u is the bearing capacity of monopile, Q_{su} is the total side resistance, Q_{pu} is the total tip resistance, u_i is the circumference of pile in layer i, l_i is the thickness of layer i, q_{sui} is unit side resistance of layer i, q_{pu} is unit tip resistance of layer i, and A_p is pile tip area.

The calculation results of No. 1-4 piles are compared with the measured values as shown in Figure 3.

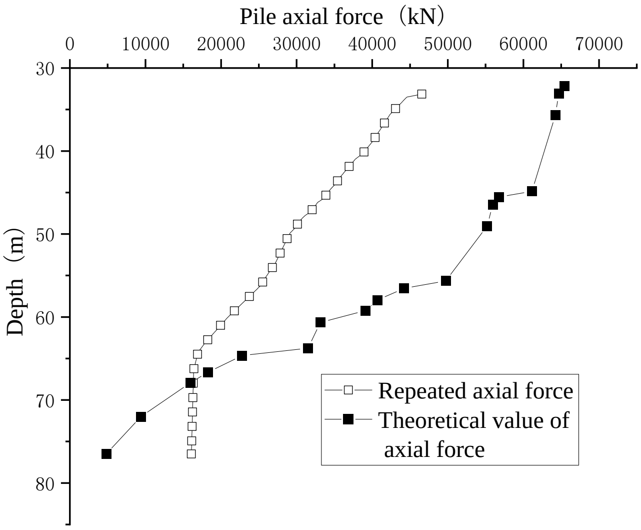

(1）No. 1 pile

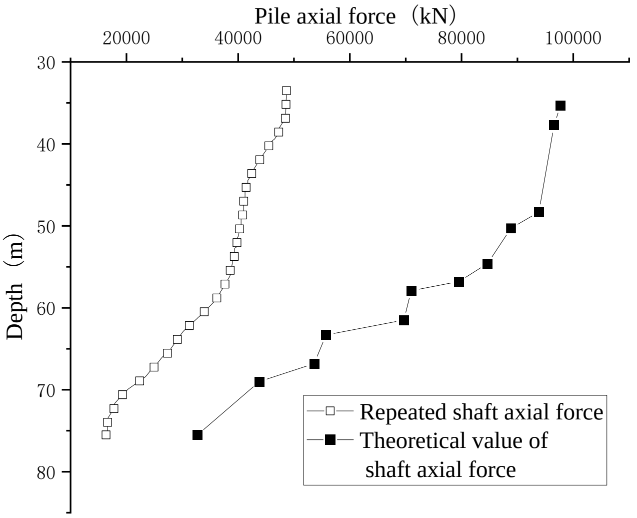

(2）No. 2 pile

Fig. 3 – Repeated driving and theoretical value of axial force

DOI 10.14311/CEJ.2022.03.0037

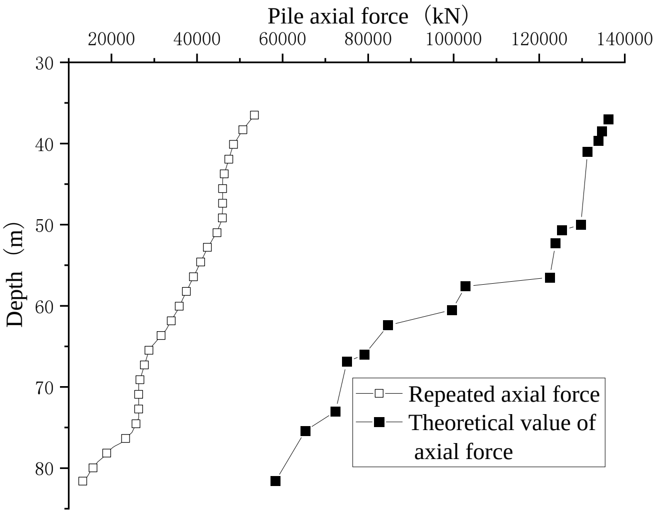

(3) No. 3 pile

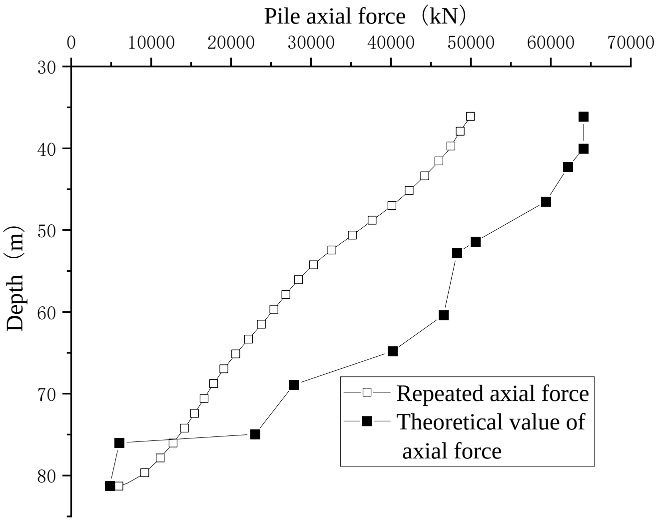

(4) No. 4 pile

Fig. 3 – Repeated driving and theoretical value of axial force

According to literature [15], the axial force of the pile can be recovered by more than 90% after being driven for 6d. The rest period of this test is far beyond 6d, and the soil shear test parameters obtained from the indoor test cannot accurately calculate the axial force. It can be seen from Figure 3 that there is a huge difference between the measured value and the calculated value. Therefore, a more effective way is needed to predict the axial force.

Depth fitting method

Since the time-dependent increase of side resistance and tip resistance is relatively discrete, it cannot be calculated based on the stressed area and the strength per unit area. However, the change of the axial force increment shows a good linear relationship with the depth, as shown in Figure 4, and the axial force increment has a relatively consistent change trend, which can be predicted according to formula (2), with a good assurance rate.

$$\Delta Q = -415\mathrm{h} + 36315 \pm l \tag{2}$$

Where, ΔQ is the axial force increment (kN), h is the depth (m), and l is the upper and lower limit adjustment coefficient of 95% prediction band (5460kN in this example).

The existing large-diameter monopiles have high strain detection after the pile penetration process. The pile shaft axial force lower limit value with a 95% assurance rate can be superimposed on the initial driving bearing capacity to provide a good basis for the design.

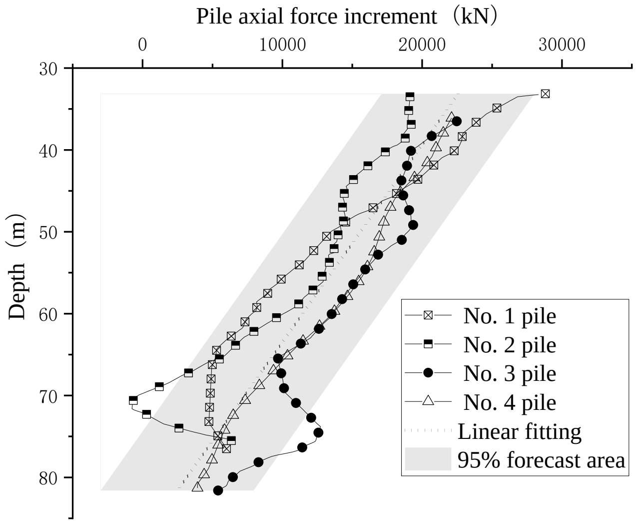

Fig. 4 –Variation trend of axial force increment

CONCLUSION

Due to the disturbance of the soil around the pile during the driving process, the bearing capacity of the driven pile is difficult to be calculated by the existing formula. Based on the initial high strain detection and repeated high strain detection, this paper explores the time-dependent increments in tip resistance, side resistance and total resistance, and believes that the bearing capacity of monopiles cannot be accurately predicted by soil shear and compression parameters, and the axial force increment of monopiles is closely related to depth, which can be accurately predicted by formulas. The main conclusions are as follows:

(1) The total resistance of offshore large diameter monopiles increases by 65%-162% after the 10d-84d rest period.
(2) A method for predicting the time-dependent increment of bearing capacity of offshore large-diameter monopiles is proposed;
(3) In this paper, the prediction is only based on 7.2m-7.4m large diameter monopiles, and the time-dependent of another diameter monopiles still needs to be further verified.

REFERENCES

[1] Xiaoni Wu, Yu Hu, Ye Li, et al. Foundations of offshore wind turbines: A review, Renewable and Sustainable Energy Reviews, 2019, 104: 379-393

[2] Subhamoy Bhattacharya. Design of Foundations for Offshore Wind Turbines, 1st ed.; John Wiley & Sons Ltd.: Chichester, UK, 2019.

[3] Jit Kheng Lim, Barry Lehane. Time effects on shaft capacity of jacked piles in sand, Canadian Geotechnical Journal, 2015, 52: 1830-1838. https://doi.org/10.1139/cgj-2014-0463

[4] Suchun Yang, Junwei Liu, Ankit Garg, et al. Analytical solution for estimating bearing capacity of a closed soil plug: Verification using an On-Site static pile test, Journal of Marine Science and Engineering, 2020, 8: 490. https://doi.org/10.3390/jmse8070490

[5] Suchun Yang, Junwei Liu, Longfei Xu, et al. A new approach to explore the surface profile of clay soil using white light interferometry, Sensors, 2020, 20: 3009. https://doi.org/10.3390/s20113009

[6] Suchun Yang, Junwei Liu, Mingyi Zhang, et al. Analytical solution and field test of critical bearing capacity and settlement of pile tip, CIVIL ENGINEERING JOURNAL-STAVEBNI OBZOR, 2020, 1: 61-74. https://doi.org/10.14311/CEJ.2020.01.0006

[7] Suchun Yang, Mingyi Zhang, Songkui Sang. Dem study on the penetration of jacked piles into layered soft clay, CIVIL ENGINEERING JOURNAL-STAVEBNI OBZOR, 2020, 3: 370-384. https://doi.org/10.14311/CEJ.2020.03.0033

[8] Yang Su-Chun, Zhang Ming-Yi, Wang Yong-Hong, et al. Field test on pile tip resistance of closed-end jacked pipe pile penetrating into layered foundation, ROCK AND SOIL MECHANICS, 2018, 39: 91-99. https://doi.org/10.16285/j.rsm.2018.0961

[9] American Petroleum Institute. Planning, designing, and constructing fixed offshore platforms: working stress design. American Petroleum Institute; 2014.

[10] G. L. DNV. Design of offshore wind turbine structures, DNV GL: Oslo, Norway, 2014.

[11] Matlock H. Correlations for design of laterally loaded piles in soft clay. Proceedings of the 2nd Annual Offshore Technology Conference. Houston: Texas, 1970.

[12] Lymon C. Reese, Robert C. Welch. Lateral loading of deep foundations in stiff clay, Journal of the Geotechnical engineering division, 1975, 101: 633-649

[13] Bin Zhu, Zhou-Jie Zhu, Tao Li, et al. Field tests of offshore driven piles subjected to lateral monotonic and cyclic loads in soft clay, Journal of Waterway Port Coastal and Ocean Engineering, 2017, 143. https://doi.org/10.1061/(ASCE)WW.1943-5460.0000399

[14] Huxinghao, Wang Xing, Lou Xueqian, et al. experimental study on timeliness of large diameter steel pipe piles under complex geological conditions at sea, ocean engineering, 2019, 37: 93-100.

[15] Lin Li, Jingpei Li, De An Sun, et al. Analysis of time-dependent bearing capacity of a driven pile in clayey soils by total stress method, International Journal of Geomechanics, 2017, 17: 4016156.

MECHANICAL CHARACTERISTICS AND DEFORMATION LAW OF TUNNEL IN DIATOMITE CONSIDERING VARIOUS SOFTENING CONDITIONS

Wei Fang[1], Huijian Zhang[2], Shufeng Gao[1], Yuchao Zheng[4], Gongning Liu[5]

1. *China Railway Design Corporation, Tianjin, Hebei District, 300000, China; 2876568700@qq.com, 2488247689@qq.com*
2. *Southwest Jiaotong University, Key Laboratory of Transportation Tunnel Engineering, Ministry of Education, Chengdu, No. 111, North Section, Second Ring Road, Jinniu District, 610031, China; huijianz@163.com*
3. *Southwest Jiaotong University, Key Laboratory of Transportation Tunnel Engineering, Ministry of Education, Chengdu, No. 111, North Section, Second Ring Road, Jinniu District, 610031, China; yczh@home.swjtu.edu.cn, 2995484603@qq.com*

ABSTRACT

At present, the research considering multi-factor softening conditions is rarely performed, and the research on the deformation law and mechanical properties of the tunnel in diatomite is even rarer. Diatomite is easy to soften in water, and its physical and mechanical properties change greatly after softening. Therefore, take the high-speed railway tunnel that passes through the diatomite stratum in East China as an example, considering various softening conditions (including softening degree and softening position), the deformation law and mechanical characteristics of the tunnel are obtained, and corresponding suggestions are also put forward according to different softening conditions. The results show that the deformation law and mechanical characteristics of the tunnel are greatly affected by the symmetry of softening part. The deformation of the inverted arch caused by the lower surrounding rock softening of the tunnel is the largest, and the maximum stress occurs at the arch foot when the upper surrounding rock of the tunnel softens. Different softening degrees and positions have a great influence on the mechanical characteristics and deformation law of the tunnel. The results obtained in this paper may provide some important references for similar projects in the future.

KEYWORDS

High-speed railway tunnel, Diatomite layer, Softening degree, Deformation law, Mechanical characteristic

INTRODUCTION

Diatomite stratum is mainly located in Jilin province and Zhejiang Province of China, due to the properties of poor stability and weak bearing capacity, diatomite is prone to collapse when exposed to water [1-2], which is different from other kinds of soil (like sand, silt, etc) [3-6]. Tran and Nguyen [7] used numerical methods to predict the damage area of tunnel lining under blast loads, and the blast peaks on the tunnel construction face was also determined. Guo et al [8] considered the adverse effect of karst seepage effect on the water-resistant rock mass of the karst tunnel and obtained a calculation method for the critical safety thickness of the water-resistant rock mass.

Through various tests on the physical and mechanical properties of diatomite microstructure, it was found that diatomite has a unique porous microstructure and high compressibility, which is closely related to its multiple pores [9-11]. Wang et al [12] analyzed the fractal characteristics and pore structure characteristics of natural diatomite under different consolidation pressures using the principle of image segmentation and optimal threshold method, then the relationship between the consolidation pressures fractal dimension of diatomite and isotropic isobars was obtained. The distribution characteristics and formation mechanism of diatomite landslides were studied based on an actual engineering project, and it was found that the mechanical strength of the soil on the slope was reduced due to the strong stratification and increased expansion, which led to the failure of the lining structure [13,14]. Zhang et al [15] analyzed the genesis, species, soil structure, and chemical composition of diatomite in different regions, and found that the diatomite lithology was not universal.

Water would accelerate the softening and reduce the matrix suction and strength of the soil, and pose a certain threat to the safety of the tunnel in severe cases [16, 17]. Softening degree of the surrounding rock was mainly reflected by water content, and some scholars had carried out some research on it. Wang [18] analyzed the deformation law of tunnels in loess area with moisture content through the test and suggested construction methods with different water contents. The deformation characteristics of tunnels in full-weathered red sandstone and Sigda area under different water contents were studied, and intensified precipitation measures and optimization schemes of tunnel lining parameters were put forward [19, 20]. Ye et al [21] analyzed the influence of water contents on the deformation of tunnels in expansive red clay area and lining structures, and the reserved deformation value for the tunnel was also proposed. The existing research mainly focused on the mechanical properties and engineering properties of slopes in diatomite area [22], while the research on the characteristics of tunnel engineering in diatomite area is rare. The deformation characteristics of tunnel in other soils (such as loess and expansive soil, etc.) had been studied considering softening degree of the surrounding rock, and previous studies mostly focused on the condition of a single variable of water content. However, the research on the deformation law and mechanical properties of tunnels under multiple softening conditions (including the softening degrees and positions) was rarely involved, and the research on the mechanical properties of tunnel in diatomite area was even rarer.

Therefore, in this paper, take the Feifengshan tunnel that passes through the diatomite area in East China as the engineering background, using the numerical simulation method, the influence of softening conditions on the mechanical properties and deformation law of the tunnel is further revealed by considering various softening conditions (including the softening degrees and positions), which may provide a design basis and reference for the related tunnel engineering in diatomite area in the future.

PROJECT OVERVIEW

The Feifengshan Tunnel passes through the diatomite area in East China. Before this, there is no systematic experience in the construction of railway tunnels in diatomite. Also, diatomite shows obvious differences in the origin, species, soil structure, and chemical composition in different regions. The local diatomite properties are not universal and can only be used as a reference. The construction standards for high-speed railway tunnel engineering are high, and because the tunnel is usually buried in the stratum, all mechanical behaviors are closely related to the stratum characteristics. However, at present, there is little construction experience for railway tunnels crossing the diatom area, and diatomite has not been included in the special geotechnical and unfavourable geology in the design specification of railway, its survey methods, treatment principles and empirical parameters are still unclear. Moreover, the engineering properties of tunnel in diatomite area under different softening conditions are unknown. For tunnel engineering in diatomite stratum, how determining the mechanical properties and deformation law of tunnel is the key to ensuring the safety of construction and long-term operation stability of tunnel.

In this paper, based on the Feifengshan tunnel, the mechanical characteristics and deformation law of tunnel in diatomite area under various softening conditions are studied furtherly. The size of the tunnel is: length×clear span×clear height = 115×7.8×7.2 m, and the specific section size of the tunnel lining is shown in Figure 1. The preliminary lining is C25 shotcrete (thickness is

230 mm) and steel arch, and the secondary lining is mainly C30 reinforced concrete (thickness is 400 mm). The specific lining parameters are shown in Table 1.

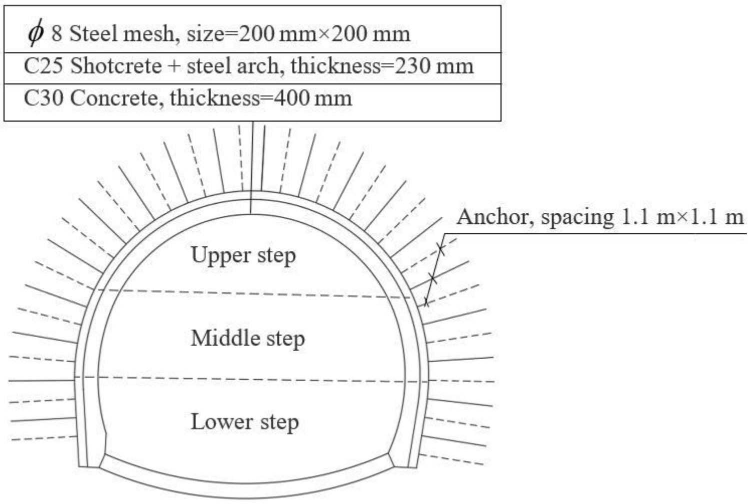

Fig. 1 - Schematic diagram of the tunnel section

Tab. 1: Lining parameters of the tunnel

Preliminary lining										Secondary lining	
C25 shotcrete		Wire mesh (φ8)		Anchor (φ22)			Steel arch			C30 concrete	
Position	Thick	Position	Spacing	Position	Length	Spacing	Position	Size	Spacing	Position	Thickness
Arch wall	230 mm	Arch wall	200×200 mm	Arch wall	3.0 m	1.1×1.1m	Arch wall	I-16	1.0 m	Full ring	400 mm

CALCULATION INSTRUCTIONS OF THE NUMERICAL SIMULATION

Calculation model

Flac3D software is used in this paper, and the typical section of the V-level surrounding rock of the tunnel is selected as the research object. To reduce the boundary effect of the calculation model [23-24], the longitudinal length of the model is selected as 98m, the calculation range is 120 m in the horizontal direction; the buried depth of the tunnel gradually increases from 11.96 m to 32.44 m along the longitudinal direction according to the actual project, and the distance between the tunnel invert and model bottom is 30 m. The excavation method of the tunnel adopts the three-step method, and the specific numerical calculation model as shown in Figures 2~3. Normal constraints are imposed on the sides of the model (namely, the direction of the front, back, left, and right), the bottom boundary of the model is fixed, and the upper boundary is set to free [25]. For the convenience of description, a schematic diagram of the key position of tunnel is drawn, as shown in Figure 4.

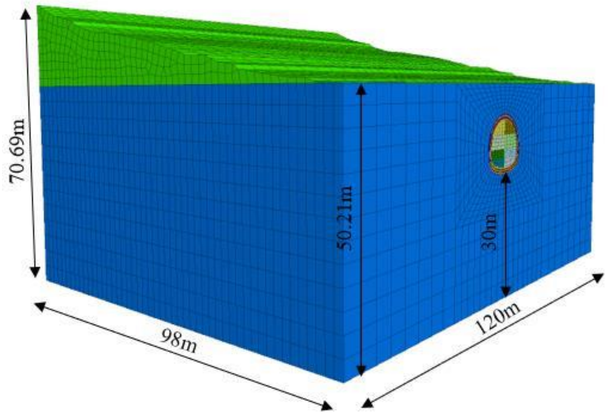

Fig. 2 - Numerical calculation model

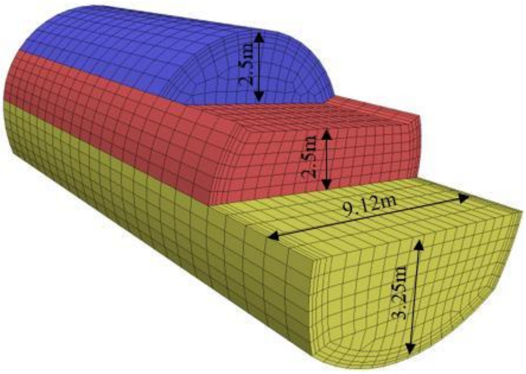

Fig. 3 - Schematic diagram of the construction method

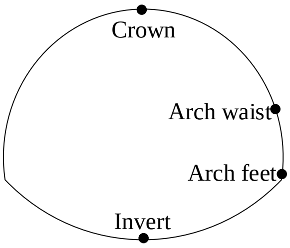

Fig. 4 - Key positions of the tunnel

The surrounding rock and secondary lining are simulated by solid elements, which obey the Mohr-Coulomb criterion and the linear elastic criterion [26], respectively. The effect of the self-weight stress field is considered. The anchor adopts the cable element, the shotcrete adopts the shell element, and the effect of the steel arch is converted to the shotcrete according to its elastic modulus [27]. The specific calculation method is as *Eq*. (1),

$$E = \frac{A_c \times E_c + A_s \times E_s}{E_c + E_s} \tag{1}$$

Where: E is the composite elastic modulus of the preliminary lining or secondary lining; A_c is the cross-sectional area of the concrete; E_c is the elastic modulus of concrete; A_s is the cross-sectional area of steel bar; E_s is the elastic modulus of the steel arch.

Calculation parameters and softening conditions

According to the geological data, diatomite is easy to soften by water, so several groups of conditions with different softening degrees are set up in this paper, namely softening conditions I~V (refer to the water content: 35%, 40%, 45%, 50%, 55%, respectively). The specific calculation parameters of surrounding rock and lining are shown in Tables 2 ~ 3.

Tab. 2: Calculation parameters of the lining

Lining type	Density /(kg/m^3)	Elastic Modulus /GPa	Poisson's ratio	Lining thickness /m
Preliminary lining	2500	25.5	0.30	0.23
Secondary lining	2500	32.0	0.30	0.40

Tab. 3: Calculation parameters of surrounding rock with different softening conditions

Softening condition	Density /(kg/m^3)	Elastic Modulus /MPa	Poisson's ratio	Cohesion /kPa	Internal friction angle /°
I	1900	28.37	0.35	42.23	19.45
II	1900	26.65	0.35	38.74	18.23
III	1900	24.93	0.35	35.25	17.00
IV	1900	23.21	0.35	31.76	15.78
V	1900	21.49	0.35	28.27	14.55

When the tunnel passes through the diatomite area, there are also some differences in the softening degree of surrounding rock in different positions, which will affect the stress and deformation of the tunnel. The present range of the softening conditions of surrounding rock is conditions 1~6, as shown in Figure 5. For different softening positions around the tunnel (the area marked in red in Figure 5) is the *II ~ V* parameter, while the white area is still kept as the *I* parameter in Figure 4. Considering the influence of different softening degrees (*I~V*) and softening positions (1~6) of the surrounding rock in diatomite stratum, the deformation law and mechanical properties of the tunnel are comparatively analyzed.

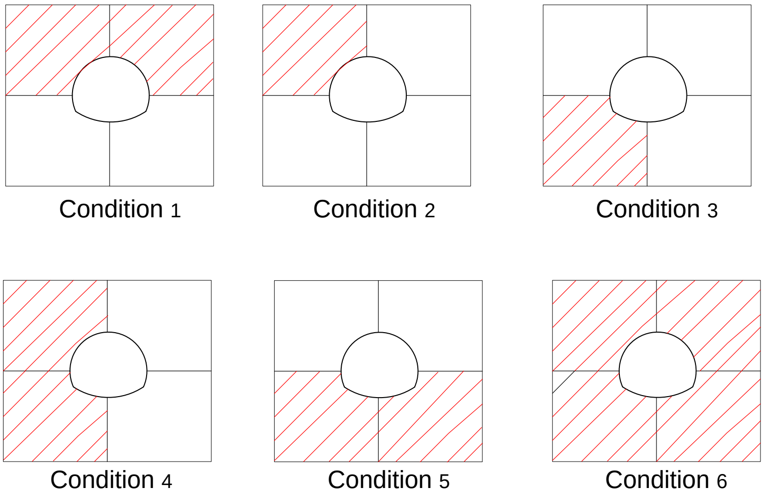
Condition 1
Condition 2
Condition 3
Condition 4
Condition 5
Condition 6

Fig. 5 - Schematic diagram of the calculation conditions for different softening positions of the surrounding rock

DEFORMATION LAW AND MECHANICAL CHARACTERISTIC OF TUNNEL IN DIATOMITE AREA CONSIDERING VARIOUS SOFTENING CONDITIONS

Considering that the spatial effect and boundary conditions of tunnel excavation may have a certain influence on the calculation results, the 50 m section of the middle part of the model is selected as the monitoring section, the deformation law and mechanical properties of the tunnel under different softening degrees and positions of the surrounding rock are studied in detail.

Deformation law of the tunnel

The overall deformation of the tunnel is analyzed when the softening positions of the surrounding rock are distributed symmetrically and asymmetrically (here, only the case when the largest softening degree of the surrounding rock is considered, that is, the parameter of condition V), the control group is the case when all positions of the tunnel surrounding rock adopting the parameter of condition I, as shown in Figure 6.

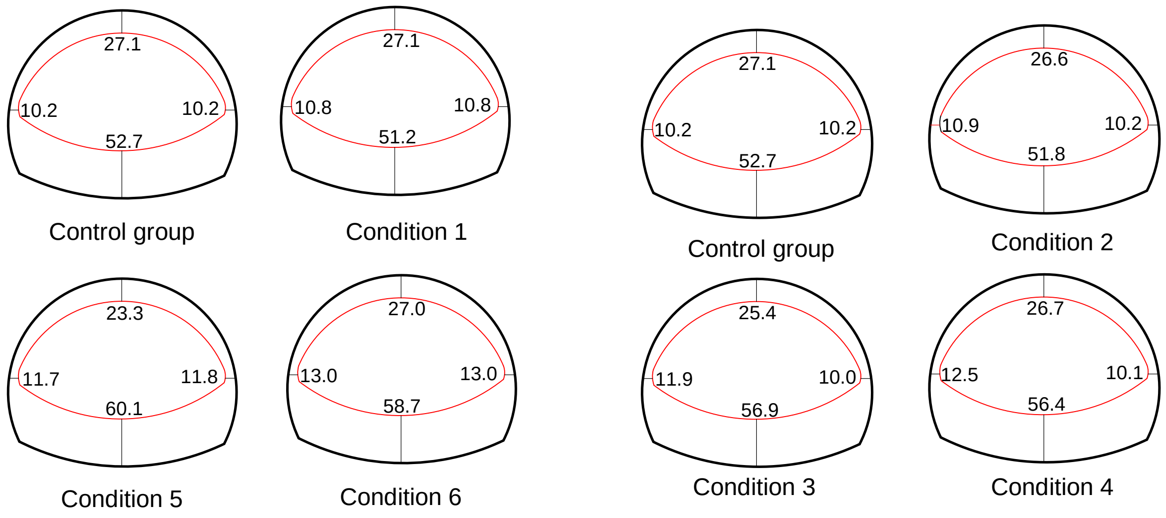

(a) Symmetrical condition *(b) Asymmetric condition*

Fig. 6 - Distribution law of tunnel deformation under different arrangements of softening positions /mm

In Figure 6-(a), under the same conditions, when the softening positions of the surrounding rock are distributed symmetrically, the distribution of horizontal displacement of the arch waist on both sides of the tunnel section is basically symmetrical and the difference is less than 0.1 mm. Comparing the crown settlement of different conditions, it can be found that the settlement values of condition 1 and condition 6 are very close, and the minimum value of crown settlement occurs in condition 5. This is because compared to other conditions (1, 2, 4), the upper half of the tunnel in condition 5 is non-softened, and the softened part is far away from the crown. Compared with condition 3 (one-sided softening), the left and right side are symmetrically softened in condition 5, so the settlement of condition 5 is more uniform and shows the minimum value. As shown in Figure 6-(b), under the same conditions, when the softening positions are distributed asymmetrically, the tunnel deformation is asymmetric, the difference of horizontal displacement at the arch waist of surrounding rock can be up to 2.4 mm, and the value of horizontal position at the side with higher softening degree is larger. In addition, it can be found that the influence degree of different softening degree of surrounding rock on different positions of the tunnel decreases in turn from invert displacement, crown settlement and horizontal displacement of arch waist.

The variation low of the displacement at the key positions of the tunnel with different softening degrees and positions are shown in Figures 7~9.

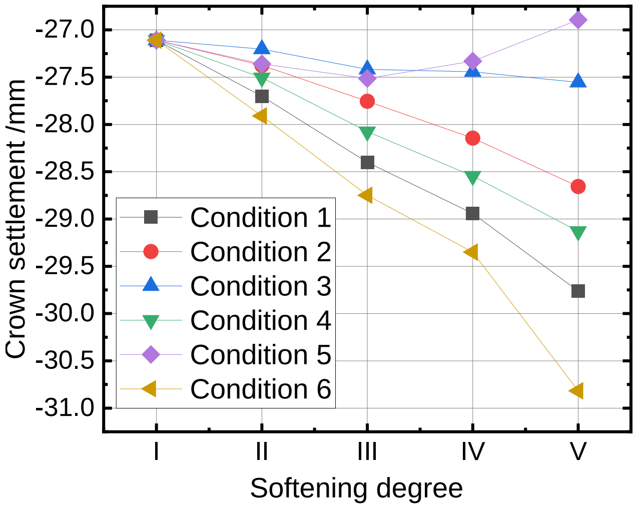

Fig. 7 - Crown settlement of the tunnel under different softening degrees and conditions

In Figure 7, the crown settlement of condition 5 increases first and then decreases with the increase of softening degree, but the change value is small (less than 1mm), and the crown settlement of the other conditions increases with the softening degree. The maximum variation value of condition 6 is 3.7 mm, which is 13.7% higher than the initial value of 27.1 mm. At the same time, it can be seen that the settlement curve changes approximately linearly when the softening degree is I~IV. But there is an inflection point at softening degree IV when the softening degree is I~V, which indicates that the settlement will increase sharply when the softening degree is large. Therefore, the monitoring should be strengthened to prevent excessive deformation of the tunnel for rock areas with severe softening.

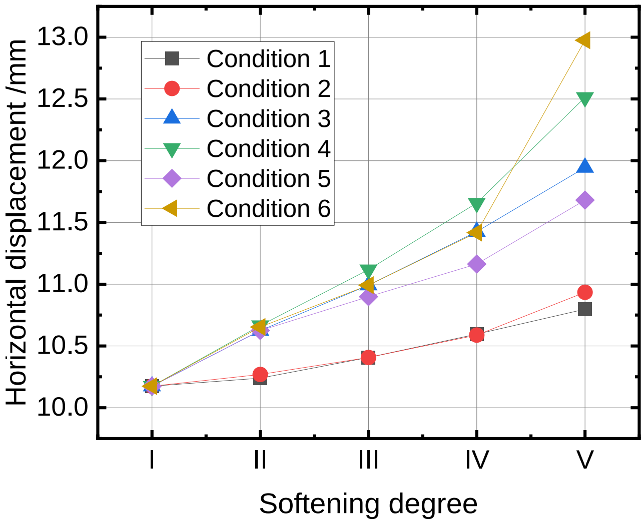

Fig. 8 – Horizontal displacement of arch waist of the tunnel under different softening degrees and conditions

In Figure 8, the horizontal displacement of the arch waist increases with the softening degree of the surrounding rock. Among them, the horizontal displacement of conditions 4 and 6 increased faster, followed by conditions 3 and 5, while the increasing trend of conditions 1 and 2 is the slowest and the difference between them is small. As the softening degree (conditions 4 and 6) increases, the horizontal displacement changes greatly. Compared with the initial value of 10.2 mm, the horizontal displacement of conditions 4 and 6 increases by 23% and 27.5%, respectively, which indicates that unilateral softening and overall softening have a great influence on the horizontal displacement of tunnel.

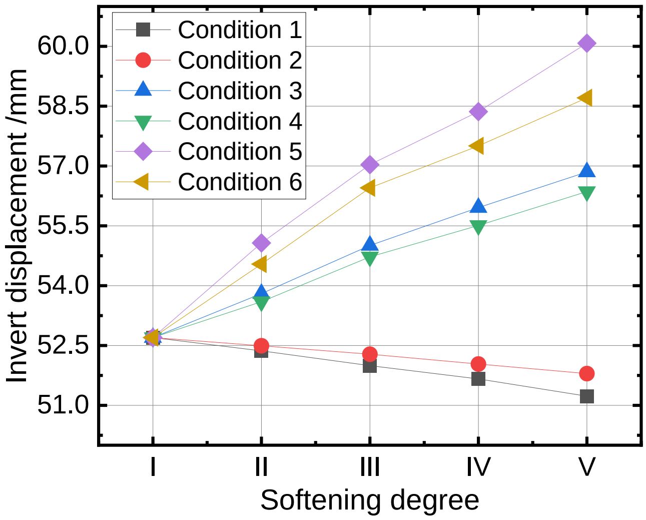

Fig. 9 – Invert displacement of the tunnel under different softening degrees and conditions

In Figure 9, the displacement of the invert under different softening conditions mainly shows three trends with the increase of softening degree: (1) conditions 1 and 2 show a decreasing trend, and the change value from the softening degree I to V is about 1.5 mm, which is 2.8% lower than the initial value. (2) Conditions 3 and 4 show a slow increase trend, and the change value from the softening degree I to V is about 4mm, which is 7.8% higher than the initial value. (3) Compared with other conditions, conditions 5 and 6 show the fastest growing trend, and the change value from the softening degree I to V is about 7 mm, which is 14% higher than the initial value. The line curve of "condition I and II", "condition III and IV", "condition V and VI" is very close, respectively. This is because the softening parts of conditions I and II, III and IV, V and VI are relatively similar, such as both softening in the top left and top right, in whole or part. In addition, since both V and VI are fully softened at the lower part of the tunnel, and the displacement of the invert is monitored, the displacement of the two is larger than that of other conditions.

In conclusion, the softening on the left side or the overall upper part of the tunnel has little effect on the horizontal displacement of the tunnel waist. The settlement of crown and horizontal displacement of arch waist increase with the softening degree of surrounding rock. Comparing all softening conditions, it can find that softening above the tunnel has the least influence on the displacement of the inverted arch, while softening below the tunnel has the greatest influence. The invert displacement of the condition when the surrounding rock of tunnel is softening as a whole is smaller than that of only the lower part of the surrounding rock is softened.

Mechanical characteristics of the tunnel

The schematic diagram of the mechanical characteristics of the tunnel with different softening degrees and positions is shown in Figure 10.

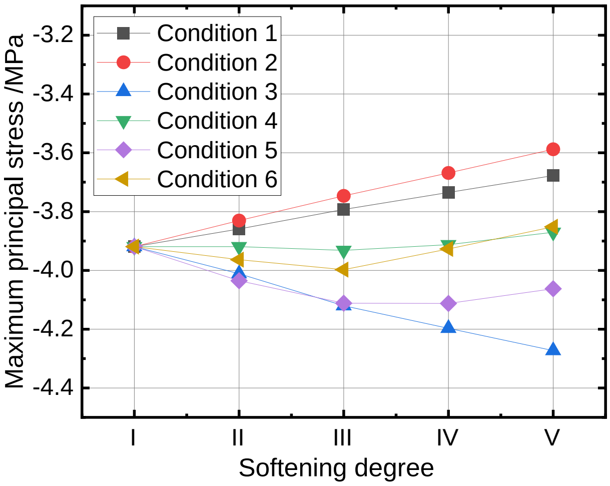

(a) Left arch foot

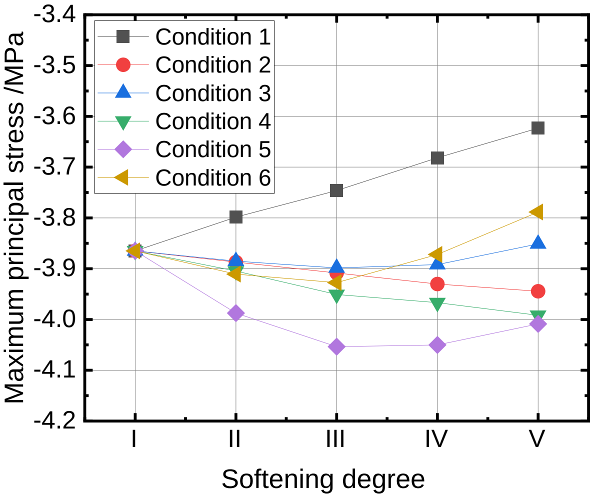

(b) Right arch foot

Fig. 10 - Change law of the mechanical characteristics of the tunnel

In Figure 10, the changing trend of maximum principal stress of the left and right foot of the tunnel is basically the same in conditions 1, 5, and 6 (the softening positions of the surrounding rock are symmetrically distributed) with softening degree. However, the changing trend of the maximum principal stress of the left and right arch foot of tunnel with softening degree is completely different in conditions 2, 3, and 4 (namely, asymmetric distribution of softening positions). In condition 1, the maximum principal stress of the left and right foot of the tunnel gradually decreases with the increase in softening degree, and the maximum principal stress decreases by 6.17%. For condition 2, when the softening degree increases, the maximum principal stress of the left arch foot decreases, while that of the right arch foot increases, and the maximum principal stress increases by 2.06%.

For condition 3, the maximum principal stress of the left arch foot of the tunnel increases with softening degree, while that of the right arch foot of the tunnel increases first and then decreases, and the maximum principal stress increases by 9.02%. For condition 4, when the softening degree increases, the maximum principal stress of the left arch foot shows the trend of “first increases and then decreases”, while that of the right arch foot of the tunnel increases, and the maximum principal stress increases by 3.28%. In conditions 5 and 6, the maximum principal stress of the left and right arch foot increases first and then decreases with softening degree, reaching the maximum value in softening degree III, and the maximum principal stress is increased by 3.66% and 1.72%, respectively.

To sum up, it can be concluded that the softening of the surrounding rock at the lower left corner of the tunnel has a great influence on the mechanical properties of the left arch foot, while the overall softening has a great influence on the mechanical properties of the right arch foot of the tunnel and the maximum principal stress is the largest. At the same time, it can also be found that when the surrounding rock above the tunnel is softened as a whole, the stress at the arch foot of the tunnel is the smallest.

CONCLUSION

Based on the actual engineering, the deformation law and mechanical characteristics of the tunnel under different softening degrees and positions are further analyzed in this paper, and the main conclusions are as follows:

(1) When the softening positions are distributed symmetrically, the tunnel deformation is basically symmetrical, but when the softening positions of the surrounding rock are distributed asymmetrically, the horizontal displacement of the arch waist is larger on the side with higher softening degree. Under different softening conditions, the change value of the invert displacement (uplift) caused by the softening at the invert is the highest, which is higher than that when the surrounding rock is softened in a whole.

(2) The softening of the left side or the overall softening above the tunnel has little effect on the horizontal displacement of the tunnel waist. The greater the softening degree, the greater the crown settlement and the horizontal displacement of the arch waist. The softening of the surrounding rock above the tunnel has the least impact on the uplift value of the invert, while the softening below the tunnel has a greater impact on it. The uplift of the invert displacement in the condition when the surrounding rock softens in a whole is smaller than that of only the lower part of the tunnel is softened.

(3) When the softening positions are distributed symmetrically, the maximum principal stress at the left and right arch foot of the tunnel is consistent with softening degrees, while that of the asymmetric conditions is completely different. The softening at the lower left corner of the tunnel has a great influence on the mechanical properties of the left arch, while the overall softening has a great influence on the right arch foot, and the stress is the largest. On the other hand, when the surrounding rock above the tunnel is softened as a whole, the stress at the arch foot is the least.

CONFLICTS OF INTEREST

The authors declare no conflicts of interest.

DATA AVAILABILITY

All data, models, and code generated or used during the study appear in the submitted article.

ACKNOWLEDGMENTS

This work was supported by the National Natural Science Foundation of China (Grant number: 52178395) and the Program of China Railway Design Corporation (Grant number: 721812).

REFERENCES

[1] Zhang, Y.S., Guo, C.B., Qu, Y.X., et al, 2012. Discovery of swelling diatomite at Tengchong, Yunnan province and its implication in engineering geology. Journal of Engineering Geology, Vol. 20, 266-275.

[2] Li, P.F., 2013. Experimental investigation on the stress-strain characteristics of diatomite. Master's Thesis, Dalian University of Technology, Dalian.

[3] Qin, Y.W., Lai, J.X., Yang, T., et al, 2022. Failure analysis and countermeasures of a tunnel constructed in loose granular stratum by shallow tunnelling method. Engineering Failure Analysis, Vol.141, 106667. https://doi.org/10.1016/j.engfailanal.2022.106667

[4] Ma, L.X., Jin, Y.F., Zhang, C., et al, 2022. Study on long-term settlements of composite stratum of clay and silt and metro tunnel in it due to train operation. Journal of Southwest Jiaotong University, 1-10.

[5] Qin, Y.W., Qiu, J.L., Lai, J.X., et al, 2022. Seepage characteristics in loess strata subjected to single point water supply. Journal of Hydrology, Vol. 609, 127611. https://doi.org/10.1016/j.jhydrol.2022.127611

[6] Zhou, A., Wang, B., Li, J.T., et al, 2022. Long-term stability analysis and deformation prediction of soft soil foundation pit in Taihu Tunnel. Journal of Zhejiang University, Vol. 56, 692-701. https://doi.org/10.3785/j.issn.1008-973X.2022.04.008

[7] Tran, T. M. and Nguyen, Q. H., 2021. Effect of blasting on the stability of lining during excavation of new tunnel near the existing tunnel. Civil Engineering Journal, Vol. 301, 47-62. https://doi.org/10.14311/CEJ.2021.01.0004

[8] Guo, J.Q., Wu, W.L., Liu, X.L., et al, 2022. Theoretical analysis on safety thickness of the water-resistant rock mass of karst tunnel face taking into account seepage effect. Geotechnical and Geological Engineering, Vol. 40, 697-709. https://doi.org/10.1007/s10706-021-01916-7

[9] Hong, Z.S., Li, S.Y.X., Deng, Y.F., 2004. Relationship between entrance pore distribution and stress level of natural sedimentary diatomaceous soil. Rock and Soil Mechanics, 1023-1026.

[10] Hong, Z.S., Li, S.Y.X., Deng, Y.F., 2004. Mechanical behavior of a strongly-structured natural sedimentary soil. Rock and Soil Mechanics, 1201-1204. https://doi.org/10.16285/j.rsm.2004.08.005

[11] Fang, Y.Y., Jiang, J., Jiang, H.H., 2019. Research on the microstructure and the mechanical properties of Shengzhou diatomite. Low Temperature Architecture Technology, Vol. 41, 75-77. https://doi.org/10.13905/j.cnki.dwjz.2019.02.021

[12] Wang, Y.X., Ji, F., Gu, H.D., et al, 2017. Fractal characteristics of natural sedimentary diatomaceous earth based on SEM images. Hydro-science and Engineering, 96-102. https://doi.org/10.16198/j.cnki.1009-640x.2017.05.014

[13] Guo, C.B., Zhou, N.J., Fu, X.X., et al, 2013. The optimization design of the research on the formation mechanism, prevention and control of landslide along clayey diatomite highway in Tengchong, Yunnan Province. Geological Bulletin of China, Vol. 32, 2021-2030.

[14] Guo, Y.K., Ma, Q.H., Guo, Z.S., 2018. Numerical analysis of tunnel deformation and stress behavior of support under rainfall infiltration. Journal of Civil Engineering and Management, Vol. 35, 52-57. https://doi.org/10.13579/j.cnki.2095-0985.2018.04.008

[15] Zhang, Y.S., Guo, C.B., Qu, Y.X., et al, 2013. Research on mechanical properties of swelling diatomite and their geohazard effects. Rock and Soil Mechanics, Vol. 34, 23-30. https://doi.org/10.16285/j.rsm.2013.01.024

[16] Zhang, R. and Yang, X.L., 2018. Limit analysis of active and passive mechanisms of shallow tunnels in nonassociative soil with changing water table. International Journal of Geomechanics, Vol. 18, 04018063. https://doi.org/10.1061/(ASCE)GM.1943-5622.0001167

[17] Fan, S.Y., Song, Z.P., Zhang, Y.W., et al, 2020. Case study of the effect of rainfall infiltration on a tunnel underlying the roadbed slope with weak inter-layer. KSCE Journal of Civil Engineering, Vol. 24, 1607-1619. https://doi.org/10.1007/s12205-020-1165-0

[18] Wang, X.D., 2018. Deformation characteristics and construction method for large section loess tunnel with high water content. Railway Engineering, Vol. 58, 59-61.

[19] Wang, Z.J. and Yang, Y., 2017. Research on effect of moisture content on initial support safety of large cross-section tunnel in Xigeda Fm strata. Railway Standard Design, Vol. 61, 100-105. https://doi.org/10.13238/j.issn.1004-2954.2017.11.021

[20] Zhou, P., Wang, Z.J., Xu, H.Y., et al, 2017. Stability and sub-classification study on the tunnel surrounding rock of Xigeda strata considering the influence of moisture content. China Civil Engineering Journal, Vol. 50, 97-110. https://doi.org/10.15951/j.tmgcxb.2017.12.012

[21] Ye, W.J., Cui, C.Y., Xie, Z.W., et al, 2019. Influence of water content difference on construction mechanical behavior of expansive red clay tunnel. Tunnel Construction, Vol. 39, 1940-1948.

[22] Gao, H.X., Yin, K.L., Zhou, C.M., 2007. Diatomite landslides stability analysis and time forecast. Journal of Northwest University, 127-130.

[23] Shi, Y.F., Cao, C.W., Tan, Y.F., et al, 2022. Study on dynamic response and long-term settlement of water-saturated weathered soft rocks at the base of subway tunnels. Modern Tunnelling Technology, Vol. 59, 86-95. https://doi.org/10.13807/j.cnki.mt.2022.02.011

[24] Qiu, J.L., Fan, F.F., Zhang, C.P., et al, 2022. Response mechanism of metro tunnel structure under local collapse in loess strata. Environmental Earth Sciences, Vol. 81, 164. https://doi.org/10.1007/s12665-022-10256-5

[25] Liu, J.G., 2022. Study on the influence of construction sequence on the crossing tunnel with ultra-small distance. Modern Tunnelling Technology, 1-7.

[26] An, Y.L., Li, J.H., Zhou, J., et al, 2022. Construction optimization and dynamic proximity zoning of upper and lower interchange tunnels. Journal of Railway Science and Engineering, Vol.19, 470-479. https://doi.org/10.19713/j.cnki.43-1423/u.t20210214

[27] Wu, B., Gao, B., Suo, X.M., et al, 2005. Mechanical simulation and analysis of construction behavior of urban metro tunnelling with small interval. China Journal of Highway and Transport, 84-89. https://doi.org/10.19721/j.cnki.1001-7372.2005.03.019